Reduced-Order Aerothermoelastic Analysis of Hypersonic Vehicle Structures

by

Nathan J. Falkiewicz

A dissertation submitted in partial fulfillment
of the requirements for the degree of
Doctor of Philosophy
(Aerospace Engineering)
in The University of Michigan
2012

Doctoral Committee:

Professor Carlos E. S. Cesnik, Chair
Professor Sherif El-Tawil
Associate Professor Joaquim R. R. A. Martins
Senior Aerospace Engineer Stephen Michael Spottswood, AFRL

To my parents.

Acknowledgments

This dissertation would not have been possible without all of the support that I have received throughout my studies. I would like to thank my parents, Rick and Julie Falkiewicz, for their never-ending love and encouragement. They have given me to opportunity to succeed and without them I would not be where I am today. For all of their time and devotion, I will be forever grateful. Thanks to my brother, Tim Falkiewicz, for always being willing to offer advice when I needed it. I would also like to thank my grandparents, aunts, and uncles for their constant encouragement.

I could not have gotten to this point without the mentoring of my advisor, Prof. Carlos Cesnik. I would like to sincerely thank Prof. Cesnik for his dedication to my development both as a student and as a person. He has given me the freedom to pursue my specific research interests and has never failed to provide support and direction when it was needed. Prof. Cesnik has challenged me to push the limits of my ability and has enabled me to grow as a researcher and engineer. I am especially grateful for the opportunities he has provided for me to attend technical conferences which have been instrumental in broadening my knowledge and exposing me to a broad spectrum of research areas. My time spent under Prof. Cesnik has provided me with skills that will be invaluable throughout my engineering career. I would also like to thank the rest of my dissertation committee, Prof. Sherif El-Tawil, Prof. Joaquim Martins, and Dr. S. Michael Spottswood, for their time and contributions to my dissertation. This dissertation has also benefited from valuable insights that I have received throughout the years. I would like to thank Dr. Michael Bolender, Dr. David Doman, and Dr. Michael Oppenheimer at the Control Design and Analysis Branch

of the Air Force Research Laboratory for their interactions regarding flight dynamics and control considerations of hypersonic vehicles. With regard to aerothermal modeling aspects of the research, the contributions and collaborations of Prof. Jack McNamara and Mr. Andrew Crowell of The Ohio State University have been instrumental in completing the reduced-order aerothermoelastic framework presented in this dissertation. Also, I would like to thank Dr. S. Michael Spottswood at the Structural Sciences Center of the Air Force Research Laboratory for his insights and discussions regarding reduced-order modeling of structures.

My time at the University of Michigan would not have been the same without the countless friends I have made. I am grateful for the friendships and support of Torstens Skujins, Scott Stapleton, Jorge Pernillo, Wonbin Hong, Justin Jackson, and Ben Hallissy. My labmates Devesh Kumar, Kalyan Nadella, Carlos de Souza, Weihua Su, and Ken Salas have made for an enjoyable environment both in and out of school. Thank you to my fellow hypersonics team members at the University of Michigan, Sean Torrez, Derek Dalle, Scott Frendreis, and Matt Fotia for making the project a fun and memorable experience. I would also like to thank my roommate, Chris Salzman, for his companionship during the end of my time in Ann Arbor. Finally, I extend my gratitude to my officemates Mike Sekerak, Matt Obenchain, and Jessica Jones for providing a fun and pleasant environment to work in every day.

I would like to acknowledge the staff of the aerospace department, as their contributions truly have a significant impact on keeping the department running smoothly. My sincere appreciation goes to Denise Phelps for her dedication to the department and her willingness to help me out in any way possible, whether it be school-related or personal. With regard to computer and server issues, I would like to thank Dave McLean for always being more than generous with his time in helping resolve whatever problems I have encountered. I would also like to thank Suzanne Smith for her kind assistance in helping me with any administrative questions or issues that arose.

Finally, I would like to acknowledge the financial support provided by the Air Force Research Laboratory/Air Vehicles Directorate through the Michigan-AFRL Collaborative Center in Control Science under grant number FA 8650-07-2-3744 with Dr. Michael Bolender as program manager. This support is gratefully acknowledged.

Table of Contents

List of Figures

Figure

List of Tables

Table

List of Abbreviations

AFRL Air Force Research Laboratory

BC boundary condition

CFD computational fluid dynamics

DARPA Defense Advanced Research Projects Agency

DCM dynamic correction method

DMAP direct matrix abstraction program

DOF degree of freedom

EELV evolved expendable launch vehicle

EOM equations of motion

ERM elementary reduced model

FDM force-derivative method

FEA finite element analysis

FEM finite element model

HSV hypersonic vehicle

LHS latin hypercube sampling

MAC modal assurance criterion

MAM mode-acceleration method

MASIV Michigan/AFRL Scramjet In Vehicle

MDM mode-displacement method

MDO multidisciplinary design optimization

NASP National Aerospace Plane

NRMSE normalized root mean squared error

POD proper orthogonal decomposition

ROAM reduced-order aerothermal model

RLV reusable launch vehicle

ROM reduced-order model

SVD singular value decomposition

TPS thermal protection system

List of Symbols

A	=	POD snapshot matrix, area
a	=	speed of sound
$a^{(j)}$	=	j-th snapshot corresponding to j-th column of A
$\breve{a}^{(j)}$	=	j-th thermal snapshot after normalization to unit magnitude
B	=	shape function derivative matrix
b	=	right hand side vector of recurrence relation for numerical time stepping algorithm, kriging input vector
C	=	POD correlation matrix
$C(b, X)$	=	kriging correlation matrix
C_p	=	coefficient of pressure
c	=	POD modal coordinates, chord length
$\tilde{c}$	=	POD modal coordinate of diagonalized thermal system
c_f	=	skin friction coefficient
c_p	=	specific heat at constant pressure
D	=	number of degrees of freedom in element, elasticity tensor
d	=	vector of structural modal coordinates
E	=	Young's modulus of elasticity
e	=	spatial error norm

F_b = vector of body forces

F_S = structural load vector of full system in physical space

F_T = thermal load vector of full system in physical space

Full = solution vector of full-order model

f_i = fuselage ordinary natural frequencies

f_S = generalized structural load vector of reduced system in modal space

G = incident irradiation

G = Gaussian correlation function for kriging model

G_T = transformed thermal load vector of full system in physical space

$\tilde{g}$ = generalized thermal load vector after diagonalization of coefficient matrices

$g(b, X)$ = correlation vector between untried point and sample data

g_T = generalized transformed thermal load vector of reduced system in modal space

H_i = coefficient matrices in numerical integration for structural response

$H(t)$ = scalar time-dependent coefficient, Heaviside step function

h = convective heat transfer coefficient, altitude, enthalpy

h_i = thickness of i-th layer

I = identity matrix

J = finite element Jacobian matrix

K_G = geometric stiffness matrix

K_S = structural stiffness matrix

K_S^* = modified structural stiffness matrix

K_T = thermal conductivity matrix of full system in physical space

k_S = generalized structural stiffness matrix

k_S^* = generalized modified stiffness matrix of reduced system in modal space

k_T = generalized thermal conductivity matrix of reduced system in modal space

$\tilde{k}_T$ = generalized thermal conductivity matrix after diagonalization

L = coefficient matrix of recurrence relation for numerical time stepping algorithm, length, aerodynamic lift

L_∞ = L_∞ error

l = number of augmented mode shapes

lb_i = lower bound for i-th POD modal coordinate

M = Mach number

M_S = structural mass matrix of full system in physical space

M_T = thermal capacitance matrix of full system in physical space

$\text{MAC}_{i,j}$ = modal assurance criterion value for modes i and j

MS_L = margin of safety with respect to POD lower bounds

MS_U = margin of safety with respect to POD upper bounds

$\max_i$ = maximum value of i-th POD modal coordinate

$\min_i$ = minimum value of i-th POD modal coordinate

m_S = generalized mass matrix of reduced system in modal space

m_T = generalized thermal capacitance matrix of reduced system in modal space

$\tilde{m}_T$ = generalized thermal capacitance matrix after diagonalization

N = number of steps

N_i = i-th finite element shape function

NRMSE = normalized root mean squared error

$\hat{n}$ = surface normal

n = number of snapshots used to create thermal POD ROM, number of aerothermoelastic simulations used to generate POD bounds

n_b = number of basis terms used in kriging regression model

n_e = number of kriging evaluation points

n_{dv} = number of design variables in kriging model

n_F = number of specified load vectors in load-dependent Ritz vector algorithm

n_k = number of kriging sample points

n_p = number of output parameters in kriging snapshot

n_R = number of load-dependent Ritz vectors per specified load vector

n_s = number of structural parameters in ROAM

n_t = number of thermal parameters in ROAM

n_V = number of free vibration modes used in structural basis

$\mathcal{O}$ = order of kriging regression model

$P_{\bar{\Psi},r}$ = orthogonal projector projecting onto subspace spanned by $\bar{\Psi}$

P_i = i-th point load

Pr = Prandtl number

p = pressure

p_k = kriging fitting parameter in correlation function

Q = internal heat generation rate per unit volume, orthogonal matrix in full QR factorization

$\dot{q}$ = heat flow rate vector

q = number of kriging output uantities

R = upper triangular matrix in full QR factorization, kriging regression function, ideal gas constant

$\mathcal{R}$ = residual

R_x = matrix of kriging basis functions evaluated at each snapshot

Re_x = Reynolds number

ROM = solution vector of reduced-order model

r = number of DOFs of reduced system in modal space after modal truncation

r_f = recovery factor

r_x = vector of kriging regression functions

S = Sutherland's constant

S_i = i-th boundary surface of structure

St = Stanton number

s = number of DOFs of full-order system in physical space, entropy

$\hat{s}$ = surface tangent

T = vector of discrete nodal temperatures, flow temperature

$\hat{T}$ = excess of temperature over initial condition

$\mathcal{T}^{(e)}$ = spatially varying temperature over domain of element

$\mathcal{T}^{(0)}$ = scalar value of uniform initial temperature distribution

T_{max} = maximum application temperature

T_r = recovery temperature

T_s = vector of surface tractions

t = time, element thickness

t_E = time to evaluate kriging model

t_K = time to generate kriging model

t_T = = time to generate kriging training data

U = matrix of left singular vectors of A, strain energy, transformation matrix between x_u^C and x_r

$\bar{U}$ = truncated matrix of left singular vectors of A

u = velocity component perpendicular to shock

u_i = i-th left singular vector of A

ub_i = upper bound for i-th POD modal coordinate

V = matrix containing right singular vectors of A, velocity

V_n = flow velocity normal to freestream

$v_i^{(k)}$ = i-th entry of k-th eigenvector of POD correlation matrix

W = matrix of eigenvectors of generalized eigenvalue problem

w = velocity component parallel to shock

w_a = enforced z displacement at control surface attachment

w_d = structural displacement normal to flow direction

w_i = i-th eigenvector of generalized eigenvalue problem

X = matrix of kriging sample points for training data

x = structural degrees of freedom in physical space, freestream direction

x_B = body-fixed x axis

x_d = distance from leading edge to location of interest

x, y, z = cartesian coordinate directions

$Y(x)$ = snapshot matrix of training data for kriging model

$\hat{y}(b)$ = kriging approximation to function at point b

$y_i^{(j)}$ = i-th entry of response vector for j-th kriging snapshot

Z = position of surface of structure in z direction

$Z(b, X)$ = realization of stochastic process with zero mean and variance σ^2

Z_{str} = function describing outer mold line of structure

$z(X)$ = stochastic process vector evaluated at each kriging snapshots

z_B = body-fixed z axis

α = angle of attack

α_d = thermal diffusivity

α_s = surface absorptivity

α_T = material coefficient of thermal expansion

β = coefficients of basis functions in kriging regression model, shock angle, yaw angle

$\hat{\beta}$ = generalized least squares estimator of β

Γ = boundary surface

γ = ratio of specific heats

γ_i = i-th eigenvalue of generalized eigenvalue problem

γ_m = maximum eigenvalue of heat transfer system of equations

Δ = outer surface area of solid elements, increment

Δt = time step size

Δt_{cr} = critical time step for stability of numerical time-stepping algorithm

δ = maximum inclination (radians) of airfoil to freestream, control surface deflection angle

δ_{cmd} = commanded control surface deflection angle

δ_{ij} = kronecker delta

ϵ = emissivity, total strain

ϵ_e = elastic strain

ϵ_i = percentage error at degree of freedom i

ϵ_T = thermal strain

ε = absolute error in approximation of snapshots by their projection onto basis

ε_{rel} = relative error in approximation of snapshots by their projection onto basis

ε_T = relative error tolerance

ζ = finite element natural coordinate in z direction

ζ_δ = modal damping factor associated with control surface actuator

η = finite element natural coordinate in y direction

Θ = angle between local tangent and freestream direction

θ = parameter determining numerical time stepping algorithm, kriging fitting parameters in correlation function, flow turning angle

κ = thermal conductivity

λ_i = i-th eigenvalue of correlation matrix

μ = dynamic viscosity, Mach line angle

μ_i = matrix diagonality ratio for i-th row, scalar coefficients in time-dependence of enforced motion

ν = Poisson's ratio, Prandtl-Meyer function

ξ = finite element natural coordinate in x direction

Π = total potential energy

ρ = density

Σ = diagonal matrix of singular values of A

σ = Stefan-Boltzman constant, stress, variance

σ_i = i-th singular value of A

$\hat{\sigma}$ = generalized least squares estimator of σ

τ = variable of integration, time delay

τ_w = wall shear stress

Φ_S = modal matrix of structural reference modes

Φ_T = modal matrix of thermal POD basis vectors before truncation

$\bar{\Phi}_T$ = modal matrix of thermal POD basis vectors after truncation

$\phi^{(j)}$ = j-th structural free vibration mode

$\varphi^{(k)}$ = k-th POD basis vector

χ = square matrix of coefficients of full POD basis

$\bar{\chi}$ = rectangular matrix of coefficients of truncated POD basis

Ψ = arbitrary orthonormal basis

$\bar{\Psi}$ = truncated arbitrary orthonormal basis

$\psi^{(i)}$ = i-th load-dependent Ritz vector

$\bar{\psi}^{(i)}$ = i-th load-dependent Ritz vector before normalization

Ω = domain

ω_i = circular frequencies

ω_δ = frequency parameter associated with control surface actuator

∇ = del operator

Subscripts

1 = flow conditions upstream of shock/expansion

2 = flow conditions downstream of shock/expansion

AE = aeroelastic

AT = aerothermal

a = ascent

$aero$ = componenent due to aerodynamic heating

E = elastic

e = boundary layer edge property

HT = heat transfer

h = heated

min = angle of attack minimizing $\mathcal{R}$

n = component normal to shock

net = net angle of attack

net = net rate of surface heat flow

R = rigid

r = incident radiant heat flow, restrained degrees of freedom

Suth = Sutherland reference quantity

sky = atmospheric condition

$solar$ = solar condition

$spatial$ = spatially varying component

t = component tangential to shock, total or stagnation property

Tri = two-dimensional triangular element

u = unheated, unrestrained degrees of freedom

w = wall

$Wedge$ = three-dimensional wedge element

∞ = freestream

Superscripts

(0)	=	initial
A	=	component of structural load vector due to aerodynamic pressure
C	=	constraint motion
E	=	elastic displacement
(e)	=	finite element domain
f	=	full-order solution
H	=	component of structural load vector due to heating
I	=	user-determined input
(n)	=	time level
Q	=	component due to internal heat generation
q	=	component due to specified surface heating
r	=	reduced-order solution
T	=	component due to specified nodal temperature, transpose
σ	=	component due to thermal radiation
$(\cdot)^{-1}$	=	matrix inverse
$\bar{(\cdot)}$	=	truncated
$*$	=	Eckert reference quantity

Abstract

Reduced-Order Aerothermoelastic Analysis of Hypersonic Vehicle Structures

by

Nathan J. Falkiewicz

Chair: Carlos E. S. Cesnik

Design and simulation of hypersonic vehicles require simultaneous consideration of a variety of disciplines due to the highly coupled nature of the flight regime. In order to capture all of the potential effects on vehicle dynamics, one must consider the aerodynamics, aerodynamic heating, heat transfer, and structural dynamics as well as the interactions between these disciplines. The problem is further complicated by the large computational expense involved in capturing all of these effects and their interactions in a full-order sense. While high-fidelity modeling techniques exist for each of these disciplines, the use of such techniques is computationally infeasible in a vehicle design and control system simulation setting for such a highly coupled problem. Early in the design stage, many iterations of analyses may need to be carried out as the vehicle design matures, thus requiring quick analysis turn-around time. Additionally, the number of states used in the analyses must be small enough to allow for efficient control simulation and design. As a result, alternative approaches must be considered for vehicle simulations.

This dissertation presents a fully coupled, reduced-order aerothermoelastic framework for the modeling and analysis of hypersonic vehicle structures. The reduced-order transient thermal solution used to obtain the instantaneous temperature distribution is based on

the projection of the governing equations onto a modal subspace which is obtained via the proper orthogonal decomposition (POD). The proper orthogonal decomposition is used for the thermal problem due to its optimality properties which are described in the dissertation. The reduced-order structural dynamic solution is also based on projection of the governing equations onto a modal subspace. However, for the structural dynamics, the modal subspace is composed of a set of Ritz modes which include both free vibration modes and load-dependent Ritz vectors. In order to avoid the need to reassemble the temperature-dependent stiffness matrix and thermal load vector at each time step, a technique is developed for directly updating these quantities as a function of the POD modal coordinates. A fundamental assumption underlying both the transient thermal and structural dynamic reduced-order models is that the bases are robust under variation in the boundary conditions and flight conditions and need not be updated during the course of a simulation. The use of fixed-basis reduced-order models is advantageous in that it avoids the need to return to the high-fidelity models during the course of the aerothermoelastic simulation. Both reduced-order and fundamental models are employed for the aerodynamic heating computation, and a fundamental model is used for the unsteady aerodynamic component of the solution.

The aerothermoelastic modeling framework is outlined and detailed studies are conducted to assess the accuracy and robustness of the reduced-order transient thermal and structural dynamic models under variation in boundary conditions and flight conditions. The framework is then applied to representative hypersonic vehicle control surface structures and a variety of studies are conducted to assess the impact of aerothermoelastic effects on hypersonic vehicle dynamics. The effect of structural deformation under thermal and aerodynamic loads on control surface aerodynamic performance is evaluated and is found to result in up to an 8% change in lift and 21% change in drag for the cases considered. The necessary change in control surface deflection angle required to account for aerothermoelastic effects is found to be up to 8% for the cases considered. The impact of inertial

loads due to control surface structural dynamics under a commanded change in control surface deflection angle is examined and inertial loads are found to result in an increase in hinge moments by over a factor of 500 as compared with a quasi-static case. The results presented in this dissertation demonstrate the ability of the proposed reduced-order framework to perform aerothermoelastic analysis in an efficient manner. Using this framework, it is shown that aerothermoelastic effects can significantly impact hypersonic vehicle dynamics and must be considered.

Chapter I

Introduction and Literature Review

The current chapter provides an overview of the problem of aerothermoelastic modeling and simulation of hypersonic vehicle structures. A brief history of hypersonic flight is presented and the coupling mechanisms exhibited between different disciplines in the flight regime are summarized. Literature relevant to the main topics of this dissertation is then reviewed. The literature review includes discussion of research regarding aerothermoelasticity, hypersonic aerodynamics and aerodynamic heating, hypersonic vehicle flight dynamics and control, the impact of aerodynamics and aerodynamic heating on flight dynamics, and reduced-order modeling. The review of reduced-order modeling research includes efforts involving the modal identification method, various basis augmentation strategies, higher order modal solution techniques, and the use of the proper orthogonal decomposition. Finally, a summary of the main objectives of this dissertation is given and the key novel contributions of the research are highlighted.

1.1 Introduction

Hypersonic flight, which is roughly defined as the flight regime constituting Mach numbers of five and above [1], has been a reality for over half of a century since a WAC Corporal rocket launched from a V-2 rocket accelerated to 5,150 miles per hour over White Sands, New Mexico on February 24, 1949 [2, 3, 1]. Since that flight, a multitude of hypersonic ve-

hicle (HSV) development efforts have been undertaken. The rocket-propelled NASA X-15 research airplane, developed in the 1950s and 1960s, significantly impacted the design of hypersonic launch vehicles [4, 5, 6]. The X-20 Dyna-Soar program was based on an Air Force vision for three separate hypersonic boost-glider programs [7, 8]. The Dyna-Soar program became a reality on December 10, 1957 as a result of the consolidation of three previous Air Force feasibility studies. This vehicle was conceived as a delivery platform for nuclear weapons and was eventually considered for the purposes of satellite interceptions. The cancellation of the Dyna-Soar program was announced by Secretary of Defense Robert S. McNamara on December 10, 1963 due to inability to clearly define the objectives of the program.

The next major effort in HSV research and development was the National Aerospace Plane (NASP) which started in the 1986 and was eventually terminated in 1995 due to inability to meet design requirements [4,9]. Since these early programs, there has been significant recent interest in HSV research and development. Such recent programs include [4] the X-33 Reusable Launch Vehicle program [10], the NASA Hyper-X program [11], the University of Queensland HyShot Program [12], the NASA Fundamental Aeronautics Hypersonics Project [13], the Defense Advanced Research Projects Agency (DARPA)/United States Air Force Falcon program [14], the Air Force Research Laboratory (AFRL)/DARPA X-51 Scramjet Engine Demonstrator [15], and the AFRL/Australian Defence Science and Technology Organisation HIFiRE program [16]. One important motivating factor in HSV research is associated with the fact that current launch systems, which use evolved expendable launch vehicles (EELVs), require years of preparation time and must be custom-tailored for specific payloads [15]. Furthermore, the cost to put one pound of payload into low earth orbit using an EELV is approximately $10,000 [15], therefore limiting the number of payloads that can be put into orbit. However, it is believed that HSV technology will enable the development of reusable launch vehicles (RLVs) that would greatly surpass the capabilities of current EELVs [15]. Though the hypersonic research initiatives described

above have provided significant progress toward the goal of hypersonic flight, significant challenges still remain in this field largely due to the complexity of the hypersonic regime.

Design and simulation of hypersonic vehicles (HSVs) require consideration of a variety of disciplines due to the highly coupled nature of their flight regime [1]. Specifically, HSVs exhibit complex interactions between aerodynamics, aerodynamic heating, heat transfer, structural dynamics, and the propulsion system. The highly integrated nature of hypersonic flight stems from various factors specific to these types of vehicles. Air-breathing hypersonic vehicles typically consist of a lifting body design which includes a tightly integrated scramjet propulsion system. An example of such a configuration is the NASA X-43A Hyper-X test vehicle which is shown in Fig. 1.1. Such air-breathing hypersonic vehicles must operate over a wide range of Mach numbers and fly within the atmosphere for sustained lengths of time [15, 17, 16, 6], thus making the design and analysis of such a vehicle a complex task. The forward fuselage of the vehicle represents the compression ramp which produces the necessary flow conditions for the inlet of the propulsion system. This results in a pressure distribution which causes a nose-up pitching moment. The aft section of the vehicle consists of an external exhaust nozzle shaped to allow for expansion of the flow exiting the engine. Additionally, the location of the engine below the vehicle center of gravity results in a nose-up pitching moment due to the thrust which must be balanced [18]. Further complicating the coupling between the propulsion system and the airframe are the elastic deformations of the forebody and the vehicle pitch response which affect the inlet conditions to the engine [19]. Thus to assess the overall vehicle performance, the effect of flexibility must be considered.

In addition to the effects described above, aerodynamic heating due to flow stagnation and boundary layer friction can have a significant impact on HSVs [1, 20]. Hypersonic vehicles with air-breathing propulsion systems must fly at relatively low altitudes to maintain the dynamic pressure required for optimal engine performance [20]. One consequence of this requirement is that the high dynamic pressure and high Reynolds number lead to

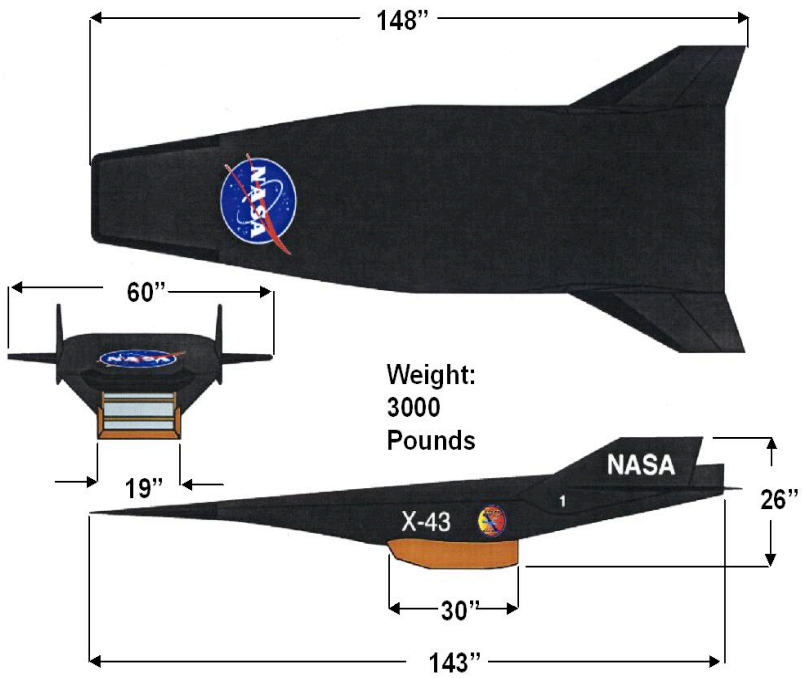

Figure 1.1: NASA X-43A Hyper-X air-breathing hypersonic vehicle [17].

surface heating becoming a major design driver. The surface heating in turn leads to heat being conducted through the internal vehicle structure. The spatial variation of temperature throughout the structure leads to a change in stiffness distribution through two effects: degradation of material properties due to temperature-dependence and geometric stiffening effects due to internal thermal stresses. The effect of aerodynamic heating on the control surfaces is particularly important to consider as the control surfaces experience a large variation in temperature and the resulting change in stiffness and the deformation due to thermal loads can alter the vehicle flight dynamics.

Though HSVs typically consist of a lifting body design to accomodate the propulsion system, the control surfaces are expected to provide a significant contribution to the aerodynamic lift, drag, and moments acting on the vehicle. This leads to the necessity to conduct a thorough analysis of the major interactions between the control surfaces and other vehicle components in order to accurately predict vehicle performance. Under combined aerodynamic and thermal loading, the control surfaces will displace relative to their undeformed configurations. This deformation results in a modification of the aerodynamic profile of the

airfoil, resulting in altered aerodynamic performance. Because the temperature distribution and aerodynamic pressures are transient over the flight trajectory, the aerodynamic performance of the control surfaces will change throughout flight. To characterize the forces and moments acting on the vehicle, it is necessary to assess the extent to which the aerodynamic performance of the control surfaces changes over a trajectory. In order to capture such an effect on HSV performance, integrated aerothermoelastic analysis is required.

Due to the strongly coupled nature of HSV vehicle design, multidisciplinary computational tools are needed to assess overall vehicle and control law performance early in the design stage. Design and flight dynamic simulation of HSVs are complicated by the large computational expense involved in capturing aerothermoelastic effects and their interactions in a full-order sense. While high-fidelity modeling techniques exist for each of these disciplines, the use of such techniques is computationally in sible in a vehicle design and simulation setting for such a highly coupled problem. Early in the design stage, many iterations of analyses may need to be carried out as the vehicle design matures, thus requiring quick analysis turn-around time. Additionally, the number of states and number of degrees of freedom used in the analyses must be small enough to allow for efficient control simulation and design. As a result, alternative approaches must be considered for vehicle simulations. There are two methodologies that can be utilized in the generation of low-order models. The first approach is to apply simplifying assumptions that enable the use of first-principles models. These models are characterized by their low-order form and they can often be solved analytically, thus preventing the need to time-march the solution. The second approach involves the use of reduced-order models (ROMs) that are derived from high-fidelity analysis tools. Use of high-fidelity tools alone is infeasible due to their high order and long run time. However, by using the output of these tools along with reduced-order modeling techniques, computationally tractable systems of governing equations with low numbers of states can be obtained. As opposed to a first-principles modeling approach, by first modeling as much of the physics as possible and then system-

atically reducing the order of the system, the error incurred through model reduction can be controlled and quantified. Use of reduced-order models also allows for tailoring of the number of states and degrees of freedom as different levels of fidelity may be required as the vehicle configuration matures.

1.2 Literature Review

As described above, complex coupling of multiple disciplines occurs in hypersonic flow. In order to accurately predict HSV performance, it is therefore necessary to consider aerothermoelastic effects within the simulation framework. Due to the computational cost associated with modeling the various disciplines involved in hypersonic aerothermoelasticity, reduced-order models are required. This dissertation builds on previous research in three primary areas: 1) aerothermoelastic modeling of hypersonic vehicle structures, 2) reduced-order modeling methodologies for transient thermal and structural dynamic analysis, and 3) assessment of the impact of aerothermoelasticity on HSV flight dynamics and controllability. In order to provide a context for the research outlined in this dissertation, the relevant literature in these areas is reviewed in the current section.

First, a review of previous work on aerothermoelastic modeling is presented. This section begins with an overview of aerothermoelasticity and its associated coupling mechanisms. A variety of studies associated with aerothermoelastic response and stability of HSV panels are then described. Next, previous research involving aerothermoelastic analysis of functionally grade panels is presented. Finally, research into two specific areas of hypersonic aerothermoelasticity, namely aerodynamics and aeroheating, is discussed.

The next subsection of the literature review consists of discussion of research involving reduced-order modeling methodologies for transient thermal and structural dynamic analysis. Review of the reduced-order modeling literature is motivated due to the computational cost associated with full-order aerothermoelastic modeling. This subsection reviews numerous works that utilized modal methods for reducing the size of the problem of interest.

The modal basis in many of these works is composed of the system eigenvectors. Additionally, efforts to augment the eigenvector basis are outlined. Alternative approaches which instead use the system output to construct the basis are also discussed.

As one of the motivating factors for this work is to assess the impact of aerothermoelastic effects on HSV flight dynamics and controllability, research involving the flight dynamics and control analysis of HSVs is reviewed. The progression of development of comprehensive HSV flight dynamic models is outlined by describing the relevant papers. As these comprensive models are intended to be used to assess vehicle controllability, a discussion of research into HSV control law assessment and stability analysis is also presented. This subsection also discusses efforts to analyze the impact of aerodynamic effects such as unsteadiness and viscosity on flight dynamics and vehicle stability. Finally, research into the effect of aeroheating on HSV dynamics is highlighted. Collectively, the current section is aimed at providing a thorough review of the literature relevant to the major topics covered in this dissertation.

1.2.1 Aerothermoelasticity

As a result of the complex coupling exhibited between the aerodynamics, aerodynamic heating, heat transfer, and structural dynamics exhibited in hypersonic flight as described in Section 1.1, aerothermoelasticity is an important consideration in the design and analysis of HSVs. As such, it has been the subject of a variety of research efforts. Figure 1.2 shows a generalization of the classical collar triangle of aeroelasticity into a hexahedron of aeroservothermoelasticity [21] which adds thermal and control system effects to the classical representation. The triangular domain consisting of elastic, aerodynamic, and inertia effects represents classical aeroelasticity. The upper tetrehedron containing the elements of classical aeroelasticity plus control system effects represents aeroservoelasticity. The lower tetrahedron which contains the elements of classical aeroelasticity plus thermal effects represents aerothermoelasticity. The current section will focus primarily on literature

associated with aerothermoelastic effects and will thus be mainly concerned with the lower tetrahedron of Fig. 1.2.

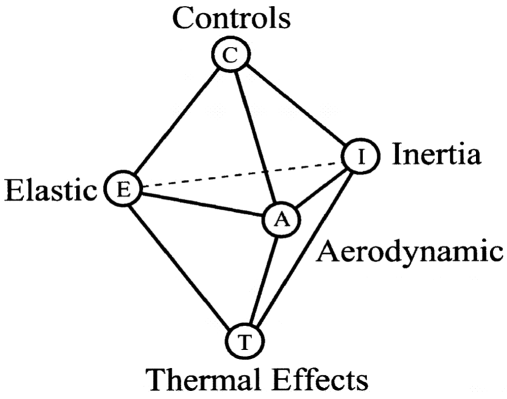

Figure 1.2: Expanded collar triangle: aeroservothermoelastic hexahedron [21].

Two recent review papers [22, 4] provide a review of previous hypersonics research and relevant modeling methodologies for the various disciplines involved in hypersonic aerothermoelasticity. One aspect discussed in these review papers is associated with the degree of aerothermoelastic coupling exhibited in hypersonic flight. Due to the different time scales and physics associated with the various aspects of hypersonic aerothermoelasticity, the strength of the coupling varies between the various disciplines. Figure 1.3 gives a summary of the strength of coupling exhibited between the different disciplines in hypersonic aerothermoelasticity [23, 24, 25]. The dashed lines in the figure indicate weak coupling, while the solid lines indicate strong coupling. As seen in the figure, the coupling between the aerodynamic heat input and the aerodynamic pressure input, elastic forces, and inertial forces is a weak coupling. This is largely a result of the disparity between the aeroelastic time scale and the aerothermal time scale. In certain cases, the problem may be simplified by neglecting these weak couplings, resulting in what is referred to in the literature as "one-way coupling" [24, 26, 23, 27, 28, 29]. In the papers discussed in this section, varying degrees of aerothermoelastic coupling are considered based on the problem under consideration.

A variety of studies on hypersonic aerothermoelasticity have focused on the aerother-

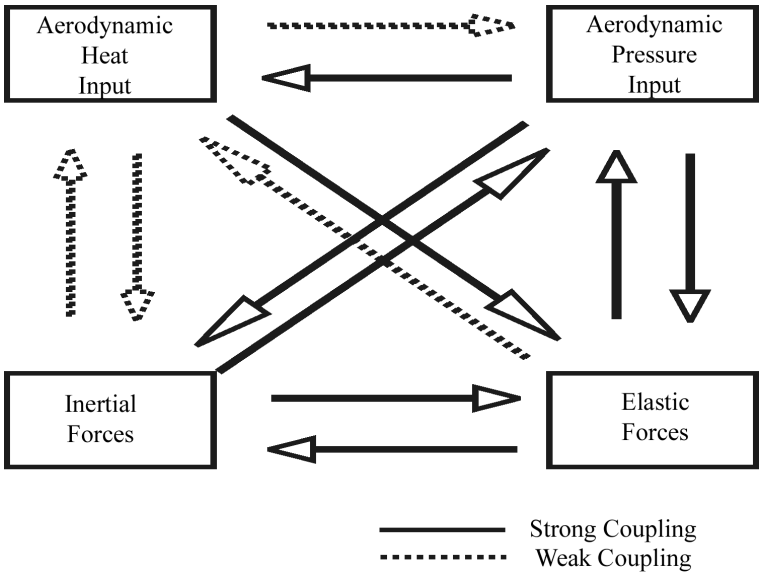

Figure 1.3: Degree of coupling exhibited in hypersonic aerothermoelasticity [23, 24, 25].

moelastic response and stability of panels using varying degrees of aerothermoelastic coupling. A review paper summarized various analytical methods for nonlinear panel flutter at supersonic and hypersonic speeds [30]. The methods are grouped into two main areas: 1) classical methods including Galerkin in conjunction with numerical integration, harmonic balance, and perturbation methods, and 2) finite element methods in the frequency or time domain. Two specific studies [31, 32] considered nonlinear panel flutter for high-Mach number flows under aerothermoelastic effects. These studies both made use of von Kármán plate theory for large displacements and both include geometric nonlinearity due to compressive load. The panel temperature was taken to be equal to the instantaneous flow temperature and was assumed to be uniform to allow for a lumped-capacity approach to the solution of the heat transfer equations. Two related works used an explicit Taylor-Galerkin algorithm to solve the coupled fluid-thermal-structural equations to assess the impact of aerothermoelastic effects on leading edges [33] and panels [34]. These works employed an integrated finite-element approach which solved the Navier-Stokes equations, energy equation, and quasi-static structural equations of motion in an integrated framework. Results from both works showed that structural deformation has a strong effect on flow properties

and that severe aerodynamic heating can lead to large stresses due to steep temperature gradients. Another work [35] focused on the thermal analysis of thermal protection panels in hypersonic flow under an imposed deflection. The framework consisted of a finite volume Navier-Stokes computational fluid dynamics (CFD) code coupled with a boundary element formulation of the transient heat transfer process. The ability of the framework to handle deflection was assessed by imposing a deformed structural configuration, calculating the thermal boundary conditions over the deformed panel, and solving for the transient temperature distribution.

In a recent study [36], the flow-thermal-structural coupling of a two dimensional skin panel in hypersonic flow was examined. This work focused on panel flutter analysis of a simply supported HSV skin panel located on the upper surface of a rigid wedge-shaped forebody. The analysis framework consisted of von Kármán plate theory for the structural dynamic response, third-order piston theory for the unsteady aerodynamics, and Eckert's reference enthalpy method for the aerodynamic heating. Fully turbulent flow over the length of the panel was assumed with transition taken to occur one meter upstream of its leading edge. A thermal structure was assumed to consist of an outer radiation shield, a middle insulation layer, and an internal plate structure. Heat transfer was considered to occur in two directions (chord-wise and through-thickness) and was calculated using a finite difference approach. For the thermal boundary conditions, aerodynamic heat flux and radiation to the environment were included at the outer surface, and the interior surface and edges of the panel were taken to be adiabatic. To calculate the structural deformation, a semi-infinite panel in cylindrical bending with simple supports was assumed. An analytical approach was used to solve the equations of motion. For the complete aerothermoelastic solution, a partitioned approach was proposed in which different size time steps were taken in the aerothermal and aeroelastic solutions. Specific attention was given to the effects of using 1-way versus 2-way aerothermal-aeroelastic coupling. The most important coupling mechanism with respect to the flutter boundary was found to be the effect of material prop-

erty degradation due to elevated temperature. The effect of two-way coupling was found to increase the rate of material degradation in localized regions, thus reducing the flight time to onset of flutter. Additionally, it was found that inertial effects have little impact on deformation prior to flutter and that including inertial effects in the pre-flutter analysis has a small effect on flutter boundary predictions.

In a related work [37], a study was conducted to assess the effect of aerothermoelasticity on a 3D HSV skin panel. In a manner similar to that of Ref. 36, third-order piston theory was used for the unsteady aerodynamics and the Eckert reference enthalpy method was used to compute the aerodynamic heating. In constrast with the framework employed in Ref. 36, a 3D finite element model was used to obtain both the structural response and thermal response. Loads on the structure consisted of aerodynamic pressure loads, fluctuating pressure loads due to sound pressure level in the turbulent boundary layer, and thermal loads due to temperature gradients. One major goal of the study was to investigate the effect of using a quasi-static versus a transient dynamic structural solution. Results demonstrated that the significance of fluid-thermal-structural coupling for quasi-static response prediction is a strong function of in-plane boundary conditions. Additionally, potential for panel failure was found to result from uncertainty in structural boundary conditions.

Another research area in which aerothermoelasticity in high-speed flows has been studied widely is the area of functionally graded panels [38, 39, 40, 41, 42, 43]. These works include aerothermoelastic effects to varying extents and are motivated largely by the need to assess the response of the structure as well as its aerothermoelastic stability. Praveen and Reddy [38] included thermal effects by imposing temperatures at the ceramic-rich and metal-rich surfaces and solving a simple steady state heat transfer problem to obtain the through-thickness temperature distribution of the plate. Temperature was taken to be uniform in the plane of the plate. Structural equations of motion were based on a combination of first-order plate theory and von Kármán strains. Static and dynamic finite element analysis (FEA) was performed and the plate deflections and stresses were analyzed.

Prakash and Ganapathi [43] also included thermal loads by imposing temperatures at the outer surfaces of the structure. This work investigated the influence of thermal loads on the supersonic flutter behavior of functionally graded flat panels. In contrast to Ref. 38, this study included aerodynamic loads by considering the first-order high-Mach number approximation to linear potential flow theory. The equations of motion were formulated using Lagrange's equations and eigenvalue solutions were used to assess the critical aerodynamic pressure for flutter.

A later work [42] extended the study of Ref. 43 by using piston theory to incorporate quasi-steady aerodynamic loads, however, this study did not include thermal effects. In a related work [41], thermal effects were incorporated along with the quasi-steady piston theory formulation. The temperature distribution was again obtained by considering temperature variation in the thickness direction only, specifying temperatures at the upper and lower surfaces, and solving the steady state heat transfer equation subject to these Dirichlet boundary conditions. Two other works [40, 39] also utilized quasi-steady first-order piston theory and included thermal effects by imposing a uniform temperature change on the plate. While the works described in this section provide progress on aerothermoelastic modeling in high-speed flows, the solution of the heat transfer problem by assuming surface temperatures, using a state state thermal solutions, or semi-empirical methods is insufficient for the problem at hand. Additionally, this dissertation will utilize an unsteady aerodynamic model as opposed to a quasi-static model as structural dynamic effects will be considered.

Various research efforts have also been carried out to develop reduced-order modeling methodologies for unsteady thermoelastic response. Perez, Wang, and Mignolet [44] developed nonlinear reduced-order models for the thermoelastodynamic response of isotropic and functionally graded panels. The reduced-order models were based on modal representations of both the transient temperature distribution and the structural dynamic response. The structural model also included geometric nonlinearities. The approach was first applied to an isotropic beam model and the impact of thermal effects on the stability of the

structure was studied. Subsequently, the performance of the methodology as applied to a functionally graded material panel was assessed. For both cases, the reduced-order model was found to accurately predict both the thermal and structural dynamic response.

In a related study [45], modal-based ROMs were used to capture the transient temperature distribution and structural dynamic response of a flat panel for the case of a one-way coupled thermal-structural configuration. The focus of the study was the unsteady temperature distribution and structural response induced by an oscillating heat flux on the top surface of a flat panel. The goal of the study was to model the effect of an oscillating shock on the thermal and structural response. A 10-mode thermal model and 17-mode structural model were found to accurately represent the full-order solution for the case study. Additionally, the combined effects of an oscillating or steady heat flux along with acoustic loads were investigated. It was observed that the differences in the power spectra of the displacements in the steady and oscillating flux cases occurred primarily in the low frequency regime and were most critical with respect to the in-plane motion.

While Refs. 44 and 45 provide progress in the area of reduced-order thermoelastic modeling of hypersonic vehicle structures, the formulations did not include the capability to compute aerodynamic pressure loads and aerodynamic heat flux. In both works, the thermal boundary conditions were taken to be prescribed functions and not computed based on instantaneous aerodynamic flow properties. While acoustic loads on the structure were considered, aerodynamic pressure loads were not included. The inclusion of unsteady aerodynamic and aerodynamic heating models is necessary in order to accurately predict the loads on the structure as well as the thermal boundary conditions. Furthermore, the works of Ref. 44 and 45 employed only a one-way coupling strategy in which a steady-state thermal analysis was conducted and the resulting temperatures are then applied to the structure. This dissertation expands on these works by employing fully coupled reduced-order transient thermal, structural dynamic, and aerodynamic heating models along with an unsteady aerodynamic representation.

1.2.2 Hypersonic Aerodynamics and Aerodynamic Heating

With regard to hypersonic aerodynamics, three recent works [46,47,48] investigated the applicability of piston theory, Euler CFD, and Navier-Stokes CFD with regard to aeroelastic stability. The first of these studies [46] investigated the aeroelastic and aerothermoelastic stability of a double-wedge airfoil typical cross-section in hypersonic flow. Time-domain aeroelastic results were computed and used to obtain frequency and damping characteristics of the system. The differences between the aerodynamic models were found to increase as the flutter boundary was approached. The effect of viscosity was also found to be insignificant with respect to aeroelastic stability. The second of these works [47] used both piston theory and Euler aerodynamics to assess the aeroelastic and aerothermoelastic stability of a three-dimensional low aspect ratio wing. Comparison of the aeroelastic behavior of the wing when using Euler aerodynamics was found to be similar to that computed using third-order piston theory aerodynamics. This study also assessed the transonic aeroelastic behavior of the wing using Euler aerodynamics and found it to be stable throughout this regime. The most recent of these three works [48] investigated the aeroelastic behavior of a hypersonic low aspect ratio wing using third-order piston theory, Euler aerodynamics, and Navier-Stokes aerodynamics. Comparison of the aeroelastic behavior of the wing using the three different aerodynamic theories demonstrated that they yield similar results. A result common to all three of these papers is that aerodynamic heating was found to reduce the aeroelastic stability of the structure, therefore providing evidence that aerothermal effects are imporant to consider.

Specific studies have focused on aerothermal modeling within an aerothermoelastic framework. Recent research into the aerothermoelastic stability of a hypersonic vehicle control surface used computational fluid dynamics (CFD) to compute the aerodynamic heating along with finite element thermal and structural models to assess its behavior in hypersonic flow [49]. In this study the aerodynamic heat flux was found using rigid-body CFD solutions to compute the adiabatic wall temperature and heat transfer coefficient at

the surface of the control surface structure. The resulting thermal boundary conditions were applied to a transient thermal finite element analysis and the resulting temperatures were applied to the structural dynamic finite element model. Free vibration frequencies and mode shapes of the heated structure were calculated under both material property degradation with temperature and thermal stresses at each desired point in time. The mode shapes were used in a modal representation of the equations of motion to obtain the aeroelastic response. Third-order piston theory and Euler aerodynamics were used to obtain the generalized loads.

The use of CFD for solution of the aeroheating problem provides capability for capturing complex effects such as shock/boundary layer interaction and 3-D flow effects. However, the computational cost associated with CFD is prohibitive in a vehicle design and control simulation setting, and thus the use of an aerothermal ROM is warranted. As such, subsequent efforts [50, 51, 52, 53] have focused on the development of a reduced-order aerothermodynamic model for more efficient aerodynamic heating predictions. The reduced-order aerothermodynamic modeling methodology developed in these works uses steady-state CFD output to construct a function which gives the aerodynamic heating at the outer surface as a function of input parameters. Input parameters consisted of freestream Mach number, angle of attack, side-slip angle, altitude, deformation, and surface temperature. In these works, both proper orthogonal decomposition (POD) and the kriging methodology have been investigated for use in generating the reduced-order aerothermodynamic model. Results presented in Ref. 52 illustrated that the developed aerothermodynamic ROMs required on the order of hundredths of a second to compute the surface heat flux distribution and generally had less than 5% error. Reference 53 extended the methodology to correct the surrogate for unsteady effects using piston theory aerodynamics. Results in that study showed errors of less than 1%.

1.2.3 Hypersonic Vehicle Flight Dynamics and Control

While aerothermoelastic analysis of hypersonic vehicle structures and reduced-order modeling are two of the main focuses of this dissertation, consideration of these disciplines is motivated by the goal to develop a 6 degree of freedom (DOF) hypersonic vehicle flight dynamics simulation framework which includes flexibility as well as aerothermoelastic effects. As such, the current section summarizes previous research efforts aimed at assessing the flight dynamics and control of hypersonic vehicles. The challenges associated with flight dynamics and control analysis of air-breathing HSVs have been reviewed in the literature [54, 55]. To address these challenges, previous research into the flight dynamics of hypersonic vehicles has largely utilized analytical models of the various disciplines. The closed-form nature of these models allows for characterization of the vehicle dynamics early in the design cycle and permits evaluation of stability derivatives more readily than with numerical models.

One of the first efforts to develop a comprehensive analytical HSV model was conducted by Chavez and Schmidt [19]. That work used Newtonian impact theory for the aerodynamic pressures, 1D aero/thermo analysis for the propulsion system, and a lumped-mass modal model for the structural dynamics with in vacuo vibration modes. The methodology was applied to a 2D hypersonic vehicle geometry in which the control effectors consisted of aerodynamic pitch-control surfaces as well as the engine fuel flow and diffuser area ratio. The derived equations of motion were linearized and analytical expressions were obtained for the stability and control derivatives. It was shown that aerodynamic and propulsive forces are both significant in the evaluation of key stability derivatives governing the vehicle's dynamic characteristics. Additionally, the vehicle was found to be highly unstable in pitch and exhibited strong coupling between the airframe, engine, and elasticity with respect to aeroelastic and attitude dynamics. This study therefore concluded that both aeropropulsive and aeroelastic effects are important to consider and that an integrated modeling approach is required for accurate HSV flight dynamic simulation.

A subsequent work [56] employed a Lagrangian approach to capture the rigid-body motion, elastic deformation, fluid flow, rotating machinery, and spherical rotating Earth. The resulting equations of motion governing the rigid body and elastic degrees of freedom were derived and a preliminary study of the significance of selected terms in the equations was presented. A three degree-of-freedom, point-mass dynamic model was also outlined and the equations were presented. For a single-stage-to-orbit configuration, the Coriolis force was found to reach values up to 6% of the vehicle weight. Furthermore, the forces and moments due to fluid flow were found to be significant.

Another work [18] presented a nonlinear physics-based model of the longitudinal dynamics for an air-breathing HSV. The equations of motion for the flexible aircraft were derived using Lagrange's equations. Oblique shock and Prandtl-Meyer expansion theory were used to obtain the pressure distribution at the outer surface of the vehicle. Propulsive effects were considered via a scramjet model which consisted of an isentropic diffuser, a constant-area, frictionless combustor, and a diverging, isentropic nozzle. The vehicle analyzed in Ref. 18 included an elastic fuselage and elevator control surfaces which were modeled as a rigid flat plates hinged at their mid-chord points. The fuselage structure was modeled as two cantilever beams clamped at the center of mass of the fuselage and the equations of motion were discretized using free vibration mode shapes. The equations of motion were derived and linearized to assess vehicle stability and coupling between the rigid body and elastic dynamics. Results demonstrated that significant inertial coupling occurs between the rigid-body motion and elastic deformation. The linearized aircraft model was shown to contain unstable short-period and phugoid modes and exhibit non-minimum phase behavior. Finally, the short-period mode was shown to be strongly coupled with the fuselage bending mode.

In another approach [57], a closed form, control-oriented model was obtained by replacing complex force and moment functions from a truth model with curve-fitted approximations. The truth model was taken to be based on that developed in a previous work [18].

The use of a curve-fitted model was motivated by the fact that the model of Ref. 18 was too complex to assess its suitability for nonlinear control techniques. Thus, curve-fit approximations of the lift, drag, thrust, pitching moment, and generalized forces were developed in order to render the model analytically tractable. The resulting system was used to demonstrate an example control design based on approximate feedback linearization. The inclusion of additional flexible effects was found to render the original control design ineffective and an additional canard actuator was needed to enhance the control authority of the vehicle. The canard was found to eliminate the non-minimum phase behavior of the rigid-body dynamics and resulted in stabilization of a high-frequency aeroelastic mode.

1.2.4 Impact of Hypersonic Aerodynamics and Aerodynamic Heating on Flight Dynamics

Though the inclusion of forward canard control surfaces was shown to improve control system performance in Ref. 57, the addition of such surfaces can also have an adverse effect on aerodynamic performance through disturbance to the airflow impinging on aft elevator or elevon control surfaces. To assess such canard-elevon aerodynamic interactions, two separate studies were carried out [58, 59]. Oppenheimer et al. [58] investigated the use of two different techniques for calculating the flow at the trailing edge of a foreward canard control surface with the goal of assessing the resulting aerodynamic effect on an aft elevon control surface. The first technique involved the use of the oblique shock and Prandtl-Meyer expansion fan relations at both the leading and trailing edges with iterations such that the top and bottom surface pressures were forced to be equal at the trailing edge. The second technique involved the use of a Taylor series expansion which relates the pressure change in the flow to the turning angle of the flow. This technique also included iterations in order to equalize the pressures at the trailing edge. The ultimate goal of this study was to quantify the effect of the canard on the effectiveness of the elevon. One aspect of the work involved characterizing the slipline at the trailing edge of the canard due to a difference in

pressure between the flow coming off of the top and bottom surfaces. Once the properties of the flow impacting the elevon were characterized, a study of the effectiveness of the elevon was conducted. Results showed that the slipline at the trailing edge of the canard can lead to a decrease in the elevon effectiveness.

In a related study, Skujins et al. [59] conducted Euler CFD studies to quantify the level of interaction between a canard and elevon for a geometry similar to that considered in Ref. 58. Parametric studies were conducted to assess the range of validity of an analytical shock and expansion fan formulation. Following these studies, an ensemble of CFD cases were generated to assess how the elevon effectiveness was impacted by the canard. The parameters considered in the CFD cases consisted of Mach number, angle of attack, canard deflection angle, elevon deflection angle, airfoil thickness, and two geometric parameters corresponding to the spacing between the canard and elevon. In order to choose the parameter values to use for each case, the method of nearly-orthogonal Latin hypercube sampling was employed. Results showed that the slipline coming off of the trailing edge of the canard does have an impact on the control effectiveness of the elevon. The effect of the slipline on the elevon was found to diminish as the separation between the two airfoils increased. Though the results presented in this study provided insight into the interactions between a canard and an elevon control surface, the aerodynamic theories utilized did not include unsteady effects. Due to perturbations in rigid-body velocities as well as structural elasticity, unsteady aerodynamic effects are important in the flight dynamic analysis of HSVs.

As highlighted in Section 1.2.1, piston theory is a popular method for unsteady aerodynamics in hypersonic flight. In addition to its use within aerothermoelastic modeling frameworks, it has been used in various works [60, 61, 62] to perform flight dynamics analysis of HSVs. Oppenheimer and Doman [60] used first-order piston theory to calculate the aerodynamic forces and moments for a hypersonic vehicle with consideration of unsteady effects due to perturbations in linear velocities and angular rates resulting from rigid body motion. The total forces and moments on the vehicle were then calculated and stability

derivatives were found. Flow over the body surfaces and elevator control surfaces, which were hinged at their mid-chord points, was considered. Initial simulation results showed that the unsteady aerodynamic components have an impact on the total forces and moments acting on the vehicle. The unsteady pitching moment was found to have the greatest effect on the vehicle dynamics, followed by the unsteady z force.

In a related work [61], first-order piston theory was again used to calculate surface pressure distributions, but in this case flexibility effects were also considered. Also in this study, a canard control surface was considered in addition to the elevator surface addressed in Ref. 60. Unsteady effects included perturbations in linear velocities and angular rates due to rigid body motion as well as vehicle flexibility. The flexible HSV fuselage was modeled using two cantilevered beams clamped at the vehicle center of gravity. Control surface effects were considered by modeling the velocity and angular rate perturbations on them resulting from fuselage flexibility. Unsteady aerodynamic effects were shown to have a significant effect on the poles and zeros of the linearized dynamics. Specifically, unsteady aerodynamics resulted in a more unstable system while increasing the frequency of the non-minimum phase zero.

In a study similar to that of Ref. 61, Bolender, Oppenheimer, and Doman [62] assessed the impact of including both viscous and unsteady effects in the aerodynamic model. First-order piston theory was again used for the unsteady aerodynamics. In order to compute the local skin friction coefficients, the Eckert reference temperature method was employed. Results showed that viscous forces have a significant impact on the drag and pitching moment of the HSV. Unsteady aerodynamics were found to destabilize the short-period dynamics of the system and move the right-half plane zeros of the elevator-to-flight path angle transfer function away from the imaginary axis. The result of this effect is an increase in the available bandwidth to stabilize the system. While the studies of Refs. 60, Ref. 61, and Ref. 62 provided insight into the impact of unsteady and viscous aerodynamic effects on the flight dynamics of HSVs, the effect of aerodynamic heating was not included in the

analyses. As described previously, aerodynamic heating is important to consider as it can have a significant impact on structural dynamic response.

The effects of aerodynamic heating on the rigid-body and structural dynamics of an air-breathing HSV were examined in a study by Culler, Williams, and Bolender [63]. A skin-stiffened vehicle with a conceptual thermal protection system (TPS) was taken as the application example. The aerodynamic heat flux at the surface was found using the Eckert reference temperature method for turbulent, high speed flow over a flat plate. A finite difference method was used to calculate the nodal temperatures through the thickness of the structure. In this work, dynamics were considered by using an analytical formulation of the free-free beam equations solved using the assumed modes method. The authors investigated both the effect of mass change due to propellant burn and material stiffness degradation due to aerodynamic heating on the structural dynamics with the overall goal of assessing vehicle dynamics and control. Results showed that the effect of aerodynamic heating largely offset the effect of mass change due to propellant burn, resulting in insignificant changes to the first mode throughout hypersonic cruise. The effects of aerodynamic heating on the rigid-body poles and zeros were found to be negligible, however the real transmission zeros associated with the flight path angle dynamics were found to move to the right, thus providing additional bandwidth to the inner loop control law.

1.2.5 Reduced-Order Modeling

As demonstrated in the studies described in the previous sections, significant research has been conducted in the areas of hypersonic aerothermoelasticity, fluid-thermal-structural coupling, and hypersonic vehicle flight dynamics and control. While the previously described studies have led to significant progress in this field, further development is still needed to make aerothermoelastic analysis feasible within a vehicle design and control simulation setting. Specifically, one area that has been addressed little in the above studies involves reduction of the number of states and degrees of freedom (DOFs) in the problem.

Consideration of this aspect of the problem is necessary in order to make aerothermoelastic analysis of hypersonic vehicle structures practical.

As described in Section 1.2.1, complex coupling between multiple disciplines must be considered in the design and simulation of HSVs. Due to the computational expense associated with modeling each of these disciplines in a full-order sense, the use of reduced-order models has recently become more prevalent in the hypersonics research community. This dissertation makes use of reduced-order models for the solution of the transient thermal and structural dynamics systems of equations. As such, the current section provides a summary of previous work on reduced-order modeling in these two disciplines. As the form of the transient thermal equations is similar to that of the structural dynamics equations of motion, most of the reduced-order modeling methodologies described in this section are applicable to either discipline.

There have been a variety of methods employed in the literature to reduce the order of transient thermal and structural dynamics problems. The well known structural dynamics reduction methods of Guyan Reduction [64] and component modes synthesis [65] have been extended for use in both linear and nonlinear transient thermal problems [66, 67, 68]. One paper [69] utilized Guyan Reduction and component modes synthesis for reduction of the thermal problem in conjunction with nonlinear identification techniques for solution of the structural and fluid problems for coupled solid/fluid analysis of a turbine disk model. Results of this study showed that both Guyan reduction and component modes synthesis provided sufficient reduction of the problem for efficient computation of temperature histories at selected locations of the model. However, a disadvantage to both of these methods is that tuning of the reduced-order model was necessary to obtain the desired accuracy as the error of a particular reduced-order model cannot be determined *a priori*. In particular, Guyan reduction requires selection of the set of active and omitted degrees of freedom while the component modes synthesis methodology used in these works requires the selection of a subset of eigenmodes related to the set of omitted temperatures.

1.2.5.1 Modal Identification Method

Another technique that has been used for reduction of both linear and nonlinear transient thermal problems is the modal identification method [70, 71, 72, 73]. The use of this technique is largely motivated by inverse heat transfer problems in which one desires to determine boundary conditions to a thermal problem based on measured temperature evolutions at selected locations. Given a state-space representation of the full-order system, this technique seeks another state-space representation of the dynamics which is of much lower order than the original system and gives a good approximation to the output of the original system. As the reduced-order state-space representation is written in modal space, the identification of a subset of eigenmodes of the system is required. The primary advantage of the modal identification method is that no knowledge of the thermal capacitance and thermal conductivity matrices is required for calculation of the eigenmodes of the system. Rather than solving an eigenvalue problem of the full system, the eigenmodes are identified through the minimization of a quadratic criterion related to the difference between the output vector of the full-order model and that of the reduced-order model. Therefore, this method is useful for situations in which the computational cost of a large-scale eigenvalue problem cannot be afforded and for problems in which the thermal matrices of a system are unknown.

The modal identification method was developed and implemented for linear multivariable systems with multiple inputs and outputs and was shown to reduce a model of order 1643 to one of order 26 while still maintaining sufficient accuracy [70]. Due to the ill-posedness of the inverse problem, computational difficulties in its solution can arise due to the ill-conditioning of the involved matrices. As such, a regularization procedure was implemented in another work [71] for the reduced-order solution of a linear heat conduction system that made use of modal identification. Application of the methodology to a three-dimensional example problem showed good agreement between the full-order and reduced models for reduction from order 1331 to order 9. A subsequent two-part work extended the

modal identification method for use in nonlinear systems [72, 73] for single-input/multi-output configurations. The methodology employed in these works was similar to the one employed for linear systems in that it identified a state-space representation of reduced order to approximate the high-fidelity system. However, for the nonlinear case, additional manipulation was needed to separate the linear and nonlinear terms in the equation. This work introduced nonlinearity through a linear variation of the thermal conductivity with temperature. The methodology as applied to a three-dimensional cube demonstrated that the reduced-order model was able to obtain solutions for the inverse problem whereas the detailed model was not for the same time integration scheme.

While the modal identification method provides a significant computational advantage for certain problems such as inverse heat transfer problems, its applicability within the aerothermoelastic framework of this work is questionable. Though one of its major advantages lies in the fact that the matrices of the governing equation need not be known, in this work the thermophysical properties of the system will be known, so this factor does not come into play. The methodology in the described studies was applied to systems with a relatively low number of inputs (1 - 3) and outputs (2 - 27), while the models considered in this dissertation are on the order of thousands of inputs and outputs due to continuous variation of the heat flux boundary condition and temperature distribution in space. The complexity associated with the large number of inputs is due to the fact that, in the linear case, the modal identification method requires an elementary reduced model (ERM) for each input and superposition is then used to reconstruct the solution. For the cases considered in this dissertation where each node at the surface of the airfoil represents an input to the system, creation of an ERM for each node is impractial. More fundamentally, while an eigenmode basis will likely provide some means for reduction of the problem, it may not be the optimal basis for capturing the dynamics of the system with the fewest possible number of modes. Therefore, consideration of alternatives to an eigenvector basis must be considered prior to selecting a reduced-order modeling methodology.

1.2.5.2 Basis Augmentation

Within the area of reduced-basis modal methods, attempts have been made to augment the eigenmode basis of a system or develop an alternative basis for representation of the system [74, 75, 76, 77, 78, 79, 80]. Shore [74] utilized an eigenvector basis for nonlinear thermal problems consisting of the eigenvectors based on thermal properties evaluated at the initial temperature conditions and those based on thermal properties evaluated for a temperature distribution corresponding to a nonlinear steady-state problem. To enhance the accuracy and efficiency of the solution, the eigenvector basis was augmented with additional adaptive vectors and analytically generated vectors. Large reductions in size were achieved for conduction-dominated problems with simple geometry and boundary conditions. For problems with complex spatial and temporal variation in heating, additional effort was employed to generate alternative basis vectors.

As opposed to an eigenvector basis, Nour-Omid [80] utilized a Lanczos vector basis for reduction of the transient heat transfer problem. The advantage of such an approach is that the vectors can be generated relatively inexpensively, can produce more accurate solutions than those obtained with an eigenvector basis, and can lead to a reduced system in tridiagonal form for a more computationally efficient solution. An adaptation of this methodology was developed by Cardona and Idelsohn [79] who obtained the first basis vector as the system response for the first time step and then introduced this vector into the Lanczos algorithm. The authors also extended the method and solved nonlinear thermal problems by introducing new basis vectors which are derivatives of the pre-existing basis vectors with respect to their own amplitude parameters. Another work [78] discussed the selection of a starting vector to the Lanczos algorithm which is related to the time variation of the heat supply vector.

Another technique that has been used for basis augmentation is associated with structural dynamics and involves the computation of Ritz vectors which are static solutions of the system subjected to representative loads [81, 82, 83, 84, 85, 86]. This approach is advan-

tageous in that it enriches the original basis and allows for capturing quasi-static response due to slowly changing or static loads that would not otherwise be contained within an eigenvector space. The load-dependent Ritz vector methodology of Wilson, Yuan, and Dickens [85] is aimed at achieving this goal. This technique is an iterative method for generating Ritz vectors based on specified loads and enables reduction the size of a linear structural dynamics system of equations. The use of load-dependent Ritz vectors was shown to produce more accurate results than were achieved using eigenvectors as the basis for mode superposition. Additionally, the computer time required to generate the load-dependent Ritz vectors was less than that required to generate the system eigenvectors. A subsequent work [86] extended the methodology of Ref. 85 for nonlinear structural dynamics problems. The methodology was based on augmentation of the original basis by adding derivatives with respect to the generalized displacement amplitudes. Results show that the methodology allows for more efficient basis generation and similar or better accuracy as compared with the use of tangent modes and their derivatives. Ricles and Léger [84] later used the load-dependent Ritz vector methodology to perform structural dynamic response analysis of the space station Freedom and demonstrated displacement convergence with a small number of vectors.

1.2.5.3 Higher-Order Modal Solutions

As opposed to basis augmentation techniques, a different approach that has been used to obtain reduced-order solutions to transient thermal and structural dynamics problems involves the method of higher-order solutions. In contrast to basis augmentation which focuses on obtaining an accurate basis while using a standard mode-displacement superposition, higher-order modal solution techniques focus on obtaining higher-order solutions with a given basis. One such higher-order modal solution technique is known as the force-derivative method (FDM) [75, 87, 76, 77, 88]. This approach is advantageous in that these higher-order solutions converge to an accurate response using fewer modes than lower-

order methods such as the mode-displacement method (MDM) or the mode-acceleration method (MAM). The work of Ref. 88 was one of the first steps toward development of the FDM as it revealed that the MAM can be derived via integration by parts with respect to time of the convolution integral form of the original mode-displacement method. Reference 88 further showed that successively higher-order modal methods may be obtained by further integration by parts. The FDM produces an additional term that depends on the forcing function and subsequent terms that depend on the time derivatives of the forcing function. These additional terms offer an improved approximation of the higher-frequency modes which would otherwise be neglected in a standard mode-displacement approach. The first-order force-displacement relation can be recognized as the mode-acceleration method with one correction term that depends on the forcing function. This method was applied with success to linear structural dynamic and transient thermal systems [76, 77]. Results in these works demonstrated that the FDM produces more accurate results than would be obtained using the MDM or the MAM and that responses obtained using the FDM converge using fewer modes. The FDM was later extended for application to nonlinear transient thermal problems [75] and was shown to achieve significant reduction with respect to MDM solutions with comparable accuracy.

Another higher-order modal approach that has been used to reduce the order of structural dynamics systems of differential equations is the dynamic correction method (DCM) [89] which employs a correction to the traditional MDM by solving an additional set of differential equations to obtain a vector of corrective displacements. The main difference between the original set of equations of motion and the additional set is that the additional set is subjected to a force vector that is generated in such a way as to correct for the error incurred due to modal truncation. There exists a relationship between the DCM and FDM in that the FDM becomes the DCM if an infinite number of integrations-by-parts are performed in the FDM [90]. Therefore, the DCM is a generalization of the FDM. In the DCM, the vector of physical displacements is expressed as the sum of the approximate

physical displacements obtained from the MDM and a vector of corrective displacements. The DCM, or variants of it, has been applied to structural dynamics problems in seismic analysis of classically and non-classically damped structures [90], stochastic analysis of structural systems [91], and linear dynamic response analysis [92].

1.2.5.4 Proper Orthogonal Decomposition

While the above reduced-basis methods provide efficient techniques for reducing the order of transient thermal and structural dynamics problems while maintaining sufficient accuracy, they rely largely on the matrices constituting the governing system of equations rather than the actual response of the system to excitations that it will likely see in practice. Methods using an eigenvector basis require solution of a large eigenvalue problem, while augmentation of the eigenvector basis often requires trial and error to capture the correct subspace. Higher-order modal solutions provide added accuracy, albeit at the expense of additional computational cost. Furthermore, the use of an eigenvector basis may not be optimal in the sense of capturing the most energy with the fewest number of modes for a given problem. Therefore, in certain situations, alternatives to eigenvector basis representations can prove to be advantageous. Specifically, for situations in which the characteristic transient response of the system can be adequately characterized *a priori*, a technique with established optimality properties, known as the proper orthogonal decomposition (POD), may be able to provide greater reduction than an eigenvector-based solution while maintaining similar or better accuracy.

The POD, also known as the Karhunen-Loève decomposition, principal components analysis, singular systems analysis, and singular value decomposition, is a modal technique in which empirical data is processed using statistical methods to obtain models which capture the dominant physics of a system using a finite number of modes [93]. The fundamental basis for use of POD as a reduced-order modeling method is its ability to represent high-dimensional systems in a low-dimensional, approximate manner while still maintain-

ing a high degree of accuracy. The main advantage of the POD basis as opposed to any other basis such as an eigenvector basis is due to its established optimality condition of providing the most efficient way of capturing the dominant modes of a system with a finite number of modes [94]. The POD has been used in numerous applications such as heat transfer problem [95] turbulence [96], structural dynamics [97,98], aerodynamics [99], and control theory [100] among others. As POD is employed for transient thermal solution in this dissertation, the literature provided below focuses on its use in thermal applications.

The use of POD for thermal problems is prevalent in the literature. In two relevant works, the method was applied to a linear transient thermal system in which the governing equations were decoupled in order to solve them analytically over time [101, 102]. Application of the method to cases with time-independent and time-varying loading showed relative errors of less than 1% and less than 3%, respectively [101]. In a related work [95] POD was applied to a nonlinear transient thermal system and a technique was developed for updating the system matrices in cases where the thermal conductivity must be recomputed at every time step. This strategy involved separating the solution-dependent part of the element matrix from the geometry-dependent part to reduce computation times. Application of the methodology to systems with nonlinearity due to temperature-dependent material properties showed average relative error of less than 1% with respect to the full-order model. Furthermore, it was shown that for a certain range of degrees of freedom, significant improvement in computation time can be achieved using the methodology outlined in Ref. 95. In another study [103], an approach was developed to incorporate an understanding of the input operator to the system. A low-order model was developed using POD in which an external control input is included by separating the external stimuli from the ordinary differential equations resulting from projection onto the reduced subspace.

In addition to its use in solving forward heat transfer problems, POD has also been applied in the solution of nonlinear inverse heat transfer problems. One example of this application is its use in estimating the time-varying strength of a heat source in a two-

dimensional system [104]. The system studied in that work consisted of a square domain with a time-varying heat source at a known location. Thermal conductivity was taken to be a strong function of temperature, thus resulting in nonlinear governing equations. Drastic reduction in the number of degrees of freedom was achieved using the proposed method while maintaining solution accuracy on the same level as that of a traditional method. A subsequent work utilized POD in the solution of nonlinear inverse natural convection problems [105]. The goal was to estimate the time-varying strength of a heat source while reducing the order of the computations involved. The reduced-order solution was compared with that obtained using the traditional method of employing the Boussinesq equation. Use of POD was shown to accurately reproduce the results obtained using the traditional method for various shapes of the heat source function at reduced computational cost. A later work [106] applied POD to the inverse problem of estimating the unknown thermal conductivity and convective heat transfer coefficient of a system. The modal coordinates of the basis vectors were allowed to be a nonlinear function of the retrieved parameters. Results showed that the method was robust and numerically stabilizing while also exhibiting favorable regularization due to the ability of POD to filter out high frequency error.

1.3 Objectives of this Dissertation

As described above, the literature indicates that significant advances have been made in the areas of aerothermoelastic modeling of HSV structures, reduced-order transient thermal and structural dynamic modeling, and flight dynamics and control analysis of HSVs. Various modeling techniques and coupling strategies have been investigated in the literature for use in aerothermoelastic response prediction of HSV structures. Using these various techniques, aerothermoelastic effects were shown to have a significant impact on structural stability and response in previous works. The effects of aerodynamic heating, unsteady hypersonic aerodynamics, and structural deformation were also shown to be an important consideration in the design of HSV control systems. Therefore, the ability to efficiently

model the aerothermoelasticity of HSVs is critical in their design.

Despite the large body of literature described in the previous sections, there exist shortcomings in HSV analysis capabilities which have motivated various aspects of the research presented in this dissertation. For example, two recent reports [107, 108] highlighted existing knowledge gaps with respect to predictive capability for hypersonic structural response prediction. Though numerous efforts have focused on the development of coupled flow-thermal-structural analysis methodologies, little attention has been given to the use of reduced-order models to improve the computational cost of aerothermoelastic analysis. As described in the introduction, HSV control analysis and vehicle design require efficient models with low numbers of states. Many of the papers discussed in Section 1.2.1 addressed the issue of computational cost by neglecting certain couplings or by making simplifying approximations. While such approximations may be valid in certain cases, one objective of this dissertation is to develop a general, comprehensive, and fully coupled aerothermoelastic framework for HSVs. One of the main challenges associated with the development of a fully coupled aerothermoelastic model is the significant computational cost and large number of states that result from modeling each of the relevant disciplines and their interactions in a full-order sense. Therefore, in order to make aerothermoelastic analysis feasible for vehicle design and control simulation purposes while still retaining the essential physics, the use of reduced-order models within the framework is proposed.

The reduced-order modeling methodologies developed in this dissertation build on the literature described in Section 1.2.5. However, the majority of the efforts described in that section focus on the reduced-order modeling of one specific discpline in isolation. Thus, certain issues associated with the use of reduced-order models within a fully coupled aerothermoelastic framework for HSVs must be addressed. A major goal of this dissertation is to develop a framework based on ROMs which can be generated *a priori* without the need to update them during the course of a simulation. Development of ROMs even for a single trajectory is challenging due to certain effects experienced in hypersonic flight.

The thermal boundary conditions over a trajectory are time-dependent and thus the thermal ROM must be robust with respect to variations in heat flux. Note that in this dissertation, ROM robustness refers to the ability of the model to span the space of the solution over the complete set of conditions that may be expected to be experienced during simulation. As the material properties and thermal stresses of HSV structures vary over the trajectory due to transient heating, the structural ROM must be robust to variation in the stiffness matrix. This dissertation aims to take the issue of ROM validity a step further by addressing the use of the same ROMs for multiple HSV simulations which constitute a range of flight conditions (i.e., a range of Mach numbers, angles of attack, and altitudes). This makes the development of the ROMs even more challenging as they will be required to be even more robust than would be necessary if the ROMs were only used for simulation over a single trajectory.

The papers highlighted in Section 1.2.3 have provided progress with regard to the development of comprehensive HSV models for flight dynamics and control analysis. However, many of those studies made simplying assumptions in order to enable the use of analytical models in the framework. The use of analytical models has a drawback associated with error quantification. In order to use analytical models, up-front assumptions must be made which result in the elimination of certain physics from the model. The effect of elimination of these physics from the problem is difficult to quantify. However, by starting with a high-fidelity model which contains as much of the essential physics as possible, and then systematically reducing the order of the system, greater ability to quantify the error incurred due to model reduction is provided. Additionally, little work has been conducted to assess the impact of control surface structural dynamics and elasticity on overall vehicle dynamics. Rather, the inclusion of HSV control surfaces within full-vehicle models is often accomplished by modeling the surfaces as rigid flat plates. The inclusion of control surface structural dynamics is important as the resulting inertial coupling can adversely affect the elevator-to-pitch rate dynamics and the speed of response of the system [109]. As

such, another objective of this dissertation is to apply the reduced-order aerothermoelastic modeling methodology to a representative HSV control surface and assess the impact of control surface aerothermoelastic effects on overall vehicle dynamics. Furthermore, this dissertation aims to formulate the control surface aerothermoelastic model in such a way as to allow for straightforward incorporation of the control surface model into a 6-DOF HSV flight dynamics simulation framework. Such an implementation will enable a capability which is absent in the present literature, namely, the ability to efficiently model the elasticity and inertial effects of the control surfaces under unsteady hypersonic aerodynamics and aerodynamic heating within a full-vehicle flight dynamics simulation framework.

Based on the discussion above, the main objectives of this dissertation are as follows:

1. Develop a transient thermal reduced-order modeling methodology that is robust to time variation in thermal boundary conditions, valid over a wide range of flight parameters, and that significantly reduces the computational cost and number of states involved in the thermal solution. The thermal ROM is addressed in Chapters II and III. Chapter II outlines the formulation for the reduced-order transient thermal modeling methodology and Chapter III presents studies aimed at assessing the validity of the approach.

2. Investigate techniques for performing accurate reduced-order structural dynamic analysis of HSV structures under variation in stiffness due to temperature-dependent material properties and geometric stiffening subject to unsteady aerodynamic, transient thermal, and base excitation loads. This element of the framework is discussed in Chapters IV and V of the dissertation. Chapter IV investigates the impact of material property degradation and geometric stiffening under transient heating on the free vibration mode shapes and natural frequencies of representative control surface structures. Chapter V discusses the development of enhanced modal solution techniques aimed at improving the efficiency and accuracy of the structural dynamic ROM.

3. Incorporate the reduced-order models into a fully coupled aerothermoelastic simulation framework that is of sufficient order as to allow for feasible vehicle design and control analysis. Chapter VII discusses a quasi-steady aerothermoelastic framework which consists of a localized shock/expansion formulation for the hypersonic aerodynamics, an Eckert reference temperature formulation for the aerodynamic heating, a full-order transient thermal solution for the heat transfer, and a full-order static structural solution at each time step to compute the deformation. In Chapter VIII, the fully unsteady, reduced-order aerothermoelastic framework is outlined.

4. Employ the aerothermoelastic framework to investigate the robustness of the transient thermal and structural dynamic reduced-order models to variations in flight condition parameters such as Mach number, angle of attack, and altitude. The accuracy of the transient thermal and structural dynamics ROMs within a fully coupled aerothermoelastic environment is discussed in Section 8.3.2.1 of Chapter VIII.

5. Assess the impact of control surface aerothermoelastic effects on overall HSV response. Section 8.3.3 in Chapter VIII investigates the impact of aerothermoelastic effects on the aerodynamic lift and drag generated by an HSV control surface. Additionally, that section investigates the control surface angle of attack necessary to match the lift of an elastic control surface under aerothermoelastic effects to that of a rigid control surface for representative trajectories.

6. Develop a general approach for incorporating the aerothermoelastic control surface model into 6-DOF HSV flight dynamics simulation framework. The formulation for this approach is described in Section 9.3 of Chapter IX. Results associated with the approach are given in Section 9.6 of Chapter IX.

As mentioned in the last item above, the ultimate goal of this dissertation is to develop an efficient methodology for incorporating aerothermoelastic effects into full-vehicle 6-DOF HSV simulations. A schematic illustrating the various components of the 6-DOF

framework as well as the couplings between the various disciplines is given in Fig. 1.4. Figure 1.4 highlights the fundamental, reduced-order, and high-fidelity modeling options that are available for each discipline. Furthermore, Fig. 1.4 also emphasizes the inputs and outputs required for each of the different components of the 6-DOF solution.

For the thermal component of the solution, no straightforward fundamental or first-principles representation exists (indicated by "N/A" in the figure), and thus the development of a reduced-order thermal model becomes critical. The high-fidelity thermal solution is based on FEA, and the thermal ROM is obtained from POD. For the elastic solution, fundamental representations of the vehicle are available via the use of beam mode shapes within a Ritz-based analytical solution to the structural dynamics. The high-fidelity elastic solution is again based on FEA, and the ROM developed in this work uses a subset of Ritz modes. For the aerodynamic heating solution, a first-principles model based on the Eckert reference temperature method is employed in this dissertation. Additionally, the research presented here investigates the use of a kriging-based aerodynamic heating ROM extracted from CFD as developed by Crowell and McNamara [52, 53, 26, 110, 51]. The unsteady aerodynamic solution considered in this work is based on a first-principles piston theory representation of the flow. However, the methodology is intentionally general so as to allow for the use of an unsteady aerodynamic ROM, such as the convolution-based ROM extracted from CFD solutions as developed by Skujins and Cesnik [111, 112, 113].

The thermal, elastic, aerodynamic heating, and unsteady aerodynamic components just described compose the aerothermoelastic framework that is presented in this dissertation. Additionally, a general methodology is developed for incorporating the vehicle substructures into a 6-DOF simulation framework. The substructure coupling methodology is based on the exchange of information at the interface as depicted in Fig. 1.4. The 6-DOF model is based on the work of Frendreis et al. [114, 115], and includes vehicle flexibility. Also included in the 6-DOF model is a scramjet propulsion system. Fundamental modeling of the propulsion system is often accomplished via the use of the quasi-1D flow assump-

tion. While CFD can be used to simulate the propulsion system, its use within the overall HSV framework is infeasible due to the number of states and computational cost. Thus, a reduced-order propulsion representation denoted as the Michigan/AFRL Scramjet In Vehicle (MASIV) model has been developed [116, 117, 118, 119, 120, 121, 122] for efficient propulsion modeling.

This dissertation focuses on the thermal, elastic, aeroheating, and unsteady aerodynamic components of the framework shown in Fig. 1.4. The reduced-order modeling development efforts in this work are applied only to the thermal and elastic components of the solution, and thus these aspects are the main elements of this research. However, in order to develop the fully coupled aerothermoelastic framework, aerodynamic heating and unsteady aerodynamic effects must also be incorporated. For the aerodynamic heating, both an Eckert reference temperature formulation and aerothermal ROM are employed. For the unsteady aerodynamics, the third-order piston theory approach is implemented. While the propulsion system, control system, and 6-DOF vehicle model are not part of the framework developed in this dissertation, these components are shown in Fig. 1.4 to illustrate the manner in which the aerothermoelastic model interacts with the other components of the solution.

1.4 Key Novel Contributions of this Dissertation

Achievement of the objectives summarized above will result in significant advancement to the state-of-the art in the areas of aerothermoelastic modeling of hypersonic structures, reduced-order transient thermal and structural dynamic modeling, and flight dynamic simulation of HSVs. The following key novel contributions made by this dissertation are summarized below:

1. A transient thermal reduced-order modeling methodology based on the proper orthogonal decomposition is developed and implemented. The methodology is shown

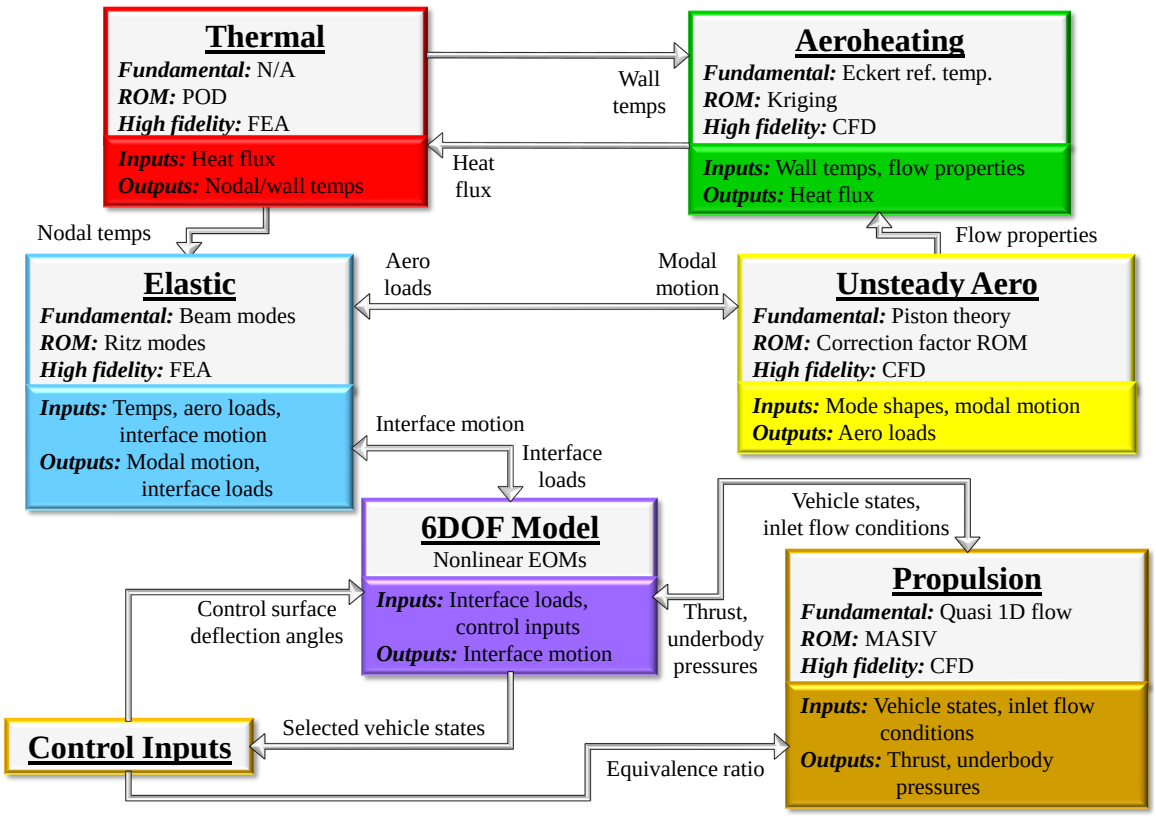

Figure 1.4: Overview of 6-DOF HSV simulation framework.

to be robust under time-dependent thermal boundary conditions and variation in flight condition parameters. Studies of the accuracy of the thermal ROM for the cases of time-independent and time-dependent thermal boundary conditions are given in Sections 3.2.1 and 3.2.2, respectively, in Chapter III.

2. A Ritz-based modal method is developed for reduced-order structural dynamic response computation within HSV aerothermoelastic simulations. A description of the structural dynamic ROM formulation is given in Section 4.2 of Chapter IV. The fixed-basis structural dynamic ROM is shown to be robust under variation in stiffness due to temperature-dependent material properties and thermal stresses. Results associated with the error of the structural dynamic ROM under transient heating are given in Section 5.2.2 of Chapter V and Section 8.3.2.1 of Chapter VIII.

3. The impact of transient aerodynamic heating in hypersonic flow on the evolution of free vibration mode shapes is quantified and found to have an insignificant impact on the space spanned by the modes over time for one particular case. Results associated with this aspect of the dissertation are given in Section 4.4 of Chapter IV.

4. An efficient approach for directly updating the generalized structural stiffness matrix and thermal load vector as a function of transient temperature distribution is created. The formulation associated with this approach is given in Section 5.1 of Chapter V.

5. Reduced-order transient thermal, structural dynamic, and aerodynamic heating models are incorporated into a fully coupled, reduced-order aerothermoelastic framework. The development of this framework represents the first attempt to perform fully-coupled, reduced-order aerothermoelastic simulations of an HSV structure using multiple coupled dissimilar reduced-order models. The unsteady, reduced-order aerothermoelastic framework is presented in Chapter VI and results associated with that framework are given in Chapter VIII.

6. Aerothermoelastic effects are found to impact HSV control surface lift and drag force generation, control surface effectiveness, and necessary control input required to maintain a commanded trajectory. An assessment of the effect of aerothermoelasticity on control surface performance is given in Section 8.3.3 of Chapter VIII.

7. A partitioned, iterative solution methodology for the coupling of a control surface and fuselage structure is formulated and validated. The formulation associated with the partitioned solution is given in Section 9.3 of Chapter IX and results associated with the validation of that formulation are given in Section 9.6.1 of Chapter IX.

8. Control surface inertial effects are found to have a significant impact on the forces and moments exerted on the fuselage at the attachment point. Results associated with the impact of control surface inertia are given in Section 9.6.2 and Section 9.6.3 of Chapter IX.

Chapter II

Transient Thermal Modeling

As transient heating is expected to impact the structural response due to thermal loads and variation in stiffness, it is necessary to model the heat transfer throughout the structure in order to accurately obtain the temperature distribution. This chapter begins with an overview of the equations governing the transient heat transfer process. The spatial discretization of the governing equations using a finite element approach is then described, leading to the full-order system of transient thermal equations. Boundary conditions to the thermal problem consisting of aerodynamic heat flux as well as radiation at the outer surface are also discussed.

Due to the large number of degrees of freedom associated with transient heat transfer analysis of hypersonic vehicle structures in a full-order sense, reduction of the system is required so that thermal analysis can be carried out in a computationally efficient manner with a lower number of states. The methodology introduced in this dissertation to reduce the order of the transient thermal equations makes use of the proper orthogonal decomposition which is a projection-based modal technique. Section 2.2.1 describes the process for generating the POD basis vectors. This section also discusses certain properties of the POD which make it desirable for use in model reduction. Section 2.2.2 describes two approaches used for solving the reduced-order thermal system for the POD modal coordinates. The first approach makes use of an analytical solution to the reduced-order system

by decoupling the equations and solving each independently. In the second approach, the coupled reduced-order system is integrated numerically. Details of the second-order Crank-Nicolson scheme used for the numerical integration of the reduced-order system are also provided in this section.

2.1 Derivation of Governing Transient Thermal Equations

The finite element formulation for the transient heat transfer problem begins with the governing energy equation for heat transfer in a three-dimensional anisotropic solid, Ω, bounded by outer surface Γ given by [123]

$$-\left(\frac{\partial \dot{q}_x}{\partial x}+\frac{\partial \dot{q}_y}{\partial y}+\frac{\partial \dot{q}_z}{\partial z}\right)+Q=\rho c_p\frac{\partial T}{\partial t}, \tag{2.1}$$

where $\dot{q}_x$, $\dot{q}_y$, and $\dot{q}_z$ are the components of the heat flow rate vector in cartesian coordinates, Q is the volumetric internal heat generation rate, ρ is the density of the structure, c_p is the specific heat of the structure, T denotes temperature, and t denotes time. For an isotropic medium, the components of the heat flow rate vector are given by

$$\dot{q}=-\kappa\nabla T, \tag{2.2}$$

where κ is the thermal conductivity of the material. Note that the minus sign is needed due to the fact that heat is transferred from warmer regions to cooler regions. Substituting Eq. (2.2) into Eq. (2.1) and assuming constant thermal properties and no internal heat generation yields the heat equation given by

$$\nabla^2 T=\frac{1}{\alpha_d}\frac{\partial T}{\partial t}, \tag{2.3}$$

where α_d is the thermal diffusivity given by

$$\alpha_d = \frac{\kappa}{\rho c_p}. \tag{2.4}$$

Now that the governing equations have been given, we will derive the resulting finite element equations for a single element for simplicity. Using the method of weighted residuals with the governing equation, we require

$$\int_{\Omega^{(e)}} \left(\frac{\partial \dot{q}_x}{\partial x} + \frac{\partial \dot{q}_y}{\partial y} + \frac{\partial \dot{q}_z}{\partial z} - Q + \rho c_p \frac{\partial T}{\partial t} \right) N_i \, d\Omega = 0, \tag{2.5}$$

where $\Omega^{(e)}$ is the domain for element (e) and N_i are the element shape functions. As the finite element models used in this work contain both two-dimensional triangular elements and three-dimensional wedge elements, the formulation will require the shape functions for both element types. The shape functions for the two-dimensional triangular element are given by [124]

$$N_{1,Tri} = \xi \tag{2.6a}$$

$$N_{2,Tri} = \eta \tag{2.6b}$$

$$N_{3,Tri} = 1 - \xi - \eta, \tag{2.6c}$$

where ξ and η are the natural coordinates of the local element coordinate system in the x and y directions, respectively, each with limits from 0 to 1. The shape functions for the

three-dimensional wedge element are given by [125]

$$N_{1,Wedge} = (1-\xi-\eta)(1-\zeta)/2 \tag{2.7a}$$

$$N_{2,Wedge} = \xi(1-\zeta)/2 \tag{2.7b}$$

$$N_{3,Wedge} = \eta(1-\zeta)/2 \tag{2.7c}$$

$$N_{4,Wedge} = (1-\xi-\eta)(1+\zeta)/2 \tag{2.7d}$$

$$N_{5,Wedge} = \xi(1+\zeta) \tag{2.7e}$$

$$N_{6,Wedge} = \eta(1+\zeta)/2, \tag{2.7f}$$

where ζ is the natural coordinate of the local element coordinate system in the z direction. The limits of the natural coordinates for the three-dimensional wedge element are

$$0 \leq \xi, \eta \leq 1 \tag{2.8a}$$

$$-1 \leq \zeta \leq 1 \tag{2.8b}$$

$$\xi + \eta \leq 1. \tag{2.8c}$$

Integrating the term

$$\int\limits_{\Omega^{(e)}} \left(\frac{\partial \dot{q}_x}{\partial x} + \frac{\partial \dot{q}_y}{\partial y} + \frac{\partial \dot{q}_z}{\partial z} \right) N_i \, d\Omega,$$

in Eq. (2.5) by Gauss's theorem introduces surface integrals of the heat flow across the element boundary. After this integration, Eq. (2.5) becomes

$$\begin{aligned} \int\limits_{\Omega^{(e)}} \rho c_p \frac{\partial T}{\partial t} N_i \, d\Omega - \int\limits_{\Omega^{(e)}} \left[\frac{\partial N_i}{\partial x} \; \frac{\partial N_i}{\partial y} \; \frac{\partial N_i}{\partial z} \right] \left\{ \begin{array}{c} \dot{q}_x \\ \dot{q}_y \\ \dot{q}_y \end{array} \right\} d\Omega \\ = \int\limits_{\Omega^{(e)}} Q N_i \, d\Omega - \int\limits_{\Gamma^{(e)}} (\dot{q} \cdot \hat{n}) \, N_i \, d\Gamma, \quad i = 1, 2, \ldots, D, \end{aligned} \tag{2.9}$$

where $\hat{n}$ is the unit normal to the surface, $\Gamma^{(e)}$ is the element surface boundary, and D is the number of degrees of freedom in the element. The surface integral in Eq. (2.9) is now written as the sum of the integral over the portion of the surface with specified temperature boundary conditions, S_1, specified heat flow boundary conditions, S_2, convective heat exchange boundary conditions, S_3, and radiation heat exchange boundary conditions, S_4, leading to

$$\begin{aligned}
&\int_{\Omega^{(e)}} \rho c_p \frac{\partial T}{\partial t} N_i \, d\Omega - \int_{\Omega^{(e)}} \left[\frac{\partial N_i}{\partial x} \; \frac{\partial N_i}{\partial y} \; \frac{\partial N_i}{\partial z} \right] \left\{ \begin{array}{c} \dot{q}_x \\ \dot{q}_y \\ \dot{q}_y \end{array} \right\} d\Omega \\
&\quad = \int_{\Omega^{(e)}} Q N_i \, d\Omega - \int_{S_1} (\dot{q} \cdot \hat{n}) \, N_i \, d\Gamma + \int_{S_2} \dot{q}_{aero} N_i \, d\Gamma - \int_{S_3} h \, (T_w - T_e) \, N_i \, d\Gamma \\
&\qquad - \int_{S_4} \left(\sigma \epsilon T_w^4 - \alpha_s \dot{q}_r \right) N_i \, d\Gamma, \quad i = 1, 2, \ldots, D,
\end{aligned} \tag{2.10}$$

where $\dot{q}_{aero}$ is the heat flow rate per unit area due to aerodynamic heating (positive into the surface), h is the convective heat transfer coefficient, T_w is the wall temperature, σ is the Stefan-Boltzman constant, ϵ is the surface emissivity, α_s is the surface absorptivity, and $\dot{q}_r$ is the incident radiant heat flow per unit area. We now express the temperatures and temperature gradients in terms of the shape functions and nodal values of temperature using

$$\mathcal{T}^{(e)}(x, y, z, t) = N(x, y, z) T(t) \tag{2.11}$$

$$\frac{\partial \mathcal{T}^{(e)}(x, y, z, t)}{\partial x_i} = B(x, y, z) T(t), \tag{2.12}$$

where B is the shape function derivative matrix, $\mathcal{T}^{(e)}$ gives the spatial distribution of the temperature over the domain of the element and x_i indicates the three cartesian coordinate directions. The resulting system of equations for the finite element formulation then

becomes

$$M_T\dot{T}(t) + K_T T(t) = F_T^Q + F_T^T + F_T^q + F_T^h + F_T^\sigma, \tag{2.13}$$

where M_T is the thermal capacitance matrix and K_T is the thermal conductivity matrix. The vectors F_T^Q, F_T^T, F_T^q, F_T^h, and F_T^σ are the thermal load vectors due to internal heat generation, specified nodal temperatures, specified surface heating, surface convection, and thermal radiation, respectively. The full-order system is solved using the same Crank-Nicolson scheme that is used to solve the reduced-order system. The formulation of the Crank-Nicolson integration scheme is given in a subsequent section.

For the aerothermoelastic problem under consideration, the boundary conditions consist of only aerodynamic heating and thermal radiation. For the loads due to aerodynamic heating, separate models (to be described in a subsequent section) are used and thus the aerodynamic heating treated as a specified surface heating condition for the purposes of the heat transfer model. Therefore, only the F_T^q and F_T^σ terms involving S_2 and S_4 on the right-hand side in Eq. (2.10), are included in the formulation. The radiation boundary condition is modeled by considering the outer surface of the structure to be gray and diffuse. To correctly model the radiation between the surface of the structure and the atmosphere, it must be taken into account that the gas molecules and suspended particles in the atmosphere emit and absorb radiation [126]. Though atmospheric emission is far from resembling that of a blackbody, it is common to treat the atmosphere as a blackbody at a fictitious temperature, T_{sky}, that emits an equivalent amount of radiation [126]. While the value of T_{sky} varies depending on atmospheric conditions, we will take T_{sky} to be the atmospheric temperature, T_∞, corresponding to the given flight altitude. The atmospheric irradation on a surface due to the atmosphere, G_{sky} can be expressed as [126]

$$G_{sky} = \sigma T_{sky}^4. \tag{2.14}$$

The net radiation heat transfer to a surface exposed to solar and atmospheric radiation,

$\dot{q}_{net,rad}$, is then given by

$$\dot{q}_{net,rad} = \alpha_s G_{solar} + \alpha_s \sigma T_{sky}^4 - \epsilon \sigma T_w^4, \tag{2.15}$$

where G_{solar} is the irradiation on the surface due to solar energy. In this work, solar irradiation will be neglected as the solar energy reaching the earth's surface on a clear day, about 950 W/m^2, will be much less than the incoming heat flux due to aerodynamic heating. Kirchoff's identity, given by [127]

$$\alpha_s = \epsilon, \tag{2.16}$$

will be employed to approximate the surface absorptivity and thus the thermal load vector in physical space, F_T, becomes

$$F_T = F_T^q + F_T^\sigma = \int_S \left[\dot{q}_{aero} + \sigma\epsilon\left(T_{sky}^4 - T_w^4\right)\right] N_i \, d\Gamma, \tag{2.17}$$

where the subscript on S is dropped because both the specified heat flux and radiation boundary conditions exist on the entire outer surface of the structure. The element load vector for the outer surface of the wedge element is calculated by integrating the shape functions for the two-dimensional triangular element, $N_{i,Tri}$, over the domain of the triangular outer surface of the element, i.e.,

$$F_{T,1}^{(e)} = \dot{q}_{net} \int_{\Gamma^{(e)}} N_{1,Tri} \, d\Gamma^{(e)} = \dot{q}_{net} \int_0^1 \int_0^{1-\xi} \xi \, |J| \; d\eta \, d\xi = \frac{\Delta}{3} \dot{q}_{net} \tag{2.18a}$$

$$F_{T,2}^{(e)} = \dot{q}_{net} \int_{\Gamma^{(e)}} N_{2,Tri} \, d\Gamma^{(e)} = \dot{q}_{net} \int_0^1 \int_0^{1-\xi} \eta \, |J| \; d\eta \, d\xi = \frac{\Delta}{3} \dot{q}_{net} \tag{2.18b}$$

$$F_{T,3}^{(e)} = \dot{q}_{net} \int_{\Gamma^{(e)}} N_{3,Tri} \, d\Gamma^{(e)} = \dot{q}_{net} \int_0^1 \int_0^{1-\xi} (1 - \xi - \eta) \, |J| \; d\eta \, d\xi = \frac{\Delta}{3} \dot{q}_{net}, \tag{2.18c}$$

where,

$$\dot{q}_{net} = \dot{q}_{aero} + \sigma\epsilon\left(T_{sky}^4 - T_w^4\right), \tag{2.19}$$

was taken out of the integral because it is assumed constant over each element, $|J|$ is the determinant of the finite element Jacobian matrix which is equal to twice the area of the outer surface of the solid element, Δ [124].

2.2 Proper Orthogonal Decomposition for Reduced-Order Transient Thermal Modeling

2.2.1 Creation of POD Basis

This work makes use of POD for reduced-order solution of the transient thermal problem. As described in the introduction, the choice of the POD basis as opposed to any other basis such as an eigenvector basis is due to its optimality condition of providing the most efficient way of capturing the dominant components of a system with a finite number of modes [94]. The method of snapshots [128] is used for determination of the POD basis vectors. In this case, the snapshots are defined as vectors of nodal temperatures at various time instants and are computed from high-fidelity finite element analysis. The goal of the POD formulation is to express the vector of nodal temperatures, T, at any time instant as a linear combination of the basis, $\varphi(x, y, z)$, with coefficients $c(t)$, i.e.,

$$\begin{Bmatrix} T_1 \\ \vdots \\ T_s \end{Bmatrix} = c_1(t) \begin{Bmatrix} \varphi_1^{(1)} \\ \vdots \\ \varphi_s^{(1)} \end{Bmatrix} + c_2(t) \begin{Bmatrix} \varphi_1^{(2)} \\ \vdots \\ \varphi_s^{(2)} \end{Bmatrix} + \cdots + c_r(t) \begin{Bmatrix} \varphi_1^{(r)} \\ \vdots \\ \varphi_s^{(r)} \end{Bmatrix}, \tag{2.20}$$

where s is the total number of degrees of freedom in the finite element model and r is the total number of POD basis vectors retained after truncation. The basis is computed by first

generating the snapshot matrix, A, given by,

$$A = \begin{bmatrix} T_1^{(1)} & T_1^{(2)} & \dots & T_1^{(n)} \\ T_2^{(1)} & T_2^{(2)} & \dots & T_2^{(n)} \\ \vdots & \vdots & \ddots & \vdots \\ T_s^{(1)} & T_s^{(2)} & \dots & T_s^{(n)} \end{bmatrix} = \left[a^{(1)}, a^{(2)}, \dots, a^{(n)}\right], \tag{2.21}$$

where $T_i^{(j)}$ indicates the i-th entry of the j-th snapshot, n is the number of snapshots taken and $a^{(j)}$ refers to column vector corresponding to the j-th snapshot. The correlation matrix, C, is then found, whose entries are the inner products of the corresponding snapshots, given by

$$C = \frac{1}{n} A^T A, \tag{2.22}$$

where $(\cdot)^T$ indicates the transpose. Solution of the eigenvalue problem,

$$C v^{(k)} = \lambda_i v^{(k)}, \tag{2.23}$$

yields the eigenvectors and eigenvalues of the correlation matrix where $v^{(k)}$ with $\|v^{(k)}\| = 1$ indicates the k-th eigenvector of C corresponding to the k-th largest eigenvalue of C. Note that the eigenvectors are arranged such that they correspond with eigenvalues that are sorted in decreasing magnitude so that the POD basis vectors will be sorted in order of decreasing energy. The eigenvalues, λ, and eigenvectors, v, of the correlation matrix are then used to generate the POD basis vectors, φ, which are expressed as a linear combination of the snapshots, i.e.,

$$\varphi^{(k)} = \frac{1}{\sqrt{n\lambda_k}} \sum_{i=1}^{n} v_i^{(k)} a_i = \frac{1}{\sqrt{n\lambda_k}} A v^{(k)}, \tag{2.24}$$

where $v_i^{(k)}$ is the i-th entry of the k-th eigenvector. The POD modal matrix, Φ_T, can then be assembled with the POD basis vectors, φ_i, stored as columns of the matrix. The POD basis is then truncated to a reduced set of POD vectors, $\bar{\Phi}_T$, thus leading to a reduction in

the number of degrees of freedom in the problem. Note that both the full and truncated POD sets are orthonormal, i.e.

$$\Phi_T^T \Phi_T = I_n \tag{2.25a}$$

$$\bar{\Phi}_T^T \bar{\Phi}_T = I_r, \tag{2.25b}$$

where I_n represents the identity matrix of dimension n and I_r refers the the identity matrix of dimension r.

The columns of the snapshot matrix can be expressed as linear combinations of the basis vectors with coefficients χ using the expression [101]

$$A = \Phi_T \chi, \tag{2.26}$$

where χ is a square matrix of coefficients of the full set of POD basis vectors and can be calculated by making use of the orthogonality of the POD basis as

$$\chi = \Phi_T^T A. \tag{2.27}$$

As the basis will be truncated to reduce the problem, the snapshot matrix can at best be approximated via a linear combination of the truncated POD modal matrix, $\bar{\Phi}_T$, given by

$$A \approx \bar{\Phi}_T \bar{\chi}, \tag{2.28}$$

where $\bar{\chi}$ is a rectangular matrix of coefficients of the truncated set of POD basis vectors and can be calculated in a manner similar to that of Eq. (2.27) using

$$\bar{\chi} = \bar{\Phi}_T^T A, \tag{2.29}$$

where the orthogonality of $\bar{\Phi}_T$ is utilized. As the truncated basis can only approximate the

snapshots, the goal is to find the optimal basis such that the approximated snapshot matrix, $\bar{\Phi}_T\bar{\chi}$, represents as closely as possible the actual snapshot matrix, $\Phi_T\chi$. Let Ψ represent an arbitrary orthonormal $s \times n$ basis and $\bar{\Psi}$ represent the corresponding $s \times r$ truncated basis. Let the error incurred as a result of basis truncation, ε, be given by [101, 129]

$$\varepsilon = \|A - \bar{\Psi}\bar{\chi}\|^2. \tag{2.30}$$

Using Eq. (2.29) in Eq. (2.30) and substituting the truncated arbitrary basis, $\bar{\Psi}$, for the truncated POD basis, $\bar{\Phi}_T$, the error expression becomes [101]

$$\varepsilon = \|A - \bar{\Psi}\bar{\Psi}^T A\|^2. \tag{2.31}$$

At this point, the quantity $\bar{\Psi}\bar{\Psi}^T$ is recognized as the orthogonal projector that projects onto the r-dimensional subspace spanned by the basis, $\bar{\Psi}$ [129, 130]. Thus, Eq. (2.31) can be written as

$$\varepsilon = \|A - P_{\bar{\Psi},r}A\|^2, \tag{2.32}$$

where $P_{\bar{\Psi},r}$ is the orthogonal projector onto the r-dimensional subspace. The error due to basis truncation can then be interpreted as the amount by which the projection of the snapshots onto the truncated basis differs from the snapshots themselves. The objective is therefore to find an orthonormal basis such that for a specified error, ε, a minimum number of columns of the set of basis vectors must be retained. A supplementary condition following from Eq. (2.26) is that the basis is a linear combination of the snapshots as seen in Eq. (2.24). It has been shown [94] that along with this supplementary condition, the minimum error in Eq. (2.32) occurs when the basis, $\bar{\Psi}$, is chosen to be the POD basis, $\bar{\Phi}_T$, as given in Eq. (2.24). Thus the POD basis is optimal with respect to any other linear modal representation in that the first k POD modes contain more energy than the first k modes of any other basis [93].

An alternative method for calculating the POD basis involves the singular value decomposition (SVD). The full SVD of the $s \times n$ snapshot matrix, A, is given by [131]

$$A = U\Sigma V^T, \tag{2.33}$$

where U is an $s \times s$ orthogonal matrix, V is an $n \times n$ orthogonal matrix, and Σ is a $s \times n$ diagonal matrix containing the singular values of A, σ, such that

$$\sigma_{ij} = \begin{cases} 0 & \text{for } i \neq j \\ \sigma_i \geq 0 & \text{for } i = j \end{cases}. \tag{2.34}$$

The singular values of A are ordered in decreasing order such that $\sigma_1 \geq \sigma_2 \geq \ldots \geq 0$. The columns of U and V are the left and right singular vectors of A, respectively. The correspondence between the POD basis as derived using the eigenvalues of the correlation matrix, λ_i, and that derived using the SVD can be shown by relating λ_i to σ_i. Performing the SVD of C in terms of the SVD of A, we have

$$C = \frac{1}{n}A^T A = \frac{1}{n}\left(U\Sigma V^T\right)^T U\Sigma V^T = \frac{1}{n}V\Sigma^T U^T U\Sigma V^T. \tag{2.35}$$

Taking advantage of the orthogonality of U, Eq. (2.35) becomes

$$C = \frac{1}{n}V\left(\Sigma^T\Sigma\right)V^T. \tag{2.36}$$

From Eq. (2.36) we can see that V is the matrix of eigenvectors of C and the singular values of A are related to the eigenvalues of C according to [129]

$$\sigma_i^2 = n\lambda_i. \tag{2.37}$$

The POD basis vectors can be shown to correspond to the left singular vectors of the snap-

shot matrix, [129] if we re-write Eq. (2.24) in terms of the SVD of A, i.e.,

$$\varphi_k = \frac{1}{\sqrt{n\lambda_k}} U\Sigma V^T v_k. \tag{2.38}$$

Due to orthogonality of V, Eq. (2.38) simplifies to

$$\varphi_k = \frac{1}{\sqrt{n\lambda_k}} u_k \sigma_k, \tag{2.39}$$

where u_k is the k-th left singular vector of A. Utilizing Eq. (2.37), we have $\varphi_k = u_k$. The connection between POD and SVD allows for justification of the claim of basis optimality due to the ability of the SVD to provide an optimal low-rank approximation to a matrix. Consider an approximation to A written as a partial sum of rank-one matrices formed from the outer product of the left and right singular vectors with the singular value as the scalar coefficient, given by

$$A = \sum_{j=1}^{r} \sigma_j u_j v_j^T, \tag{2.40}$$

where r corresponds to the number of POD basis vectors retained after truncation. It can be shown that the r-th partial sum captures the maximum possible amount of energy of A, where energy is defined in either the 2-norm or Frobenius norm sense [130, 132, 131]. Alternatively stated, no other rank r matrix can be closer to A in the 2-norm or in the Frobenius norm. To examine the connection between this optimality property of the SVD and the optimality of the POD basis, consider Eq. (2.30) written in terms of the truncated set of left singular vectors, $\bar{U}$, corresponding to the truncated set of POD basis vectors, $\bar{\Phi}_T$, given by

$$\varepsilon = \|A - \bar{U}\bar{U}^T A\|^2. \tag{2.41}$$

Now, expressing A in terms of its full SVD leads to,

$$\varepsilon = \|U\Sigma V^T - \bar{U}\bar{U}^T U\Sigma V^T\|^2. \tag{2.42}$$

At this point, the quantity $\bar{U}\bar{U}^T U$ is recognized as the projection of U onto the space spanned by $\bar{U}$ and performs the action of zeroing the columns of U that correspond to the excluded POD basis vectors. Thus, Eq. (2.42) becomes

$$\varepsilon = \|\sum_{j=1}^{n} \sigma_j u_j v_j^T - \sum_{j=1}^{r} \sigma_j u_j v_j^T\|^2, \tag{2.43}$$

and the optimality of the POD basis is demonstrated due to the optimality property of the SVD described above. The absolute error associated with the r-dimensional POD subspace is associated with the eigenvalues of the correlation matrix, C, and the singular values of the snapshot matrix, A, and is given by [129]

$$\varepsilon = \sum_{j=r+1}^{n} \sigma_j^2 = n \sum_{j=r+1}^{n} \lambda_j, \tag{2.44}$$

where ε is defined in the Frobenius norm sense. A relative error tolerance, ε_{rel}, can be defined such that if the relative error is to be less than an error tolerance, ε_T, i.e.,

$$\frac{\varepsilon}{\|A\|^2} = \varepsilon_{rel} \leq \varepsilon_T, \tag{2.45}$$

the number of basis vectors retained, r, should be the smallest integer that

$$\frac{\sum_{j=1}^{r} \sigma_j^2}{\sum_{j=1}^{n} \sigma_j^2} = \frac{\sum_{j=1}^{r} \lambda_j}{\sum_{j=1}^{n} \lambda_j} \geq 1 - \varepsilon_T. \tag{2.46}$$

Note that the left-hand side of Eq. (2.46) can be interpreted as the energy of the included basis vectors relative to the energy of the full set of basis vectors. Furthermore, ε_{rel} can be interpreted as the energy of the excluded basis vectors relative to the energy of the full set of basis vectors, given by

$$\varepsilon_{rel} = \frac{\varepsilon}{\|A\|^2} = \frac{\sum_{j=r+1}^{n} \sigma_j^2}{\sum_{j=1}^{n} \sigma_j^2} = \frac{\sum_{j=r+1}^{n} \lambda_j}{\sum_{j=1}^{n} \lambda_j}. \tag{2.47}$$

Thus, the magnitude of each of the eigenvalues of the correlation matrix can be used in determining the number of POD basis vectors that can be removed from the set.

2.2.2 Solution of System for POD Modal Coordinates

2.2.2.1 Decoupled System: Analytical Solution

One method employed in this work to solve the system of ordinary differential equations for the modal coordinates of the POD basis vectors involves decoupling the equations and solving each analytically. The advantage of the analytical solution is that it avoids the need to time-march the solution and allows for direct generation of the temperature distribution at any time instant of interest. Additionally, it eliminates any error incurred due to numerical integration. The analytical solution is also useful in assessing the accuracy of approximate numerical solutions for linear cases in which the load vector is a known function of time due to its ability to provide an exact solution. The procedure begins with the original system of transient thermal finite element equations given by

$$M_T \dot{T}(t) + K_T T(t) = F_T(t), \tag{2.48}$$

where M_T is the thermal capacitance matrix, K_T is the thermal conductivity matrix, and F_T is the thermal load vector. Note that at this stage we assume that both K_T and M_T are not diagonal. As the set of equations given in Eq. (2.48) is first order in time, we must also specify a vector of initial temperatures,

$$T(t = 0) = T^{(0)}. \tag{2.49}$$

Because the initial condition must be specified for each equation in the analytical solution, it is convenient to work with a homogeneous initial condition. Thus we define a new temperature variable given by $\hat{T} = T - T^{(0)}$ [101]. This transformation results in transforming

Eq. (2.48) such that it becomes

$$M_T\dot{\hat{T}} + K_T\hat{T} = G_T(t), \tag{2.50}$$

where $G_T(t) = F_T(t) - K_T T^{(0)}$. The next step is to transform the system from physical space to modal space, thus reducing from an s by s system to an r by r system. This is accomplished by first expressing the temperature vector as a linear combination of the truncated set of POD basis vectors, $\hat{T} = \bar{\Phi}c$, and then premultiplying the equation by $\bar{\Phi}^T$. The system of equations is then of the form

$$\bar{\Phi}^T M_T \bar{\Phi}\dot{c} + \bar{\Phi}^T K_T \bar{\Phi} c = \bar{\Phi}^T G_T. \tag{2.51}$$

The generalized thermal capacitance matrix, m_T, generalized thermal conductivity matrix, k_T, and generalized load vector, g_T are then identified such that

$$m_T = \bar{\Phi}^T M_T \bar{\Phi} \tag{2.52a}$$

$$k_T = \bar{\Phi}^T K_T \bar{\Phi} \tag{2.52b}$$

$$g_T = \bar{\Phi}^T G_T. \tag{2.52c}$$

Note that because the POD basis vectors are not eigenvectors of the generalized eigenvalue problem, m_T and k_T will still not be diagonal at this stage. Thus, we now solve the generalized eigenvalue problem given by

$$\left(k_T - \gamma_i m_T\right) w_i = 0, \tag{2.53}$$

where γ_i is the i-th eigenvalue and w_i is the corresponding i-th eigenvector. Note that this step is intentionally performed after transformation to modal space so that the size of the eigenvalue problem to be solved is minimized. After assembling the eigenvectors w_i as

columns of the modal matrix W, we now express c as a linear combination of the eigenvectors of the generalized eigenvalue problem so that $c = W\tilde{c}$. The system of equations is then premultiplied by W^T such that the system becomes

$$W^T m_T W\dot{\tilde{c}} + W^T k_T W\tilde{c} = W^T g_T. \tag{2.54}$$

The transformed generalized thermal capacitance matrix, $\tilde{m}_T$, transformed generalized thermal conductivity matrix, $\tilde{k}_T$, and transformed generalized load vector, $\tilde{g}_T$, are then identified such that

$$\tilde{m}_T = W^T m_T W \tag{2.55a}$$

$$\tilde{k}_T = W^T k_T W \tag{2.55b}$$

$$\tilde{g}_T = W^T g_T. \tag{2.55c}$$

Due to orthogonality of the eigenvectors with respect to m_T and k_T, $\tilde{m}_T$ and $\tilde{k}_T$ will be diagonal matrices, thus decoupling the system of ordinary differential equations. Furthermore, by enforcing the eigenvectors, W, to be normalized with respect to m_T, $\tilde{m}_T$ is reduced to the identity matrix and the i-th equation of the system can be expressed as

$$\dot{\tilde{c}}_i + \tilde{k}_{T,i}\tilde{c}_i = \tilde{g}_{T,i}, \tag{2.56}$$

where $\tilde{k}_{T,i}$ is the i-th diagonal entry of $\tilde{k}_T$. Using the fact that the initial condition was made to be homogeneous, the solution of the i-th equation for an arbitrary time-dependent generalized load, $\tilde{g}_T(t)$, is given by

$$\tilde{c}_i(t) = \mathrm{e}^{-\tilde{k}_{T,i}t} \int_0^t \tilde{g}_{T,i}(\tau)\mathrm{e}^{\tilde{k}_{T,i}\tau}\, d\tau, \quad i = 1, \ldots, r, \tag{2.57}$$

where τ is a dummy variable of integration and t is the time instant of interest. For a generalized load that is independent of time, the solution is given by

$$\tilde{c}_i(t) = \tilde{g}_{T,i} \frac{1 - \mathrm{e}^{-\tilde{k}_{T,i} t}}{\tilde{k}_{T,i}}, \quad i = 1, \ldots, r. \tag{2.58}$$

Once all of the transformed modal coordinates have been calculated, the sequence of transformations can be reversed to obtain the physical temperatures using

$$T(t) = \bar{\Phi} W \tilde{c}(t) + T^{(0)}. \tag{2.59}$$

Note that for the linear case, the matrix product $\bar{\Phi}W$ must only be evaluated once, and solution of the transient thermal problem is reduced to a matrix-vector product and a vector sum. An overview of the sequence of equation transformations is given in Fig. 2.1.

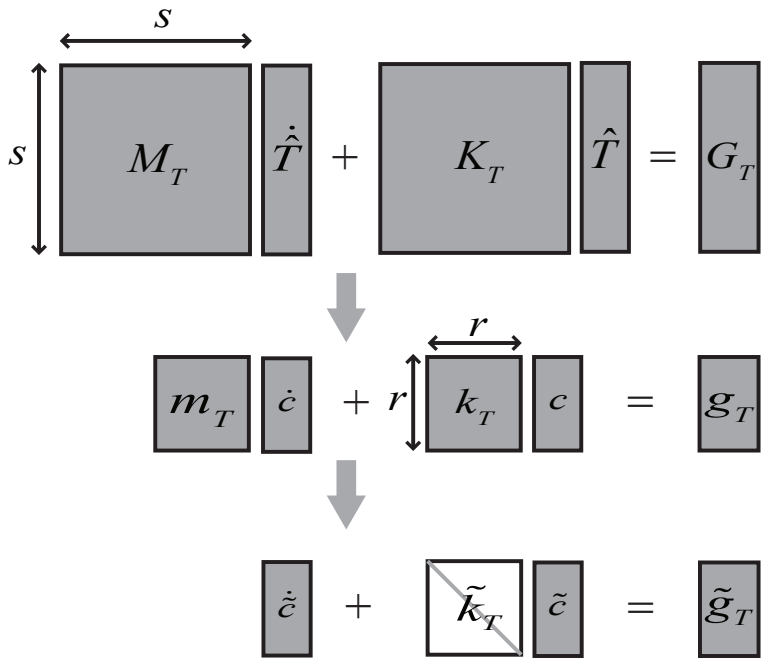

Figure 2.1: Sequence of transformations of heat transfer equations from full system to decoupled reduced-order system.

2.2.2.2 Coupled System: Numerical Integration

In addition to decoupling the system and solving the equations analytically, results are also obtained in this dissertation via numerical solutions of the coupled system. Numerical solutions of the coupled thermal problem may prove to be more useful than decoupled analytical solutions within hypersonic vehicle aerothermoelastic simulation frameworks. This is due to the fact that the heat flux depends on various factors such as deformation and aerodynamic flow properties that are not known ahead of time. The thermal load vector must therefore be sampled at specific time instants and integrated over time numerically, thus the analytical solution loses its utility in these cases. Note that one could perform the integral in Eq. (2.57) numerically and still use the decoupled solution method. However at that point it may be more computationally efficient to integrate the equations numerically and avoid diagonalizing the system matrices. Solving the coupled system directly avoids the need to solve an eigenvalue problem to decouple the equations. This is especially important for nonlinear problems in which the thermal capacitance matrix and thermal conductivity matrix change with temperature and an eigenvalue problem would need to be solved at every time step if the equations were to be decoupled.

For the numerical solution, the transient thermal equations are solved using a numerical time-marching algorithm [123, 133]. For nonlinear cases in which the system matrices or load vector depend on the temperatures at the current time step, Newton-Raphson iterations can be employed within each time step. To begin the formulation, consider a general system of first-order coupled ordinary differential equations of the form

$$M_T\dot{T} + K_T T = F_T\left(t\right). \tag{2.60}$$

The first step will be to reduce the system and transform from physical space to modal space using Eq. (2.52). Additionally, the effect of initial conditions is again removed as described in the previous section. For the numerical solution, we will not perform the additional step

to solve the eigenvalue problem and decouple the equations. Rather, the reduced-order coupled system will be integrated numerically at this stage. We denote a time instant in the response of the system by $t^{(n)}$ such that the time instant at the next time step is given by by $t^{(n+1)} = t^{(n)} + \Delta t$, where $n = 0, 1, 2, \ldots, N$. A parameter θ is introduced to represent the response of the system at an intermediate time, $t^{(\theta)}$, such that $t^{(\theta)} = t^{(n)} + \theta\Delta t$, where $0 \leq \theta \leq 1$. Expressing Eq. (2.60) at time $t^{(\theta)}$ in modal space, we have,

$$m_T \dot{c}^{(\theta)} + k_T c^{(\theta)} = g_T \left(t^{(\theta)}\right), \tag{2.61}$$

where the superscript θ indicates the vector of unknowns, at time instant $t^{(\theta)}$. We now introduce approximations to c, its time-derivative, and g_T at $t^{(\theta)}$ given by

$$\dot{c}^{(\theta)} = \frac{c^{(n+1)} - c^{(n)}}{\Delta t} \tag{2.62a}$$

$$c^{(\theta)} = (1-\theta)c^{(n)} + \theta c^{(n+1)} \tag{2.62b}$$

$$g_T \left(t^{(\theta)}\right) = (1-\theta)\, g^{(n)} + \theta g^{(n+1)}. \tag{2.62c}$$

Substituting Eqs. (2.62) into Eq. (2.61) leads to the recurrence relation given by [123]

$$\left[\theta k_T + \frac{1}{\Delta t} m_T\right] c^{(n+1)} = \left[-(1-\theta)k_T + \frac{1}{\Delta t} m_T\right] c^{(n)} + (1-\theta)\, g^{(n)} + \theta g^{(n+1)}, \tag{2.63}$$

where $c^{(n+1)}$ is the unknown to be found and $c^{(n)}$ is the solution from the previous time step. The recurrence relation given in Eq. (2.63) is of the form

$$L c^{(n+1)} = b^{(n+1)}, \tag{2.64}$$

where

$$L = \theta k_T + \frac{1}{\Delta t} m_T \tag{2.65a}$$

$$b^{(n+1)} = \left[-\left(1-\theta\right) k_T + \frac{1}{\Delta t} m_T \right] c_n + \left(1-\theta\right) g^{(n)} + \theta g^{(n+1)}. \tag{2.65b}$$

Equation (2.63) represents a family of recurrence relations in which the particular numerical scheme depends on the chosen value of θ. For $\theta = 0$, $\frac{1}{2}$, $\frac{2}{3}$, and 1, the algorithm represents the forward Euler, Crank-Nicolson, Galerkin, and backward Euler method, respectively. Additionally, if $\theta = 0$, the algorithm is explicit, while for $\theta > 0$, the algorithm is implicit. The requirements for convergence of the selected numerical scheme are given by the Lax Equivalence Theorem which states that for a well-posed initial value problem and a consistent discretization scheme, stability is the necessary and sufficient condition for convergence [134, 131]. The family of θ algorithms described above is unconditionally stable in the linear case for $\theta \geq \frac{1}{2}$ while an extension for nonlinear systems [135] was also shown to be unconditionally stable for $\theta \geq \frac{1}{2}$. For $\theta < \frac{1}{2}$, the algorithm is conditionally stable and the eigenvalue stability region is such that the critical time step is given by

$$\Delta t_{cr} = \frac{2}{1-2\theta} \frac{1}{\gamma_m}, \tag{2.66}$$

where γ_m is the largest system eigenvalue. For this work, the Crank-Nicolson scheme corresponding to $\theta = \frac{1}{2}$ is used due to its second-order accuracy.

Since the equations are solved in modal space and the initial temperatures are known in physical space, the initial values of the POD modal coordinates must first be calculated before time-marching can proceed. Using the transformation between physical space and modal space, we begin by expressing the vector of initial temperatures in physical space as

$$T^{(0)} = \bar{\Phi} c^{(0)}, \tag{2.67}$$

where $c^{(0)}$ is the vector of initial values of the modal coordinates. Expanding this expression in terms of the individual POD vectors, Eq. (2.67) becomes

$$T^{(0)} = c_1^{(0)}\varphi^{(1)} + c_2^{(0)}\varphi^{(2)} + \cdots + c_r^{(0)}\varphi^{(r)}, \tag{2.68}$$

where $\varphi^{(i)}$ indicates the i-th basis vector and $c_i^{(0)}$ refers to the corresponding i-th modal coordinate at time $t^{(0)}$. To find the initial value of the i-th modal coordinate, Eq. (2.68) is premultiplied by the transpose of the i-th basis vector, $\varphi^{(i)T}$, to obtain

$$\varphi^{(i)T}T^{(0)} = c_1^{(0)}\varphi^{(i)T}\varphi^{(1)} + c_2^{(0)}\varphi^{(i)T}\varphi^{(2)} + \cdots + c_r^{(0)}\varphi^{(i)T}\varphi^{(r)}. \tag{2.69}$$

Recall that the basis vectors are an orthonormal set such that

$$\varphi^{(i)T}\varphi^{(j)} = \delta_{ij}, \tag{2.70}$$

where δ_{ij} is the Kronecker delta. Thus, the right-hand side of Eq. (2.69) reduces to $c_i^{(0)}$ and the left-hand side gives its value. By premultiplying Eq. (2.68) by each of the basis vectors, the complete vector of initial modal coordinates can be found and time-marching of the system can proceed.

Chapter III

Assessment of Reduced-Order Transient Thermal Modeling Methodology

One of the main assumptions of the transient thermal modeling methodology is that the POD basis is capable of spanning the space of the solution through the complete time-history of the simulation. The boundary conditions to the thermal problem will be time-dependent and not known *a priori*. Furthermore, it is desired to use the same POD basis for aerothermoelastic simulations with varying flight conditions. As such, it is critical to evaluate the accuracy of the reduced-order thermal modeling approach under the conditions in which it is to be applied. The current chapter begins by describing a hypersonic vehicle control surface model to be used as a case study. Assessments of the accuracy of the POD approach are performed under both time-independent and time-dependent boundary conditions. Additionally, comparisons are made between the approach in which the thermal equations are decoupled and solved analytically and that in which the coupled system is solved numerically. The results presented in this chapter provide evidence with regard to the robustness of the POD basis under time-varying flight conditions and thermal boundary conditions.

3.1 Control Surface Model

The methodology developed in this work is applied to a representative control surface structure as the control surfaces are expected to have a strong contribution to the dynamics of the vehicle. The hypersonic vehicle configuration considered in this study, as developed in a previous work [60], is shown in Fig. 3.1. A finite element model of a representative hypersonic vehicle elevator has been created for use in this study. The airfoil cross-section is that of a double wedge. The thickness from the top skin layer to the bottom skin layer is 4% chord length [136, 137, 138]. The top and bottom skin layers are each equipped with two 3.8 mm thick thermal protection system layers, and thus the thickness of the outer mold line is 4% chord length plus the 15.2 mm of thermal protection system material. The chord length at the root is 5.2 m (17 ft) [60] and the leading edge is swept by 34° while the trailing edge is swept by 18° [25]. Planform and cross-sectional views of the airfoil are given in Fig. 3.2 and Fig. 3.3, respectively.

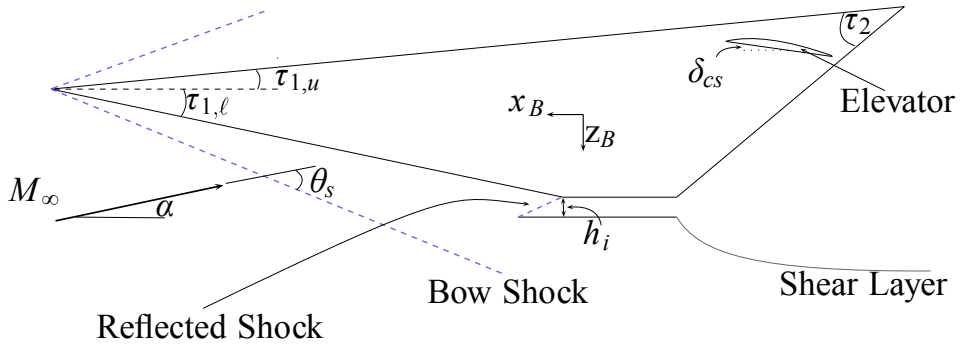

Figure 3.1: Overall HSV geometry illustrating position of control surface [18].

Due to the severe aerodynamic heating experienced in hypersonic flight, layers of thermal protection material are needed to keep the temperature of the structure below maximum temperature limits. A survey of the literature reveals a wide range of design strategies for mitigating the high temperatures experienced in hypersonic flight [139, 140, 141, 142, 143, 144, 145, 146]. This study considers a thermal protection system consisting of an outer heat shield and middle insulation layer on top of the structure as shown in Fig. 3.4. The material

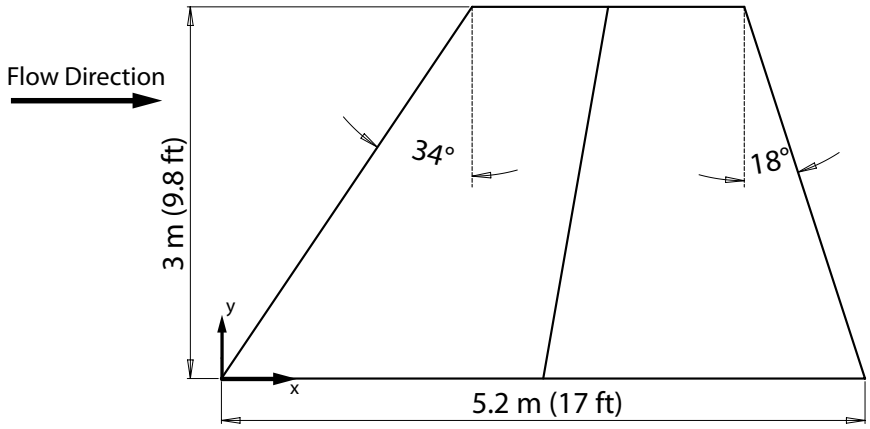

Figure 3.2: Planform geometry of control surface model.

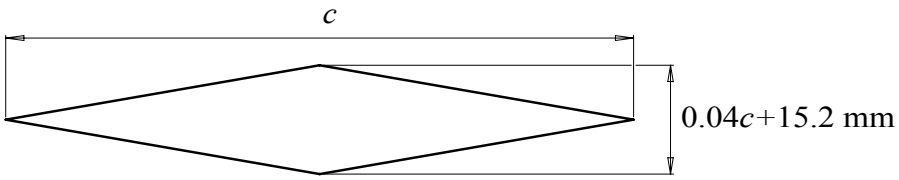

Figure 3.3: Cross-sectional geometry of control surface model.

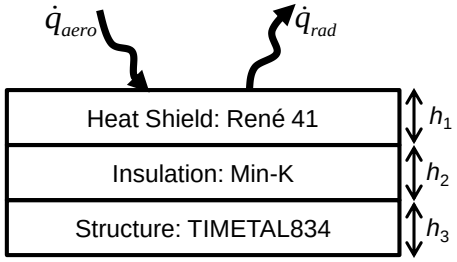

Figure 3.4: Schematic of material stacking scheme at outer mold line of structure.

Table 3.1: Structural material properties used in control surface model [151].

	ρ $[kg/m^3]$	E $[Pa]$	ν	h $[mm]$
René 41	8240	T-dep.	0.31	3.8
Min-K	256	Neglect	Neglect	3.8
TIMETAL 834	4550	T-dep.	0.31	3.175

for the heat shield is chosen to be René 41 as it was found to be efficient in terms of mechanical properties at elevated temperatures [145]. For the insulation layer, three different materials were considered in the preliminary materials evaluation: Internal Multiscreen Insulation (IMI) [140], High Temperature Flexible Min-K [145], and Q-Fiber Felt [140]. Of these, the Min-K insulation, which is a proprietary silica based material faced with Astroquartz cloth [145], is selected due to its relatively low thermal diffusivity. For the structure, the Titanium alloy TIMETAL 834 (formerly known as IMI 834) is chosen. The advantage of using this alloy is its maximum application temperature, T_{max}, of $600°\mathrm{C}$ compared with that of Ti-6242S ($520°\mathrm{C}$), Ti-6242 ($450°\mathrm{C}$), Ti-811 ($400°\mathrm{C}$), and Ti-6-4 ($300°\mathrm{C}$) [147]. The thermal and mechanical properties of the three materials employed in the model are shown in Table 3.1 and Table 3.2, where "T-dep." indicates that the property is temperature-dependent [148, 149, 145, 25]. In the tables, ρ is the density, E is the Young's modulus of elasticity, ν is the Poisson's ratio, α_T is the cofficient of thermal expansion, κ is the thermal conductivity, c_p is the specific heat, and h_i is the thickness of the i-th layer. Note that the temperature-dependent material properties for René 41 are extrapolated beyond the available data and the maximum application temperature, T_{max}, is set to 1,500 K. In addition to these properties, the emissivity, ϵ, of the heat shield is taken to be 0.85 [25, 150].

The finite element mesh used in this study is shown in Fig. 3.5. The model contains 2,812 degrees of freedom and 5,580 elements. The heat shield and insulation layer are each modeled using one layer of 6-node solid wedge elements while the top and bottom skins and stiffeners are modeled using 3-node, 2-dimensional triangular elements. While refinement of the mesh in the thickness direction may provide a more accurate representation of the

Table 3.2: Thermal material properties used in control surface model [151].

	α_T $[\mu m/m/K]$	κ $[W/m/K]$	c_p $[J/kg/K]$	T_{max} $[K]$
René 41	T-dep.	18	541	1500
Min-K	Neglect	0.052	858	1250
TIMETAL 834	11	7	525	873

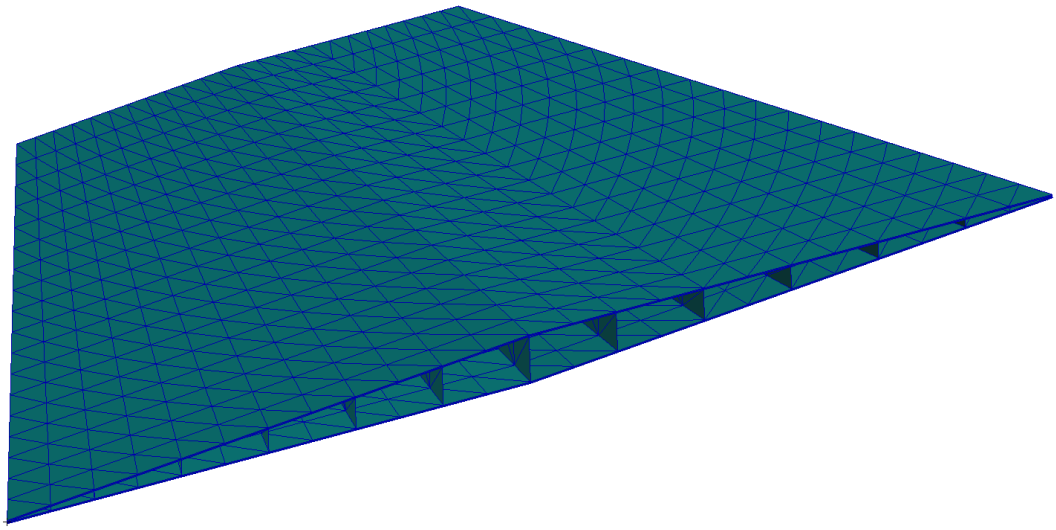

Figure 3.5: Finite element model of control surface used for assessment of reduced-order thermal modeling methodology.

temperature distribution, the purpose of this study is to examine the ability of the POD solution to represent the reference solution, which is taken to be the solution of the current the full-order model. Of the 5,580 elements in the model, 3,456 are solid elements and 2,124 are triangular elements. The control surface is taken to be all-moveable about a hinge line located at the mid-chord [60] and will thus be connected to the vehicle main body through a torque tube.

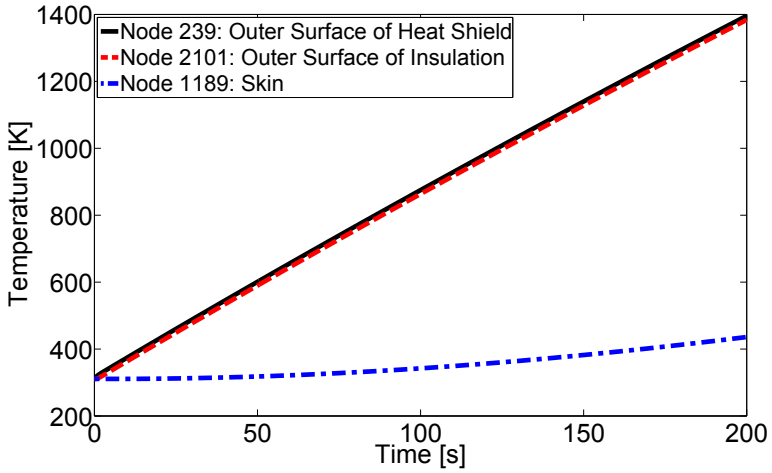

Figure 3.6: Temperature history of three selected nodes for constant heat flux case.

3.2 Results

3.2.1 Time-Independent Thermal Load Vector

The first case that will be considered consists of a uniform heat flux of 10 $\mathrm{W/cm^2}$ that is constant in time and applied at the outer surfaces of the model. The time range considered in this example is 0 - 200 s. A plot of the temperature-history of a selected node at the outer surface of the heat shield, outer surface of the insulation, and skin within the time range considered is given in Fig. 3.6. These three nodes are located at the mid-chord, mid-span location on the bottom surface of the control surface. Selection of the location at which the plot the temperature-histories is arbitrary and these results are given solely for illustration purposes. Note that the temperature decreases significantly between node 2101 and node 1189 due to the effect of the insulation.

For the purposes of this study, the high-fidelity finite element solution will be treated as the truth model and error calculations will be made with respect to it. To assess the effect of number of snapshots taken throughout the range of time considered, a high-fidelity transient thermal finite element analysis (FEA) was carried between 0 – 200 s out using Sol 159 within the finite element code MSC.Nastran. POD bases were then generated based on 5, 21, 81, and 401 snapshots of the high-fidelity solution, which correspond to snapshots

taken in evenly spaced intervals every 50, 10, 2.5, and 0.5 seconds, respectively, between 0 - 200 s. The reduced system was solved using the decoupled analytical approach for all of the results in this section. To quantify the percentage error of the POD solution, a spatial error norm, e, is defined such that

$$e = \sqrt{\sum_{i=1}^{s} \left(\frac{T_i^r - T_i^f}{T_i^f} \right)^2} \times 100\%, \tag{3.1}$$

where T_i^f is the temperature at node i from the full-order solution and T_i^r is the temperature at node i from the reduced-order solution. Defined in this manner, e can be interpreted as the 2-norm of the vector of percentage errors of the nodes at a given time instant. Results were generated for cases with one, two, and three POD basis vectors retained after truncation. The relative errors as defined in Eq. (2.47) for the case of 401 snapshots with one, two, and three retained POD basis vectors are given in Table 3.3. Results of reduced-order simulations with varying number of retained modes and number of snapshots are given in Fig. 3.7 with e calculated in 0.5 s intervals.

Table 3.3: Relative energy of excluded modes for cases of one, two, and three retained modes.

Number of retained modes	ε_{rel}
1	3.90×10^{-4}
2	7.04×10^{-6}
3	1.22×10^{-9}

As expected, the error decreases as more POD basis vectors are used in the reduced-order solution regardless of the number of snapshots taken. However, from the results shown, one cannot conclude that taking more snapshots will result in a smaller error for any arbitrary time instant regardless of the number of basis vectors retained. Though in general it appears that taking more snapshots is advantageous, for certain time intervals the error is lower for the cases of fewer snapshots. To understand the underlying causes of this, the effect of number of snapshots on the POD error was investigated at the specific time

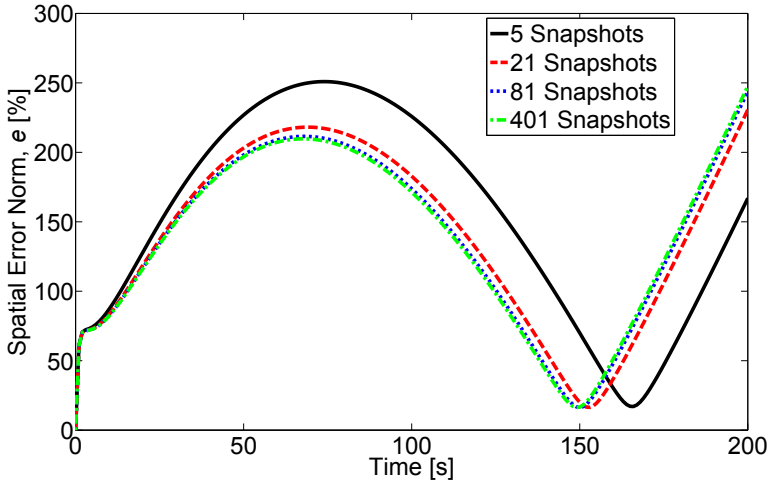

(a) One basis vector retained.

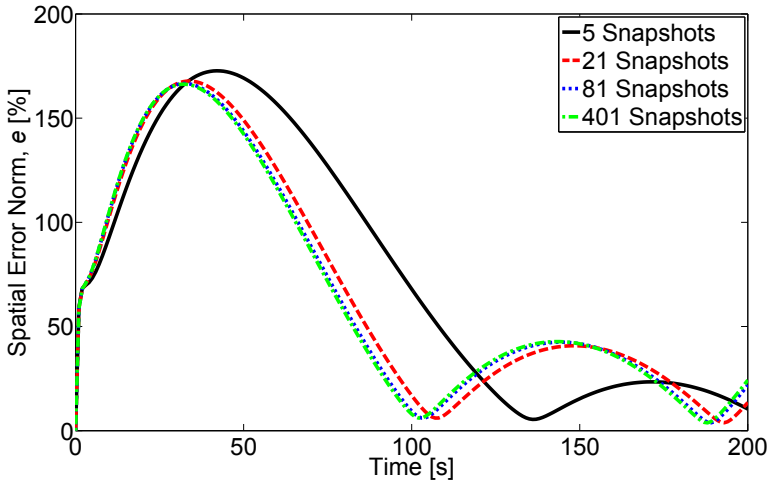

(b) Two basis vectors retained.

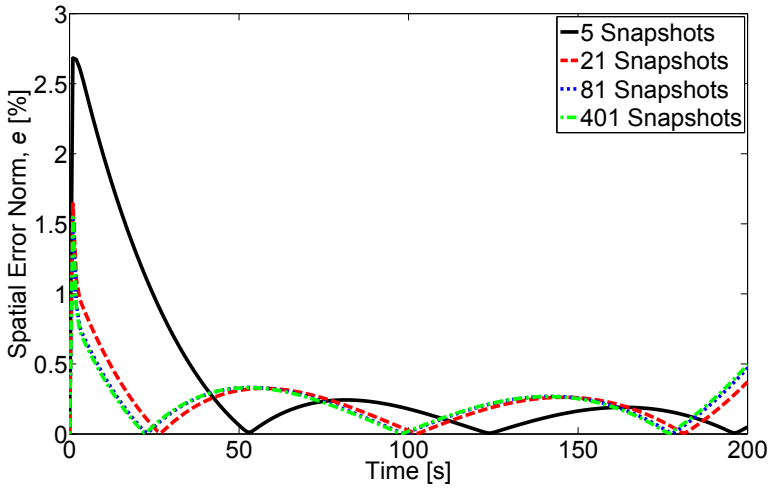

(c) Three basis vectors retained.

Figure 3.7: POD percentage error for varying number of snapshots and retained number of basis vectors.

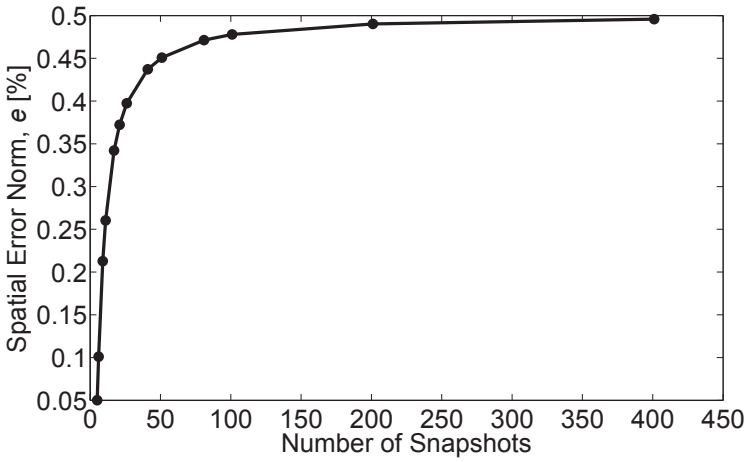

Figure 3.8: POD error for varying number of snapshots at 200 s.

instant of 200 s. POD bases were generated for cases with varying numbers of snapshots ranging from 5 to 401. For each case, the error of the POD solution using 3 POD basis vectors at 200 s was calculated. Results are given in Fig. 3.8.

From Fig. 3.8, one can see that the increase in error with number of snapshots is in agreement with the results shown in Fig. 3.7 at 200 s in that the error increases asymptotically with number of snapshots. To further investigate the error of the POD basis as a function of number of snapshots, the relative energy of the excluded basis vectors, given by Eq. (2.47), was calculated for varying numbers of snapshots as shown in Fig. 3.9. Again, three basis vectors were retained and the number of snapshots ranged from 5 - 401.

The trend in Fig. 3.9 is similar to that in Fig. 3.8 and indicates that the energy of the first three POD vectors relative to that of the full set decreases asymptotically with increasing number of snapshots. It is believed that the reason for the increase in error with number of snapshots is due to spreading of the energy to higher modes with increasing number of snapshots. The number of POD basis vectors obtained is equal to the number of snapshots taken. Because taking more snapshots results in more POD basis vectors being created, it is possible that as more snapshots are taken, the proportion of energy contained in the first three basis vectors relative to the total energy of the set may decrease. The energy of the first three POD modes increases at a slower rate than the that of the higher modes with

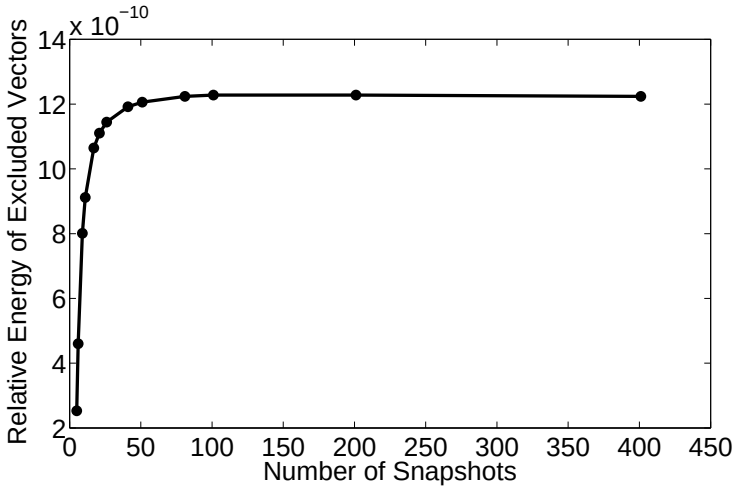

Figure 3.9: Relative energy of excluded basis vectors for varying number of snapshots at 200 s.

number of snapshots for this particular case.

To understand the relevance of each of the first three POD modes to the solution, the modal coordinates of these modes were plotted as a function of number of snapshots again at 200 s and the results are given in Fig. 3.10. Again, in this case only the first three modes were used for the solution. Although the change is small, the modal coordinate of the first POD vector decreases with increasing number of snapshots. Those of the second and third POD vectors increase with increasing number of snapshots. These trends indicate that some of the energy of the first POD mode is being spread to the higher POD modes as the number of snapshots increases.

Finally, the utility of taking additional snapshots is measured by calculating the projections of the snapshots onto the subspaces spanned by the first snapshot, the first two snapshots, the first three snapshots, and the first four snapshots. Snapshots lying in the space already spanned by previous snapshots provide no additional information while snapshots orthogonal to the space already spanned by previous snapshots provide maximum information. The full QR factorization of the snapshot matrix is first computed such that $A = QR$ where Q is an orthogonal $s \times s$ matrix and R is an upper triangular $s \times n$ matrix. The columns of Q have the property that they span the same subspace as the corresponding

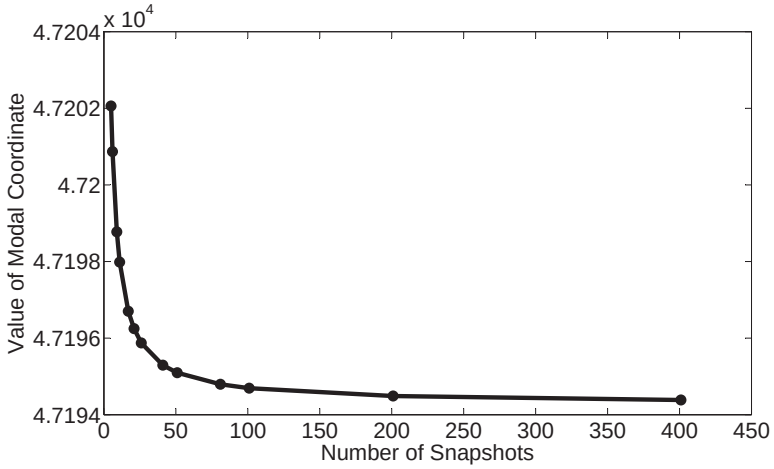

(a) Modal coordinate of first POD basis vector.

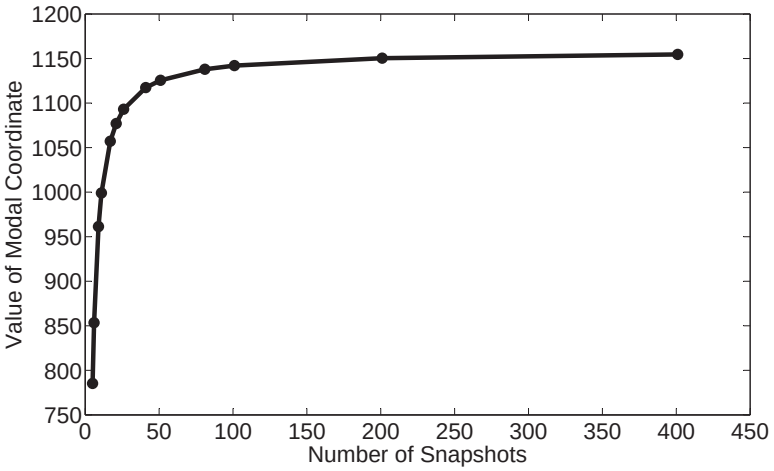

(b) Modal coordinate of second POD basis vector.

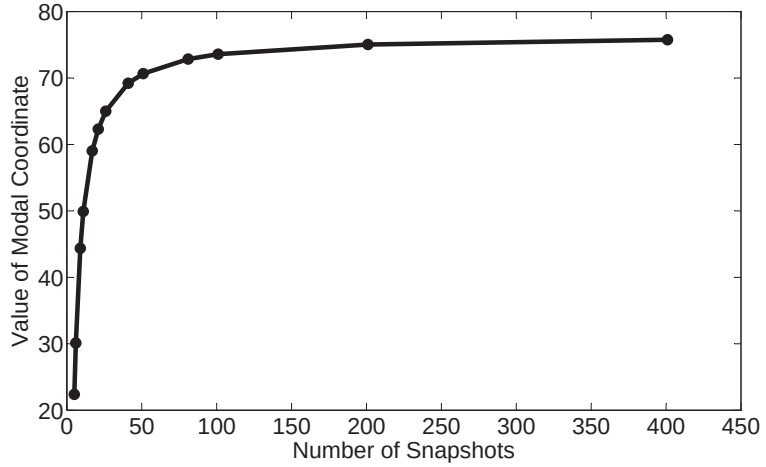

(c) Modal coordinate of third POD basis vector.

Figure 3.10: Modal coordinates of first three POD basis vectors for varying number of snapshots at 200 s.

columns of A such that [130]

$$\begin{aligned}
\langle q_1 \rangle &= \langle a_1 \rangle \\
\langle q_1, q_2 \rangle &= \langle a_1, a_2 \rangle \\
\langle q_1, q_2, q_3 \rangle &= \langle a_1, a_2, a_3 \rangle \\
&\vdots \\
\langle q_1, q_2, \ldots, q_j \rangle &= \langle a_1, a_2, \ldots, a_j \rangle,
\end{aligned} \tag{3.2}$$

where $\langle \cdot \rangle$ indicates the subspace spanned by the vectors enclosed in the brackets. One can therefore use the columns of Q to form orthonormal subspaces that span the subspaces of the corresponding columns of the snapshot matrix. Each snapshot is first normalized to unit magnitude, i.e.

$$\|\breve{a}^{(j)}\|_2 = 1, \quad i = 1, \ldots, n, \tag{3.3}$$

where $\breve{a}^{(j)}$ is the j-th normalized snapshot, so that the magnitude of the projection of each snapshot onto the various subspaces will lie between zero and one. If we take $\bar{Q}$ to be the truncated version of Q containing the first j columns of Q, the projection onto the space spanned by $\bar{Q}$ is given by $\bar{Q}\bar{Q}^T$. If a snapshot $\breve{a}^{(j)}$ lies in the span of $\bar{Q}$, then applying the projection results in $\breve{a}^{(j)}$ itself, i.e., [130]

$$\bar{Q}\bar{Q}^T\breve{a}^{(j)} = \breve{a}^{(j)}. \tag{3.4}$$

Define the residual, $\mathcal{R}$, as the normed difference between the projection of the j-th snapshot onto the subspace and the actual snapshot given by

$$\mathcal{R} = \|\bar{Q}\bar{Q}^T\breve{a}^{(j)} - \breve{a}^{(j)}\|_2, \tag{3.5}$$

where a zero value of $\mathcal{R}$ indicates that the snapshot already lies in the subspace while a value of one indicates that the snapshot is orthogonal to the subspace. Results are given in Fig. 3.11 for projection of each of the snapshots onto the subspaces spanned by the first, first two, first three, and first four snapshots.

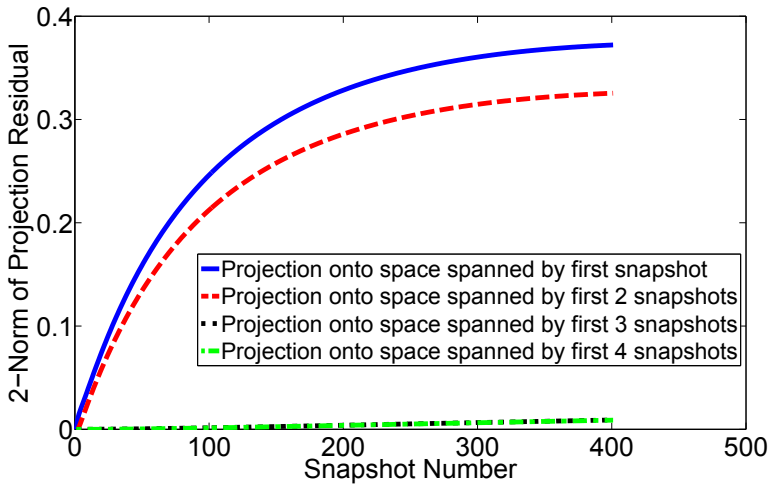

Figure 3.11: Residual of projection of snapshots onto various subspaces.

The results shown in Fig. 3.11 indicate that the space spanned by just the first three snapshots comes close to containing all of the snapshots. Projection of the snapshots onto the subspace spanned by the first four snapshots shows almost no noticeable difference from that onto the subspace spanned by the first three snapshots, indicating there is little new information introduced by including the fourth snapshot. These results indicate that the first three snapshots capture most of the dynamics necessary for creation of the POD basis. This is not unexpected as the constant, uniform heat flux should lead to system dynamics which are easily captured as opposed to a case with more complex spatial variation in the boundary conditions.

3.2.2 Time-Dependent Thermal Load Vector

The next case considered is that of a time-dependent thermal load vector whose functional form is specified *a priori*. One of the fundamental approximations to be examined in

this case study is the use of a fixed POD basis for cases with time-varying natural boundary conditions. The advantage of using the same basis throughout the transient is that the need to perform the time-consuming computation of regenerating the basis during the course of a simulation is avoided. Additionally, the actual thermal loads on the HSV will not be known ahead of time, and the basis must therefore be robust to changes in the boundary conditions. The POD basis vectors are treated as Ritz vectors, similar to their use in structural dynamics. The basis vectors must only satisfy the Dirichlet boundary conditions [152] (fixed-temperature boundary conditions in this case), and since the boundary conditions will only be of the Neumann type, the POD basis will satisfy the necessary conditions of Ritz modes throughout the transient. This case will be also used to compare the accuracy of the decoupled analytical POD solution with that of the numerically integrated POD solution with the goal of assessing the effect of the size of the time step on the numerical solution. The form of the thermal load vector used for this case is given by

$$F_T(x, y, z, t) = H(t) F_{T,spatial}(x, y, z), \tag{3.6}$$

where $H(t)$ is a scalar time-dependent coefficient and $F_{T,spatial}(x, y, z)$ is a spatially varying vector. For this study, $H(t)$ is taken to be $\sin(\omega t)$ with ω = 0.01 Hz and $F_{T,spatial}(x, y, z)$ is obtained from the uniform 10 W/cm^2 case above. The i-th decoupled equation will then be of the form

$$\dot{\tilde{c}}_i(t) + \tilde{k}_i \tilde{c}_i(t) = \sin(\omega t)\, \tilde{g}_i, \tag{3.7}$$

and the solution subject to the initial condition $\tilde{c}(t = 0) = 0$ is given by

$$\tilde{c}_i(t) = \frac{\tilde{g}_i \mathrm{e}^{-\tilde{k}_i t}\omega - \tilde{g}_i \omega \cos(\omega t) + \tilde{g}_i \tilde{k}_i \sin(\omega t)}{\tilde{k}_i^2 + \omega^2}. \tag{3.8}$$

The POD basis was first created by taking 501 snapshots in evenly spaced intervals between 0 and 500 seconds with one snapshot per second. Note that the snapshots were taken by

decoupling the full system using the full eigendecomposition of the system and solving each equation analytically to eliminate any error that would be incurred due to numerical time-stepping. The temperature response from 0 to 2,000 s for a node at the outer surface of the heat shield, outer surface of the insulation layer, and on the bottom skin is given in Fig. 3.12.

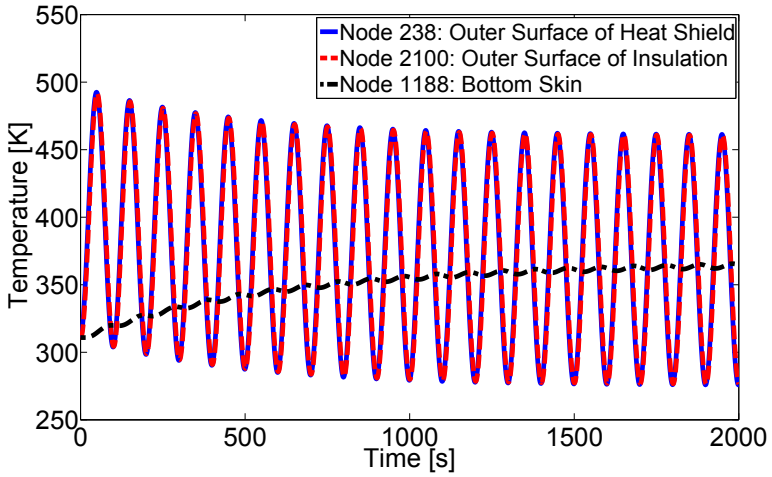

Figure 3.12: Temperature response for three selected nodes for the case of time-varying heat flux.

Once the snapshots are taken, the correlation matrix and its eigendecomposition are found. The magnitudes of the first nine eigenvalues of the correlation matrix are given in Fig. 3.13. Based on the eigenvalues of the correlation matrix, only the first four POD modes were retained in the solution. Note that the relative energy of the excluded POD modes as calculated using Eq. (2.47) is 1.58×10^{-9}. The following sections investigate the accuracy of the reduced-order solution through decoupling and solving the equations analytically as well as directly integrating the coupled system numerically.

3.2.2.1 Decoupled Analytical Solution

The first step is to compare the full-order solution with the solution obtained by introducing the POD modes, decoupling the equations, and solving them analytically, hereafter referred to as the POD-analytical solution. Using e from Eq. (3.1), the error of the POD-

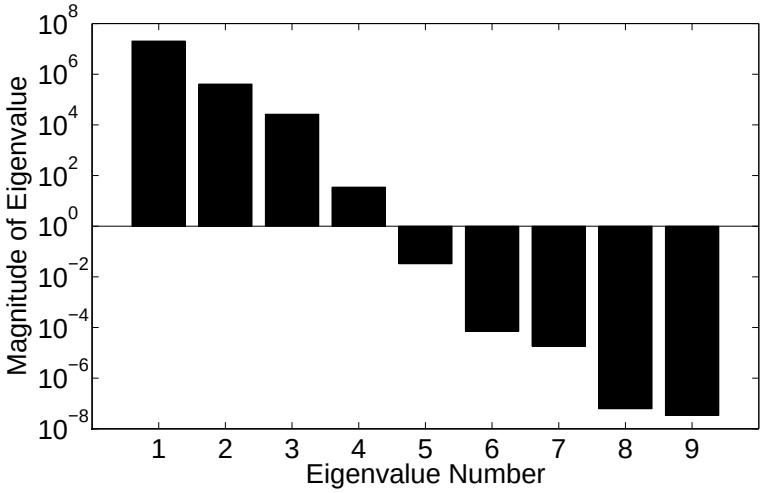

Figure 3.13: First nine eigenvalues of correlation matrix for the case of time-varying heat flux.

analytical solution is given in Fig. 3.14 for the time interval 0 – 500 s. Recall that the thermal snapshots were also taken between 0 – 500 s, and thus the results presented in Fig. 3.14 show the corresponding error obtained when the POD modes are used in the reduced-order solution for only the time range in which the system was sampled to generate the thermal snapshots.

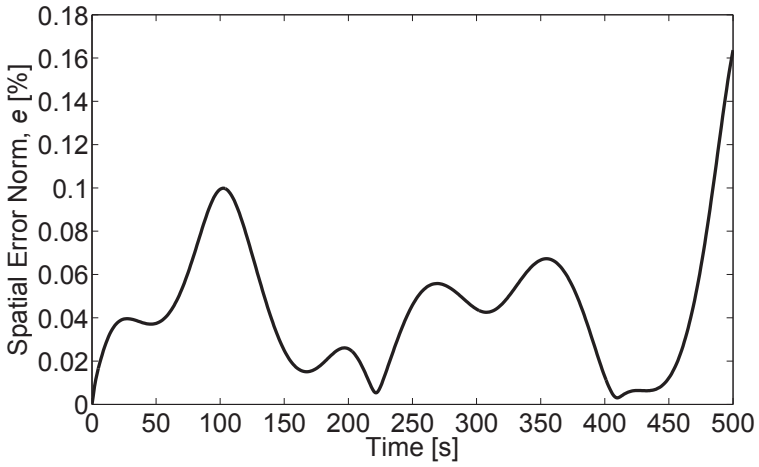

Figure 3.14: POD-analytical solution error.

Though the POD-analytical solution shows good agreement with the full-order solution within the time range in which the snapshots were taken, it is likely that the reduced-order

solution will be required to extrapolate temperature distributions for time instants that are outside of the time interval in which the snapshots are taken for the actual HSV simulations. Thus, the POD-analytical solution was compared with the full-order solution for the time range from 0 – 2,000 s to investigate the accuracy of the reduced-order solution outside of the time interval in which the snapshots were taken. Results for cases with three, four, five, and six POD basis vectors retained in the POD-analytical solution are given in Fig. 3.15. As seen in the figure, the overall accuracy of the reduced-order solution outside of the time range in which the snapshots were taken is lower than that within the time range in which the snapshots were taken. Furthermore, though retaining more than four POD basis vectors results in little improvement in solution accuracy between 0 and 500 s, the use of additional basis vectors has a more prominent effect on the error for times beyond 500 s.

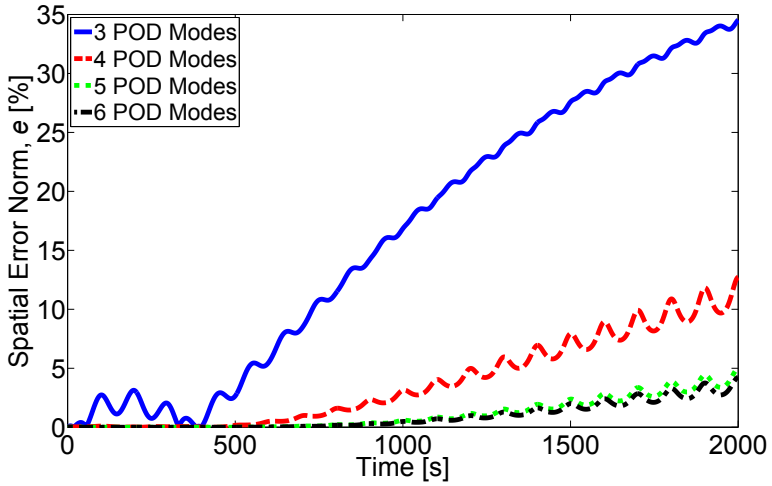

Figure 3.15: Error of POD-analytical solution from 0 - 2,000 s for varying number of basis vectors.

In actual aerothermoelastic simulations of HSVs, the time-dependence of the thermal boundary conditions will not be known ahead of time as the heat flux will depend on flow parameters which are influenced by the structural dynamic response. Furthermore, the ability to use the same POD basis for a variety of flight conditions (i.e., Mach number, angle of attack, altitude, and wall temperatures) is desirable as updating the POD modes requires returning to the full-order model. The simulations used to take the snapshots and create the

POD basis may not therefore represent the thermal boundary conditions that the structure will encounter in the actual reduced-order simulations. In order to most closely capture the space in which the solution is likely to lie, it is necessary to design the simulations to excite all of the system dynamics which are expected throughout the mission.

To examine the effect of extracting POD modes from simulations with boundary conditions that are different from those present in the actual simulation, the POD basis from the previous constant heat flux case was used to obtain reduced-order solutions for the current case of a pre-specified time-varying heat flux. The error between the full-order and POD-analytical solution was calculated between 0 - 2,000 s using varying number of basis vectors and results are given in Fig. 3.16. Note that the errors for the cases of four and five basis vectors retained are virtually identical. Comparing Fig. 3.16 with Fig. 3.15, it is observed that there is not a dramatic loss of error when the POD modes are taken from snapshots of simulations with boundary conditions that are different from those in the actual solution. Though more POD modes may be needed if the time-dependence of the boundary conditions is not known ahead of time, this result strengthens the case that it may be possible to use POD modes that are obtained *a priori* for the full aerothermoelastic HSVs simulations with unknown thermal boundary conditions.

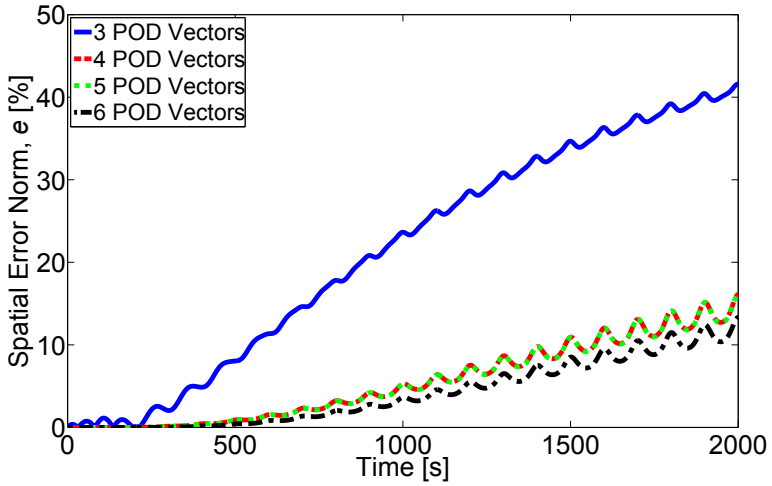

Figure 3.16: Error of POD-analytical solution from 0 to 2,000 s using POD modes obtained from time-independent heat flux case.

3.2.2.2 Coupled Numerical Solution

The accuracy of the coupled, numerically integrated POD solution, hereafter referred to as POD-numerical, is now investigated. The numerical solution is carried out using the Crank-Nicolson scheme as described previously using the first four POD basis vectors. Recall that the temperatures at the end of each time step $T^{(n+1)}$ depend on the thermal load vector at the end of the time step, $g^{(n+1)}$, as shown in Eq. (2.63). As we have specified the time-dependence of the thermal load vector ahead of time, for the first case we will use this information by calculating the actual value of $g^{(n+1)}$ and using it in the calculation of the temperatures, $T^{(n+1)}$. The transient temperature history for this case for node 238 which is approximately at the mid-chord, mid-span location on the bottom outer surface of the heat shield of the control surface is given in Fig. 3.17 for the full-order solution and POD-numerical solution with Δt = 10 s and Δt = 25 s. Again, note that the full order solution is obtained analytically and thus does not contain numerical error.

The error of the POD-numerical solution with respect to the full order solution is calculated over time using the spatial error norm, e, for various time step sizes. Error results are given in Fig. 3.18. As expected, there exists a noticeable increase in error as Δt increases, and therefore time step selection within the aerothermoelastic simulation framework must be carefully considered.

While using the known time-dependence of the thermal load vector at the time instant at which the solution is desired results in reasonable accuracy, this is not possible within actual HSV aerothermoelastic simulations as the thermal load vector will not be known ahead of time. This is due to the fact that it depends on the instantaneous flow parameters, which change as the structure deforms. A nonlinear or iterative solution is undesirable as this would counteract the computational savings of using reduced-order models. As the cost of time-marching the transient thermal solution has been made relatively inexpensive through the use of POD, reducing the size of the time step and performing a linear solution at each time step is expected to achieve the desired computational efficiency while still

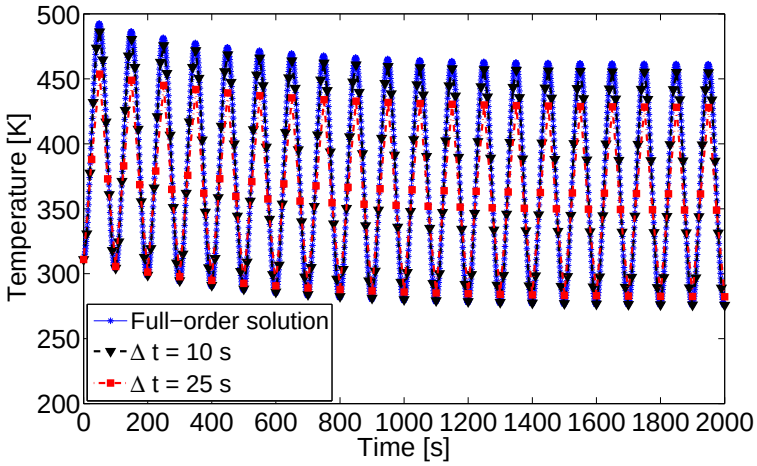

Figure 3.17: Temperatures at Node 238 for full order and POD-numerical solution with varying time step sizes.

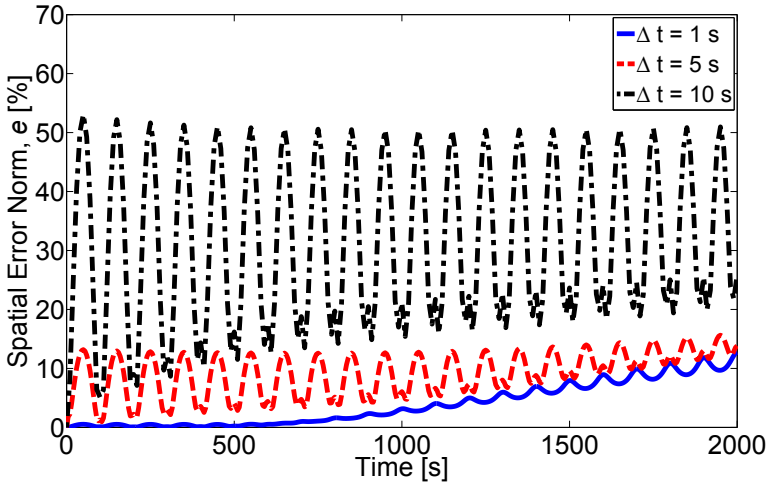

Figure 3.18: Error of POD-numerical solution using known time-dependence of thermal load vector.

maintaining reasonable accuracy. As such, the error of the POD-numerical solution was again calculated, except the problem was treated as if the thermal load vector is not known ahead of time. Instead, it was treated as piecewise constant such that $g^{(n+1)} = g^{(n)}$ between each set of time steps. Once the temperature is calculated at the current time instant, the thermal load vector is updated and again assumed constant until the next update. The error of the POD-numerical solution with this approximation is given in Fig. 3.19 for various size time steps.

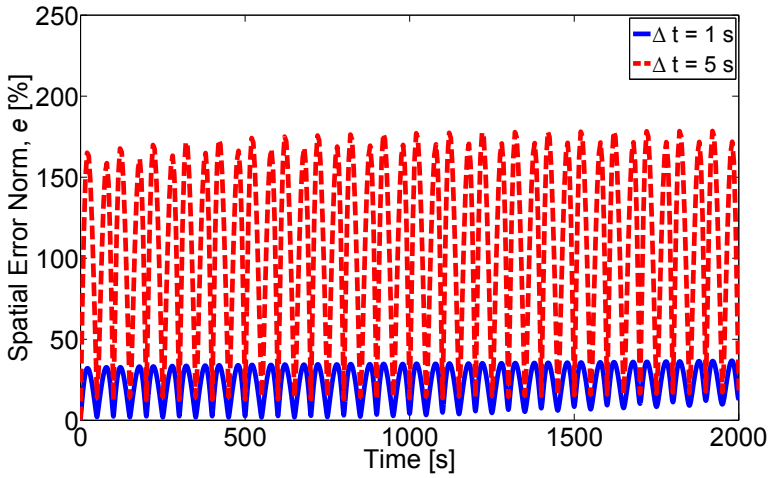

Figure 3.19: Error of POD-numerical solution with piecewise constant approximation to thermal load vector.

Comparing Fig. 3.19 with Fig. 3.18, we see that the error introduced through the piecewise constant approximation of the thermal load vector can significantly increase the error of the POD-numerical solution. Thus, careful attention must be paid to the time step selection or alternative approximations should be made in the actual HSV simulations. The approach taken in this work is to sufficiently reduce the size of the transient heat transfer time step such that the piecewise approximation to the thermal loads provides an accurate representation of the actual thermal loads.

3.2.2.3 Assessment of Computational Cost

To assess the computational savings achieved via the use of the POD solution, thermal transients are calculated for a period of two hours using both the reduced-order and full-order models. The time-dependent thermal load vector employed in the previous subsections is used for the boundary conditions and the first four POD basis vectors are used in the reduced-order solution. Both the full-order and reduced-order solutions are computed using the decoupled analytical solution as well as the numerical solution. The heat transfer time step is taken to be 1 s for all cases. The computation time and number of states required to obtain two hours of thermal response for each case are given in Table 3.4. Ratios of computation time and number of states for the full-order solution to those of the reduced-order solution are given for both the analytical and numerical cases. The last column in the table gives the time-averaged error between the full-order and reduced-order solutions for both the analytical and numerical case. As shown in the table, the use of POD for reduced-order thermal solution provides significant computational savings both in terms of computation time and number of states.

Table 3.4: Comparison of computational cost between full-order and reduced-order models for two hours of response time.

Case	CPU Time[c][s]	Ratio, CPU Time	# states	Ratio, # States	Avg. e
Full-Order Analytical	180		2,812		
Reduced-Order Analytical	2.10	85.7	6	469	8.21%
Full-Order Numerical	258		2,812		
Reduced-Order Numerical	0.693	372	6	469	8.20%

[c] One 2.66-GHz Intel 6700 processor, 3.0 GB RAM.

3.3 Concluding Remarks

A reduced-order formulation for solution of the transient heat transfer problem based on POD has been employed in this chapter. This method has been chosen due to the optimality of the POD basis in representing the dominant modes of a system with the smallest possible number of basis vectors. The basis was been obtained in this work by taking snapshots of the solution over time from representative full-order simulations and detecting the correlation between snapshots. The solution of the reduced-order system of transient thermal equations resulting from projection onto the truncated basis was carried out using two different methods: one in which the equations were decoupled and solved analytically and another in which the equations were numerically integrated directly. The methodology was applied to a representative hypersonic vehicle control surface model as such a structure is expected to have a significant contribution to the dynamics of the vehicle.

The first case analyzed was that of a time-independent, uniform thermal load vector. Results indicated good agreement between the full-order and reduced-order solutions. Investigation into the effect of number of snapshots on the solution indicated that the error incurred in the reduced-order solution does not always decrease with number of snapshots. This can be at least partly attributed to the increase in relative energy of the excluded basis vectors with increasing number of snapshots. Additionally, it was shown that for this case, the contribution of additional snapshots degrades rapidly after approximately three snapshots due to the fact that subsequent snapshots come close to lying in the subspace already captured by the first three snapshots.

Application of the methodology to a case with a pre-specified time-varying thermal load vector allowed for investigation of the error incurred by not updating the basis as the natural boundary conditions change. Results from the POD-analytical solution showed good accuracy in the time range considered by the snapshots, however the error was found to increase outside of the time range considered by the snapshots. Use of the basis from the constant heat flux case for solution in the time-varying case showed that although there

is an increase an error, acceptable accuracy may be obtained even if the time-dependence of the boundary conditions is not known *a priori*. This provides support for the use of the same basis for aerothermoelastic solution under a range of flight conditions. Solution of the reduced-order system using a numerical integration scheme showed that the accuracy is strongly dependent on the size of the time step chosen. Furthermore, results indicate that investigation into methods for approximating the time-dependence of the thermal loads in between updates may be warranted. The use of proper orthogonal decomposition for transient thermal solution will contribute to reducing the computational burden and number of states in hypersonic aerothermoelastic simulations.

Chapter IV

Structural Dynamic Modeling

The next component of the aerothermoelastic framework to be described in this dissertation consists of the solution for the structural dynamic response of the HSV structure. This chapter begins with an overview of the governing full-order structural dynamic equations of motion. One specific feature of the structural dynamics considered in this work is associated with the coupling of the solution from the transient thermal problem with that of the structural dynamic response. The result of this coupling is that thermal loads are applied to the structure due to thermal expansion under changing temperature. Additionally, the transient temperature distribution results in a modification of the structural stiffness matrix due to variation of the conventional stiffness matrix via temperature-dependent material properties, as well as geometric stiffening effects due to thermal stresses. Therefore, the influence of thermal effects on the structural dynamic equations of motion is critical and is addressed in the current chapter.

As described in Chapter I, the order of the equations of motion must be reduced for the purposes of efficient vehicle design and control system simulation. Thus, following the derivation of the full-order structural dynamic equations of motion, a reduced-order modeling methodology for structural dynamic response computation is outlined. The approach employed for reduction of the structural dynamic equations of motion is a Ritz-based modal method in which the full-order equations are projected onto the basis in a manner similar

to that used for reduction of the transient thermal problem. Additionally, a numerical integration scheme to be used for time-marching of the equations of motion is presented.

Following the formulation of the reduced-order structural dynamic equations of motion, a series of results are presented with the goal of assessing the validity of the methodology under transient thermal effects. Specifically, the impact of temperature-dependent material properties on the diagonality of the generalized stiffness matrix is examined in order to provide insight into the effect of temperature on the generalized equations of motion. Additionally, results are presented which examine the effect of heating on the free vibration mode shapes under material property degradation and geometric stiffening with the goal of assessing the robustness of a fixed-basis structural dynamic solution under the influence of a time-varying temperature distribution.

4.1 Derivation of Governing Structural Dynamic Equations of Motion

The full-order system of structural dynamic equations of motion in physical space is given by

$$M_S\ddot{x}(t) + K_S^*(T)x(t) = F_S(t), \tag{4.1}$$

where M_S is the mass matrix, F_S is the structural load vector, and x is the vector of physical degrees of freedom. Note that viscous damping is not present in the current formulation, though this effect can be easily handled by the methodology and does not effect the process described in this dissertation. In this work, two components of the loading on the structure are considered: thermal loads due to differential thermal expansion of the structure and unsteady aerodynamic loads due to the aerodynamic pressure acting at the outer surface of the structure. Thus, the structural load vector can be written as

$$F_S(t) = F_S^H(t) + F_S^A(t), \tag{4.2}$$

where F_S^H is the structural load vector due to heating and F_S^A is the structural load vector due to aerodynamic pressures. Note that F_S^A contains a normal pressure component as well as a wall shear stress component calculated using the local element skin friction coefficients. At each aeroelastic time step, vectors normal and tangent to the deformed configuration at each finite element are computed in order to correctly determine the orientation of the local normal and shear stress pressure components over the outer surface. A description of the formulation used to compute the local skin friction coefficients is given in a subsequent section. The nodal values of the aerodynamic loads contained within $F_S^A(t)$ are obtained by assuming the normal and shear pressure values to be uniform over the outer surface of each finite element. The element-uniform pressures are then distributed over the element, resulting in equivalent nodal forces in the various directions.

For an isotropic material, a change in temperature, ΔT, gives rise to only normal strain, and the resulting thermal strains, $\epsilon_{ij,T}$, for an isotropic material are given by

$$\epsilon_{xx,T} = \epsilon_{yy,T} = \epsilon_{zz,T} = \alpha_T \Delta T, \;\; \epsilon_{xy,T} = \epsilon_{yz,T} = \epsilon_{xz,T} = 0, \tag{4.3}$$

where ϵ_{ij} represents the ij component of the strain, α_T is the material coefficient of thermal expansion, and the subscript T indicates strains due to thermal effects. The stresses can be found from the strains using the constitutive relation given by

$$\sigma = D\left(\epsilon - \epsilon_T\right), \tag{4.4}$$

where D is the elasticity tensor and ϵ is the tensor of total strains. The total potential energy of the structure, Π, is given by

$$\Pi = \frac{1}{2}\int_A \epsilon_e^T D \epsilon_e t \, dA - \int_A x^T F_b t \, dA - \int_L x^T T_s t \, dl - \sum_i x_i^T P_i, \tag{4.5}$$

where ϵ_e is the elastic strain, t is the element thickness, A is area, F_b is the vector of body

forces acting on the structure, T_s is the vector of surface tractions acting on the structure, L is the length of the edge containing the surface tractions, and P_i are the point loads acting on the structure. The relationship between elastic strain, ϵ_e, thermal strain, ϵ_T, and total strain, ϵ, is given by [153]

$$\epsilon_e = \epsilon - \epsilon_T. \tag{4.6}$$

The first term in Eq. (4.5) is the strain energy term, U, which gives rise to the thermal loads. Including the effect of thermal strain in the expression of potential energy, the strain energy term becomes [124]

$$\begin{aligned} U &= \frac{1}{2}\int_A \left(\epsilon - \epsilon_T\right)^T D\left(\epsilon - \epsilon_T\right) t\, dA \\ &= \frac{1}{2}\int_A \left(\epsilon^T D\epsilon - 2\epsilon^T D\epsilon_T + \epsilon_T^T D\epsilon_T\right) t\, dA, \end{aligned} \tag{4.7}$$

where t and A are the thickness and area of the structure, respectively. Upon minimization of the potential energy, the first term in the above gives the standard element stiffness matrix, the last term disappears, and the middle term yields the element thermal load vector given by [124]

$$F_S^{H,(e)} = t^{(e)} A^{(e)} B^T D\epsilon_T, \tag{4.8}$$

where B is the shape function derivative matrix.

The modified stiffness matrix, K_S^*, shown in Eq. (4.1) is given by

$$K_S^*(T) \equiv K_S(T) + K_G(T), \tag{4.9}$$

where $K_S(T)$ is the conventional stiffness matrix that varies due to the temperature-dependence of the material properties and $K_G(T)$ is the geometric stiffness matrix resulting from thermal stresses. Updating of the conventional stiffness matrix is performed using the temperature-dependence of the material properties of the various materials. The element

contributions to $K_S(T)$ are each computed based on the local temperatures and the global stiffness matrix is assembled from the element ones. The geometric stiffness matrix is updated by solving a static finite element problem based on the thermal loads from temperatures at the current time step and the material coefficients of thermal expansion. The resulting internal loads calculated from the static finite element problem are then used to assemble the geometric stiffness matrix.

4.2 Reduced-Order Modal Solution to Structural Dynamic Equations of Motion

While the full-order system of structural dynamic equations of motion is used for comparison purposes, its solution within the aerothermoelastic framework presented here is not suitable for vehicle design and control analysis purposes. The problem of solving for the structural dynamic response of hypersonic vehicle structures within a design and simulation framework is complicated by various factors. Due to the large number of degrees of freedom involved in a traditional finite element solution, steps must be taken to reduce the order of the structural dynamics system of equations. A common approach is to employ a modal transformation in which the structural displacements are expressed as a linear combination of a small number of basis vectors which are the free vibration mode shapes of the structure. However, this approach cannot be applied directly for hypersonic vehicle applications as the mode shapes change over time due to modification of the stiffness from geometric stiffness and material degradation effects.

The approach taken in this work is to first perform an off-line calculation and select a reduced number of Ritz modes to use in reducing the order of the equations of motion. These Ritz modes are then used as the modal basis for solution of the structural dynamic response throughout the simulation. Furthermore, it is desirable to use the same set of Ritz modes for simulations over varying flight conditions. This procedure is applicable as the

Ritz modes need only to satisfy the geometric boundary conditions [152], which will always be the case regardless of the stiffness distribution. The modal matrix containing the structural reference modes, Φ_S, is not updated throughout the simulation, thus preventing the need to solve an eigenvalue problem of the full system during the course of the simulation. Though the reference modes are not updated throughout the simulation, the stiffness matrix is updated each time the structural dynamic response is calculated to account for its dependence on temperature.

The reduced-order system is obtained by first expressing an approximation to the physical degrees of freedom as a linear combination of the structural basis vectors such that

$$x(t) = \Phi_S d(t), \tag{4.10}$$

where d represents the vector of modal coordinates of the reference modes and the modal matrix, Φ_S, contains the reference modes which are stored in a column-wise manner. Note that since the number of reference modes used in the modal expansion is much less than the number of physical degrees of freedom in the model, the computational cost of the numerical solution of the system is relatively inexpensive. Once the modified stiffness matrix is known at the current time instant, the system is reduced by substituting Eq. (4.10) into Eq. (4.1) and pre-multiplying the system by Φ_S^T to project onto the reference modes, i.e.

$$\Phi_S^T M_S \Phi_S \ddot{d}(t) + \Phi_S^T K_S^*(T) \Phi_S d(t) = \Phi_S^T \left[F_S^H(t) + F_S^A(t) \right]. \tag{4.11}$$

The generalized mass matrix, m_S, generalized stiffness matrix, k_S^*, generalized load vector due to heating, f_S^H, and generalized load vector due to aerodynamic pressure, f_S^A, are then

given by

$$m_S = \Phi_S^T M_S \Phi_S \tag{4.12a}$$

$$k_S^*(T) = \Phi_S^T K_S^*(T) \Phi_S \tag{4.12b}$$

$$f_S^H(t) = \Phi_S^T F_S^H(t) \tag{4.12c}$$

$$f_S^A(t) = \Phi_S^T F_S^A(t). \tag{4.12d}$$

As the mass of the structure is taken to be constant in this work, the reference modes are orthogonal with respect to the mass matrix and the generalized mass matrix, m_S, reduces to the identity matrix.

Since the modified stiffness matrix is continuously changing, we have no guarantee of orthogonality of the reference modes with respect to stiffness, and the equations are coupled. As such, the reduced-order system of equations in modal space is integrated numerically to calculate the vector of modal coordinates at each time instant. As the high-fidelity structural dynamic response solution is treated as the truth model, the numerical integration scheme used for the high-fidelity model (based on Nastran Sol 109) is implemented for solution of the reduced-order system for the modal coordinates, $d(t)$, to eliminate any discrepancies in the response due to differences in numerical integration schemes. The numerical integration method is similar to the Newmark-β method except that the load vector is averaged over three time instants and the stiffness matrix is modified such that the dynamic equation of motion reduces to a static solution if no inertial effects or damping exist [154]. The scheme uses a central finite difference representation for the velocity and acceleration at discrete times, given by [154]

$$\dot{d}^{(n)} = \frac{1}{2\Delta t_{AE}} \left(d^{(n+1)} - d^{(n-1)} \right) \tag{4.13a}$$

$$\ddot{d}^{(n)} = \frac{1}{\Delta t_{AE}^2} \left(d^{(n+1)} - 2d^{(n)} + d^{(n-1)} \right), \tag{4.13b}$$

where the superscript (n) refers to the time level. The initial conditions, $d^{(0)}$ and $\dot{d}^{(0)}$, are used to generate the vectors $d^{(n-1)}$, $f_S^{(n-1)}$, and $f_S^{(n)}$ for the initial time step, $n = 0$, using

$$\dot{d}^{(-1)} = d^{(0)} - \dot{d}^{(0)}\Delta t_{AE} \tag{4.14a}$$

$$f_S^{(-1)} = k_S^* d^{(-1)} \tag{4.14b}$$

$$f_S^{(0)} = k_S^* d^{(0)}. \tag{4.14c}$$

Note that this formulation assumes that the initial acceleration for all points is zero (initial velocity is constant). Substituting the finite difference approximations of the velocity and accelerations, Eqs. (4.13), into the modal equations of motion, Eq. (4.11), and averaging the applied loads over three adjacent time instants, the equations of motion are re-written as

$$H_1 d^{(n+1)} = H_2 + H_3 d^{(n)} + H_4 d^{(n-1)}, \tag{4.15}$$

where,

$$H_1 = \frac{1}{\Delta t_{AE}^2} m_S + \frac{1}{3} k_S^* \tag{4.16a}$$

$$H_2 = \frac{1}{3}\left(f_S^{(n+1)} + f_S^{(n)} + f_S^{(n-1)}\right) \tag{4.16b}$$

$$H_3 = \frac{2}{\Delta t_{AE}^2} m_S - \frac{1}{3} k_S^* \tag{4.16c}$$

$$H_4 = \frac{-1}{\Delta t_{AE}^2} m_S - \frac{1}{3} k_S^*. \tag{4.16d}$$

The solution vector at the next time step, $d^{(n+1)}$, is obtained by decomposing H_1 and applying it to the right-hand side of Eq. (4.15), i.e.

$$d^{(n+1)} = H_1^{-1}\left[H_2 + H_3 d^{(n)} + H_4 d^{(n-1)}\right], \tag{4.17}$$

where $(\cdot)^{-1}$ indicates the matrix inverse. Finally, the structural response at the end of the time step in physical space, $x^{(n+1)}$, can be obtained from the structural modal coordinates

using

$$x^{(n+1)} = \Phi_s d^{(n+1)}. \tag{4.18}$$

4.3 Impact of Temperature-Dependent Modulus on Diagonality of Generalized Stiffness

One result of the fact that the free vibration modes of the structure are not updated during the course of the simulation is that the structural modal matrix, Φ_S, will not be orthogonal with respect to the physical stiffness matrix. This is due to the fact that the modal matrix is evaluated at a reference thermal state, however, the stiffness matrix is continuously changing over time due to the transient temperature distribution. Thus, the modal equations of motion will only be diagonalized at the reference thermal state at which the reference modes were evaluated, and will be coupled at any other thermal state.

In order to exemplify this phenomenon, consider the case of a one-dimensional heat conduction problem with different heat flux boundary conditions specified at either end and uniform initial conditions as shown in Fig. 4.1. The one-dimensional beam is taken to have a 1 m $\times$ 1 m cross section and a length of 60 m. The boundary conditions and initial conditions are applied and FEA is used to solve for the transient thermal response. The spatial temperature distribution is output every 50 s in the interval from 0 – 200 s. The temperature distributions at these five different time instants are shown in Fig. 4.2.

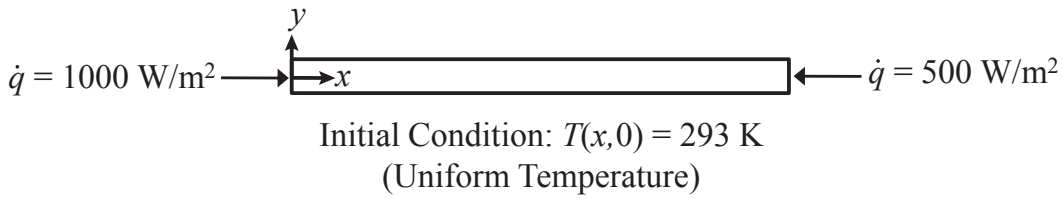

Figure 4.1: Boundary conditions and initial conditions for one-dimensional thermal problem.

In order to assess the effect of the transient heating on the diagonality of the generalized stiffness matrix, the nodal temperatures shown in Fig. 4.2 are mapped onto a structural

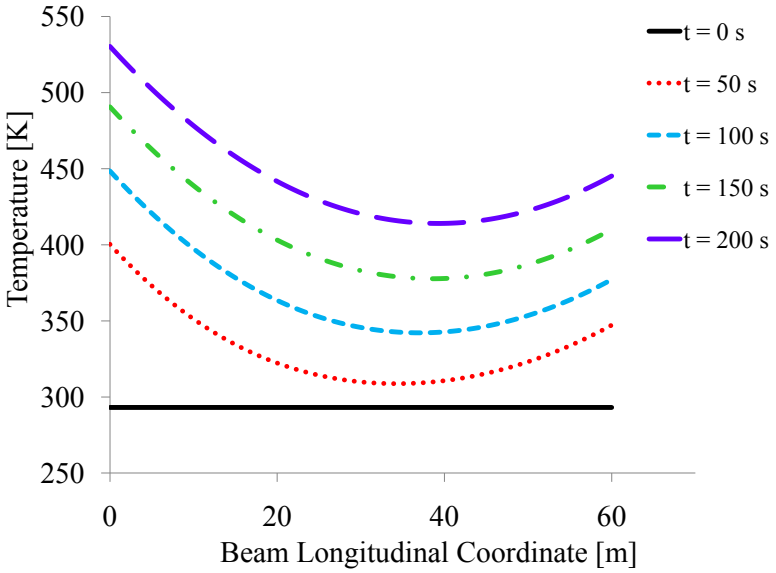

Figure 4.2: Temperature distributions at selected time instants from thermal FEA.

cantilever beam finite element model with the left end ($x = 0$) clamped. The grids used for the thermal and structural models are taken to be the same. As the structural model contains a temperature varying Young's modulus, the applied thermal loading will modify the stiffness of the structure due to material property degradation. The material of the beam is taken to be Titanium and the temperature-dependence of Young's modulus is extrapolated based on data from Vosteen [155]. The approximate linear representation used for the Young's modulus, as computed based on the data from Ref. 155, is given in Fig. 4.3

A thermal load case is created at each 50 s interval and Nastran structural analysis is conducted with a DMAP (Direct Matrix Abstraction Program) alter in the input file requesting output of the physical structural stiffness matrix for each thermal load case. Note that this case only considers the conventional stiffness matrix, K_S, due to the fact that this example only investigates the impact of temperature-dependent material properties. Therefore, geometric stiffening effects are not included in this example. The physical stiffness matrix at each time instant is then used to calculate the corresponding generalized stiffness

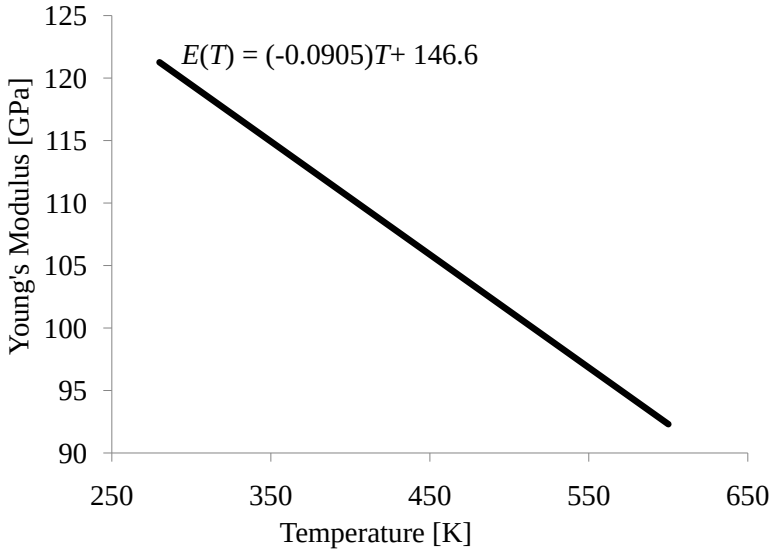

Figure 4.3: Temperature dependence of Young's modulus for Titanium used for beam case study [155].

matrix by pre- and post-multiplying by the modal matrix, i.e.

$$k_S(T) = \Phi_S^T K_S(T) \Phi_S. \tag{4.19}$$

For this study, Φ_S is composed of the first five free vibration modes of the structure evaluated based on the thermal loads at the $t = 100$ s thermal state. In order to quantify the diagonality of $k_S(T)$ at the various time instants, a matrix diagonality ratio, μ, is calculated for each row of the 5×5 generalized stiffness matrix and is given by

$$\mu_i = \frac{|\text{Largest off-diagonal entry in row } i|}{|\text{Diagonal entry in row } i|}. \tag{4.20}$$

A plot of μ_i for each of the five rows of $k_S(T)$ as a function of time is given in Fig. 4.4. As seen in the figure, the generalized stiffness matrix becomes more diagonal in moving from $t = 0$ s to $t = 100$ s, which is the time instant at which the free vibration modes were evaluated. Conversely, from 100 s to 200 s, μ_i increases for all five rows as the temperature distribution moves away from the reference thermal state at which the free

vibration modes were evaluated. Recall that this study does not include geometric stiffening effects due to thermal stresses which would result in further modification of the stiffness matrix as the temperature variation evolves. Furthermore, the maximum nodal temperature for this case is 530 K, while the maximum temperature in actual hypersonic simulations is expected to be significantly higher. Thus, the structure will therefore experience larger temperature excursions in actual applications. As a result of these factors, the diagonality of the generalized stiffness matrix is expected to be lower in hypersonic simulations, resulting in even stronger coupling of the equations of motion.

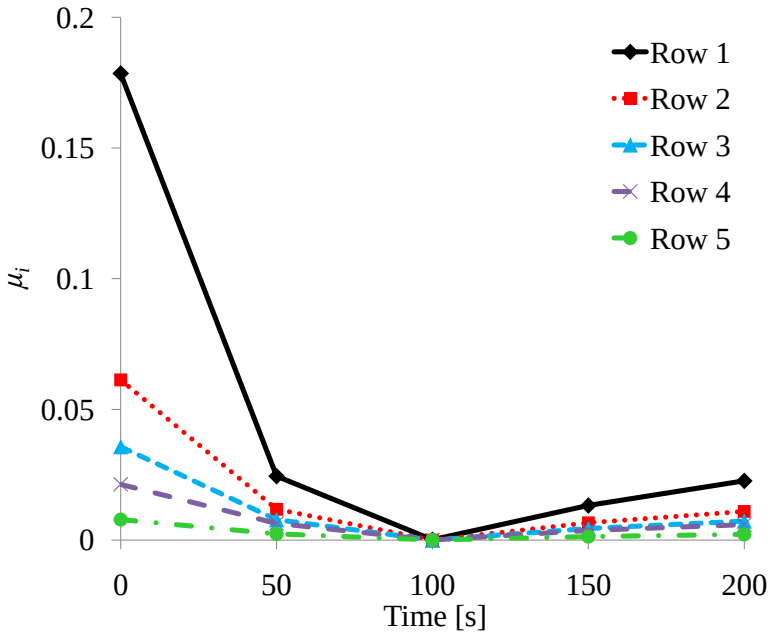

Figure 4.4: Matrix diagonality ratios for each row of generalized stiffness matrix vs. time.

4.4 Impact of Transient Heating on Evolution of Free Vibration Mode Shapes and Frequencies

As described in section 4.2, the structural reference modes are not updated during the course of the aerothermoelastic simulation and it is thus important to characterize the effect of transient heating on the free vibration mode shapes of the structure. In order to maintain

an accurate reduced-order structural dynamic model, the fixed structural basis must be robust with respect to variation in the stiffness matrix due to transient heating. Two separate case studies are described in the subsequent subsections to provide insight into this effect. Both cases involve the use of representative control surface structures to exemplify the methodology, although different geometries are used for each case.

4.4.1 Case 1: Impact of Material Property Degradation and Thermal Stresses on Free Vibration Mode Shapes and Frequencies Under Elevated Thermal Loading

A top view of the control surface geometry used for the first case in assessing the impact of heating on the free vibration modes is given in Fig. 4.5. Note that this figure shows both the planform of the control surface as well as the interior stiffener pattern. The structure is taken to be made of PM 2000 due to its high-temperature performance. The thermal and structural material properties as used in this study are given in Table 4.1, where "T-dep." indicates that a property is temperature-dependent and h gives the thickness used for both the stiffeners and top and bottom skins. As shown in the table, material property degradation is a result of the temperature-dependence of the Young's modulus, E, which is incorporated in tabular form into the finite element representation. The functional form of the Young's modulus is given in Fig. 4.6 [156].

Table 4.1: Structural and thermal material properties for PM 2000 [156].

ρ $[kg/m^3]$	E $[Pa]$	ν	α_T $[\mu m/m/K]$	κ $[W/m/K]$	c_p $[J/kg/K]$	h $[mm]$
7180	T-dep.	0.33	10.7	28	740	6.35

Based on the geometry shown, a finite element model of the control surface has been created for the thermal and structural analyses. The model consists of a top and bottom skin surface and is stiffened by internal stiffeners as well as stiffeners around the outer perimeter according to the dimensions specified in Fig. 4.5. The finite element model is shown in

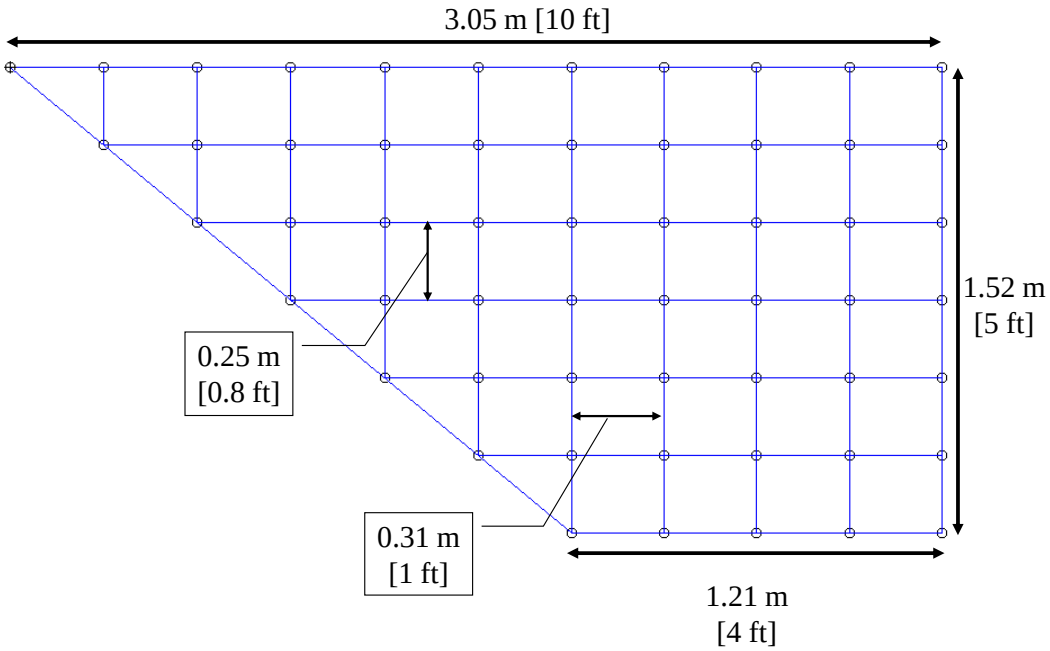

Figure 4.5: Top view of control surface geometry and stiffness pattern with dimensions.

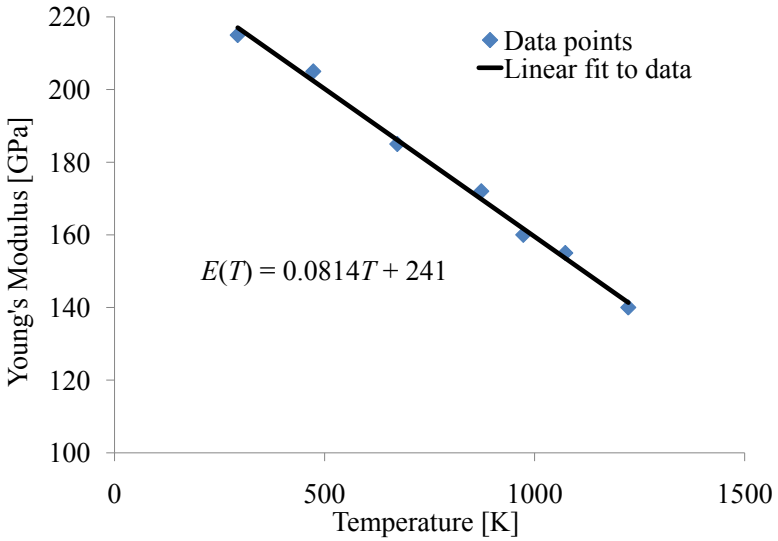

Figure 4.6: Temperature dependence of PM 2000 used in finite element model to capture the effect of material property degradation with temperature [156].

Fig. 4.7 with one of the skin surfaces removed for visualization purposes. The model is composed of 9,200 three-node triangular elements all having a thickness of 6.35 mm (0.25 in). The circle indicates the approximate attachment region which contains displacement constraints in all six degrees of freedom.

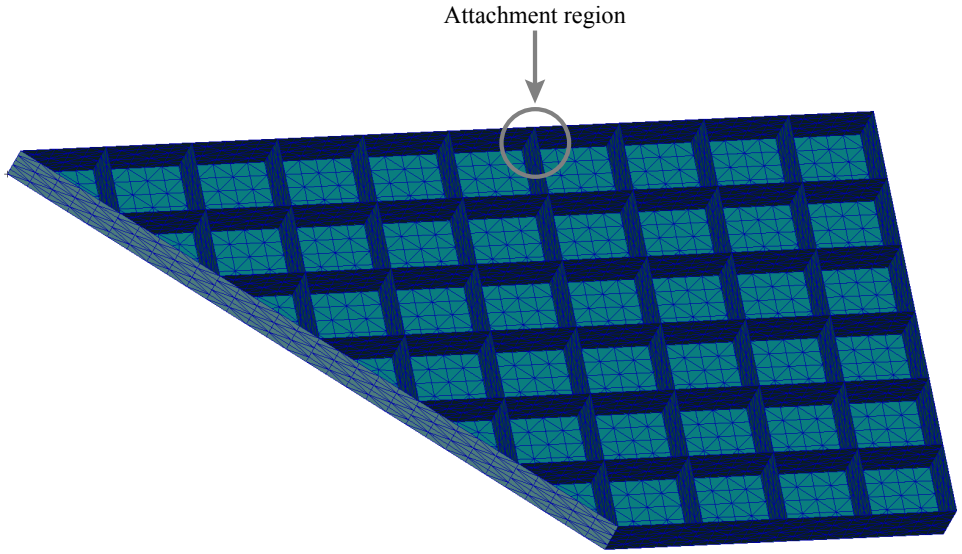

Figure 4.7: Control surface finite element model.

The first step taken in assessing the impact of heating on the mode shapes is to select the thermal state at which to evaluate the modes. For this case, the thermal state is generated by first applying a uniform heat flux of 10 W/cm^2 to the bottom surface of the finite element model. Transient thermal analysis is conducted and the temperature distribution obtained at 320 s into the transient is selected as the thermal state at which to compute the free vibration mode shapes and frequencies. A contour plot of the temperature distribution at this time instant is given in Fig. 4.8.

For this case study, the main objective is to assess the effect of material property degradation and thermal stresses on the mode shapes and natural frequencies of the structure under thermal loading. As such, four different simulations are carried out. For each simulation, normal modes analysis is conducted using MSC.Nastran under thermal loads based on the temperature distribution shown in Fig. 4.8. For each case, a different combination of

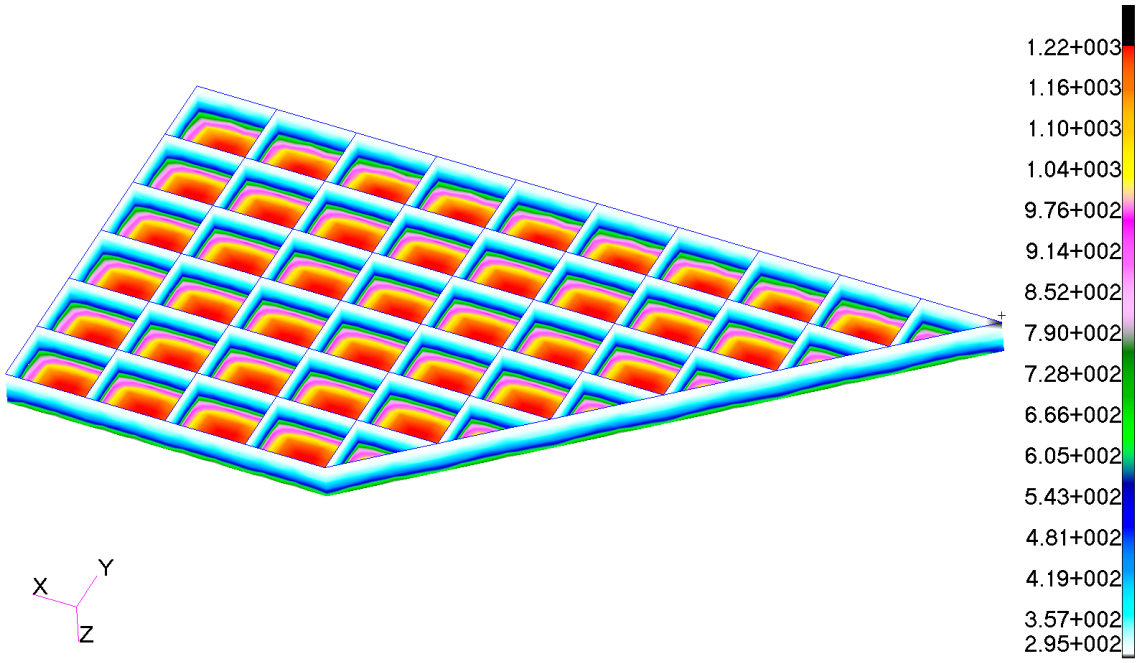

Figure 4.8: Temperature distribution at 320 s resulting from uniform heat flux of 10 W/cm^2 applied to bottom surface.

material property degradation due to temperature-dependent material properties and thermal stress effects are used in order to assess the impact of each of these effects. The first case does not include either material property degradation or thermal stress and is denoted "no degradation, no thermal stress". The second case contains material property degradation and no thermal stress, and is denoted "with degradation, no thermal stress". Conversely, the third case contains no material property degradation, but does contain thermal stress and is denoted "no degradation, with thermal stress". Finally, the fourth case includes both material property degradation and thermal stress, and is denoted "with degradation, with thermal stress".

A plot of the natural frequencies for each of these cases for the first ten structural modes is given in Fig. 4.9. As seen in the figure, the effect of material property degradation and thermal stress is more pronounced for the higher frequency modes than for the lower frequency modes. Material property degradation and thermal stresses appear to have a cancelling effect which results in reasonably close agreement between the "no degradation, no

thermal stress" case, and the "with degradation, with thermal stress" case. The maximum percentage error in natural frequency of the "no degradation, no thermal stress" case with respect to the "with degradation, with thermal stress" case is found to be 8.6%.

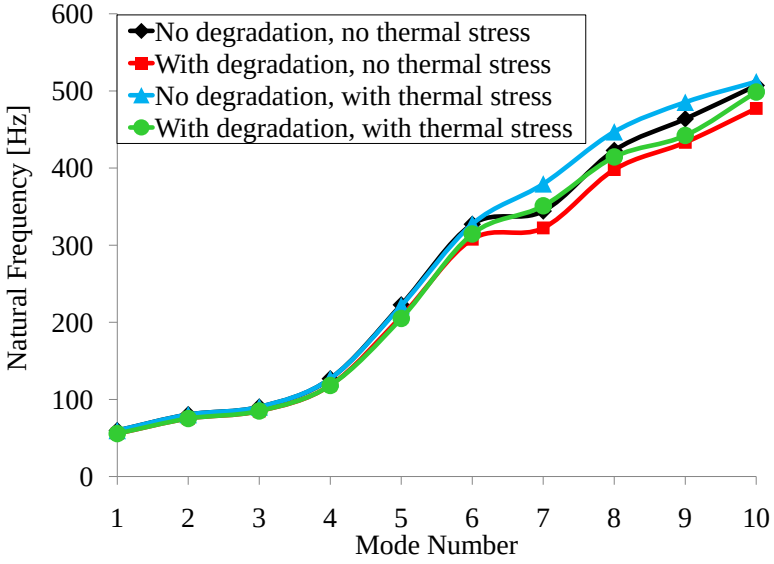

Figure 4.9: Natural frequencies of first ten free vibration modes under thermal loads at 320 s illustrating effect of both material property degradation with temperature and geometric stiffening due to thermal stresses.

The next aspect of this case study is associated with the effect of material property degradation and thermal stresses on the mode shapes of the control surface structure. As such, the free vibration mode shapes are investigated for each of the four cases shown in Fig. 4.9. Again, the mode shapes are computed at the temperature distribution shown in Fig. 4.8. The first four mode shapes for the case of no material property degradation and no thermal stress are given in Fig. 4.10. Note that the top surface of the finite element model is removed in the figures for visualization purposes. The corresponding modes for the three remaining cases are given in Figs. 4.11 – 4.13. Comparing the modes between each of the four cases, there does not exist a significant difference between the modes for the various cases other than an inversion of certain modes due to scaling by a factor of negative one. Quantification of the impact of thermal effects on free vibration modes will be discussed in subsequent sections. However, an important aspect to consider is that the mode shapes

in Figs. 4.11, 4.12, and 4.13 are numbered based on a qualitative comparison against the mode shapes in Fig. 4.10 such that the modes in Figs. 4.11, 4.12, and 4.13 qualitatively correspond to the modes of the "no degradation, no thermal stress" case. This is important to note because the mode shapes shown in Figs. 4.11, 4.12, and 4.13 do not correspond with the first four modes numbered sequentially in order of increasing naturally frequency for these cases. This is due to the fact that when material property degradation and thermal stresses are included in the normal modes analysis, certain modes that were originally at a frequency higher than that of the fourth mode for the "no degradation, no thermal stress" case will drop in frequency such that their frequencies become less than that of the fourth mode for the "no degradation, no thermal stress" case.

As an example of this phenomenon, consider the case which includes both material property degradation and thermal stress. As a result of including these effects, localized panel modes appear for this case at lower frequencies than they did for the "no degradation, no thermal stress" case. This is due to the fact that the bottom surface is attempting to expand due to its higher temperature, but it is restrained by the stiffeners, resulting in compression of the panel sections between stiffeners. This compression lowers the stiffness of the localized panels and therefore lowers their natural frequencies. Therefore, when material property degradation and thermal stress are considered, these localized panel modes appear earlier in the modal sequence than they did when these effects were not considered. Four examples of such modes are given in Fig. 4.14, where the "$+$" and "$-$" modifiers indicate the position of the mode with respect to the modal sequence in the "no degradation, no thermal stress" case. Note that the first pure panel mode in the "no degradation, no thermal stress" case does not appear until mode 12 at 530 Hz, indicating that thermal effects can significantly reduce the natural frequencies of such localized modes in cases where stiffeners are spaced far apart. It remains to be determined what, if any, effect these modes would have on the aerothermoelastic response of the structure, and the effect that not including these modes in the modal basis would have on the reduced-order structural

dynamic response computation.

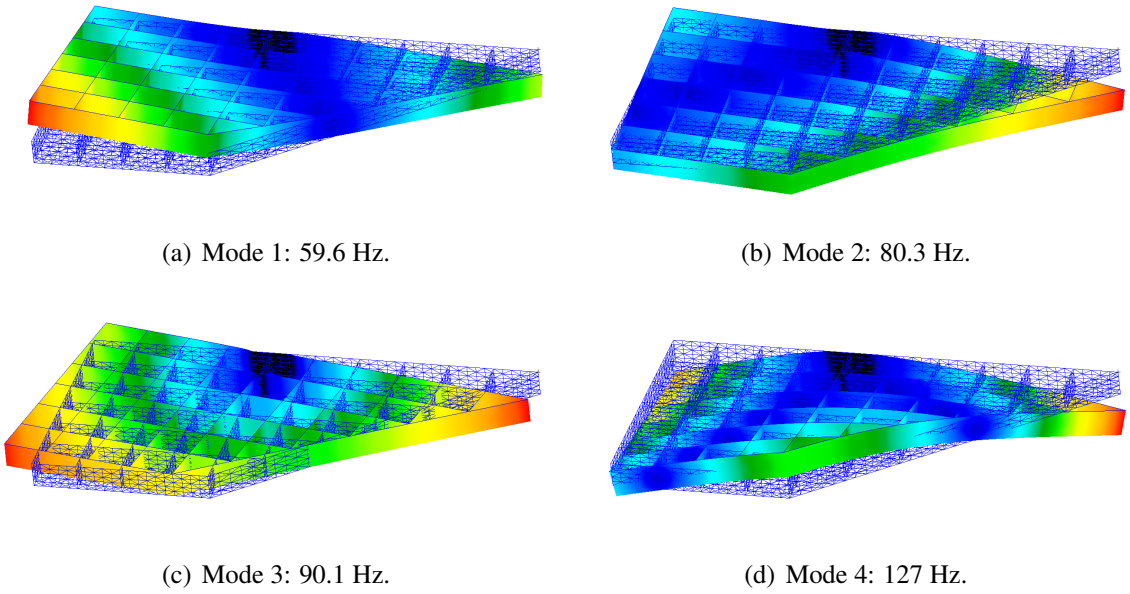

(a) Mode 1: 59.6 Hz.

(b) Mode 2: 80.3 Hz.

(c) Mode 3: 90.1 Hz.

(d) Mode 4: 127 Hz.

Figure 4.10: First four structural mode shapes with no material property degradation and no thermal stress.

4.4.2 Case 2: Quantification of the Effect of Transient Heating on the Evolution of the Free Vibration Mode Shapes and Frequencies

The next case study in this section involves quantification of the evolution of the free vibration structural mode shapes and frequencies under transient heating. While the case study in the previous section provided insight into the effect of material property degradation and thermal stresses on the structural mode shapes and frequencies, the analysis was conducted at a single thermal state. Thus, the current section extends the analysis by considering the effect of transient heating as computed from a representative aerodynamic heating model on the free vibration modes and frequencies.

The finite element model used for the thermal and structural modeling aspects of the case study is shown in Fig. 4.15 with the top surface removed for visualization purposes. The model is similar to that used for assessment of the thermal modeling methodology as described in Chapter III and the material properties for the current model are those given

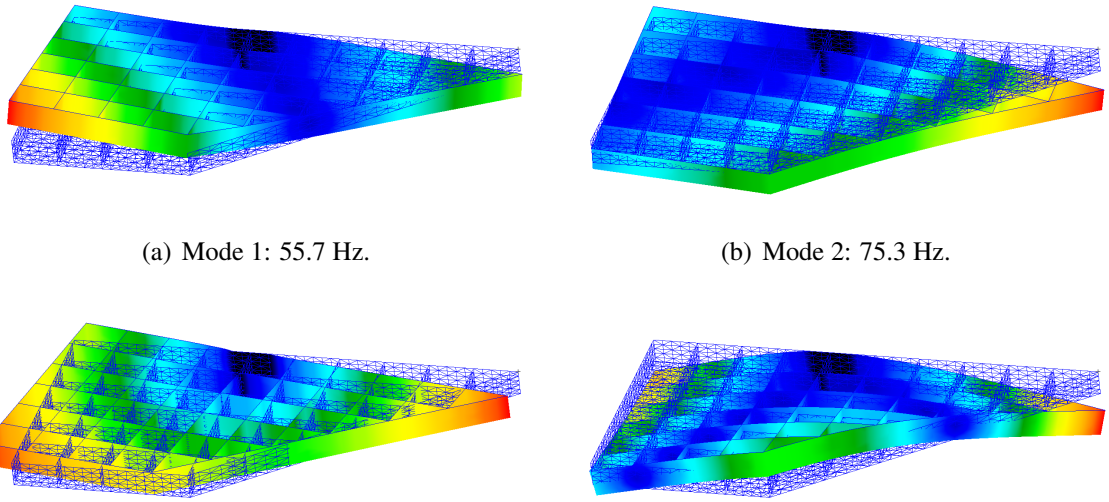

(a) Mode 1: 55.7 Hz.

(b) Mode 2: 75.3 Hz.

(c) Mode 3: 85.0 Hz.

(d) Mode 4: 118 Hz.

Figure 4.11: First four structural mode shapes with material property degradation and no thermal stress.

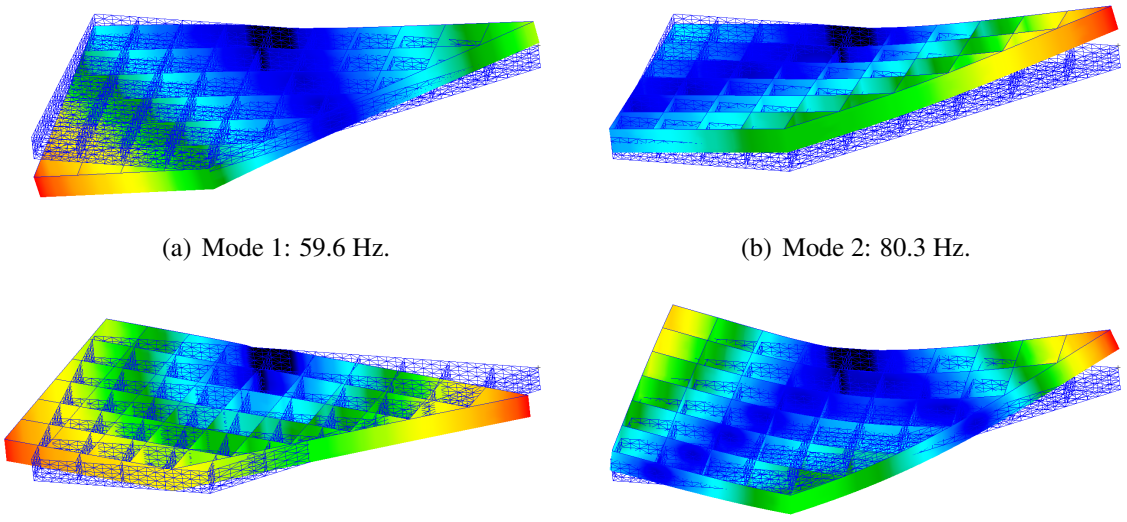

(a) Mode 1: 59.6 Hz.

(b) Mode 2: 80.3 Hz.

(c) Mode 3: 90.3 Hz.

(d) Mode 4: 127 Hz.

Figure 4.12: First four structural mode shapes with no material property degradation and with thermal stress.

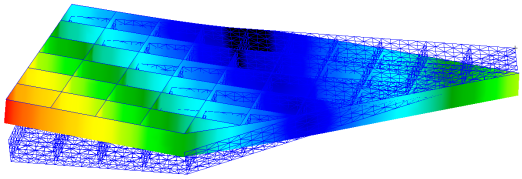

(a) Mode 1: 55.7 Hz.

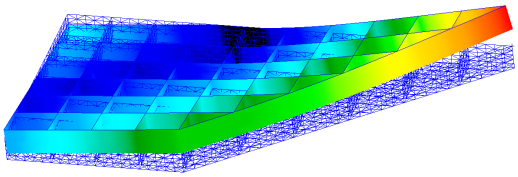

(b) Mode 2: 75.2 Hz.

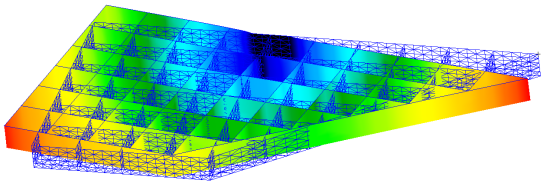

(c) Mode 3: 85.1 Hz.

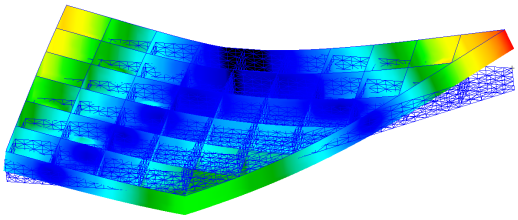

(d) Mode 4: 118 Hz.

Figure 4.13: First four structural mode shapes with material property degradation and with thermal stress.

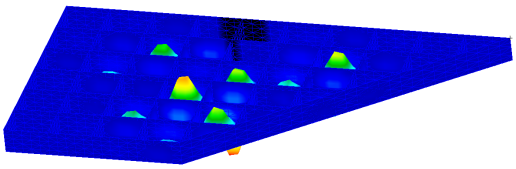

(a) Mode 1−: 26.7 Hz.

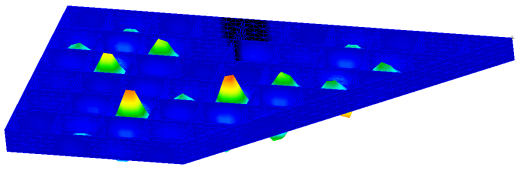

(b) Mode 3+: 107.3 Hz.

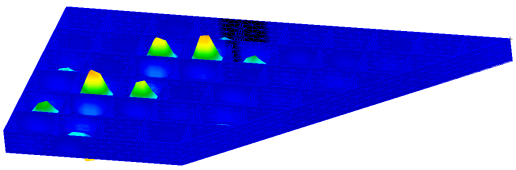

(c) Mode 4+: 125 Hz.

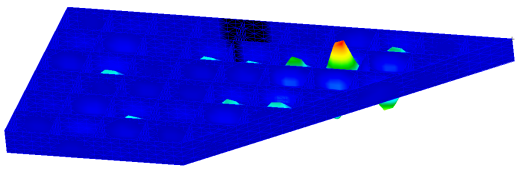

(d) Mode 5−: 129 Hz.

Figure 4.14: Four localized panel mode shapes from case with material property degradation and with thermal stress illustrating the impact of thermal loads on the reduction in frequency of such localized modes.

in Table 3.1 and Table 3.2 in Chapter III. However, additional stiffeners are included in this configuration to satisfy strength requirements under transient thermal loads. This model also differs from the one used in Chapter III in that the skin thickness of the model used in the current section is taken to be 6.35 mm instead of 3.175 mm. The model consists of the thermal protection system layers shown in Fig. 3.4 of Chapter III along with chordwise and spanwise stiffeners. The material used for the stiffeners is TIMETAL 834 and the thickness of all stiffeners is 25.4 mm (1 in). The model contains 2,812 thermal degrees of freedom and 8,074 structural degrees of freedom. The heat shield and insulation layer are each modeled using 6-node solid wedge elements while the top and bottom skins and stiffeners are modeled using 3-node, 2-dimensional triangular elements. Of the 6,886 elements in the model, 3,456 are solid elements and 3,430 are triangular elements. The control surface is taken to be all-moveable about a hinge line located at the mid-chord [60] and will thus be connected to the vehicle main body through a torque tube. This attachment is modeled by constraining the region indicated by the circle in Fig. 4.15 in all degrees of freedom. In addition, the nodes at the root are constrained against translation in the y direction. Because the stiffness of the insulation layer is neglected, rigid (RBE2) elements are used between each skin node and the corresponding node at the outer surface of the insulation layer to prevent singularities in the solution.

The structural mode shapes under transient heating are computed as a function of time for representative flight conditions. This case study investigates the evolution of the modes for two cases. The first case involves analysis of the evolution of the structural mode shapes when geometric stiffening due to thermal stress is included, but material property degradation with temperature is excluded. For this case, all material properties are evaluated at room temperature. The second case includes both geometric stiffening due to thermal stresses and material property degradation with temperature. The flight conditions for the simulations are taken to be Mach 8 at an altitude of 26 km with an angle of attack of 3° and a uniform initial temperature distribution of 293 K. Note that the Eckert Reference Tem-

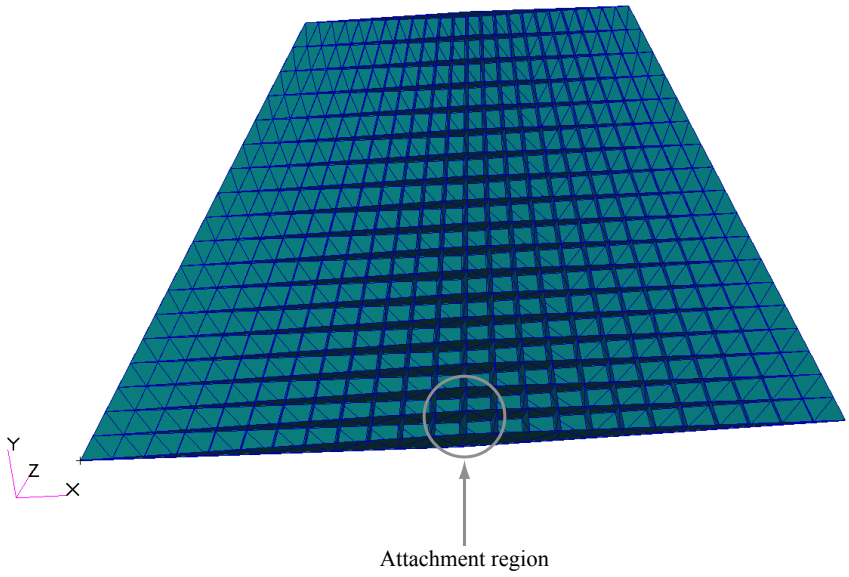

Figure 4.15: Finite element model of control surface used in study.

perature method is used to compute the aerodynamic heat flux, and the flow properties are computed using third-order piston theory. The formulations for both of these methodologies are provided in subsequent sections. The heat transfer time step, Δt_{HT}, is taken to be 1 s and the aerothermal time step, Δt_{AT}, is taken to be 5 s. The structure is taken to be rigid for the purposes of aerodynamics and thus the initial flow properties calculated over the undeformed configuration are held constant for the duration of the simulation. A time history of 2 hours (7,200 s) is obtained from the simulations. Note that the full-order thermal model is used for the simulations to eliminate any errors due to model reduction. Plots of the maximum and minimum nodal temperatures are given in Figs. 4.16(a) and 4.16(b), respectively. The maximum temperature approaches an equilibrium value within the duration of the simulation while the minimum temperature is still increasing.

In order to quantitatively assess the evolution of the mode shapes due to heating, the modal assurance criterion [157] (MAC) is employed. The MAC is a relation used to estimate the degree of correlation between two mode shape vectors. In this work, the MAC is used to quantify the correlation between the i-th heated mode, $\phi_h^{(i)}$, and the j-th unheated mode, $\phi_u^{(j)}$ at each aeroelastic time step. The unheated modes are taken to be those at the

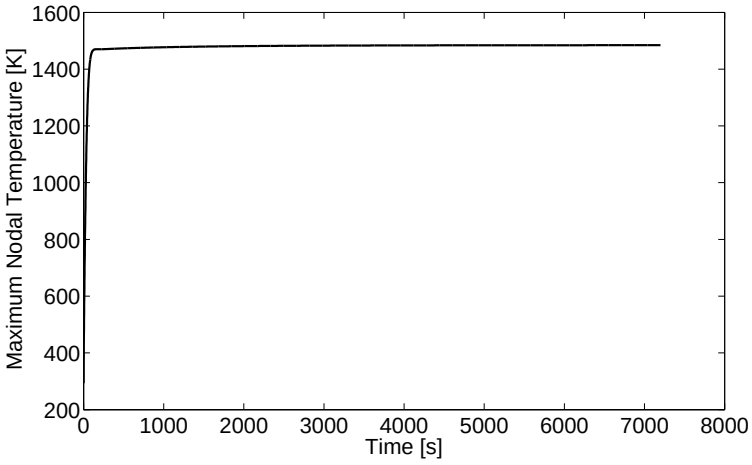

(a) Maximum nodal temperatures.

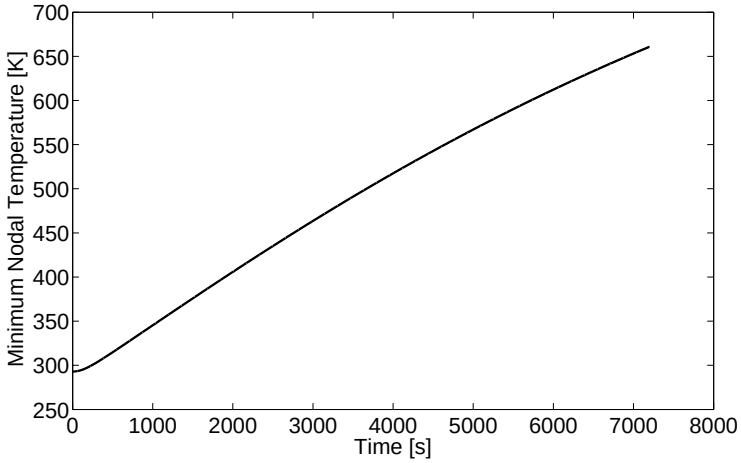

(b) Minimum nodal temperatures.

Figure 4.16: Maximum and minimum nodal temperatures vs. time for M = 8, $\alpha = 3°$, h = 26 km, T_0 = 293 K uniform.

initial uniform temperature distribution of 293 K. The MAC value, $\text{MAC}_{i,j}$, corresponding to the correlation between $\phi_h^{(i)}$ and $\phi_u^{(j)}$ is given by

$$\text{MAC}_{i,j} = \frac{\left| \left(\phi_h^{(i)}\right)^T \left(\phi_u^{(j)}\right) \right|^2}{\left[\left(\phi_h^{(i)}\right)^T \left(\phi_h^{(i)}\right) \right] \left[\left(\phi_u^{(j)}\right)^T \left(\phi_u^{(j)}\right) \right]}. \tag{4.21}$$

The MAC takes on values between zero and one, where a value of one indicates exact correspondence between two modes, and a value of zero indicates that the modes are orthogonal. A matrix can be assembled by calculating the MAC value relating each heated mode to each unheated mode. The MAC analysis described here considers the first six modes of the structure, and thus the MAC matrix is a 6×6 matrix. The first six unheated mode shapes and frequencies are given in Fig. 4.17. Note that the MAC calculation is performed at each heat transfer time step of the simulation and the heated modes are always sorted in order of increasing natural frequency. The following two subsections present results for the case which only includes geometric stiffening due to thermal stresses and for the case which includes both geometric stiffening due to thermal stresses and material property degradation with temperature.

4.4.2.1 Geometric Stiffening Due to Thermal Stresses Included and Material Property Degradation with Temperature Excluded

As described above, the first set of results is generated for the case which includes geometric stiffening due to thermal stress but excludes material property degradation with temperature. The first step of the study is to compute the diagonal values of the MAC matrix as a function of time to assess the correlation between each heated mode and the corresponding unheated mode. Plots of the diagonal values of the MAC matrix for this case are given in Fig. 4.18. As evidenced by the figures, heated modes one, two, five, and six do not deviate significantly from the corresponding unheated modes, and the diagonal

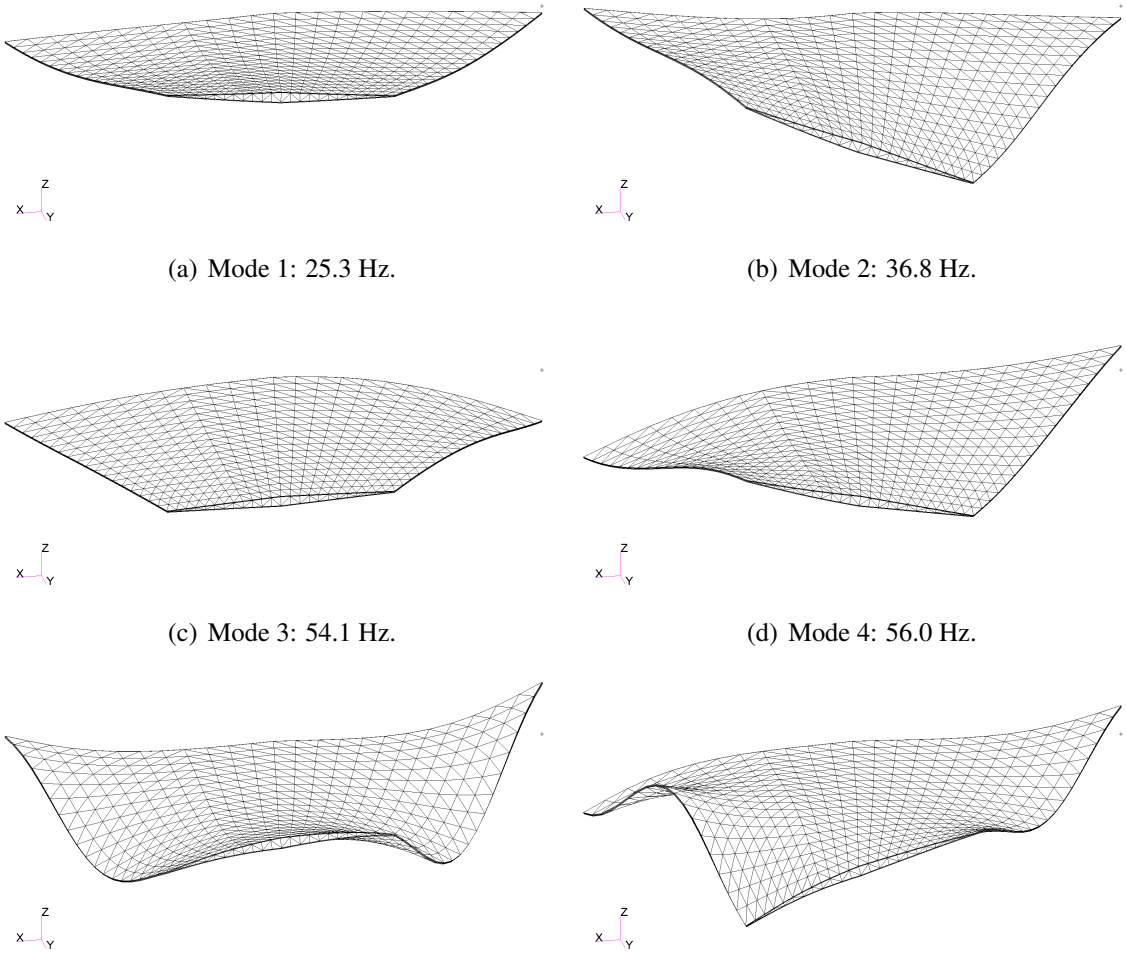

(a) Mode 1: 25.3 Hz.

(b) Mode 2: 36.8 Hz.

(c) Mode 3: 54.1 Hz.

(d) Mode 4: 56.0 Hz.

(e) Mode 5: 91.4 Hz.

(f) Mode 6: 103.3 Hz.

Figure 4.17: First six unheated mode shapes and frequencies.

values of the MAC matrix corresponding to these modes remain close to one. However, for modes three and four, there exists a decrease in the MAC values over time, indicating a loss of correspondence with the corresponding unheated modes.

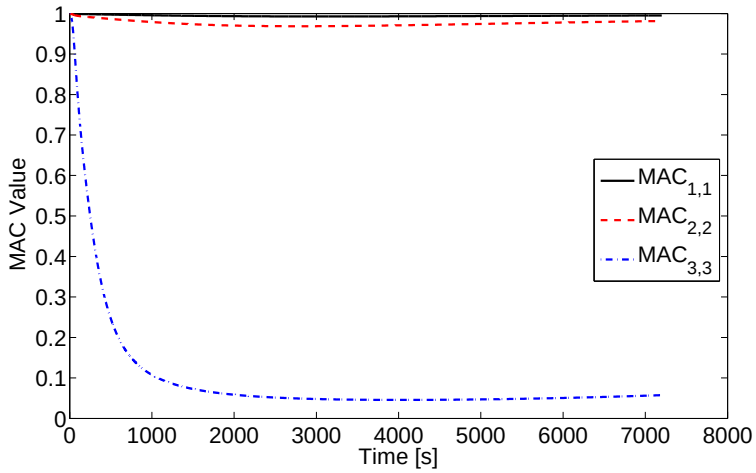

(a) Modes 1–3.

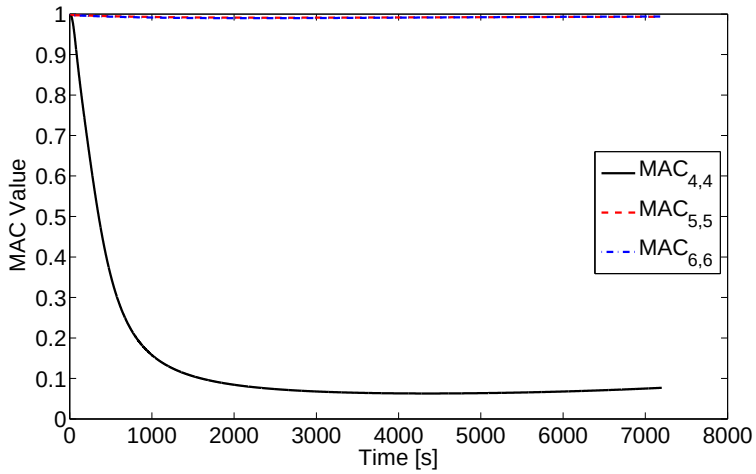

(b) Modes 4–6.

Figure 4.18: Diagonal entries of MAC matrix for first six modes vs. time for case including geometric stiffening due to thermal stresses and excluding material property degradation with temperature.

To further explore the evolution of modes three and four over time, off-diagonal terms of the MAC matrix are examined. Specifically, Fig. 4.19(a) shows $MAC_{3,3}$ and $MAC_{3,4}$ over time. These MAC values are examined in order to compare the correspondence between heated mode three and unheated mode three against heated mode three and unheated mode

four. Similarly, Fig. 4.19(b) shows $MAC_{4,4}$ and $MAC_{4,3}$ over time. The figures illustrate the fact that heated mode three begins to resemble unheated mode four over time, and heated mode four begins to resemble unheated mode three over time.

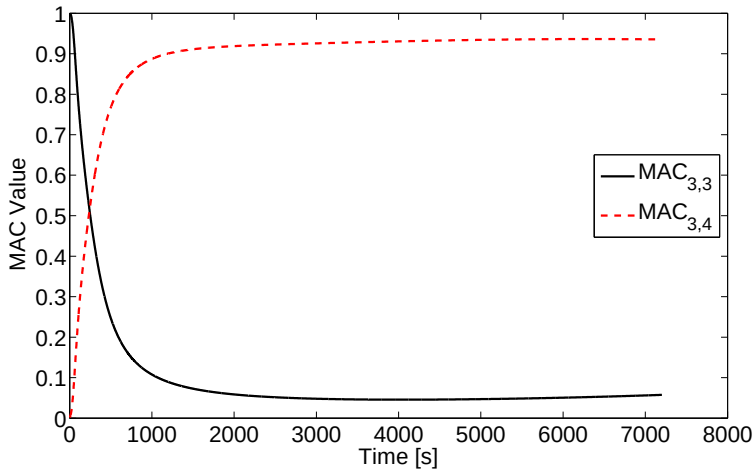

(a) $MAC_{3,3}$ vs. $MAC_{3,4}$.

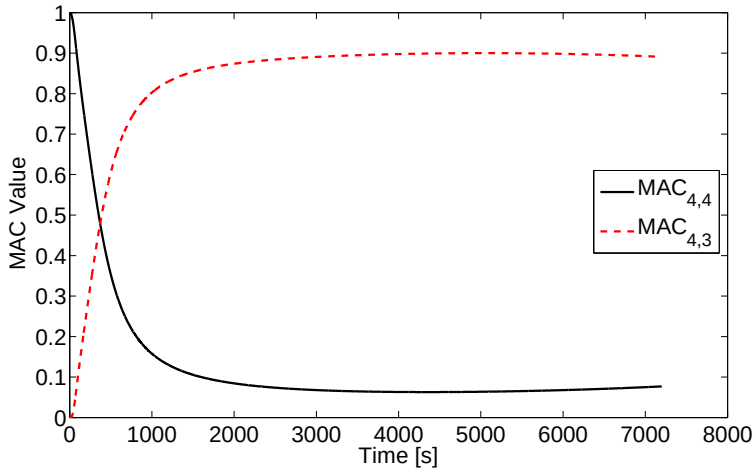

(b) $MAC_{4,4}$ vs. $MAC_{4,3}$.

Figure 4.19: Comparison of diagonal and off-diagonal entries of MAC matrix for third and fourth modes vs. time for case including geometric stiffening due to thermal stresses and excluding material property degradation with temperature.

To visualize how the third heated mode evolves over time, it is plotted at 242 s (the approximate crossover time in Fig. 4.19(a)) and at 7,200 s (the end of the transient) as shown in Fig. 4.20. Similarly, the fourth mode is plotted at 371 s (the approximate crossover time in Fig. 4.19(b)) and at 7,200 s as shown in Fig. 4.21. Comparing Fig. 4.20(b) to

Fig. 4.17(d), it is observed that heated mode three is qualitatively similar to unheated mode four at the end of the transient. Similarly, comparing Fig. 4.21(b) to Fig. 4.17(c), heated mode four appears qualitatively similar to unheated mode three at the end of the transient. These results qualitatively confirm the quantitative results shown by the MAC values in Fig. 4.19(a) and Fig. 4.19(b).

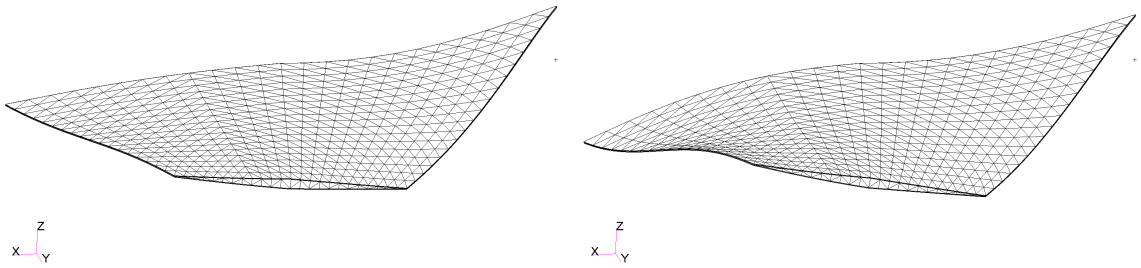

(a) Mode 3 at 242 s: 53.4 Hz. (b) Mode 3 at 7,200 s: 53.1 Hz.

Figure 4.20: Mode 3 at two different time instants showing evolution of mode shape with heating for case including geometric stiffening due to thermal stresses and excluding material property degradation with temperature.

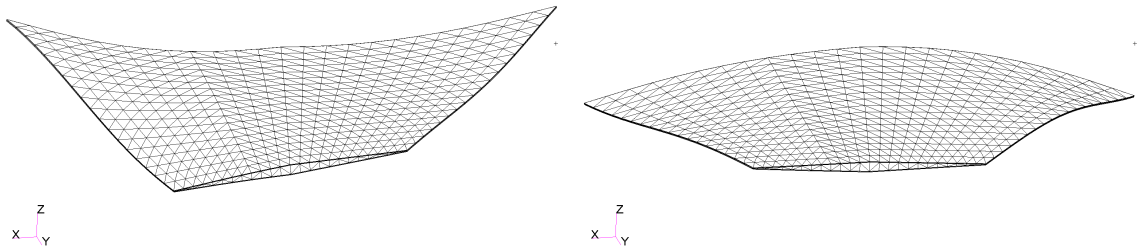

(a) Mode 4 at 371 s: 53.9 Hz. (b) Mode 4 at 7,200 s: 54.1 Hz.

Figure 4.21: Mode 4 at two different time instants showing evolution of mode shape with heating for case including geometric stiffening due to thermal stresses and excluding material property degradation with temperature.

Plots of the percentage change in the natural frequency of each heated mode with respect to the corresponding unheated frequencies are given in Fig. 4.22. Note that the heated frequencies are sorted in order of increasing magnitude at each time step. For modes 1 – 3, the greatest absolute deviation from the unheated frequency is found to be an 8% decrease, while that for modes 4 – 6 is found to be a 12% decrease. It can observed that

there is an initial decrease in natural frequency of the heated modes, but the frequency begins to increase later into the transient likely due to the development of thermal stresses. However, the heated natural frequencies are lower than the corresponding unheated natural frequencies at all time instants.

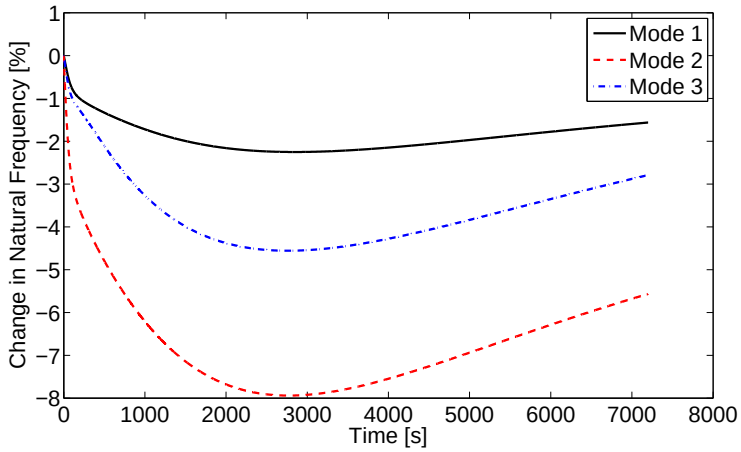

(a) Heated modes 1–3.

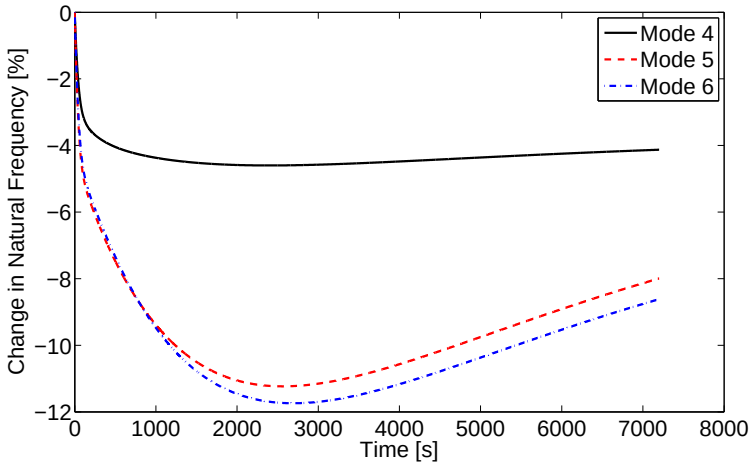

(b) Heated modes 4–6.

Figure 4.22: Percentage change in natural frequencies of first six heated modes vs. time for case including geometric stiffening due to thermal stresses and excluding material property degradation with temperature.

4.4.2.2 Both Geometric Stiffening Due to Thermal Stresses and Material Property Degradation with Temperature Included

The previous section investigated the evolution of the free vibration modes under transient heating when geometric stiffening due to thermal stresses was included, but material property degradation with temperature was excluded. In the current section, results are generated from simulations under the same flight conditions as the previous section, but which include both geometric stiffening due to thermal stresses and material property degradation with temperature. Therefore, comparison between results from the current section and those from the previous section illustrate the impact of material property degradation with temperature on the evolution of the free vibration modes under transient heating.

Plots of the diagonal entries of the MAC matrix for this case are given in Fig. 4.23. Comparing Fig. 4.23 against Fig. 4.18, it can be observed that when both geometric stiffening and material property degradation effects are included, the diagonal MAC values for heated modes one, two, five, and six deviate further from one than for the case which only includes geometric stiffening. However, for the current case, the MAC values for heated modes one, two, five, and six still remain reasonably close to one, indicating again that these modes do not change significantly under transient heating. This provides evidence that these heated modes are robust with respect to transient heating when both geometric stiffening due to thermal stresses and material property degradation with temperature are included. As was the case in Section 4.4.2.1, $\text{MAC}_{3,3}$ and $\text{MAC}_{4,4}$ deviate significantly from one, indicating loss of correspondence between the heated modes and unheated modes. However, when both geometric stiffening and material property degradation are included, the diagonal MAC entries for heated modes three and four begin to increase noticeably after they reach their minimum values. This is in contrast to the results shown in Fig. 4.18 in which the diagonal MAC entries for heated modes three and four remain approximately constant after they reach their minimum value.

As was plotted in the previous section, $\text{MAC}_{3,3}$ and $\text{MAC}_{3,4}$ are shown in Fig. 4.24(a)

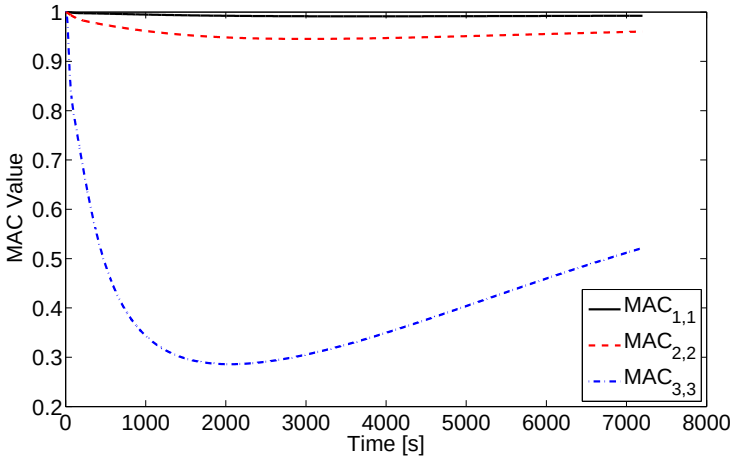

(a) Modes 1–3.

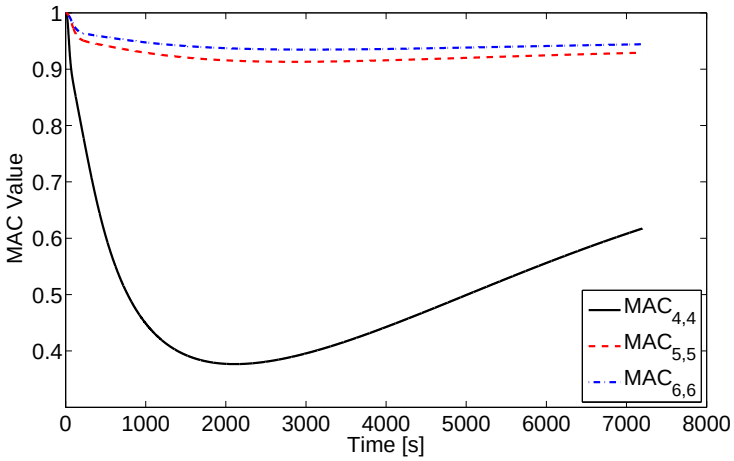

(b) Modes 4–6.

Figure 4.23: Diagonal entries of MAC matrix for first six modes vs. time for case including both geometric stiffening due to thermal stresses and material property degradation with temperature.

for the current case. From the figure, it can again be seen that transient heating result in mode switching between heated modes three and four over time. However, it can be seen by comparing Fig. 4.24(a) to Fig. 4.19(a) that inclusion of material degradation with temperature results in two crossover points between the MAC values instead of one as was the case when material property degradation was excluded. A similar result is evident for the $MAC_{4,4}$ and $MAC_{4,3}$ values as can be seen by comparing Fig. 4.24(b) against Fig. 4.19(b).

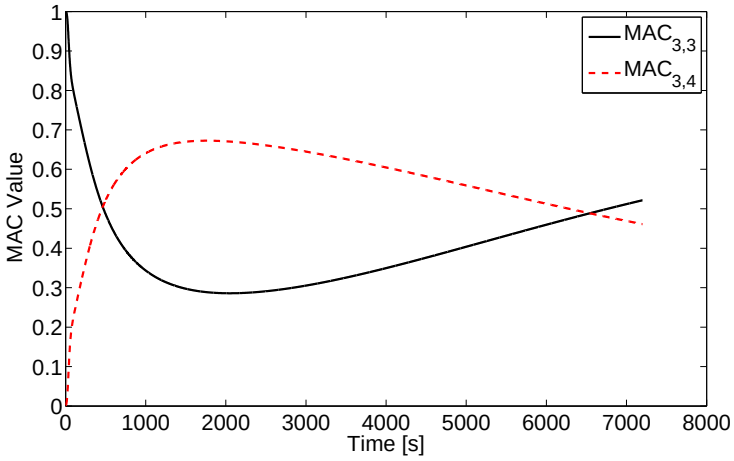

(a) $MAC_{3,3}$ vs. $MAC_{3,4}$.

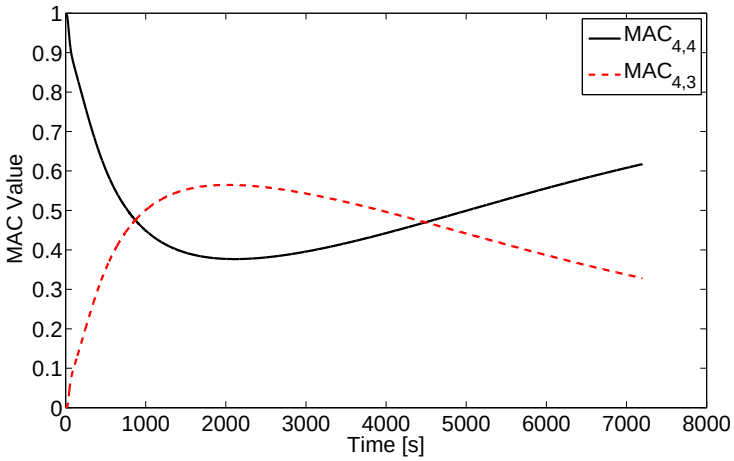

(b) $MAC_{4,4}$ vs. $MAC_{4,3}$.

Figure 4.24: Comparison of diagonal and off-diagonal entries of MAC matrix for third and fourth modes vs. time for case including both geometric stiffening due to thermal stresses and material property degradation with temperature.

To illustrate the evolution of heated mode three for the case in which both geometric

stiffening due to thermal stresses and material property degradation with temperature are included, this mode is output at two different instants during the transient. Heated mode three is shown at 464 s into the transient in Fig. 4.25(a) and at 1,764 s into the transient in Fig. 4.25(b). The mode at 464 s corresponds to the time instant of the first crossing between the two curves in Fig. 4.24(a) while the mode at 1,764 s corresponds to the time instant at which $MAC_{3,4}$ takes on its maximum value in Fig. 4.24(a). Comparing heated mode three at 1,764 s (Fig. 4.25(b)) to unheated mode four (Fig. 4.17(d)), it is observed that heated mode three is beginning to resemble unheated mode 4 at this time instant, thereby confirming the quantitive results shown by the MAC values in Fig. 4.24(a).

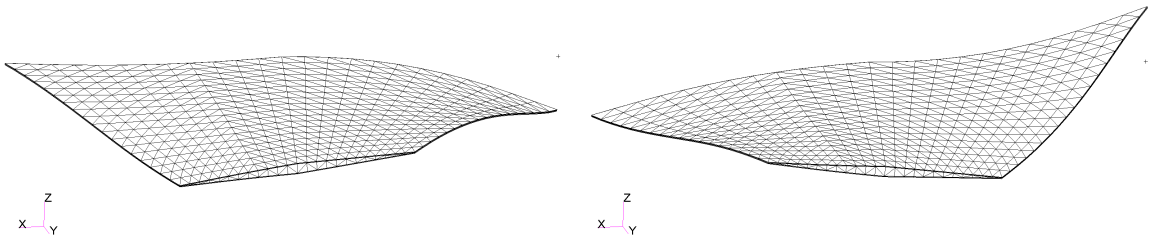

(a) Mode 3 at 464 s: 50.1 Hz. (b) Mode 3 at 1,764 s: 47.7 Hz.

Figure 4.25: Mode 3 at two different time instants showing evolution of mode shape with heating for case including both geometric stiffening due to thermal stresses and material property degradation with temperature.

Similarly, to illustrate the evolution of heated mode four for the case in which both geometric stiffening due to thermal stresses and material property degradation with temperature are included, it is output at two different time instants. This mode is generated at 870 s (the first crossover point in Fig. 4.24(b)) and at 2,030 s (the location of the maximum value of $MAC_{4,3}$ in Fig. 4.24(b)) as shown in Fig. 4.26(a) and Fig. 4.26(b), respectively. By comparing heated mode 4 at 2,030 s (Fig. 4.26(b)) to unheated mode three (Fig. 4.17(c)), it can be seen that heated mode four is qualitatively similar to unheated mode three at this time instant, again confirming the quantitative results shown in Fig. 4.24(b).

Finally, the percentage change in natural frequency for each heated mode with respect to the corresponding unheated mode is plotted for modes 1 – 3 in Fig. 4.27(a) and for modes

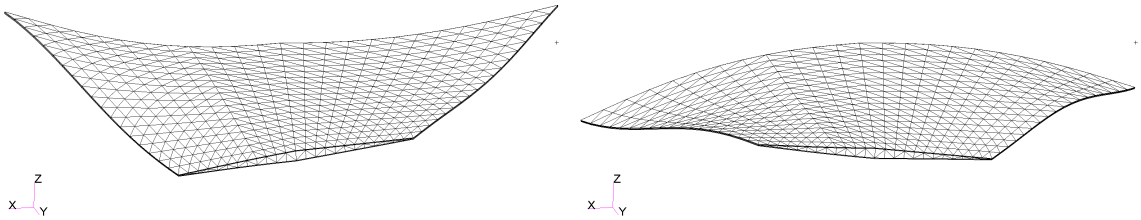

(a) Mode 4 at 870 s: 50.9 Hz. (b) Mode 4 at 2,030 s: 49.4 Hz.

Figure 4.26: Mode 4 at two different time instants showing evolution of mode shape with heating for case including both geometric stiffening due to thermal stresses and material property degradation with temperature.

4 – 6 in Fig. 4.27(b). For modes 1 – 3, the greatest absolute percentage change in natural frequency is found to be 20% while that for modes 4 – 6 is found to be 25%. By comparing Fig. 4.27 to Fig. 4.22, it can be observed that inclusion of both geometric stiffening due to thermal stresses and material property degradation results in greater overall reduction in natural frequency when compared to the case in which only geometric stiffening due to thermal stresses is included. This is likely due to the fact that an increase in temperature can either increase or decrease stiffness via geometric stiffening effects, but it always results in reduced stiffness via temperature-dependence of the Young's modulus provided that E is a monotonically decreasing function of temperature.

These results provide support for the use a fixed basis in the structural dynamic ROM over the duration of the aerothermoelastic simulation. For modes one, two, five, and six, we observe that the corresponding diagonal MAC values remain close to one, and thus there is not a significant loss in accuracy by not updating these modes as the structure is heated. Though mode switching occurs between heated modes three and four, at any time during the evolution of the mode shapes, the space spanned by the heated modes is approximately the same as the space spanned by the unheated modes. Thus, the heated modes can be well-represented at any instant in time using the unheated modes, and no update of the modes is necessary as the structure is heated for this particular structure.

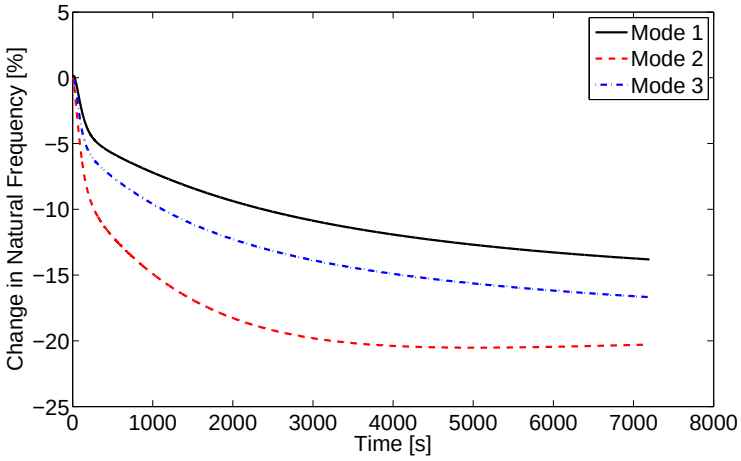

(a) Heated modes 1–3.

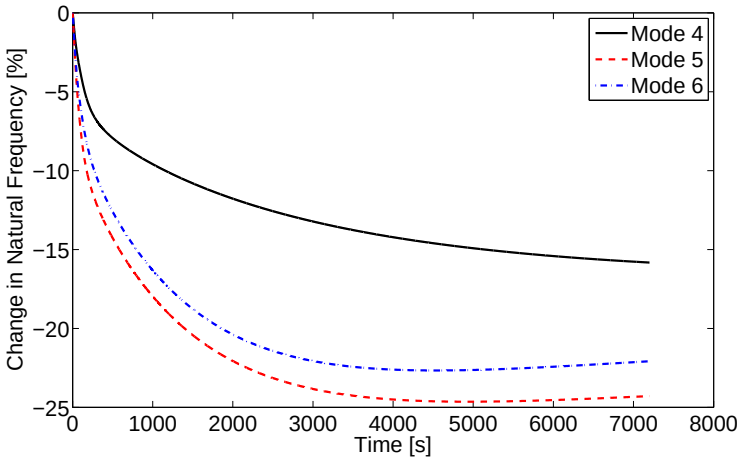

(b) Heated modes 4–6.

Figure 4.27: Percentage change in natural frequencies of first six heated modes vs. time for case including both geometric stiffening due to thermal stresses and material property degradation with temperature.

4.5 Concluding Remarks

This chapter presented a reduced-order structural dynamic modeling methodology using a fixed basis consisting of a set of Ritz vectors that are computed *a priori*. The full-order equations of motion were presented and the impact of heating on the stiffness and loads was highlighted. Specifically, the structural stiffness contains temperature-dependent material properties as well as geometric stiffening effects due to thermal stresses. The thermal loads on the structure result from differential thermal expansion under the spatially varying temperature distribution. The formulation for obtaining the reduced-order structural dynamic equations of motion was presented. As a result of the temperature-dependent stiffness, the reduced-order equations of motion are coupled. As such, a numerical integration scheme was outlined for use in obtaining the structural dynamic response at each time step. A one-dimensional example case was used to illustrate the level of coupling of the equations that results from heating effects.

The remainder of the chapter was aimed at assessing the impact of transient heating on the free vibration mode shapes and natural frequencies of the structure. The first case studied involved analyzing the effects of material property degradation and thermal stresses on the natural frequencies and free vibration modes of a representative HSV control surface. The temperature distribution of interest was taken to be that obtained from a transient thermal solution at 320 s into the simulation. Plots of the first four mode shapes were given for various combinations of the effects of material property degradation and thermal stresses. These phenomena were found to result in the appearance of localized panel modes at significantly lower frequencies than would be the case if material property degradation and thermal stresses were not included.

In the second case study of this chapter, the modal assurance criterion (MAC) was used to quantify the degree to which the natural mode shapes and frequencies of a representative hypersonic vehicle control surface change as a result of aerodynamic heating along a trajectory. This study was motivated by the fact that the structural dynamic ROM uses a fixed set

of basis vectors throughout the simulation, and the underlying assumption is therefore that the free vibration modes do not change significantly as a result of aeroheating. For the six modes tracked in this study, the MAC values of the first, second, fifth and sixth modes were found to remain close to one, indicating little change in those modes over time. However, a mode-switching phenomenon was found to occur between the third and the fourth modes. Though the third and fourth modes do evolve significantly over time, the overall modal content of modes three and four at room temperature is approximately the same as that at elevated temperature. Investigation into the evolution of natural frequencies over time including both material property degradation and thermal stresses showed a maximum departure from the room temperature natural frequencies of 25% which occurred for mode 5. In cases where natural frequency has a significant impact on the overall system dynamics, the effect of aeroheating on natural frequencies must be considered.

Chapter V

Enhanced Modal Solution Techniques for Reduced-Order Structural Dynamic Modeling

The current chapter is aimed at extending the methodology presented in Chapter IV in two separate areas. The first area involves the efficient updating of stiffness and thermal loads under transient heating. Though the formulation presented in Chapter IV successfully reduced the order the equations of motion, the cost of updating the generalized stiffness matrix and thermal load vector as a function of temperature remained costly. This was due to the fact that, at each aeroelastic time step, it was required to assemble the full-order physical stiffness matrix based on the current temperature distribution and pre- and post-multiply by the structural modes in order to obtain the generalized stiffness matrix. To assemble the generalized thermal load vector, it was required to generate each element thermal load vector in physical space, assemble these into the global thermal load vector, and pre-multiply by the structural loads. Due to the large number of degrees of freedom in the structural model, such an approach is computationally costly. This chapter therefore describes a methodology for more efficiently updating the generalized stiffness matrix and physical thermal load vector as a function of temperature.

The second area in which the structural dynamics formulation of Chapter IV is extended in the current chapter involves the selection of the structural basis vectors. While free vibration modes are useful to include in the modal set, the use of such modes in isolation

may not always be sufficient. Specifically, in cases where thermal loads are dominant and the structural response is close to quasi-static, the free vibration modes may not be excited to a significant extent. Therefore, the current chapter also examines a methodology for augmenting the basis of free vibration modes with additional modes in order to improve the accuracy of the reduced-order structural dynamic response computation. Note that the model used as an application example for the studies in this chapter is the all-moveable control surface model which was described in Section 4.4.2 of Chapter IV.

5.1 Efficient Updating of Stiffness and Thermal Loads

5.1.1 Overview of Kriging Theory

As the temperature distribution of the structure is continuously changing in time, the stiffness matrix and thermal load vector must be updated at every iteration of the structural dynamic response solution. Calculation of the generalized stiffness involves generating the physical stiffness matrix and pre- and post-multiplying by the modal matrix. Updating the physical stiffness matrix requires assembling $K_S(T)$ based on the temperature-dependence of material properties as well as solving a linear static finite element problem to generate $K_G(T)$. Computation of the generalized thermal load vector requires updating the physical thermal load vector and pre-multiplying by the modal matrix. Because the number of physical degrees of freedom in the structural model is large, reassembling the physical stiffness matrix and thermal load vector at every aeroelastic time step within an aerothermoelastic simulation framework is undesirable. One goal of this thesis is to examine techniques for reducing the computational cost of the structural ROM by avoiding the need to reassemble the physical stiffness matrix and thermal load vector at every time step. A method for directly updating the stiffness matrix and thermal loads based on a given temperature distribution is therefore proposed to reduce the computational cost of the structural ROM. The generalized load vector due to aerodynamic loads, f_S^A, is still assembled in the usual

manner as it only contains contributions to the loads at the outer surface of the structure and the associated computational cost is relatively low.

The methodology employed in this work is based on the kriging technique [158] which provides a global approximation to a function based on sampled training data. Kriging provides an approximation, $\hat{y}(b)$, to a function based on local deviations, $Z(b, X)$, from a global approximation, $R(b, X)$, of the form [159]

$$\hat{y}(b) = R(b, X) + Z(b, X), \tag{5.1}$$

where b is a vector of inputs corresponding to the untried location in the parameter space and X is a collection of the sample points used for the training data. The training response at the sample points is stored in the response matrix, $Y(X)$, such that

$$Y(X) = \begin{bmatrix} y_1^{(1)}\left(X^{(1)}\right) & y_1^{(2)}\left(X^{(2)}\right) & . . & y_1^{(n_k)}\left(X^{(n_k)}\right) \\ y_2^{(1)}\left(X^{(1)}\right) & y_2^{(2)}\left(X^{(2)}\right) & . . & y_1^{(n_k)}\left(X^{(n_k)}\right) \\ \vdots & \vdots & \ddots & \vdots \\ y_{n_p}^{(1)}\left(X^{(1)}\right) & y_{n_p}^{(2)}\left(X^{(2)}\right) & . . & y_{n_p}^{(n_k)}\left(X^{(n_k)}\right) \end{bmatrix}, \tag{5.2}$$

where $y_i^{(j)}$ indicates the i-th entry of the response vector for the j-th kriging snapshot, $X^{(j)}$, n_k is the number of kriging snapshots, and n_p is the number of output parameters in a snapshot. The regression model, $R(b, X)$, is an assumed function (usually of polynomial form), while $Z(b, X)$ is a realization of a stochastic process with zero mean, variance of σ^2, and non-zero covariance, and ensures that the kriging model interpolates the sampled data points exactly. Alternatively, $Z(b, X)$ represents uncertainty in the mean of $y(b)$ and the covariance matrix of $Z(b, X)$ for two points in the parameter space, $b^{(i)}$ and $b^{(j)}$, is given by

$$\text{Cov}\left[Z(b^{(i)}), Z(b^{(j)})\right] = \sigma^2 C[G(X^{(i)}, X^{(j)})], \tag{5.3}$$

where C is the correlation matrix that is assembled based on the chosen correlation func-

tion, $G(X^{(i)}, X^{(j)})$, and $X^{(i)}$ and $X^{(j)}$ are the i-th and j-th sample points, respectively. In Eq. (5.3), the process variance, σ^2, functions as a scale factor that can be tuned to the training data. The role of the correlation function is to account for the effect of each interpolation point on every other interpolation point and quantifies how quickly and smoothly the function moves from point $X^{(i)}$ to point $X^{(j)}$. In this work, a Gaussian correlation function is used, and is given by [159]

$$G(X^{(i)}, X^{(j)}) = \exp\left[-\sum_{k=1}^{n_{dv}} \theta_k \left| X_k^{(i)} - X_k^{(j)} \right|^{p_k}\right], \tag{5.4}$$

where n_{dv} is the number of design variables or parameters, θ_k and p_k are the unknown fitting parameters, and $X_k^{(i)}$ denotes the k-th component of the i-th sample point. The bounds on the fitting parameters are: $\theta_k > 0$ and $0 < p_k \leq 2$. As the point $X^{(i)}$ approaches $X^{(j)}$, Eq. (5.4) approaches its maximum value of one, leading to the property that the kriging surface passes through the sampled data points. Therefore, the Gaussian correlation function is intuitive in that the closer two points become in the parameter space, the greater the correlation between the two points becomes. The parameters θ_k in Eq. (5.4) serve to provide a measure of activity in the variable X_k. Large values of θ indicate that there is strong correlation only for sample points that are close together. Small values of θ indicate that sample points points spaced further apart still have a strong influence on each other because they are well correlated. An alternative interpretation of the θ_k parameters is associated with dependence of the function on the k-th design variable. If the k-th design variable is active, there exist large differences in the function values at $X_k^{(i)}$ and $X_k^{(j)}$. Thus, the corresponding θ_k parameter will be large such that even though the absolute difference between $X_k^{(i)}$ and $X_k^{(j)}$ is small, the correlation between the function values at the i-th and j-th snapshot is low due to the fact that it changes rapidly with changes in the k-th design variable. The exponents p_k are related to the smoothness of the function of interest in the direction of the k-th design variable, with increasing p_k corresponding to increasing smoothness. In order

to determine the fitting parameters, the form of $R(b, x)$ must first be chosen.

To derive the prediction equations, a vector containing the regression functions, denoted by r_x, is assembled such that

$$R(b, X) = r_x^T \beta, \tag{5.5}$$

where r_x^T is a $1 \times n_b$ row vector of basis functions with n_b being the number of basis functions associated with the regression polynomial, and β is an $n_b \times 1$ column vector of coefficients of each of the polynomial terms. The expanded design matrix, R_x, is of the form [160]

$$R_x(X) = \begin{bmatrix} r_x^T(X^{(1)}) \\ r_x^T(X^{(2)}) \\ \vdots \\ r_x^T(X^{(n_k)}) \end{bmatrix}, \tag{5.6}$$

such that i-th row of R_x corresponds to the evaluation of the n_b basis functions at the i-th kriging snapshot. If the stochastic process evaluated at the kriging snapshot points is denoted as

$$z(X) = \left[Z(X^{(1)}), Z(X^{(2)}), \ldots, Z(X^{(n_k)})\right]^T, \tag{5.7}$$

then the training data can be represented as

$$Y(X) = R_x \beta + z. \tag{5.8}$$

The goal of the kriging methodology is to obtain the best linear unbiased predictor, where unbiasedness refers to the fact that the expected value of the predictor must be equal to the expected value of Eq. (5.8). This is accomplished by solving an optimization problem to minimize the error of the predictor subjected to constraints that ensure unbiasedness. This procedure results in the kriging predictor being given by

$$\hat{y}(b) = r_x^T \hat{\beta} + g^T(b, X) G^{-1} \left(y - R_x \hat{\beta}\right), \tag{5.9}$$

where y is a column vector of length n_k containing the values of the function outputs at the sample points and $g^T(b, X)$ is a correlation vector between the untried point, b, and the sample data points, X, such that

$$g(b, X) = \left[G(b, X^{(1)}), G(b, X^{(2)}), \ldots, G(b, X^{(n_k)})\right]^T. \tag{5.10}$$

In Eq. (5.9), $\hat{\beta}$ is the generalized least squares estimator of β and is given by

$$\hat{\beta} = \left(R_x^T C^{-1} R_x\right)^{-1} R_x^T C^{-1} y. \tag{5.11}$$

At this point, it remains to determine the fitting parameters θ_k and p_k in Eq. (5.4). As the stochastic process associated with the error of the kriging regressors is assumed to be Gaussian, the optimal values of θ_k and p_k are those that maximize the likelihood that the interpolation points have been drawn from such a process. Alternatively stated, we seek to choose θ_k and p_k leading to a kriging function such that the consistency between the actual model and the kriging predictions of the model is maximized. The problem of obtaining the maximum likelihood estimates of θ_k and p_k is posed as

$$\min_{\theta_k>0,\ 0<p_k\leq 2} -\frac{n_k \ln\left(\hat{\sigma}^2\right) + \ln|C|}{2}, \tag{5.12}$$

where $|C|$ is the determinant of C and $\hat{\sigma}$ is the generalized least squares estimate of σ given by

$$\hat{\sigma}^2 = \frac{\left(y - R_x\hat{\beta}\right)^T C^{-1} \left(y - R_x\hat{\beta}\right)}{n_k}. \tag{5.13}$$

The maximum likelihood estimate given in Eq. (5.12) is a function of the θ_k and p_k parameters only, and one can thus utilize nonlinear optimization techniques to obtain these parameters. While any values of θ_k and p_k would result in a kriging model that interpolates the sample points exactly, the "best" kriging model is that which utilizes those values of θ_k

and p_k which minimize the function given in Eq. (5.12).

5.1.2 Procedure for Efficient Updating of Stiffness and Thermal Loads

In this application the quantities to be approximated using kriging, $\hat{y}$, are the entries of the stiffness matrix and the thermal load vector, and the inputs to function, b, are spatially varying temperature distributions. Because a full-order thermal model is expected to contain a large number of degrees of freedom, it is impractical to treat each thermal degree of freedom as a variable in the parameter space. This is due to the fact that the resulting parameter space would be too large to realistically sample when generating the kriging training data. However, as POD is already being used for the thermal ROM, it provides a convenient and optimal means for parameterizing the transient temperature distribution in terms of a small number of variables. By using the truncated set of thermal POD modal coordinates as the parameters to represent the complete temperature distribution, the number of parameters to be sampled is greatly reduced. The large-scale reduction in the number of design variables needed to represent the physical temperature distribution is due to the optimality of the POD basis. Recall that the POD basis is optimal in the sense that it captures the solution more accurately in a finite number of modes than any other basis representation using the same number of modes, provided that the POD snapshots adequately capture the dynamics of the system. This optimality is critical as the computational effort required to construct a kriging model is a strong function of the number of design variables involved.

Because of the large number of structural degrees of freedom, the computational cost and memory associated with updating the physical stiffness matrix, $K_S^*(T)$, and pre- and post-multiplying by the structural reference modes at every aeroelastic time step is undesirable. As such, kriging is used to directly create the generalized stiffness matrix, $k_S^*(T)$, which is of reduced size and does not possess the computational issues associated with the physical stiffness matrix. As the number of entries in the physical thermal load vector, F_S^H, is reasonable, error analysis is conducted on kriging models of both the physical and

generalized thermal load vectors to assess which one can be more accurately represented.

The first step in the process is to generate the thermal POD vectors to be used in parameterizing the transient temperature distribution. After the thermal snapshot matrix is assembled, its singular value decomposition is taken in order to generate the POD basis vectors. The eigenvalues of the correlation matrix are computed based on the singular values and are used to assess the relative contribution of each POD mode. The POD modes to be used in the parameterization of the temperature distribution are then selected and used as design variables in the kriging process.

With the design variables chosen, the next step of the process is to generate the kriging sample points to be used in construction of the ROMs. This is accomplished using the Latin Hypercube Sampling (LHS) methodology. In this case, each kriging sample point consists of a set of a pre-determined number of POD modal coordinates. Before the sample points can be generated, upper and lower bounds must be established for each design variable. This is accomplished by first calculating the vector of POD modal coordinates for each thermal snapshot based on the chosen POD basis by solving for c in the equation

$$\bar{\Phi}_T c = T, \tag{5.14}$$

where $\bar{\Phi}_T$ is the matrix containing the truncated set of POD modes, c is the vector of modal coordinates to be found, and T is a vector of temperatures corresponding to a given snapshot. Because there are more equations than unknowns in Eq. (5.14), c is computed in the least squares sense. Once c is known for each thermal snapshot, an interval is found for each modal coordinate by subtracting the minimum value of each modal coordinate from the corresponding maximum value. Because these intervals corresponds to the specific flight conditions at which the thermal POD snapshots were taken, they may not encompass the full range that the POD modal coordinates can assume across the full spectrum of flight conditions. In order to account for variability in the POD modal coordinates with flight

conditions and boundary conditions, the interval size for each POD modal coordinate is multipled by a factor of three by increasing each upper bound and decreasing each lower bound by equal amounts. Note that this procedure for bounding the POD modal coordinates is used for simplicity at this stage as the focus of the current section is on the accuracy of the methodology. In a subsequent section, a more robust approach for bounding the POD modal coordinates is presented.

With the upper and lower bounds for each modal coordinate established, the LHS methodology is used to generate the kriging sample points. Because the sampling is performed on the POD modal coordinates and not on the nodal temperatures themselves, the resulting temperature vector may be out of the expected range for the structure for certain combinations of POD modal coordinates. To account for this, bounds are also established on minimum and maximum allowable values of the resulting nodal temperatures. After the sample points are generated, the temperature vector corresponding to each sample point is found using the chosen POD basis. A filtering process is then employed that eliminates sample points whose corresponding minimum and maximum nodal temperature values lie outside the range of 293 K – 1,500 K. It is therefore necessary to generate more sample points than desired as not all sample points will be accepted.

Once the inputs for each training run are generated, high-fidelity analysis is conducted to generate the training data for each sample point. This step consists of generating the temperature distribution corresponding to the selected POD modal coordinates and computing the resulting stiffness matrix and thermal load vector at that temperature distribution. The generalized stiffness matrix calculation is performed by assembling the physical stiffness matrix and pre- and post-multiplying by the chosen structural reference modes. The physical stiffness matrix is computed using Eq. (4.9) and contains contributions from both the conventional stiffness matrix with temperature-dependent material properties, $K_S(T)$, and the geometric stiffness resulting from thermal stresses, $K_G(T)$. The assembling of the matrices and vectors required for the kriging training process is accomplished via the use

of Nastran DMAP. Because the kriging ROM is necessary to evaluate the accuracy of the structural basis, the validity of this structural basis is not studied in the current section. It is used simply as a placeholder at this stage for the purpose of evaluating the accuracy of the kriging ROM with a fixed structural basis. Subsequent sections will provide detailed examination of selection of a robust structural basis.

Using the set of sample points along with the output data, kriging surrogates are created for the stiffness matrix and thermal loads using a second order polynomial regression model. Once the kriging models are generated, the errors associated with each are quantified. If the accuracy of the models is acceptable, they can then be used within the aerothermoelastic simulation framework. If greater accuracy is desired, more sample points are added and the kriging models are updated. The procedure for error quantification is based on that utilized by Crowell et al. [52] The process involves first generating an independent set of evaluation points using LHS. Again, these evaluation points are subjected to the criteria that they must generate nodal temperatures that lie within the range 293 K – 1,500 K. The number of kriging evaluation points, n_e, is chosen to be 500 in this work. For each evaluation point, the stiffness matrix and thermal load vector are calculated using both the full-order model and the kriging ROM. To quantify the error between the full-order and kriging solutions, two different error metrics are utilized. The first error metric is the normalized root mean squared error (NRMSE). Expressed as a percentage, the NRMSE is given by

$$\text{NRMSE} = \frac{\sqrt{\frac{1}{q}\sum_{i=1}^{q}\left(\text{ROM}_i - \text{Full}_i\right)^2}}{\text{Max(Full)} - \text{Min(Full)}} \times 100\%, \tag{5.15}$$

where i is the i-th output quantity, "ROM" represents a solution vector of the reduced-order model, "Full" represents a solution vector of the full-order model, and q is the total number of output quantities. Also, note that "Max" and "Min" correspond to the maximum and minimum entries, respectively, of the vector of interest. The output quantities are the entries of the generalized stiffness matrix and the physical or generalized thermal load

vector, and thus i is summed over all of the entries of the vector of interest in the numerator of Eq. (5.15). Note that the generalized stiffness matrix is reshaped into a column vector for the purpose of error analysis. The second error metric utilized is the L_∞ error. Expressed as a percentage, the L_∞ error is given by

$$L_\infty = \frac{\text{Max}\left(|\text{ROM} - \text{Full}|\right)}{\text{Max}(\text{Full}) - \text{Min}(\text{Full})} \times 100\%. \tag{5.16}$$

Note that the error metrics are calculated for each evaluation case. To determine a scalar measure of error for the ROMs, both the average and maximum values of the NRMSE and L_∞ error over all evaluation cases are examined.

5.1.3 Application of Kriging Methodology to Control Surface Example

Without loss of generality, the kriging procedure described above is applied to the control surface model shown in Fig. 4.15. The first step of the process is to extract the thermal snapshots. To accomplish this, an aerothermoelastic simulation is run for a time-history of one hour at $M = 8$, $h = 26$ km, $\alpha = 3^\circ$, and a uniform initial temperature distribution, $T^{(0)}$, of 293 K. Due to a steep initial temperature gradient as the structure heats up from room temperature, the maximum temperature increases until approximately 150 s into the transient, at which point it begins to reach a steady state. As such, two different sets of time steps are used to adequately capture the dynamics of the thermal system. For the period from 0 – 150 s, the time steps are chosen as follows: $\Delta t_{HT} = \Delta t_{AE} = 0.1$ s, and $\Delta t_{AT} = 1$ s. For the period from 150 s – 3,600 s, the time steps are chosen as follows: $\Delta t_{HT} = \Delta t_{AE} = 1$ s, and $\Delta t_{AT} = 5$ s. The goal of using smaller time steps initially is to provide more resolution for the period in which the dynamics of the thermal system are changing on a faster time scale. One thermal snapshot is taken at each heat transfer time step regardless of the size of the time step, resulting in a total of 4,951 snapshots.

The first 24 eigenvalues of the correlation matrix are shown in Fig. 5.1. The re-

tained POD modes are chosen by selecting those modes whose corresponding eigenvalue is greater than one. Based on this criteria, the first 15 POD modes are retained. The fact that the POD modal truncation results in a set of 15 modes being retained is advantageous in that the number of design variables involved in the kriging training procedure has now been reduced to a feasible level.

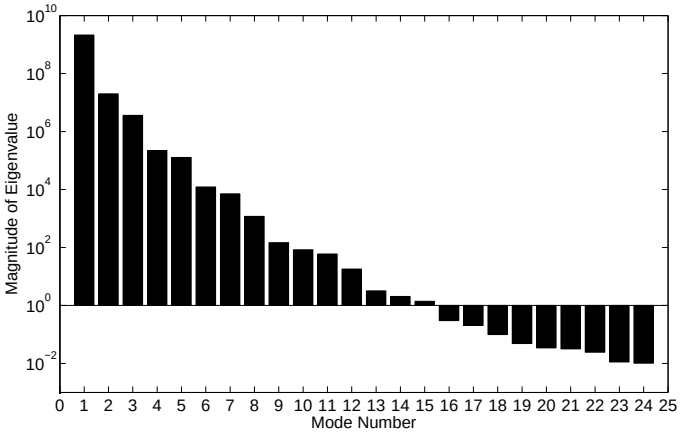

Figure 5.1: Semi-log plot of first 24 eigenvalues of correlation matrix.

Using the 15 POD modes as design variables, the kriging training process is carried out and kriging ROMs of the stiffness and thermal loads are generated. Note that for this case, the structural reference modes are chosen to be the first ten free vibration modes at the reference thermal state. The reference thermal state is obtained by averaging the 4,951 thermal snapshots used in generating the POD basis. To examine the error of the kriging ROMs as a function of number of sample points, kriging models for both the generalized stiffness matrix and generalized thermal load vector are generated using varying numbers of sample points. Two different criteria are utilized in generating the set of Latin Hypercube sample points. The first, denoted "maximin", aims to maximize the minimum distance between sample points over a specified number of iterations. The second, denoted "correlation", aims to minimize the correlation between sample points over a specified number of iterations. In both cases, the maximum allowable number of iterations is set to 500. The error metrics are computed for each kriging ROM over 500 evaluation snapshots which are

always generated using the "maximin" criterion over 500 iterations. Plots of the average NRMSE and L_∞ error for the generalized stiffness ROM as a function of number of sample points are given in Fig. 5.2(a) and Fig. 5.2(b), respectively, using both the "maximin" and "correlation" criteria. Similarly, plots of the average error for the generalized thermal load vector ROM are given in Fig. 5.3(a) and Fig. 5.3(b), respectively, using both the "maximin" and "correlation" criteria. Due to memory requirements associated with the "maximin" criterion, the maximum number of sample points used with this criterion is 3,000, while up to 6,000 are taken for the "correlation" cases. As seen in the figures, there is not a significant difference between the results obtained using the "maximin" criterion and the "correlation" criterion. Due to the higher computational cost and memory requirements associated with the "maximin" criterion, the "correlation" criterion with a maximum of 500 iterations is used from this point forward. Comparing Fig. 5.2 with Fig. 5.3, it is evident that generalized stiffness matrix ROM is significantly more accurate than the generalized thermal load vector ROM for the same number of snapshots.

To understand why the error of the generalized stiffness ROM is significantly lower than that of the generalized thermal load vector ROM, the functional dependence of the generalized stiffness matrix on the POD modal coordinates is examined. Recall that the physical stiffness matrix is the sum of the conventional stiffness matrix and geometric stiffness matrix, i.e.

$$K_S^*(T) \equiv K_S(T) + K_G(T). \tag{5.17}$$

The entries of the generalized stiffness matrix are simply linear combinations of the entries of the physical stiffness matrix and do not affect the order of its dependence on temperature. The dependence of $K_S(T)$ and $K_G(T)$ on the POD modal coordinates is through the variation of material properties with temperature. The entries of the conventional stiffness matrix, $K_S(T)$, are only dependent on the Young's modulus of the corresponding material, i.e.

$$K_{S,i} \propto E(T_i), \tag{5.18}$$

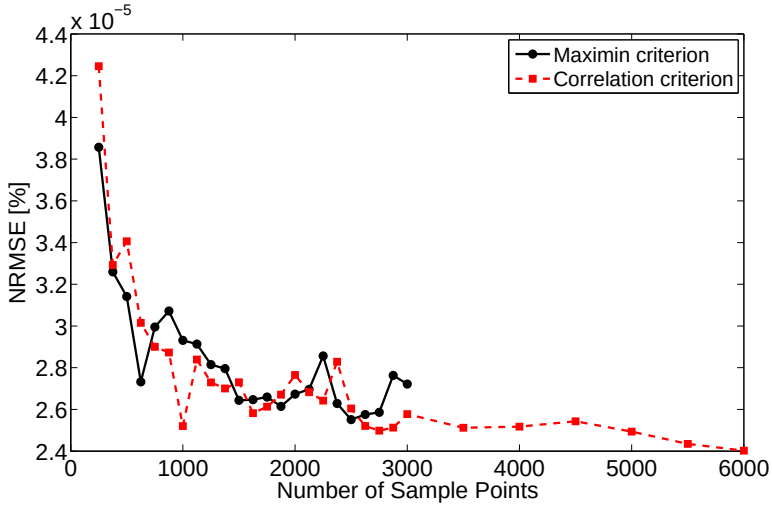

(a) Average NRMSE.

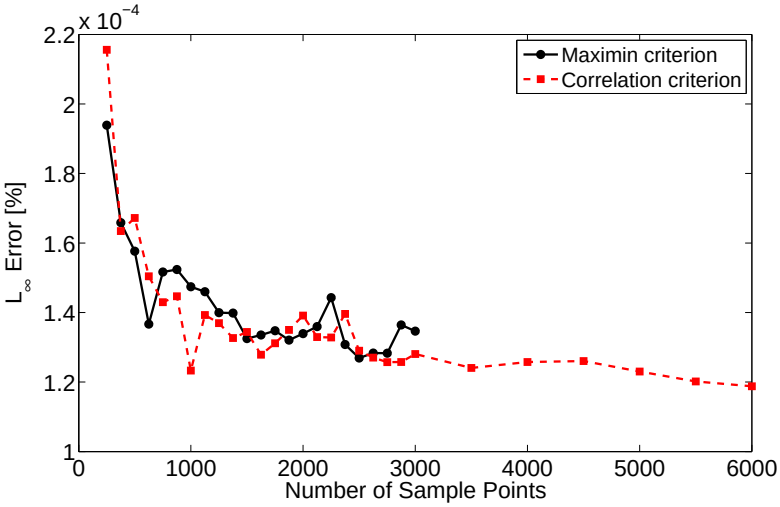

(b) Average L_∞ Error.

Figure 5.2: Average errors for generalized stiffness matrix ROM over 500 evaluation cases.

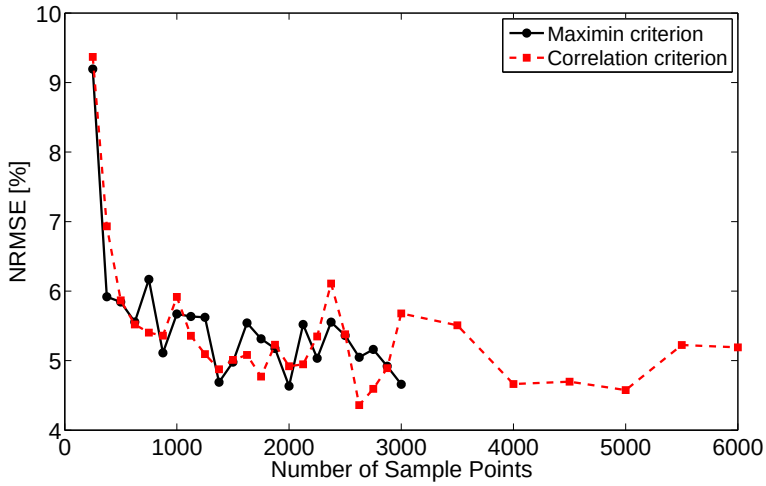

(a) Average NRMSE.

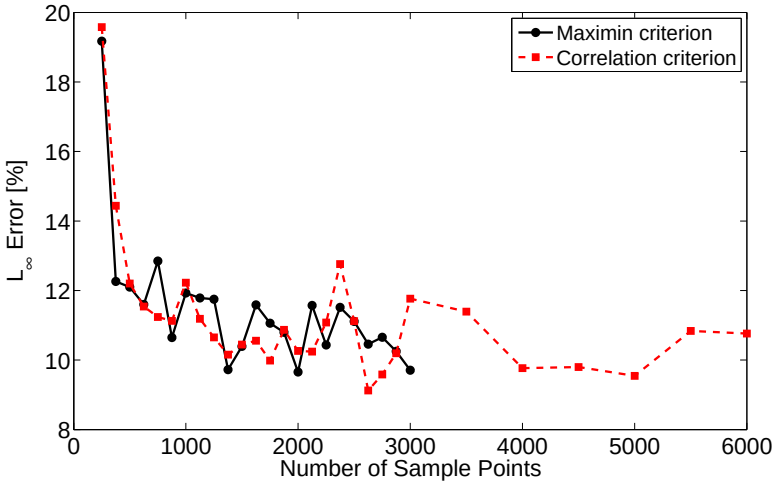

(b) Average L_∞ Error.

Figure 5.3: Average errors for generalized thermal load vector ROM over 500 evaluation cases.

Table 5.1: Orders of dependence of E and α_T on temperature.

	$E(T)$	$\alpha_T(T)$
Heat Shield (René 41)	Quadratic	Cubic
Insulation (Min-K)	N/A	N/A
Skin/Stiffeners (TIMETAL834)	Linear	Constant

where i denotes a particular degree of freedom. The entries of the geometric stiffness matrix, $K_G(T)$ are dependent on the Young's modulus, coefficient of thermal expansion, and temperature change, i.e.

$$K_{G,i} \propto E(T_i), \alpha_T(T_i), \Delta T_i, \tag{5.19}$$

where the temperature is always expressed as a linear combination of the POD basis vectors such that

$$T_i = \sum_{j=1}^{r} c_j \varphi_i^{(j)}, \tag{5.20}$$

where r is again the number of degrees of freedom in the reduced-order thermal model. In order to understand the order of the functional dependence of the entries of $K_S(T)$ and $K_G(T)$ on the POD modal coordinates, c_j, it is first necessary to know the order of the functional dependence of E and α_T on temperature for each material in the model. This information is given in Table 5.1 for each of the three materials used in the model, where each entry in the table gives the order of the polynomial representing the temperature-dependence of the material preoperty. Recall that the stiffness and thermal expansion of the insulation layer are neglected in the structural model.

Based on the information given in Table 5.1, the entries of $K_S(T)$ can depend on at most the second power of c_j, and the entries of $K_G(T)$ can depend on at most the sixth power of c_j. Because the regression model used for the kriging function is quadratic, one would expect the generalized stiffness matrix to be well approximated by the kriging model if the generalized stiffness was at most a quadratic function of the POD modal coordinates.

Thus, one potential reason that the kriging representation of the generalized stiffness matrix is of such high accuracy is that $K_S(T)$ is dominant over $K_G(T)$, and that $K_S^*(T)$ is essentially quadratic in T with small perturbations due to geometric stiffening. To examine this hypothesis, the relative magnitudes of $K_S(T)$ and $K_G(T)$ are assessed as a function of temperature. The temperature is varied by holding all modal coordinates constant except for the first, and increasing c_1 linearly. For each increment of c_1, the Frobenius norms of both $K_S(T)$ and $K_G(T)$ are computed in order quantify the relative magnitude of each. Plots of the Frobenius norms of $K_S(T)$ and $K_G(T)$ as a function of c_1 are given in Fig. 5.4(a) and Fig. 5.4(b), respectively. Comparing the two plots, $K_S(T)$ is approximately three orders of magnitude larger than $K_G(T)$ based on the chosen norm. This indicates that the generalized stiffness matrix is essentially quadratic in the POD modal coordinates with small perturbations due to geometric stiffening. Because the regression model used for the kriging ROM of the generalized stiffness matrix is also quadratic, the errors associated with the generalized stiffness matrix ROM are low.

Though the average NRMSE of the generalized thermal load vector remains below 10% as shown in Fig. 5.3(a), higher accuracy for the thermal loads is still desired. One potential means for improving the representation of the thermal loads is to perform the kriging interpolation on the physical thermal load vector, F_S^H, as opposed to the generalized thermal load vector, f_S^H. Because the number of entries in the physical thermal load vector is at a feasible level (8,074), memory and computational cost issues will not come into play as they would in the case of the physical stiffness matrix. To investigate the ability of kriging to capture the entries of the physical thermal load vector, the same error analysis as used for the generalized thermal load vector is repeated on the physical one. The "correlation" criterion with a maximum of 500 iterations is again used to generate the sample points for the training data. Plots of the average NRMSE and L_∞ error over the evaluation cases are given in Fig. 5.5(a) and Fig. 5.5(b), respectively.

Comparing Fig. 5.5 to Fig. 5.3, it is observed that greater accuracy can be obtained

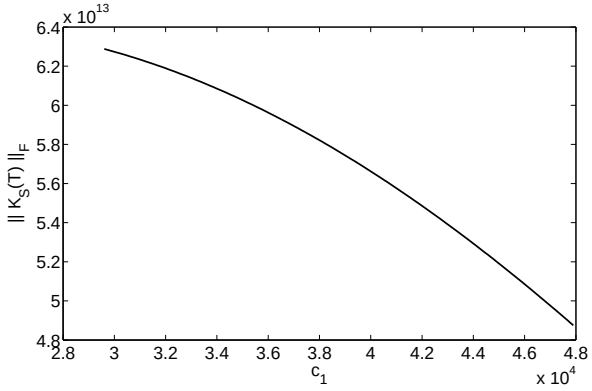

(a) Norm of $K_S(T)$.

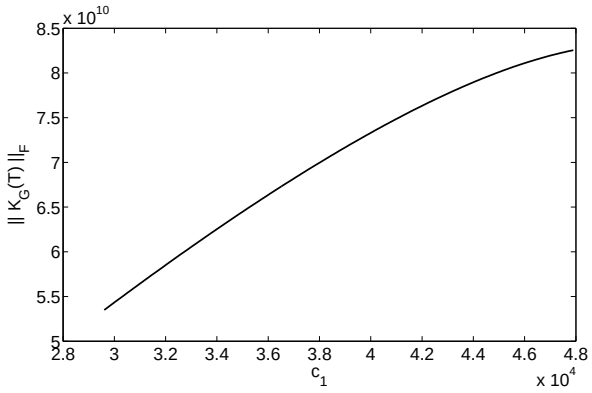

(b) Norm of $K_G(T)$.

Figure 5.4: Frobenius norms of the conventional and geometric stiffness matrices as a function of the first POD modal coordinate.

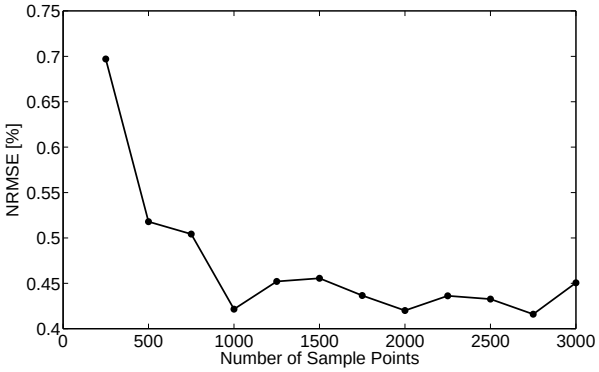

(a) Average NRMSE.

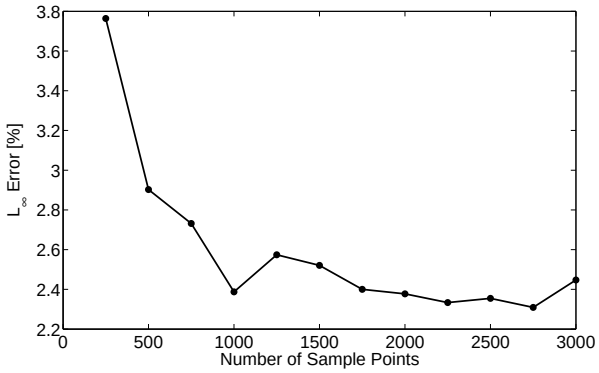

(b) Average L_∞ Error.

Figure 5.5: Average errors for physical thermal load vector ROM over 500 evaluation cases.

by performing the kriging interpolation on the physical thermal load vector instead of the generalized thermal load vector. To understand why this is the case, first consider the dependence of the entries of the physical load vector on temperature. The physical thermal load vector is proportional to the Young's Modulus, coefficient of thermal expansion, and change in temperature, i.e.

$$F_{S,i}^{H} \propto E(T_i), \alpha_T(T_i), \Delta T_i, \text{ where } T_i = \sum_{j=1}^{r} c_j \varphi_i^{(j)}. \tag{5.21}$$

Based on the information presented in Table 5.1, this means that the physical thermal load vector depends on the second power of c for skin and stiffener elements and the sixth power of c for heat shield elements. In order to compute the generalized thermal load vector, inner products between the structural modes and the physical thermal load vector are required. The i-th entry of the generalized thermal load vector is given by

$$f_{S,i}^{H} = \sum_{l=1}^{s} \phi_l^{(i)} F_{S,l}^{H}, \tag{5.22}$$

where $\phi_l^{(i)}$ denotes the l-th entry of the i-th structural reference mode and s is the total number of degrees of freedom in the structural model (8,074 in this case). Whereas the physical thermal load vector depends on the second power of c for skin and stiffener elements and the sixth power of c for heat shield elements, the generalized thermal load vector depends on the sixth power of c for all elements because it is summed over all entries of F_S^H. Therefore, the generalized thermal load vector is a more complex function of the POD modal coordinates than the physical one. The only caveat associated with using kriging to generate the physical load vector is that the physical thermal load vector must be pre-multiplied by the structural reference modes each time it is updated in order to transform to modal space. However, the computation time involved in transforming the loads from physical space to modal space is expected to be minimal. Thus, the physical thermal load vector and not the generalized thermal load vector will be approximated with kriging in

throughout the rest of this work.

Though the accuracy of the generalized stiffness matrix and physical thermal load vector ROMs appear sufficient based on the NRMSE and L_∞ plots given in Fig. 5.2 and Fig. 5.5, recall that these results are obtained by averaging the error metrics over 500 evaluation cases. As one of the objectives of this study is to bound the error of the kriging ROMs, it is necessary to investigate the worst-case error over the parameter space. As such, the maximum L_∞ error over the 500 evaluation cases is plotted for both the generalized stiffness matrix ROM and the physical thermal load vector ROM as a function of number of sample points. This metric gives the worst-case error over all degrees of freedom over all evaluation cases. Results are given in Fig. 5.6(a) and Fig. 5.6(b). Comparing the two figures, the worst-case error of the physical thermal load vector ROM is several orders of magnitude higher than that of the generalized stiffness matrix ROM. As it is desirable to reduce the worst-case error of the physical thermal load vector ROM, further investigation into the source of the higher errors is warranted. To give an indication of the spatial variation of the error, a new error metric, denoted by ϵ, is introduced. This error metric corresponds to the percentage error for each degree of freedom and given by

$$\epsilon_i = \frac{|\text{ROM}_i - \text{Full}_i|}{\text{Full}_i} \times 100\%, \tag{5.23}$$

where i denotes the i-th degree of freedom. In order to determine the sources of error for the physical thermal load vector ROM, it is necessary to determine which degrees of freedom generally show the largest discrepancy between thermal loads calculated by the full-order model and those predicted by the kriging model. To accomplish this, the degree of freedom number at which the maximum value of ϵ occurs for the physical thermal load vector ROM is recorded for each evaluation case. The number of times that the maximum percentage error occurs at each degree of freedom is then summed and plotted as a function of degree of freedom in Fig. 5.7 for the physical thermal load vector ROM generated using 3,000 sample

points. Note that the skin and stiffener elements correspond to degrees of freedom 1–2752, and the heat shield elements correspond to degrees of freedom 2753–8,074. Examining Fig. 5.7, in can be observed that the maximum percentage error generally occurs at those degrees of freedom corresponding to the heat shield. This is expected as the thermal loads for the heat shield are a higher order function of temperature than the thermal loads for the skin and stiffeners.

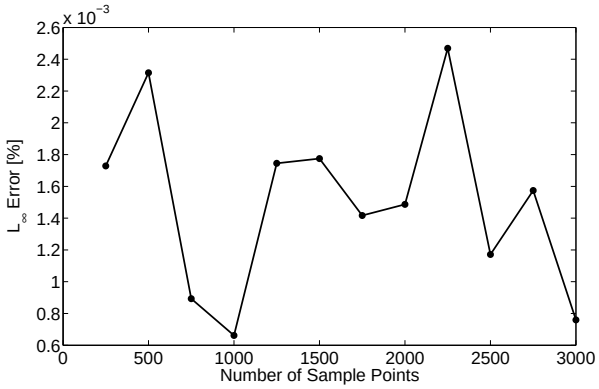

(a) Generalized stiffness matrix ROM.

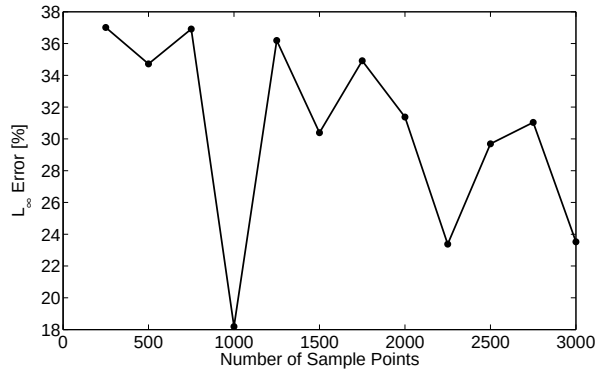

(b) Physical thermal load vector ROM.

Figure 5.6: Maximum L_∞ errors over 500 evaluation cases for kriging ROMs of $k_S^*(T)$ and $F_S^H(T)$ using 2nd order regression model.

Due to the higher order dependence of the heat shield thermal loads on temperature, it is expected that the use of a higher order regression model will improve the accuracy of the representation of the thermal loads. To examine this hypothesis, a third-order regression model is implemented for comparison against the results obtained using the second-order

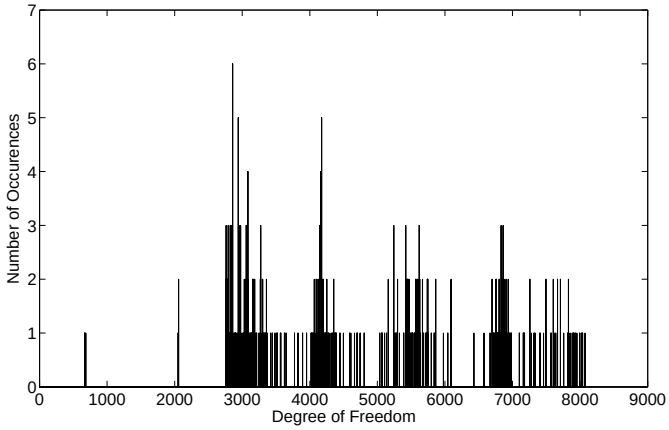

Figure 5.7: Number of occurrences of maximum percentage error at each degree of freedom for physical thermal load vector ROM generated using 3,000 sample points.

regression model. The maximum L_∞ error of the physical thermal load vector ROM over 500 evaluation cases is plotted as a function of number of sample points for both the second-order and third-order regression models as shown in Fig. 5.8. The figure shows significant improvement in capturing the thermal loads by moving from a second-order regression function to a third-order regression function. It is observed that for the third-order regression function, all data points remain at or below 5% maximum L_∞ error over the evaluation cases.

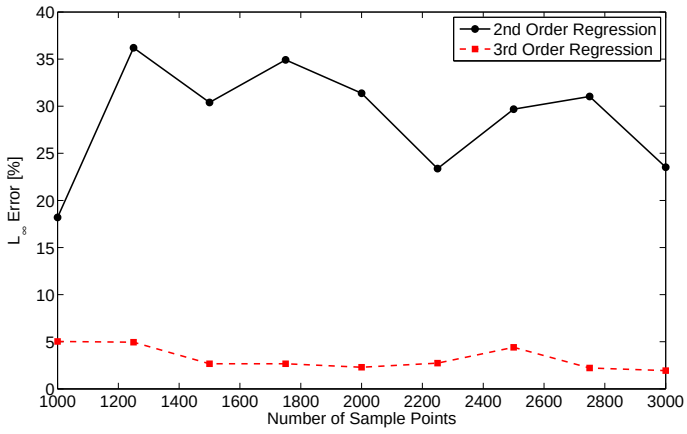

Figure 5.8: Maximum L_∞ error over 500 evaluation cases for kriging ROMs of $F_S^H(T)$ using both 2nd and 3rd order regression models.

Note that the minimum number of sample points used in Fig. 5.8 is 1,000. This is due

to the fact that there is a minimum bound on the number of sample points used to create the kriging ROM based on the number of basis functions, n_b, required by the regression model. In order to ensure that the problem is not under-constrained, the number of sample points used in creating the kriging ROM, must be equal to or greater than the number of basis functions in the regression model, i.e. $n_k \geq n_b$. Therefore, the order of the regression model must not be chosen to be arbitrarily high as there is a trade-off between the order of regression and the minimum number of required sample points. The number of basis terms, and thus the minimum number of required sample points, is given by

$$n_b = \frac{\prod_{i=1}^{\mathcal{O}} (n_{dv} + i)}{\mathcal{O}!}, \tag{5.24}$$

where $\mathcal{O}$ is the order of the regression model. For the current case in which 15 design variables are considered, n_b is 120 for a second-order regression model, 816 for a third-order regression model, and 3,876 for a fourth-order regression model. Thus, care must be taken when selecting the order of regression and number of design variables to consider as there exists an important trade-off between the accuracy of the kriging ROM, the computational expense required to create the kriging ROM, and the number of design variables included.

5.1.3.1 Methodology for Bounding POD Modal Coordinates

For the kriging results presented thus far, the bounds on the POD modal coordinates were established based on the maximum and minimum values of each for a single full-order aerothermoelastic simulation under one specific set of flight conditions. If the POD modal coordinates remain within these bounds throughout the simulations in which the kriging ROMs are used, the discussion of kriging error presented above is valid. However, there is no guarantee of accuracy if the POD modal coordinates go outside of the bounds which were used in generating the training data. As such, a robust and efficient method for bounding the POD modal coordinates is developed. An overview of the proposed method-

ology is given in Fig. 5.9.

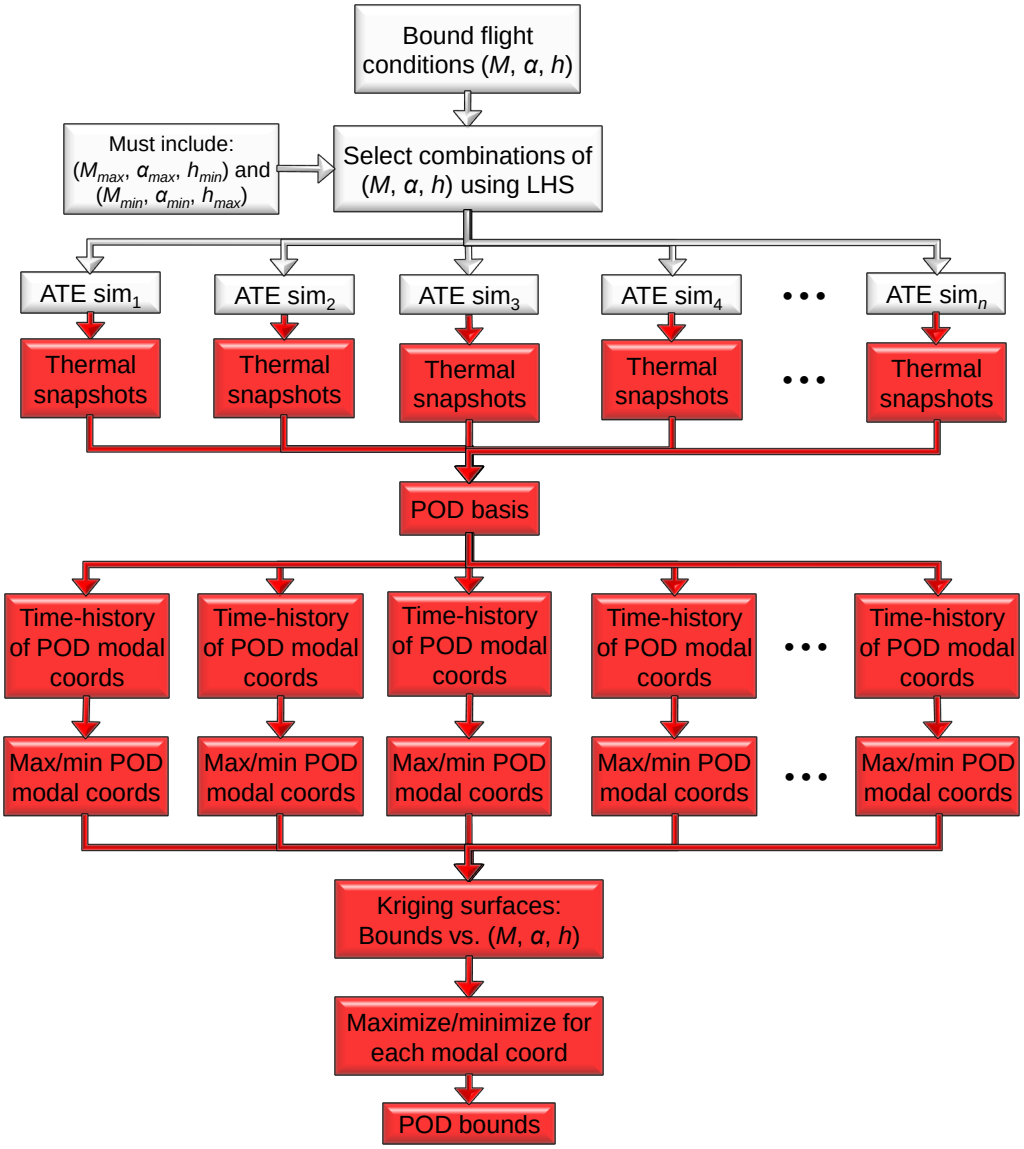

Figure 5.9: Proposed methodology for generating thermal snapshots and bounding POD modal coordinates.

The process begins by identifying the range of flight conditions for which the kriging ROMs are to be valid for. The flight conditions of interest are the Mach number, angle of attack, and altitude. Using the bounds on the flight conditions, the LHS procedure is used to generate n flight condition sets. One of the sample points must correspond to the highest dynamic pressure case (maximum Mach number, maximum angle of attack,

and minimum altitude), and another sample point must correspond to the lowest dynamic pressure case (minimum Mach number, minimum angle of attack, and maximum altitude). For each set of flight conditions, a full-order aerothermoelastic simulation is carried out and thermal snapshots are taken. Note that these simulations are performed in parallel such that the time to generate all of the thermal snapshots is the computation time for a single full-order simulation. Once the thermal snapshots are obtained from all of the full-order aerothermoelastic simulations, they are combined into a single snapshot matrix and the POD basis is generated. The POD basis is then used along with the snapshots to calculate what the time-history of the POD modal coordinates would have been had the thermal ROM been used for each set of flight conditions. For each case, the maximum and minimum values of each POD modal coordinate are identified, and this information is used to create a kriging surface that gives the bounds on each of the POD modal coordinates as a function of the Mach number, angle of attack, and altitude. This kriging surface is then used as a surrogate model for the purpose of finding the maximum possible upper bound and minimum possible lower bound for each POD modal coordinate at any location within the parameter space of the flight conditions. Once the POD bounds are established, they are used in the generation of sample points for the kriging ROMs of the stiffness matrix and thermal load vector. This framework serves two important purposes. In addition to providing robust bounds on the POD modal coordinates, the framework also leads to the generation of a rich set of thermal snapshots, thus leading to an accurate thermal POD model.

One challenge involved in bounding the POD modal coordinates is associated with their initial conditions. If the reduced-order thermal equations were solved directly for the POD modal coordinates, it is likely that the bounds will be exceeded for simulations whose initial conditions vary from those at which the bounds were generated. It is therefore desirable to generate bounds that are independent of the initial conditions. Thus, the effect of the initial conditions must be removed when bounding the POD modal coordinates. The

formulation for accomplishing this is described in Chapter II. In addition to making the bounds independent of the initial conditions, this transformation provides another benefit in terms of improving the accuracy of the thermal ROM. If the initial conditions were not made to be homogeneous, the initial value of each POD modal coordinate would be found by projecting $T^{(0)}$ in the direction of the corresponding POD basis vector, i.e.,

$$c_i(0) = \left\langle \varphi^{(i)}, T^{(0)} \right\rangle, \tag{5.25}$$

where $\langle \cdot \rangle$ denotes an inner product. Because the POD basis does not form a complete space for the physical temperatures, the initial temperature distribution cannot be represented exactly in this formulation. However, by transforming the equations to enforce homogeneous initial conditions, $c(0)$ is forced to become a vector of zeros and $T(t)$ can be represented exactly after the vector of initial conditions is added back to the solution. For the current framework in which the reduced-order thermal system is integrated numerically and the solution at each time step depends on that at the previous time step, the ability to represent the initial conditions exactly is important.

In order to account for the transformation that eliminates the effect of initial temperatures in the kriging representation of the stiffness matrix and thermal loads, additional design variables corresponding to $T^{(0)}$ must be included in the kriging functions. This is necessary because the design variables passed to the kriging functions must be capable of reproducing the physical temperature distribution including the effect of the initial condition. In this work the initial temperature distribution is assumed to always be uniform such that the physical temperature distribution can be expressed as

$$T(t) = \left[\sum_{i=1}^{r} c_i(t) \varphi^{(i)} \right] + \mathcal{T}^{(0)} \{\mathbf{1}\}, \tag{5.26}$$

where $\mathcal{T}^{(0)}$ is the scalar value of the uniform initial temperature and $\{\mathbf{1}\}$ is a vector of ones of length s. Thus, the design variables for the kriging ROMS are the POD modal coordi-

nates, c_i, and the scalar value of the initial temperature, $\mathcal{T}^{(0)}$. Because the initial condition is taken to be uniform here, only one additional design variable is required to represent the initial condition. Arbitrary spatial variation of the initial conditions can be permitted by replacing $\mathcal{T}^{(0)}\{\mathbf{1}\}$ in the right-hand side of Eq. (5.26) with a linear combination of multiple basis vectors. Note that this would require a larger number of design variables to represent the initial conditions.

The framework of Fig. 5.9 is implemented for the ranges in flight conditions shown in Table 5.2. Ten sets of flight conditions are identified using LHS. As before, two different sets of time step sizes are used in the aerothermoelastic simulations. For the period 0 – 150 s, the time step sizes are: $\Delta t_{HT} = \Delta t_{AE} = 0.1$ s, and $\Delta t_{AT} = 1$ s. For the period from 150 s – 3,600 s, the time step sizes are: $\Delta t_{HT} = \Delta t_{AE} = 1$ s, and $\Delta t_{AT} = 5$ s. One thermal snapshot is taken at each heat transfer time step. This results in total of 4,951 snapshots for each of the ten full-order aerothermoelastic simulations, and thus a total of 49,510 snapshots are used in the generation of the POD basis.

Table 5.2: Bounds on flight conditions for kriging ROM generation.

5.0	$\leq M_\infty \leq$	8.0
0.0°	$\leq \alpha \leq$	4.0°
25.0 km	$\leq h \leq$	45.0 km
293 K	$\leq \mathcal{T}^{(0)} \leq$	1500 K

Using the 49,510 snapshots obtained from the ten full-order aerothermoelastic simulations, the POD basis is generated. The eigenvalues associated with the first 50 POD modes are given in Fig. 5.10. The criterion used in the basis truncation process is to retain all POD vectors whose corresponding eigenvalue is greater than or equal to one. Thus, 32 POD vectors are retained after basis truncation in this case. Though the thermal ROM is not the focus of the current section, its accuracy is assessed for one set of flight conditions. The flight conditions used for verifying the accuracy of the POD basis are as follows: $M_\infty = 6.5$, $\alpha = 2°$, and $h = 35$ km. The time steps for this case are: $\Delta t_{AE} = \Delta t_{HT}$ = 0.1 s, and Δt_{AT} = 1 s. The NRMSE and L_∞ error of the thermal ROM are calculated with

respect to the full-order thermal model at each heat transfer time step using Eqs. (5.15) and (5.16). In the case of the thermal ROM, the vectors "Full" and "ROM" correspond to the temperatures vectors from the full-order and reduced-order thermal models at a given time step. To eliminate any additional errors, the full-order structural model is used for both cases. Time-histories of the NRMSE and L_∞ error for a simulation time of 1,200 s are given in Fig. 5.11(a) and Fig. 5.11(b), respectively. Examining these figures, the thermal ROM shows good agreement with the full-order thermal model.

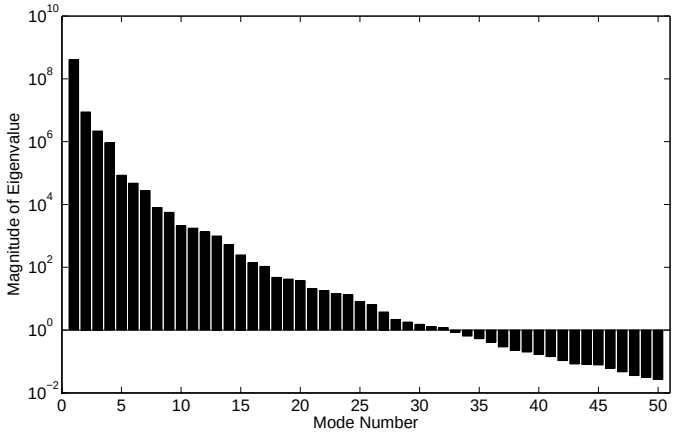

Figure 5.10: Eigenvalues associated with first 50 thermal POD modes based on 49,510 thermal snapshots.

The next step is to obtain the upper and lower bounds for each of the 32 POD modal coordinates using the procedure described above. The maximization/minimization procedures are performed using the function `fmincon` available within Matlab®. Note that the minimization/maximization steps are repeated at different starting locations within the parameter space in order to avoid the potential for obtaining local extrema. Plots of the upper and lower bounds for each of the 32 POD modal coordinates are given in Fig. 5.12(a) and Fig. 5.12(b), respectively.

In order to verify that the bounds identified in Fig. 5.12 are indeed the maximum upper bounds and minimum lower bounds over the range of flight conditions given in Table 5.2, an additional set of ten aerothermoelastic simulations is run. The Mach number, angle of attack, and altitude for these simulations are selected by using the LHS methodology along

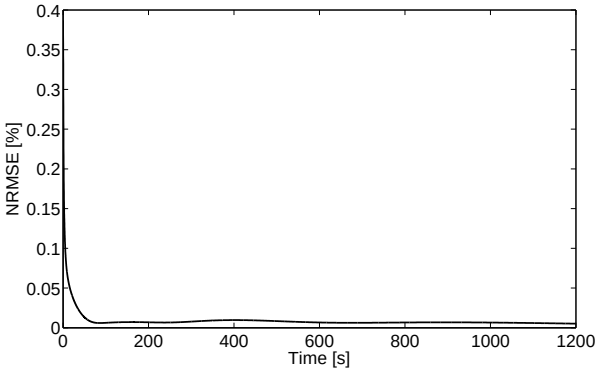

(a) NRMSE.

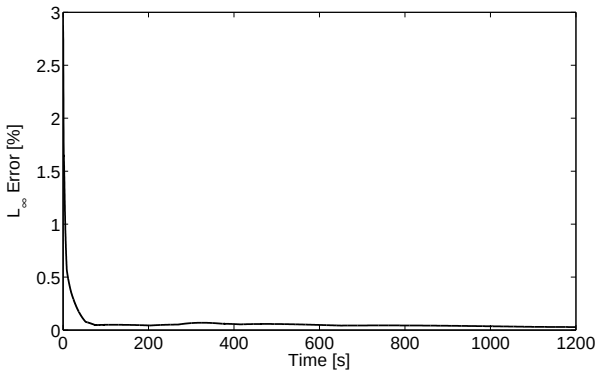

(b) L_∞ error.

Figure 5.11: NRMSE and L_∞ error of thermal POD ROM at $M_\infty = 6.5$, $\alpha = 2^\circ$, and $h = 35$ km.

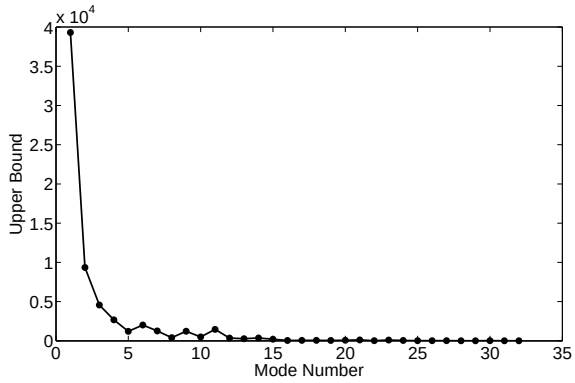

(a) Upper bounds.

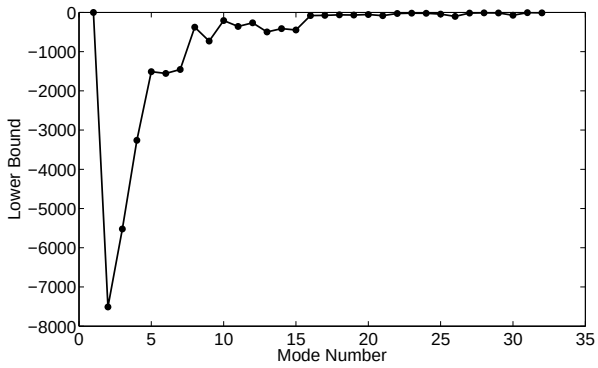

(b) Lower bounds.

Figure 5.12: Upper and lower bounds of POD modal coordinates for 32 retained POD basis vectors.

with the criterion to maximize the minimum Euclidean distance between the flight conditions of the ten new simulations and the ten simulations that were used in establishing the bounds originally. The additional ten simulations make use of the thermal ROM that consists of the 32 retained POD modes, however, the full-order structural model is used to calculate the structural dynamic response. The time step sizes for the additional simulations are the same as those that were used in the original ten aerothermoelastic simulations. At each heat transfer time step, the vector of POD modal coordinates is stored. The maximum and minimum value of each POD modal coordinate over all time steps over all of the ten simulations is then found. The bounds identified using the procedure shown in Fig. 5.9 are compared with the minimum/maximum values identified via the ten additional aerothermoelastic simulations by computing margins of safety. The margin of safety for the upper bounds, MS_U, and margin of safety for the lower bounds, MS_L, are found using

$$\text{MS}_{U,i} = \frac{\text{ub}_i - \text{max}_i}{|\text{max}_i|} \times 100\% \tag{5.27a}$$

$$\text{MS}_{L,i} = -\frac{\text{lb}_i - \text{min}_i}{|\text{min}_i|} \times 100\%, \tag{5.27b}$$

where ub_i and lb_i are the upper and lower bounds for the i-th POD modal coordinate, and max_i and min_i are the maximum and minimum values of the i-th modal coordinate identified from the ten additional aerothermoelastic simulations. In order for the upper and lower bounds to encompass the ranges of the POD modal coordinates experienced in the simulations, all elements of both MS_U and MS_L must be greater than or equal to zero. Plots of MS_U and MS_L are given in Fig. 5.13(a) and Fig. 5.13(b), respectively. In both figures, all values of MS are greater than or equal zero, and thus the bounds are valid. Note that the data point corresponding to mode 1 in Fig. 5.13(b) is not shown because both min_1 and lb_1 are zero.

Due to the prohibitive computational expense, it is not feasible to use all 32 POD modal coordinates as design variables in the kriging representations of the stiffness matrix and

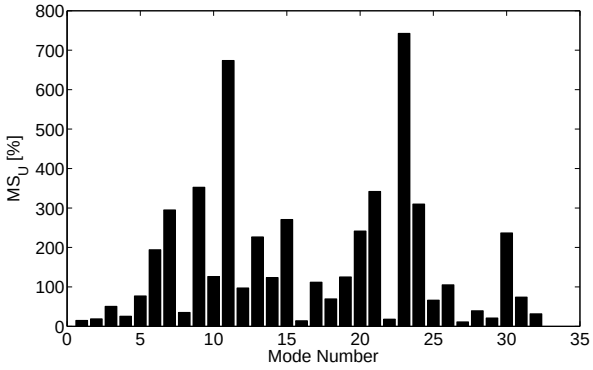

(a) Margins of safety on upper bounds.

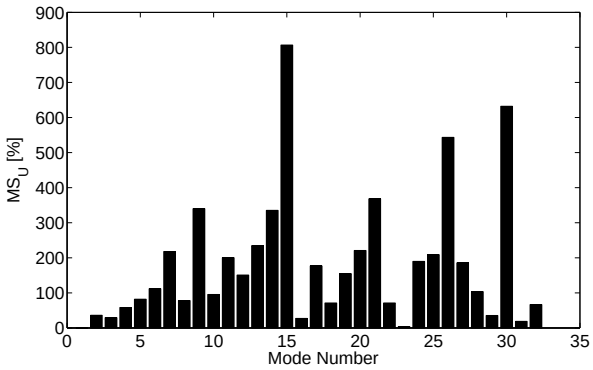

(b) Margins of safety on lower bounds.

Figure 5.13: Margins of safety on upper and lower bounds based on ten additional aerothermoelastic simulations.

thermal load vector. While all 32 POD modes will be used in the solution of the reduced thermal system, only a subset of the resulting POD modal coordinates will be passed to the kriging functions at each aeroelastic time step. Though some accuracy will be lost in representing the physical temperatures using less than 32 POD modes, the penalty is not expected to be significant due to the fact that the POD modes are sorted in order of decreasing energy and the modes that are excluded from the kriging models are chosen to be the lowest energy modes.

The number of number of design variables, number of sample points, and order of regression must be selected for both the kriging model of the thermal loads and the kriging model of the generalized stiffness. In selecting these parameters, consideration must be given to a variety of factors. The number of sample points used to generate the kriging ROMs must be sufficient to provide enough training information to achieve the desired level of accuracy. Additionally, if too few design variables are used, the temperature distribution passed to the kriging model may not be representative of the actual temperature distribution. Finally, the computation time required to generate the kriging ROMs must be balanced against the desired accuracy, number of sample points, and number of design variables required to obtain this accuracy for a given regression model. Because the computation time increases quickly with number of sample points, number of design variables, and order of regression, the trade-off between desired accuracy and computation time must be taken into account. Though the kriging models are generated *a priori* and off-line, the computation time required to generate them must still be on a reasonable order.

A summary of the parameters selected for the two kriging models as well as the errors over 500 evaluation cases are given in Table 5.3. Though the two ROMs use a different number of sample points to generate the models, both use 500 evaluation points for determining the accuracy of the ROMs. For the kriging model of the generalized stiffness, 20 design variables, 500 sample points and a 2nd order regression model are used. For the resulting kriging model of $k_S^*(T)$ based on the ten free vibration modes employed above,

the average NRMSE and maximum L_∞ error over 500 evaluation points are found to be 0.05% and 1.3%, respectively. For the kriging model of the thermal loads, 20 design variables, 5,000 sample points and a 3rd order regression model are used. For the resulting kriging model of $F_S^H(T)$, the average NRMSE and maximum L_∞ error over 500 evaluation points are found to be 0.1% and 4.7%, respectively. As both kriging models use 20 design variables, the first 19 design variables are the POD modal coordinates of the corresponding POD modes, and the 20th design variable represents the uniform initial condition as described previously.

Table 5.3: Parameters and errors associated with kriging ROMs of $k_S^*(T)$ and $F_S^H(T)$.

Model	n_{dv}	n_k	$\mathcal{O}$	Avg NRMSE [%]	Max L_∞ [%]
$k_S^*(T)$	20	500	2nd Order	0.051	1.33
$F_S^H(T)$	20	5,000	3rd Order	0.12	4.68

The computational times associated with generation of the kriging ROMs are given in Table 5.4. The last three columns in this table give the CPU times required to generate the kriging training data, t_T, create the kriging ROMs, t_K, and evaluate the kriging ROMs, t_E. Note that t_E is greater for the kriging model of $k_S^*(T)$ than for that of $F_S^H(T)$ due to the longer computation required to compute $k_S^*(T)$ at each evaluation point. The main observation to be made from Table 5.4 is that the computational time required to create the kriging ROM of $F_S^H(T)$ is significantly greater than that required to create the kriging ROM of $k_S^*(T)$. However, because kriging is used to represent the physical thermal load vector as opposed to the generalized one, this model is independent of the structural basis and does not need to be updated if the structural basis changes. Therefore, this kriging model of the thermal loads is used for the remainder of this study. Note that the generalized stiffness matrix is dependent on the structural basis, and therefore this kriging ROM must be updated each time the basis is changed. However, because less sample points and a lower order regression model are required, the computational cost of generating the kriging ROM of the generalized stiffness matrix is less than that required to generate the kriging

ROM of the thermal load vector.

Table 5.4: Computational cost associated with kriging ROMs of $k_S^*(T)$ and $F_S^H(T)$.

Model	t_T [hrs][a]	t_K [hrs][a]	t_E [hrs][a]
$k_S^*(T)$	0.81	0.051	0.78
$F_S^H(T)$	5.61	71	0.55

[a] 1 2.53-GHz Intel Xeon E5540 processor, 3.0 GB RAM.

As the motivation for the use of the kriging ROMs is to improve the computational cost of the structural dynamic solution, the computational savings achieved via the use of these ROMs must be quantified. To do so, the full-order and reduced-order structural solutions are each run for 10 time steps. The full-order solution consists of calling Nastran to generate the equations of motion in physical space and marching the solution forward one time step. The reduced-order solution consists of using the kriging ROMs to generate the equations of motion in modal space and marching the solution forward one time step. For both the full-order and reduced-order solutions, the computation time is recorded for each of the ten time steps. The maximum and minimum computation times are removed for each case, and the the remaining eight values are averaged to determine the average computation time for the reduced-order and full-order models. The average computation time for the full-order structural model was found to be 7.22 s while that for the reduced-order structural model was found to be 1.42 s, resulting in an improvement in computational cost by a factor of 5. Note that in both the full-order and reduced-order cases, the simulations were performed using one 2.53-GHz Intel Xeon E5540 processor with 3.0 GB RAM.

5.2 Techniques for Enhanced Modal Solutions

Recall that the generalized quantities in section 5.1.3 were calculated based on the first ten structural free vibration modes. Because the focus of that section was on the accuracy

of the kriging ROMs, the ability of the chosen structural modes to represent the structural dynamic response within an aerothermoelastic environment was not examined. Use of free vibration modes alone within a mode-displacement approach may not always be sufficient to capture the structural dynamic response under the aerodynamic and thermal loads experienced in hypersonic flight. Thus, the goal of the current section is to examine techniques for improving the modal representation of the structural dynamic response while still maintaining the low-order nature of the solution. Because both the thermal and structural ROMs consist of modal solutions, the techniques discussed are applicable to both. However, in this section, the techniques are applied only to the structural dynamic model. The following sections discuss a technique for obtaining robust and accurate modal solutions for the structural dynamic response of hypersonic vehicle structures.

5.2.1 Load-Dependent Ritz Vector Formulation

The technique used in this dissertation to improve the accuracy of the structural ROM involves augmentation of the original basis with additional Ritz vectors. The methodology is intentionally general so that it can be applied to both the structural dynamic and thermal response problems, but it is employed specifically for the structural dynamic response problem here. In this approach, the original structural basis containing the reference free vibration modes is augmented by inserting additional columns into the modal matrix, i.e.,

$$\Phi_S = \left[\begin{array}{cccc|ccc} \phi_1^{(1)} & \phi_1^{(2)} & \cdots & \phi_1^{(r)} & \psi_1^{(1)} & \cdots & \psi_1^{(l)} \\ \phi_2^{(1)} & \phi_2^{(2)} & \cdots & \phi_2^{(r)} & \psi_2^{(1)} & \cdots & \psi_2^{(l)} \\ \vdots & \vdots & \ddots & \vdots & \vdots & \ddots & \vdots \\ \phi_s^{(1)} & \phi_s^{(2)} & \cdots & \phi_s^{(r)} & \psi_s^{(1)} & \cdots & \psi_s^{(l)} \end{array}\right], \tag{5.28}$$

where $\psi^{(i)}$ represents the i-th augmented mode shape and l is the number of augmented modes. The specific technique used in this work to obtain the augmented mode shapes is the method of load-dependent Ritz vectors [85]. This approach is advantageous in that it

allows for the ability to capture quasi-static response due to slowly changing loads. Additionally, it provides the capability for capturing structural response that might otherwise not be contained within a particular eigenvector subspace. This is because even if the frequency of a particular eigenmode is contained in the frequency of the loading, if the spatial distribution of the loading is orthogonal to that of the eigenvector, that specific eigenvector will not contribute to the solution. Thus, load-dependent Ritz vectors provide a means for incorporating the spatial distribution of the loads into the modal representation of the structural dynamics. Load-dependent Ritz vectors can be used to augment the original basis, whether it is obtained from an eigenvalue solution in the case of the structural ROM, or from POD in the case of the thermal ROM.

A summary of the algorithm for computing the load-dependent Ritz vectors is given in Algorithm 5.2.1, where comments are denoted by the "#" symbol. The procedure begins by selecting a set of free vibration modes, ϕ. In this application the number of free vibration modes, r, is determined based on a cut-off frequency beyond which the corresponding mode shapes are not expected to contribute to the solution. The physical mass matrix, M_S, and modified stiffness matrix at a reference thermal state, K_S^*, are then obtained from the finite element model and K_S^* is decomposed into its LU factorization for efficient inversion. The first load-dependent Ritz vector, $\bar{\psi}^{(1)}$, is computed in step 4 by solving the static problem given by

$$K_S^* \bar{\psi}^{(1)} = F_S^I, \tag{5.29}$$

where F_S^I is a user-determined input. The quality of the load-dependent Ritz vectors is dependent on the degree to which F_S^I represents the loading that the structure will experience in the actual simulation. In order to make $\bar{\psi}^{(1)}$ orthogonal to the previously determined free vibration modes with respect to M_S, the modified Gram-Schmidt algorithm is invoked in step 5 which repeatedly removes from $\bar{\psi}^{(1)}$ its projection onto the previous modes according to

$$\bar{\psi}^{(1)} = \bar{\psi}^{(1)} - \phi^{(j)} \phi^{(j)T} M_S \bar{\psi}^{(1)}, \quad j = 1, \ldots, r. \tag{5.30}$$

In Eq. (5.30), each time $\bar{\psi}^{(1)}$ is updated it overwrites the previous version, thus reducing storage requirements. Note that the modified Gram-Schmidt algorithm is used in order to avoid the well-known numerical instabilities associated with the classical Gram-Schmidt algorithm. The orthogonalized solution vector $\bar{\psi}^{(1)}$ is then normalized with respect to the mass matrix to obtain $\psi^{(1)}$ using

$$\psi^{(1)} = \frac{\bar{\psi}^{(1)}}{\left(\bar{\psi}^{(1)T} M_S \bar{\psi}^{(1)}\right)^{1/2}}. \tag{5.31}$$

The static solution used to obtain $\psi^{(1)}$ neglected the inertial forces which are given by $M_S \ddot{\psi}^{(1)}$. Assuming harmonic motion in free vibration, the neglected inertial forces are of the form $\omega^2 M_S \psi^{(1)}$, where ω represents a typical frequency of the load. The vector of neglected inertial loads is then applied as a load vector in the generation of $\bar{\psi}^{(2)}$ at step 10. Again, a static solution is used to obtain $\bar{\psi}^{(2)}$, and $\psi^{(2)}$ is obtained by orthogonalizing in mass against all other modes and normalizing with respect to the mass matrix. Steps 10 – 17 are repeated until the desired number of load-dependent Ritz vectors are obtained. The procedure depicted in Algorithm 5.2.1 shows the steps taken when a single load vector, F_S^I, is specified. The algorithm can be generalized for the case in which multiple different load vectors are specified. In this case, steps 4 – 17 are repeated for each F_S^I and each time a new load-dependent Ritz vector, $\bar{\psi}$, is calculated, it is orthogonalized against all previous vectors with respect to M_S, and normalized with respect to M_S. This study will investigate the effect of number of specified load vectors, n_F, and number of load-dependent Ritz vectors per specified load vector, n_R, on solution accuracy. Note that n_R corresponds to the number of iterations performed in steps 8 – 17.

The main challenge associated with this approach is determining the representative load vectors, F_S^I, to use in step 4 of Algorithm 5.2.1. As the quality of the basis is dependent on the choice of F_S^I, it is important to choose these vectors so that they most closely represent the spatial distribution of loads that the structure will experience during flight. In order

Algorithm 5.2.1 Algorithm for generation of load-dependent Ritz vectors [85].

Select r free vibration modes, ϕ
Obtain M_S and K_S^*
$K_S^* = LU$ # Decompose K_S^* for efficient inversion
$K_S^* \bar{\psi}^{(1)} = F_S^I$ # Specify F_S^I and solve for $\bar{\psi}^{(1)}$
for $j = 1, \ldots, r$ **do** # Orthogonalize $\bar{\psi}^{(1)}$ against free vibration modes w.r.t. M_S
  $\bar{\psi}^{(1)} = \bar{\psi}^{(1)} - \phi^{(j)} \phi^{(j)T} M_s \bar{\psi}^{(1)}$ # Modified Gram-Schmidt algorithm
end for
$\psi^{(1)} = \frac{\bar{\psi}^{(1)}}{\left(\bar{\psi}^{(1)T} M_S \bar{\psi}^{(1)}\right)^{1/2}}$ # Normalize $\bar{\psi}^{(1)}$ w.r.t. M_S

for $i = 2, \ldots, l$ **do** # Loop to generate subsequent vectors
  $K_S^* \bar{\psi}^{(i)} = M_S \psi^{(i-1)}$ # Solve for $\bar{\psi}^{(i)}$ based on neglected inertia

  for $j = 1, \ldots, r$ **do** # Orthogonalize $\bar{\psi}^{(i)}$ against free vibration modes w.r.t. M_S
    $\bar{\psi}^{(i)} = \bar{\psi}^{(i)} - \phi^{(j)} \phi^{(j)T} M_s \bar{\psi}^{(i)}$ # Modified Gram-Schmidt algorithm
  end for
  for $j = 1, \ldots, i-1$ **do** # Orthogonalize $\bar{\psi}^{(i)}$ against Ritz modes w.r.t. M_S

    $\bar{\psi}^{(i)} = \bar{\psi}^{(i)} - \psi^{(j)} \psi^{(j)T} M_s \bar{\psi}^{(i)}$ # Modified Gram-Schmidt algorithm
  end for
  $\psi^{(i)} = \frac{\bar{\psi}^{(i)}}{\left(\bar{\psi}^{(i)T} M_S \bar{\psi}^{(i)}\right)^{1/2}}$ # Normalize $\bar{\psi}^{(i)}$ w.r.t. M_S
end for # Assemble modal matrix, Φ_S

to identify the dominant spatial components of the loads, a POD analysis is applied to the structural load vector, F_S, based on snapshots of F_S from high-fidelity aerothermoelastic simulations. As discussed in Chapter II, the POD is optimal in the sense that it arranges the modes such that the first mode contains the largest amount of energy, the second mode contains the second largest amount of energy, and so on. As a result of this optimality property of the proper orthogonal modes, POD can be used to identify the most dominant spatial components of the structural loads for use in the load-dependent Ritz vector procedure. The algorithm shown in Algorithm 5.2.1 will be repeated for a specified number of representative load vectors resulting in a set of load-dependent Ritz vectors to be appended to the set of free vibration modes.

As in the case of the POD procedure for the thermal ROM, snapshots of the structural load vector, F_S, must be collected to derive the corresponding POD basis vectors. These snapshots of the structural loads include contributions due to both thermal loads and aerodynamic loads, i.e.,

$$F_S(t) = F_S^H(t) + F_S^A(t). \tag{5.32}$$

The snapshots are taken by running an aerothermoelastic simulation for a period of 3,000 s. This simulation uses the thermal ROM with the 32 previously identified thermal POD modes. For the structural dynamic solution, the full-order model is used. The flight conditions for this simulation are: $M_\infty = 6.5$, $\alpha = 2^\circ$, $h = 35$ km, corresponding to the mid-points of the ranges given in Table 5.2. The initial temperature distribution is taken to be uniform 293 K. The time steps for the various solution components are as follows: $\Delta t_{AE} = \Delta t_{HT} = 0.1$ s, $\Delta t_{AT} = 1$ s. The structural load vector is stored at the end of each aerothermal time step resulting in a total of 3,000 snapshots. Once the snapshots are obtained, the snapshot matrix is assembled by storing each snapshot as a column in the snapshot matrix. The POD basis is then calculated by taking the singular value decomposition of the snapshot matrix. The eigenvalues corresponding to the first 50 POD modes are given Fig. 5.14. In the next section, the effect of the number of POD modes of F_S and

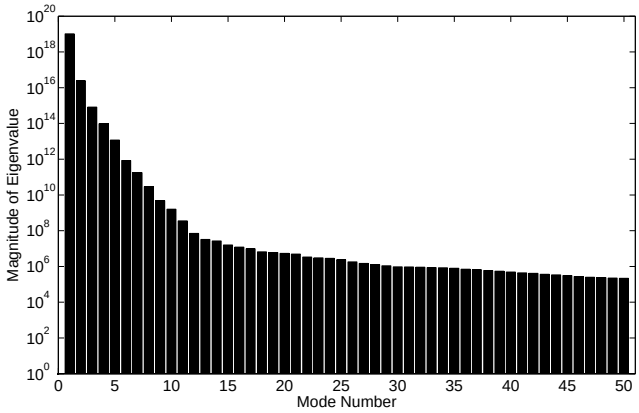

Figure 5.14: Eigenvalues associated with first 50 POD modes of F_S based on 3,000 snapshots.

number of load-dependent Ritz vectors per POD mode on solution accuracy are examined.

5.2.2 Load-Dependent Ritz Vector Results

To exercise the load-dependent Ritz vector formulation described above, aerothermoelastic simulations of the control surface model are carried out using both the full-order and reduced-order structural dynamic models. The full-order model is treated as the truth model and its solution is obtained by solving the equations of motion in physical space given by Eq. (4.1). For the full-order model, the equations of motion are generated directly using Nastran. Recall that the full-order and reduced-order models are both solved using the same Newmark-β integration scheme described in Chapter IV to eliminate discrepancies due to different numerical integration methods. The reduced-order model consists of the solving the modal equations of motion given in Eq. (4.11) where the structural modal matrix, Φ_S, can contain both reference free vibration modes and load-dependent Ritz vectors obtained using the formulation outlined in the previous section. The reduced-order model can update the equations of motion at each aeroelastic time step by calling Nastran directly or by using the kriging ROMs of the generalized stiffness matrix and physical thermal load vector obtained using the parameters n_{dv}, n_k, and $\mathcal{O}$ in Table 5.3. Both the full-order model

and reduced-order model make use of the thermal ROM with the 32-mode basis obtained in section 5.1.3.1. For the structural ROM, the basis consists of a pre-determined set of free vibration modes appended with a set of load-dependent Ritz vectors. For all studies in the current section, the number of free vibration modes, n_V, is taken to be six and the mode shapes are chosen to be the first six of the ten reference modes employed in section 5.1.3 based on a cut-off frequency of 100 Hz. This cut-off frequency is chosen based on the typical frequency range of interest for hypersonic vehicle dynamics and control considerations. The six-mode subset has a maximum frequency of 94.9 Hz. The goal of this section is to assess the effect of the number of specified load vectors, n_F, and number of load-dependent Ritz vectors per specified load vector, n_R, on the accuracy of the reduced-order structural dynamic model. Note that the total number of structural basis vectors is equal to $n_V + (n_F)(n_R)$.

To quantify the error between the full-order and reduced-order structural dynamic models, the NRMSE and L_∞ error metrics, given in Eqs. (5.15) and (5.16), are employed. In this case, the quantities "Full" and "ROM" are taken to be vectors of z-direction displacements for nodes at the OML from the full-order and reduced-order models, respectively. The parameters for the aerothermoelastic simulations used in this part of the study are given in Table 5.5. The total simulation time for this case is chosen to be 600 s.

Table 5.5: Parameters used for load-dependent Ritz vector case 1.

Case	M_∞	α	h [km]	Δt_{AE} [s]	Δt_{HT} [s]	Δt_{AT} [s]	$T^{(0)}$ [K]
1	8	4°	35	0.1	0.1	1	293

Before assessing the effect of load-dependent Ritz vectors, the impact of using kriging ROMs to generate $k_S^*(T)$ and $F_S^H(T)$ on the accuracy of the solution must first be addressed. Doing so provides insight into how much of the solution error can be attributed to error associated with the kriging ROMs as opposed to error associated with the reduced structural basis. To accomplish this, aerothermoelastic simulations are carried out for the

flight conditions of case 1 for three different subcases that are summarized in Table 5.6. For the subcase 1a, the full-order structural model is used in the simulation and the results are treated as the truth model. Subcase 1b consists of using the structural ROM with the only the six free vibration modes, (i.e., $n_V = 6$ $n_F = 0$, $n_R = 0$), and using Nastran to compute $k_S^*(T)$ and $F_S^H(T)$ at each aeroelastic time step. Subcase 1c consists of using the structural ROM again with the six free vibration modes, but employing the kriging ROMs to compute $k_S^*(T)$ and $F_S^H(T)$. It is expected that the 6-mode basis will not adequately capture the structural response represented by the full-order model. However, the goal of subcases 1a – 1c is not to assess the error associated with the reduced structural basis, but rather to evaluate the error incurred by employing the kriging models to approximate $k_S^*(T)$ and $F_S^H(T)$.

Table 5.6: Parameters for aerothermoelastic subcases used to assess error incurred due to kriging ROMs of $k_S^*(T)$ and $F_S^H(T)$.

Subcase	Structural Model	n_V	n_F	n_R	Computation of $k_S^*(T)$, $F_S^H(T)$
1a	Full-order	N/A	N/A	N/A	N/A
1b	ROM	6	0	0	Nastran
1c	ROM	6	0	0	Kriging ROMs

To assess the response levels, the z-direction displacements of node 247 (located at the mid-chord of the tip on the bottom surface) are plotted for each of the three subcases given in Table 5.6. Results are given in Fig. 5.15. To quantify the error incurred due solely to the kriging ROMs of $k_S^*(T)$ and $F_S^H(T)$, the NRMSE and L_∞ error metrics are computed for subcase 1c with respect to subcase 1b. Plots of the NRMSE and L_∞ over time are given in Fig. 5.16(a) and Fig. 5.16(b), respectively. The error metrics show an initial high error which is due to the fact that the simulation begins with the structure in the undeformed configuration. Therefore, the structural displacements are small in the initial part of the transient, which results in a small denominator in Eqs. (5.15) and (5.16), and therefore a large value of error early in the transient. However, within 10 seconds into the transient, the NRMSE and L_∞ error decrease to below 10% and 20%, respectively, and remain below

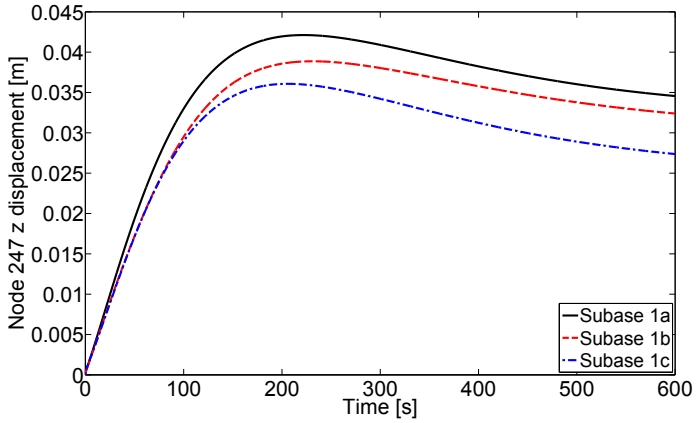

Figure 5.15: Node 247 z displacements for subcases 1a, 1b, and 1c.

these values for the remainder of the simulation.

With the error due to the kriging ROMs of $k_S^*(T)$ and $F_S^H(T)$ quantified, the next step is to assess the effect of inclusion of load-dependent Ritz vectors on the accuracy of the structural ROM. For all cases from this point forward, the kriging ROMs of $k_S^*(T)$ and $F_S^H(T)$ are used within the structural ROM. The goal of this aspect of the study is to assess the solution accuracy as a function of n_F and n_R. A summary of the subcases used to perform this assessment is given in Table 5.7. Note that the errors for these subcases are computed with respect to subcase 1a in Table 5.6 and therefore they include both error due to the kriging ROMs as well as error due to structural basis truncation.

Table 5.7: Parameters for aerothermoelastic subcases used to assess effect of load-dependent Ritz vectors on structural ROM.

Subcase	Structural Model	n_V	n_F	n_R	Computation of $k_S^*(T)$, $F_S^H(T)$
1c	ROM	6	0	0	Kriging ROMs
1d	ROM	6	1	1	Kriging ROMs
1e	ROM	6	10	1	Kriging ROMs
1f	ROM	6	1	10	Kriging ROMs

Plots of the NRMSE and L_∞ errors of subcases 1c - 1f with respect to subcase 1a are given in Fig. 5.17(a) and Fig. 5.17(b), respectively. Examining these figures, it is observed that the inclusion of load-dependent Ritz vectors in addition to the six free vibration modes

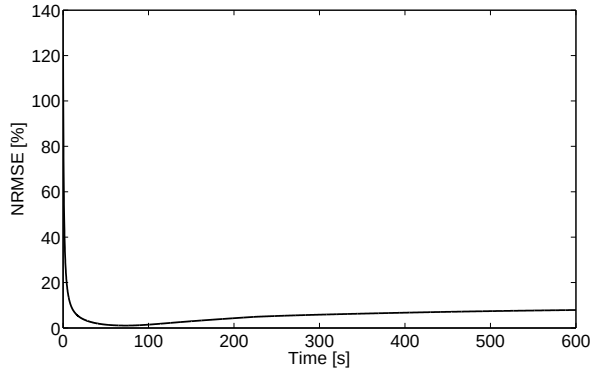

(a) NRMSE.

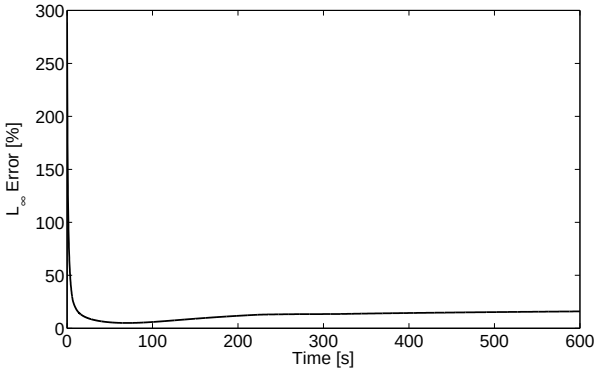

(b) L_∞ error.

Figure 5.16: Error of subcase 1c with respect to subcase 1b illustrating error incurred due kriging ROMs of $k_S^*(T)$ and $F_S^H(T)$.

results in a noticeable improvement in the structural ROM. It should be noted that there is inherent error in the structural ROM due to the use of the kriging ROMs to approximate $k_S^*(T)$ and $F_S^H(T)$, and thus the overall error of the structural ROM cannot be reduced to zero. Comparing Fig. 5.17 to Fig. 5.16, it can be observed that the error due to basis truncation has been reduced and the errors shown in Fig. 5.17 approach or surpass those shown in Fig. 5.16, especially for subcases 1e and 1f. Comparing subcase 1d to subcases 1e and 1f, it is observed that the inclusion of only one load-dependent Ritz vector in the basis does not provide the level of accuracy obtained by including multiple load-dependent Ritz vectors. The greatest difference in L_∞ error beyond 10 s between subcases 1e and 1f occurs at 78.1 s with the L_∞ error of subcase 1e being 11.2% lower than that of subcase 1f. This is not surprising as the structural response is dominated by the slowly changing thermal loads for this case, and therefore inertial effects are not significant. The maximum improvement in L_∞ error of subcase 1e with respect to subcase 1c beyond 10 s is 45% and occurs at 590.1 s. Subcase 1e gives an average improvement in L_∞ error of 38% over subcase 1c, demonstrating the advantage of using load-dependent Ritz vectors.

5.3 Concluding Remarks

The first part of this chapter focused on the development of a kriging-based method for directly updating the generalized stiffness matrix and thermal loads based on a given temperature distribution. The temperature distribution was parameterized in terms of the thermal POD modal coordinates as this allowed for a small number of design variables to be used to represent the high-dimensional temperature vector. A methodology was described for bounding the POD modal coordinates based on a set of parallel aerothermoelastic simulations. A series of studies was used to guide the selection of various parameters involved in the generation of the kriging ROMs. The resulting ROMs of the generalized stiffness matrix and physical thermal load vector were found to have maximum L_∞ errors of 1% and 5%, respectively, over 500 evaluation points, indicating good agreement with the full-

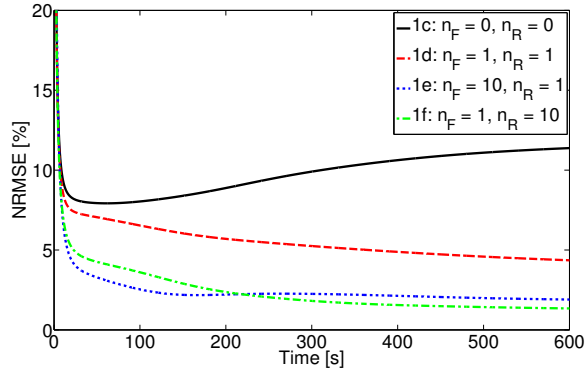

(a) NRMSE.

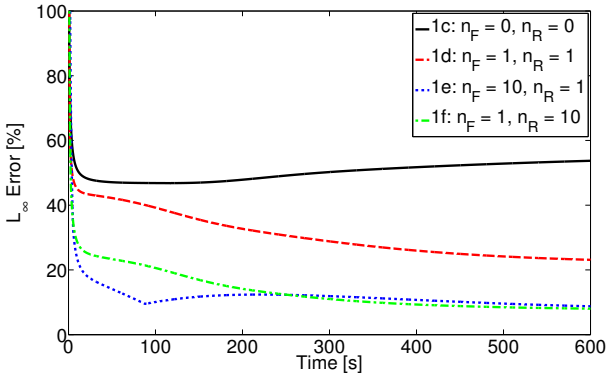

(b) L_∞ error.

Figure 5.17: Total error of structural ROMs (subcases 1c - 1f) with respect to full-order structural model (subcase 1a) using different structural bases.

order model. Comparison of computation times showed that the structural ROM with the kriging models improved the computational cost of the structural dynamic response solution by a factor of five with respect to the full-order model. The procedure for establishing bounds on the POD modal coordinates was found to be robust with a minimum margin of safety of 11.2% on the upper bounds and 3.5% on the lower bounds.

To improve the accuracy of the structural ROM, basis augmentation using load-dependent Ritz vectors was examined. Load-dependent Ritz vectors are advantageous in that they allow for incorporation of the expected spatial dependence of the structural loads into the modal matrix. In order to determine the representative load vectors to be used in generating the load-dependent Ritz vectors, proper orthogonal decomposition was employed based on snapshots of the structural load vector from representative simulations. Application of the methodology to a hypersonic cruise trajectory demonstrated an average improvement in L_∞ error of 38% for one case which employed ten load-dependent Ritz vectors and six free vibration modes compared with a case using only six free vibration modes. These results indicate that basis augmentation can be advantageous in cases where the structural dynamic response contains a quasi-static component.

Chapter VI

Reduced-Order Unsteady Aerothermoelastic Simulation Framework

Up this point, this dissertation has focused on the individual components of the reduced-order aerothermoelastic framework. The current chapter focuses on the methodology used to assemble these components into a time-domain aerothermoelastic framework for HSV simulation. It begins with a description of the mechanisms that lead to aerothermoelastic coupling in hypersonic flight. A summary of the reduced-order aerothermoelastic framework is then presented which highlights coupling between the aerodynamics, aerodynamic heating, heat transfer, and structural dynamics aspects of the problem. Next, the procedure used to generate the various ROMs of the aerothermoelastic framework is outlined. Once the ROMs are generated, it remains to march the various components of the aerothermoelastic solution in time. As such, a partitioned time-marching schedule is described which allows for different size time steps to be used for the various solution components in order to account for the disparities in time scales of the associated physics. Finally, an iterative routine is described for assessment of the control authority required to account for aerothermoelastic effects on the flight dynamics of a hypersonic vehicle.

6.1 Description of Aerothermoelastic Coupling Mechanisms

The overall goal of this dissertation is to develop a reduced-order aerothermoelastic modeling framework that can be used to for efficient vehicle design and control simulation. In order to realize such a framework, careful consideration of the coupling mechanisms between the various disciplines is essential. A flowchart illustrating the coupling of these disciplines is shown in Fig. 6.1.

Due to the high speed involved in hypersonic flight, stagnation effects and the turbulent boundary layer lead to the existence of an aerodynamic heat flux at the surface of the vehicle. To calculate the spatially and temporally varying heat flux, it is necessary to know the aerodynamic flow properties over the vehicle. Note the two-way coupling between the aerodynamic heat flux and the transient temperature distribution. The upward pointing arrow illustrates the fact that the aerodynamic heat flux represents a thermal boundary condition for the heat transfer problem. The downward pointing arrow indicates the fact that the heat flux is dependent on the wall temperature of the structure. Additionally, thermal radiation between the outer surface of the structure and the environment must be included. A two-way coupling also exists between the radiation and temperature distribution. Once the aerodynamic problem is solved and the heat flux and radiation flux are known, the boundary conditions for the heat transfer problem are generated.

The transient thermal problem is then solved, resulting in a spatially varying temperature distribution. The loads on the structure will have two components: thermal loads resulting from differential thermal expansion of the structure and aerodynamic pressure loads. Additionally, heating of the structure results in a changing stiffness distribution due to temperature-dependence of material properties such as Young's Modulus. The development of thermal stresses results in a further change in the stiffness due to geometric stiffening effects. As a result of these loads, the structure will displace relative to its undeformed configuration.

Deformation of the structure leads to a modified aerodynamic profile and the aero-

dynamic flow properties over the vehicle will change. The flow properties must then be recalculated as they will affect the loads on the structure, the aerodynamic heat flux, and the aerodynamic forces and moments on the vehicle. Once the updated aerodynamic flow parameters are known, the pressures can be integrated over the vehicle to calculate the resultant forces and moments on the vehicle. Based on the forces and moments, the vehicle equations of motion are propagated and necessary control inputs (i.e., control surface deflections) are determined based on the commanded trajectory and vehicle performance. The control surface deflections in turn change the aerodynamic flow parameters. Once the control inputs are determined, the process is repeated at the next time step. Because the control surfaces are expected to provide a significant contribution to the aerodynamic lift, drag, and moments acting on the vehicle, thorough analysis of the major couplings involved with such a structure is required in order to accurately predict vehicle performance.

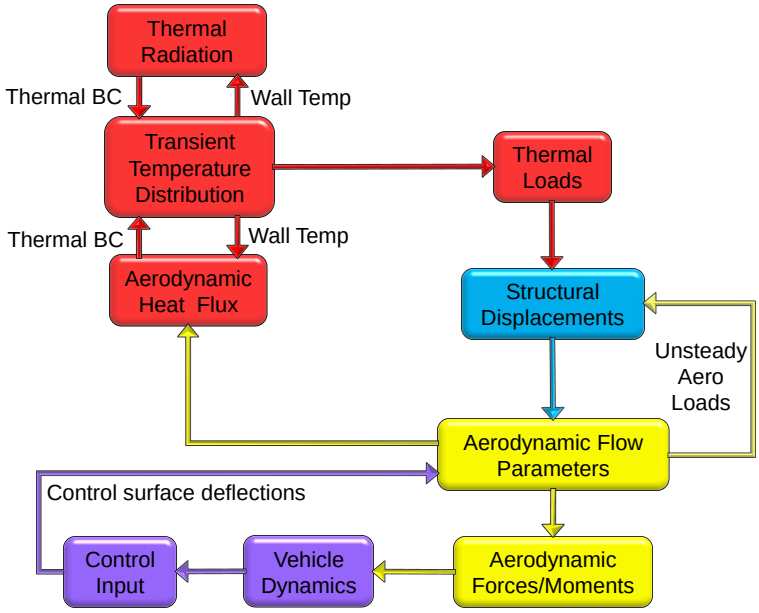

Figure 6.1: Coupling between aerodynamic heating, heat transfer, elastic airframe, aerodynamics, vehicle dynamics, and control.

6.2 Summary of Reduced-Order Aerothermoelastic Framework

A fully coupled aerothermoelastic framework, motivated by the aerothermoelastic coupling mechanisms described above, is developed in this work for HSV simulation. Note that because aerothermoelastic effects are expected to be most prominent for the HSV control surfaces, the methodology presented here is focused on such a structure. However, it is formulated in a general manner such that it is applicable to any arbitrary configuration. A flowchart of the aerothermoelastic framework developed in this dissertation is given in Fig. 6.2.

The process begins with the calculation of the heat flux boundary conditions (BC's) over the outer surface of the structure at initial time. As described in Appendix A, this is accomplished using either the Eckert reference temperature method or a CFD-based aerothermal ROM. With the boundary conditions and initial conditions of the thermal problem known, the transient temperature distribution is marched forward in time. Solution of the heat transfer problem is carried out in modal space using modes from POD to avoid the computational cost of running full-order finite element analysis. Bypassing of the full-order thermal solution via the reduced-order solution is indicated by "POD Reduction" block. The structural boundary conditions for the control surface are determined by its layout. Additionally, a subsequent chapter explores the effect of enforced motion boundary conditions due fuselage motion at the interface. This framework considers two coupling mechanisms between the thermal solution and the structural stiffness. The first involves the geometric stiffness effects due to thermal stresses that result from thermal expansion of the structure. The second is due to the temperature-dependence of the Young's modulus resulting from the high temperatures experienced in hypersonic flight. In addition to thermal effects on the geometric stiffness, the change in temperature also results in thermal loads being applied to the structure.

With the stiffness and structural loads known, the structural dynamics system of equations in physical space is transformed to a suitable Ritz modal basis. The reduced modal

system is then solved for the structural modal coordinates to obtain the structural dynamic response at the current time step. Once the response is known, it is used to compute the interface loads that the control surface exerts on the fuselage. These interface loads are passed to the fuselage equations of motion and represent force components at the degrees of freedom located at the control surface attachment point. The structural deformations of the control surface couple with the aerothermal problem due to the effect on aerodynamic flow properties, which change the heat flux. The deformations also result in a change in aerodynamic pressures which modify the structural loads. With the deformed configuration known at the current time step, the aerodynamic flow properties are updated using either the quasi-steady or fully unsteady aerodynamic model. After a pre-determined number of aeroelastic iterations have been carried out, the heat flux boundary conditions are recalculated and the thermal solution is updated. As depicted in Fig. 6.2, updating of the aeroheating boundary conditions requires the current flow properties and wall temperatures of the structure.

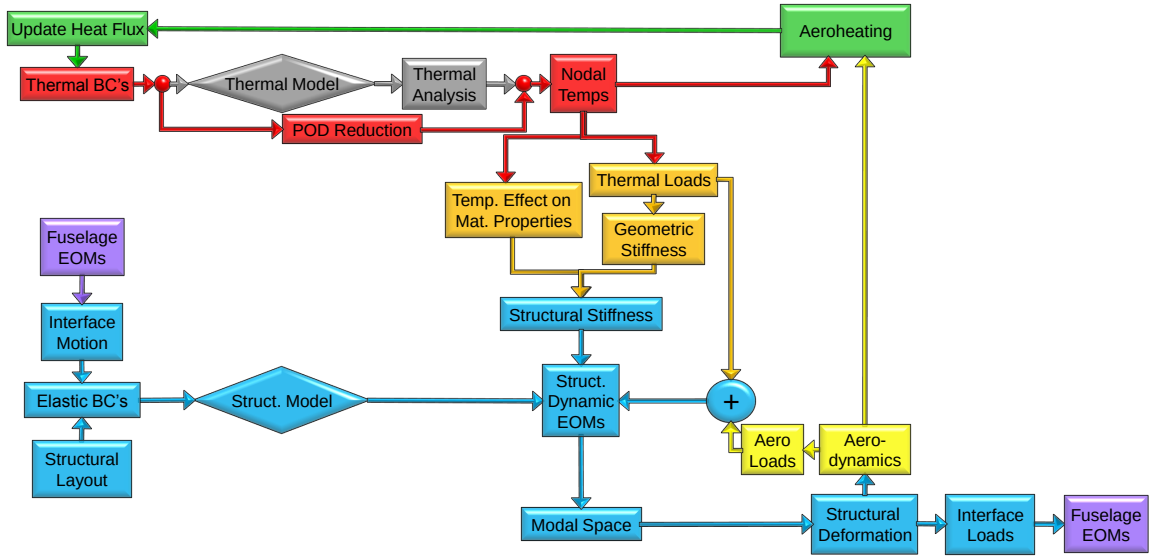

Figure 6.2: Reduced-order aerothermoelastic modeling framework as applied to the HSV control surface.

6.3 Overview of ROM Generation Process

As some of the ROMs used in the aerothermoelastic simulation process are dependent on components of other ROMs, these models must be generated in a specific order. An overview of the ROM process is given in Fig. 6.3. The green blocks in the figure describe the process for generating a kriging-based aerothermal ROM developed by Crowell et al. [52] and incorporated into the ROM framework in a recent work [110]. As described previously, this work investigates the use of the Eckert reference temperature method for computing the aerodynamic heating. However, the aerothermal ROM component is included in Fig. 6.3 to illustrate the complete ROM generation process.

The first ROM to be created is the POD model for the transient thermal component of the solution. To begin, the range of vehicle flight parameters is defined. Based on these parameters, representative simulations are defined for use in extracting the POD snapshots. Because the aerothermal ROM is dependent on the thermal ROM, the Eckert reference temperature method is used to calculate the heat flux in these simulations. Additionally, the structural dynamic ROM is dependent on the thermal ROM, and thus the high-fidelity structural model is used in these simulations. The accuracy of the thermal ROM is evaluated by running representative aerothermoelastic simulations using both the thermal ROM and full-order model and comparing their output. If greater accuracy is desired, more snapshots are taken and the thermal ROM is updated.

Once an accurate thermal ROM has been created, the next step is to identify the reference thermal state at which to evaluate the structural free vibration modes. The philosophy used in this work is to take the reference thermal state to be the average nodal temperatures over a set of thermal snapshots. Based on the frequency range of interest, a set of free vibration modes is generated by solving an eigenvalue problem at the reference thermal state including both material property degradation with temperature and geometric stiffening due to thermal stresses. While it is important to include free vibration modes in the basis, they have no association with the spatial distribution of the applied structural loads.

Additionally, in cases that are dominated by thermal loads, the structural response is close to quasi-static and the extent to which the free vibration modes are excited is minimal. Therefore, the set of free vibration is augmented by inserting into the modal matrix additional vectors calculated using the method of load-dependent Ritz vectors [85]. The goal of including load-dependent Ritz vectors is to enrich the basis such that it can capture motion that does not lie in the space of the free vibration modes. The formulation used to extract the load-dependent Ritz vectors was described in Chapter V.

Once the structural modal matrix is assembled, the kriging ROMs of the generalized stiffness matrix and physical thermal load vector are created for efficient updating of these quantities as a function of temperature. Specifically, these ROMs are used to directly update $k_S^*(T) = \Phi_S^T K_S^*(T) \Phi_S$ and $F_S^H(T)$. To generate the kriging ROMs, bounds on the POD modal coordinates are established and kriging training cases are run. At this point, the accuracy of the structural ROM is assessed by again running representative aerothermoelastic simulations and comparing the output of the structural ROM with that of the full-order structural model. If greater accuracy is desired, the structural modal basis is updated and the process is repeated.

The thermal and structural ROMs are then used in the aerothermal ROM generation process developed by Crowell and McNamara [52, 53, 26, 110, 51]. An added benefit to expressing the temperature distribution and deformation as a linear combination of modes is that it allows for parameterization of each in terms of a small number of design variables for the purpose of creating the aerothermal ROM. Bounds on the aerothermal ROM parameters are first established. Parameters for the aerothermal ROM consist of the structural and thermal modal coordinates as well as flight parameters such as angle of attack, Mach number, and altitude. Because the feasible number of parameters in the aerothermal ROM is limited, a subset of thermal and structural modes are used in its creation. Training cases are set up within the parameter space using Latin Hypercube Sampling. For each training case, CFD analysis is used to generate training data of the aerodynamic heating. Using

this training data, a kriging ROM representing the aerodynamic heat flux at the outer surface is generated. The accuracy is then evaluated using a separate set of evaluation cases. If greater accuracy is desired, more kriging sample points are added and the process is repeated. Once a satisfactory aerothermal ROM has been obtained, the ROM generation process is complete and the thermal, structural, and aerothermal ROMs can then be used for efficient aerothermoelastic simulation.

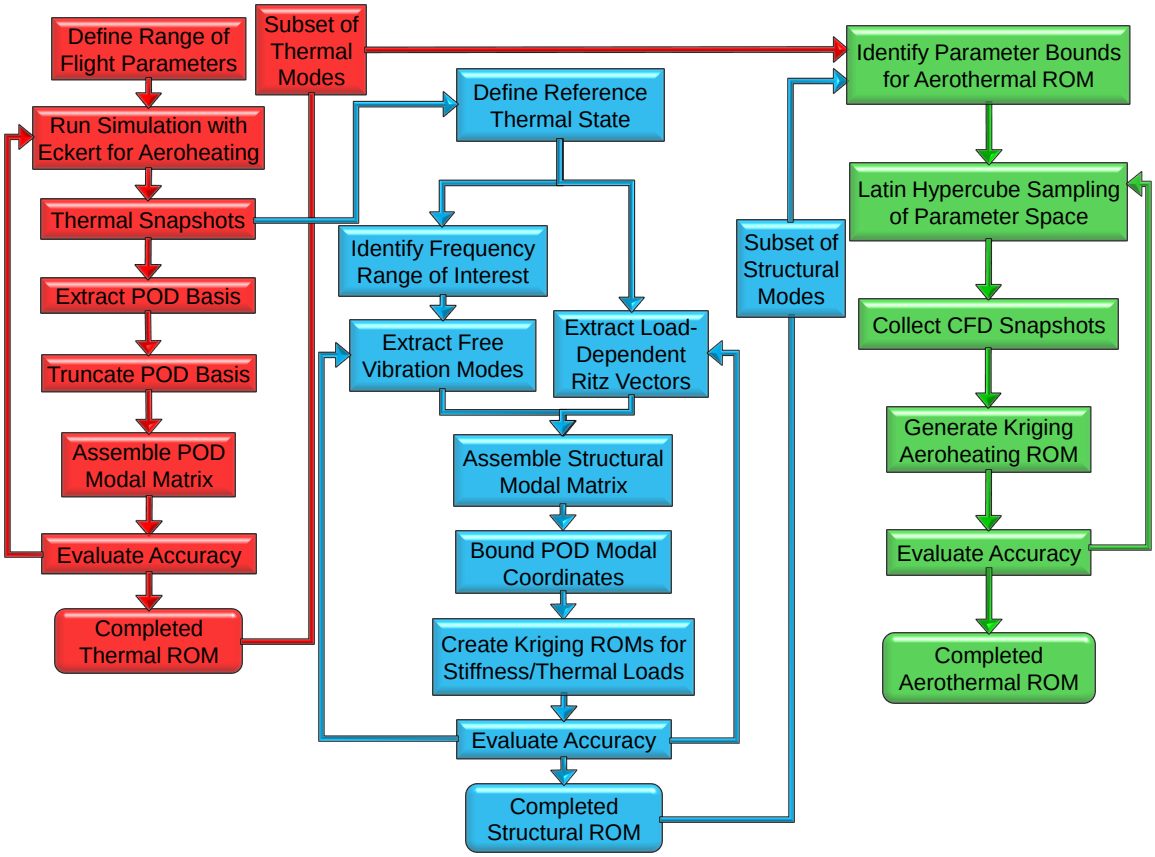

Figure 6.3: Flowchart of aerothermoelastic ROM generation process.

6.4 Description of Aerothermoelastic Time-Stepping Schedule

Once the thermal, structural dynamic, and aerothermal ROMs are generated, the aerothermoelastic framework can be used to perform time-domain simulations. As separate models are used for the aerothermal, heat transfer, structural dynamic, and aerodynamic compo-

nents of the aerothermoelastic solution, a methodology must devised for marching each of the various components in time and exchanging information between them. A time-marching procedure with updates to the thermal and structural boundary conditions at specified intervals is therefore proposed for solution of the coupled aerothermoelastic problem. An outline of the time-stepping schedule is given in Fig. 6.4. The size of the aeroelastic time step, Δt_{AE}, is smaller than the size of the aerothermal time step, Δt_{AT}, due to the fact that the aeroelastic time scale is faster than the aerothermal time scale. The procedure begins by calculating the aerodynamic flow properties over the undeformed structure at initial time, $t^{(0)}$. Using the flow properties, the heat flux at the outer surface is found using either the Eckert reference temperature method or the aerothermal ROM. Additionally, the wall shear stress is found using the local skin friction coefficients which are always found using the Eckert reference temperature method. The aerodynamic pressures and viscous drag components are then integrated to determine the aerodynamic forces and moments at initial time.

With the thermal boundary conditions known, a pre-determined number of thermal time steps are taken using POD, each of size Δt_{HT}, until the time $t^{(0)} + \Delta t_{AT}$ is reached. The thermal loads based on the temperature change between $t^{(0)}$ and $t^{(0)} + \Delta t_{AE}$ are then applied to the structural configuration at $t^{(0)}$. Additionally, the aerodynamic loads based on the already calculated flow properties are applied to the structure. The structural dynamic response solution in modal space is then marched forward one time step of size Δt_{AE}. The displacements are fed back into the aerodynamic solver and the flow properties are calculated at time $t^{(0)} + \Delta t_{AE}$ over the updated deformed configuration. Each time the flow properties are recalculated, the aerodynamic pressures are also integrated to allow for characterization of the transient aerodynamic forces and moments on the vehicle. The aeroelastic iterations continue to be carried for a pre-determined number of time steps. Once the time instant $t^{(0)} + \Delta t_{AT}$ has been reached, the instantaneous flow properties and wall temperatures are used to update the heat flux boundary conditions to the thermal prob-

lem. With the updated thermal boundary conditions known, the transient thermal solution is marched forward from the time instant $t^{(0)} + \Delta t_{AT}$ to the time instant $t^{(0)} + 2\Delta t_{AT}$ and the process is repeated.

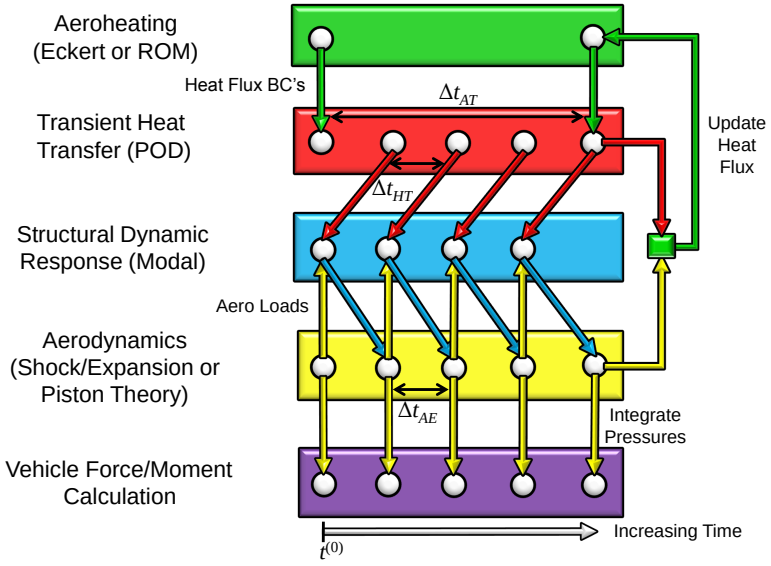

Figure 6.4: Overview of aerothermoelastic time-stepping schedule.

6.5 Iterative Routine for Assessing Influence of Aerothermoelastic Effects on Necessary Control Input

One goal of this dissertation is to assess the impact of aerothermoelastic effects on the vehicle control effectors. Aerothermoelastic effects ultimately result in changing aerodynamic forces and moments on the vehicle over time, which will in turn affect its flight dynamics. To maintain the desired trajectory, it is essential that the vehicle possess adequate control authority to account for these effects. As the HSV control surfaces are expected to have a strong influence on the dynamics of the vehicle, they are considered as a case study in this work. At each time step, the aerodynamic pressure loads and thermal loads cause the control surface to deform, leading to a change in the forces and moments acting on the vehicle and altering the trim state of the vehicle. The deflection angle of the control effec-

tors must therefore be adjusted to account for these effects. As such, an iterative routine is employed whose objective is to quantify the control input necessary to account for control surface flexibility.

A flowchart of the iterative routine developed in this dissertation is given in Fig. 6.5. The routine uses the control surface angle of attack, α, as the control input and the lift produced by a rigid control surface, L_R, as the objective. The lift produced by a rigid control surface at particular flight conditions and rigid angle of attack, α_R, is first calculated. Aerothermoelastic simulation of the elastic control surface at these flight conditions is then carried out at α_R. At pre-determined time intervals within the aerothermoelastic simulation, the analysis is paused and the deformed configuration at that time instant is stored. The deformed configuration is then used within the aerodynamic solver and the angle of attack is iterated on to minimize the residue, $\mathcal{R}$, given by

$$\mathcal{R} = |L_R - L_E|\,, \tag{6.1}$$

where L_E is the lift produced by the flexible (elastic) control surface. Note that the increment in α at each iteration is performed in a static manner such that a steady aerodynamic solution is carried out at each iteration in order to calculate L_E. The residue is minimized by iterating on α using `fminbnd`, an internal Matlab minimization routine. This routine is based on a golden section search algorithm combined with successive parabolic interpolation. The angle of attack which minimizes the residue, α_{min}, is then stored at the current time instant and the simulation resumes at the original angle of attackk, α_R, by marching forward to next time instant. The introduction of such a routine allows for investigation into the necessary robustness of the vehicle control effector under aerothermoelastic effects.

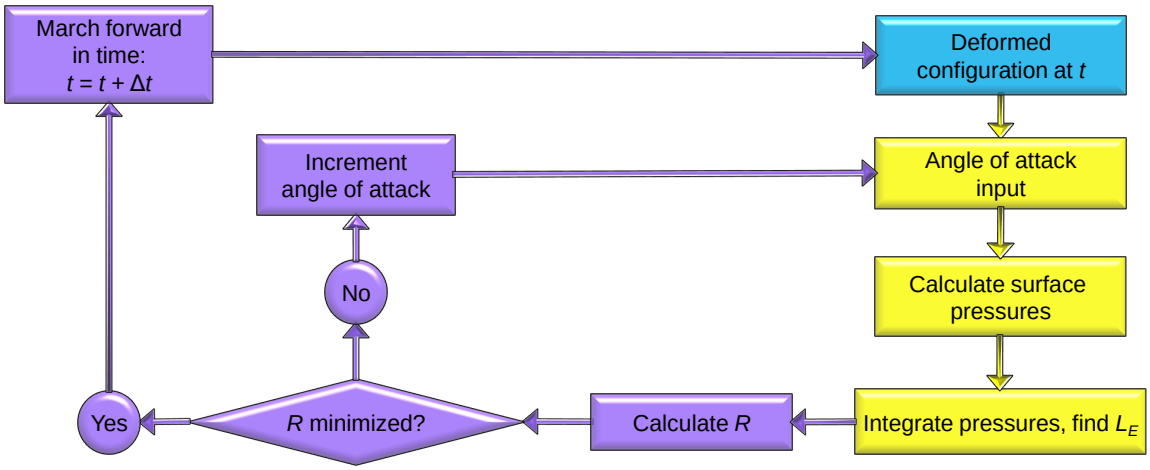

Figure 6.5: Iterative routine used to assess control authority necessary to account for aerothermoelastic effects.

Chapter VII

Quasi-Steady Aerothermoelastic Modeling

The current chapter investigates the influence of structural deformation due to thermal loads on the aerodynamic forces generated by a representative hypersonic vehicle control surface. As stated previously, the time scale associated with the heat transfer process in HSV simulations is relatively slow. Therefore, the aerothermoelastic framework utilized in the current chapter is of a quasi-steady nature. This means that the structural response is obtained by performing a static solution at each time step based on the thermal loads resulting from the current temperature distribution. Because the formulation is quasi-steady, the localized oblique shock/Prandtl-Meyer expansion fan aerodynamic solution described in Appendix A is employed for the aerodynamic solution. Full-order finite element models are used in the formulation of this chapter for the transient heat transfer and structural solutions. Discussion of the complete unsteady, reduced-order aerothermoelastic framework is reserved for the next chapter.

The chapter begins with an overview of the quasi-steady framework and highlights the coupling of the different components of the solution. The application example, consisting of a representative hypersonic vehicle control surface, is then described and material selection is discussed. Results obtained from quasi-steady aerothermoelastic simulations are presented. Results associated with the aerodynamic heating, transient heat transfer, quasi-static structural response, and quasi-steady aerodynamic pressures are included. Finally,

plots of the total lift and drag forces generated by the control surface are shown in order to illustrate the impact of aerothermoelastic effects.

7.1 Overview of Quasi-Steady Aerothermoelastic Simulation Framework

In order to assess the impact of deformation due to thermal loads on the aerodynamic forces generated by an HSV control surface, a quasi-steady aerothermoelastic simulation framework is developed. The salient features of the framework consist of:

- An aerodynamic heating model based on the Eckert reference temperature method to calculate nodal convective heating values at the outer surfaces of the control surface.
- A thermal finite element representation of the structure to solve the transient heat transfer problem in order to compute the temperatures within the structure.
- A structural finite element representation used to find the static nodal displacements resulting from aerodynamic and thermal loads.
- An quasi-steady aerodynamic model based on localized shock/expansion theory to determine the spatially varying flow parameters over the deformed structure.

A flowchart of the quasi-steady aerothermoelastic simulation framework is given in Fig. 7.1. The procedure begins by initializing the freestream flow properties. This allows for determination of the pressure, Mach number, and temperature at the edge of the boundary layer, given by p_e, M_e, and T_e, respectively, at initial time. Note that these flow parameters are determined using the quasi-steady aerodynamic formulation based on the undeformed configuration. Additionally, the initial wall temperature of the structure, T_w, is specified. Using p_e, M_e, T_e, and T_w, the Eckert reference temperature formulation is used to compute the thermal boundary conditions due to aerodynamic heating. Note that the thermal boundary conditions also include radiation to the environment.

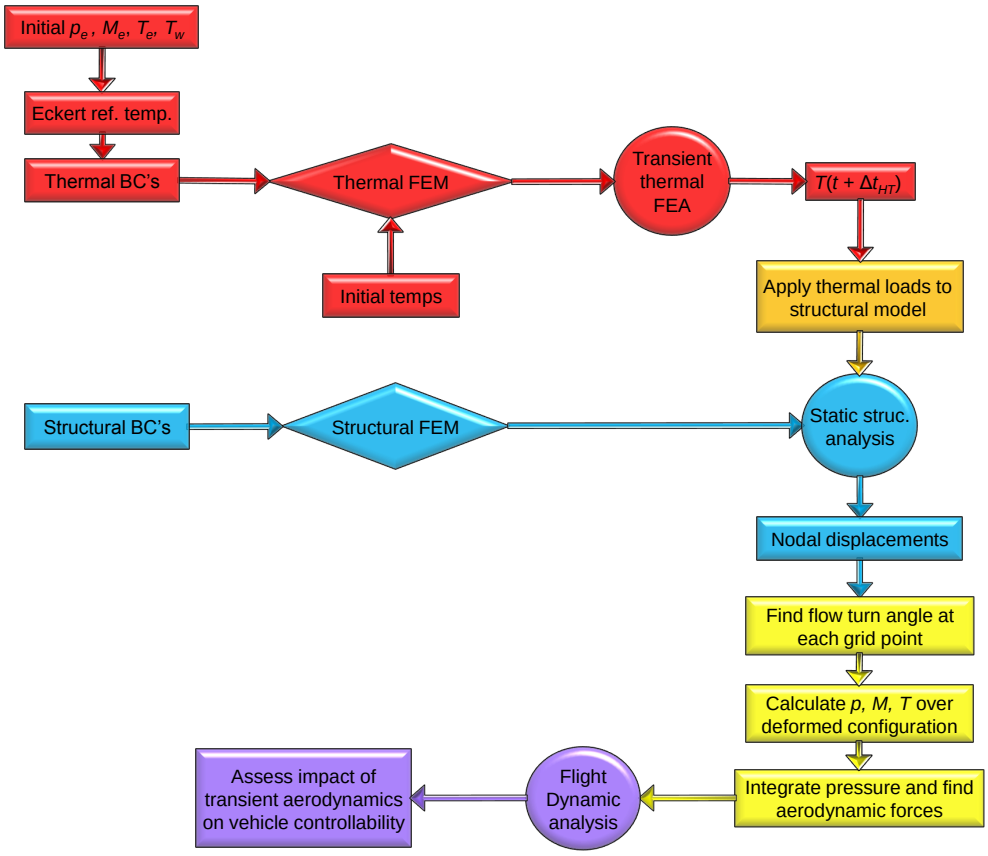

Figure 7.1: Flowchart of quasi-steady aerothermoelastic simulation framework.

Once the thermal boundary conditions are known, they are applied to the thermal finite element model. Based on the specified initial temperature distribution, full-order transient thermal analysis is carried out and the nodal temperatures at each time instant of interest are generated. Note that the transient thermal analysis is performed using Solution 159 (transient heat analysis) in the finite element code Nastran. For the structural finite element model, the boundary conditions are first applied which consist of enforced zero displacements at the control surface attachment region in this case. At each time instant of interest, the temperature distribution at that time instant is used to generate the corresponding thermal loads. These thermal loads are then applied to the structural finite element model. Static structural analysis is performed in order to determine the nodal displacements at the current time instant. Here, the static structural analysis is carried out using the Solution 101 (linear static) within the finite element code Nastran.

Once the nodal displacements are known at a given time instant, the deformed configuration is generated and used within the quasi-steady aerodynamic model. As discussed previously, the quasi-steady aerodynamic model uses the oblique shock and Prandtl-Meyer expansion fan relations to compute the flow properties at each node of the finite element model. This is accomplished by computing the local flow turning angle at each node of the finite element model and then passing the flow directly upstream through either an oblique shock or expansion fan. Once the flow properties are known over the entire outer surface of the deformed structure, the pressures are integrated in order to determine the aerodynamic forces (i.e., lift and drag) at the current time instant. Note that the pressures that are integrated at this step in the analysis include normal pressures determined from the quasi-steady aerodynamic model as well as shear stress due to skin friction as calculated from the Eckert reference temperature formulation. The time-history of the aerodynamic forces is then used to assess the impact of control surface deformation due to thermal loads on the overall vehicle controllability. It should be noted that this formulation uses the initially calculated aerodynamic heating thermal boundary conditions to generate temperature dis-

tributions throughout the complete time range of interest. Thus, in the current chapter, the aerodynamic heating thermal boundary conditions are not updated as the flow properties change. However, the radiation boundary condition is updated at each time step. Additionally, while the aerodynamic pressures are integrated over the outer surface to compute the aerodynamic forces, aerodynamic pressure loads are not included in the structural load vector when solving for the static structural displacements. Therefore, the structural displacement is a result of thermal loads only in the current chapter. This approximation enables the use of a quasi-steady aerodynamic formulation as the thermal loads are known the vary on a slow time scale. These approximations are addressed in subsequent chapters in which the fully coupled, unsteady aerothermoelastic framework is discussed.

7.2 Control Surface Representation

Motivation to consider the aerothermoelastic response of hypersonic vehicle control surfaces stems from previous development of a two-dimensional hypersonic vehicle configuration [58, 59, 60, 61, 62]. A schematic of the basic two-dimensional geometry considered in those works is given in Fig. 7.2. The configuration consists of a forebody compression ramp, an engine/nacelle segment, an aftbody expansion segment, and a flat upper surface. As shown in Fig. 7.2, the vehicle is equipped with an elevator control surface. The results presented in the current chapter therefore extend the previous two-dimensional HSV analysis by considering a fully three-dimensional control surface structure that is not rigid.

The control surface geometry used in this study is based on that employed in Chapter IV and is shown again for reference in Fig. 7.3. Based on this geometry, a finite element model of the control surface has been created for the thermal and structural analyses. This model is again based on that described in Chapter IV and is shown again Fig. 7.4 with the top skin removed for visualization purposes. The model consists of a top and bottom skin surface and is stiffened by internal stiffeners as well as stiffeners around the outer

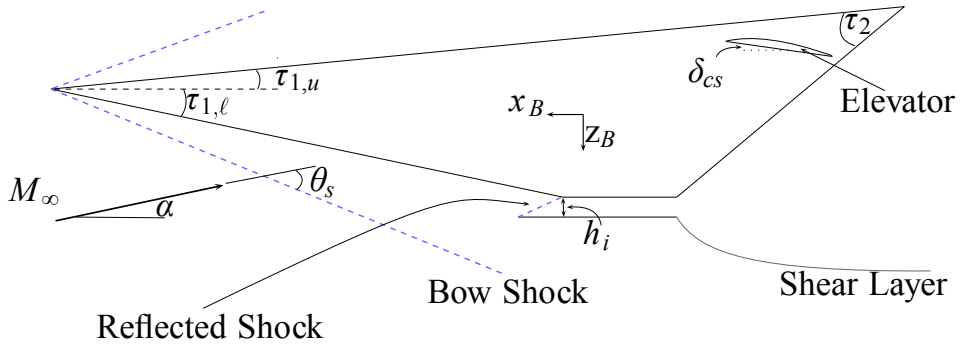

Figure 7.2: Overall HSV geometry illustrating position of control surface [18].

perimeter according to the dimensions specified in Fig. 7.3. The model is composed of 9,200 three-node triangular elements all having a thickness of 12.7 mm (0.5 in). The circle indicates the attachment region which is modeled by imposing displacement constraints in all six degrees of freedom. The structure is taken to be made of Ti-6Al-2Sn-4Zr-2Mo due to its high melting temperature and strength-to-weight ratio. The corresponding thermal and structural material properties for Ti-6Al-2Sn-4Zr-2Mo as used in this study are given in Table 7.1.

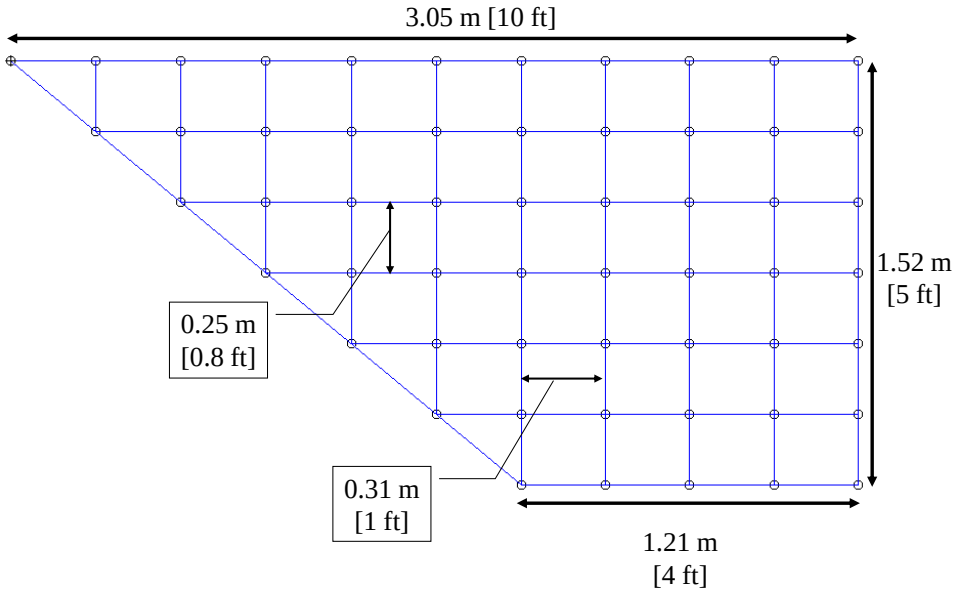

Figure 7.3: Geometry and dimensions of control surface used in current study.

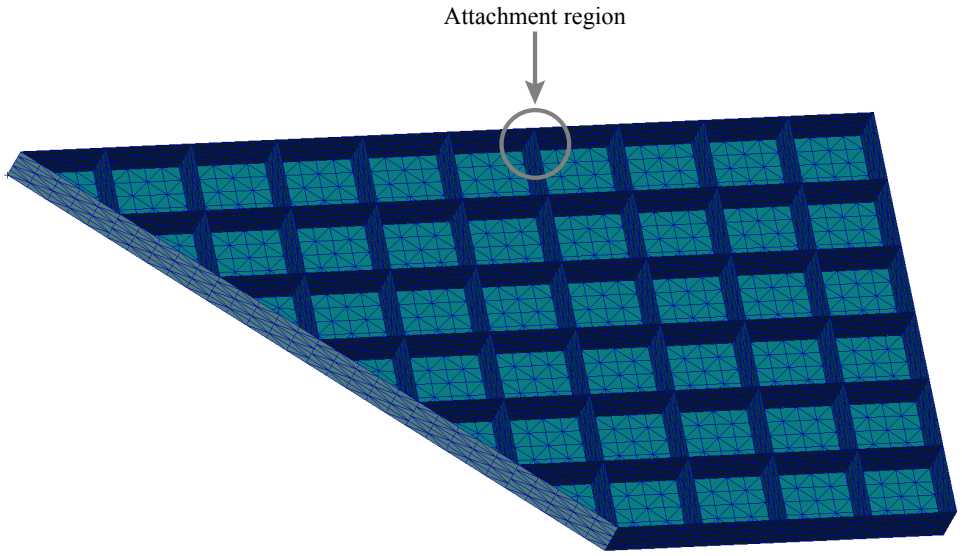

Figure 7.4: Finite element model of control surface used in thermal and structural solutions.

Table 7.1: Thermal and structural material properties for Ti-6Al-2Sn-4Zr-2Mo used in the study [161].

Thermal Conductivity, κ	6.89 W/m/K
Specific heat, c_p	463 J/kg/K
Density, ρ	4540 kg/m^3
Poisson's Ratio, ν	0.32
Young's Modulus, E	113.8 GPa
Emissivity, ϵ	0.7
Coefficient of Thermal Expansion, α_T	8.1 μm/m/K

7.3 Quasi-Steady Aerothermoelastic Simulation Results

The formulation presented in Section 7.1 is applied to the representative control surface model described in the previous section. The initial temperature conditions for the thermal problem are taken to be 311 K (100° F) throughout the structure. The vehicle is taken to be flying a cruise trajectory at an altitude of 26 km (85,000 ft) and thus the atmospheric temperature is taken to be 222.5 K for the purposes of computation of the radiation heat flux. The control surface is taken to be at an angle of attack, α, of 6° and a yaw angle, β, of 0°.

The integrated aerothermoelastic solution begins by calculating the aerodynamic heat flux over the undeformed structure. As described previously, the nodal flow properties are first found over this configuration and the heat flux is then calculated using the Eckert reference temperature method based on the flow properties and wall temperatures. Contour plots of the aerodynamic heat flux over the bottom and top surfaces of the undeformed configuration are shown in Fig. 7.5. As seen in the figure, the heat flux on the bottom surface is higher in general than that on the top surface due to the compression of the flow over the bottom surface and expansion of the flow over the top resulting from the 6° control surface angle of attack.

This heat flux distribution, the radiation boundary condition, and initial temperature condition are applied to the finite element model and transient thermal analysis is carried out with nodal temperatures output at selected time instants. Note that the thermal time step used for the transient thermal solution is 0.1 s. The temperature histories for two selected nodes are given in Fig. 7.6. Figure 7.6(a) shows the temperatures for node 1 which is located on the top surface at the leading edge of the root, while Fig. 7.6(b) shows the temperatures for node 1117 which is located on the bottom surface at the leading edge of the root. Examining the two figures, it can be observed, as expected, that the node located on the top surface is at a lower temperature than the node at the bottom surface at each time instant. It can also be observed that the node on the bottom surface of the control surface

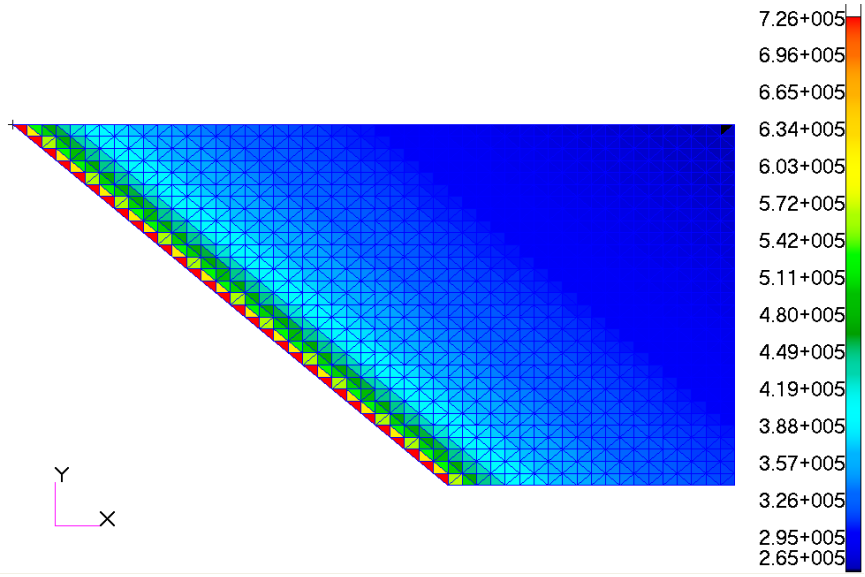

(a) Bottom surface heat flux.

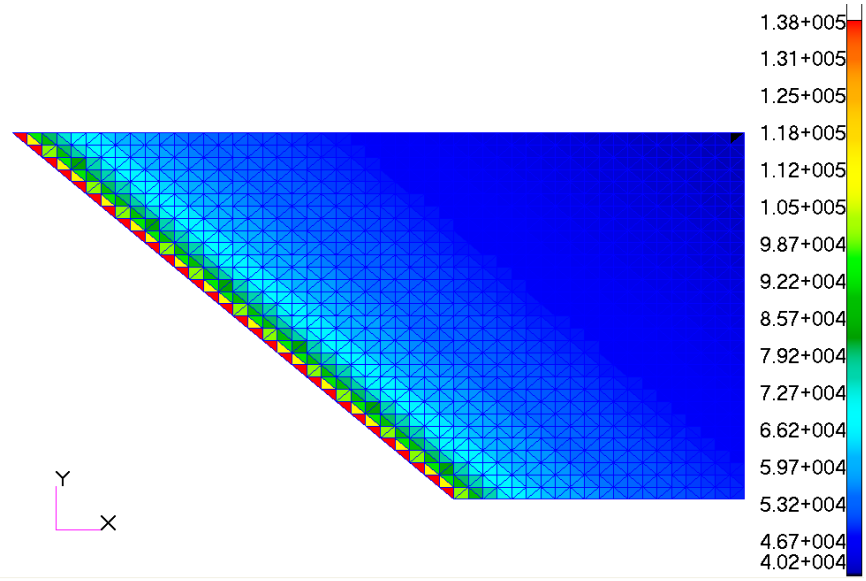

(b) Top surface heat flux.

Figure 7.5: Aerodynamic heat flux [W/m^2] on bottom and top surfaces of undeformed configuration.

approaches thermal equilibrium faster than the node on the top surface of the structure due to higher heating levels on the bottom surface.

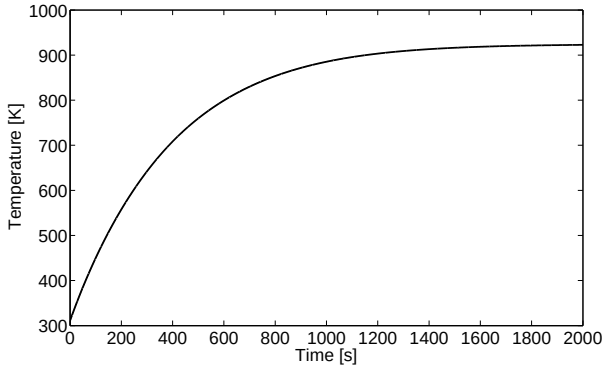

(a) Node 1 (top surface, leading edge, root).

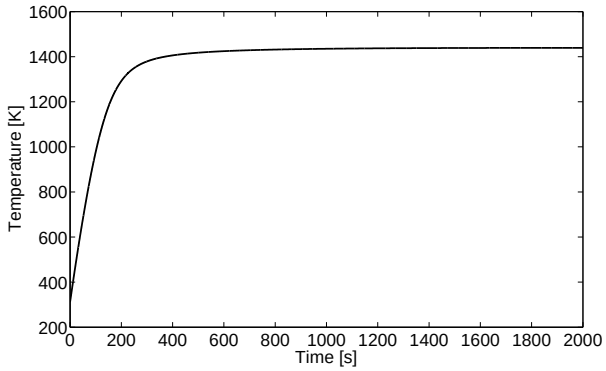

(b) Node 1117 (bottom surface, leading edge, root).

Figure 7.6: Nodal temperatures vs. time for two selected nodes.

In order to illustrate the spatial variation of temperature distribution, it is plotted at two different time instants. Contour plots of the temperature distribution at 50 s and 2,000 s are shown in Fig. 7.7(a) and Fig. 7.7(b), respectively, with the top surface hidden for visualization purposes. The figures clearly illustrate the influence of the control surface angle of attack as the bottom surface of the structure is at a higher temperature than the top surface. Additionally, the figures show that the temperature is highest in general at the leading edge and decreases from the leading edge to the trailing edge.

Once the nodal temperatures at each time instant of interest are known, they are applied to the structural configuration in order to generate thermal loads at each time instant instant

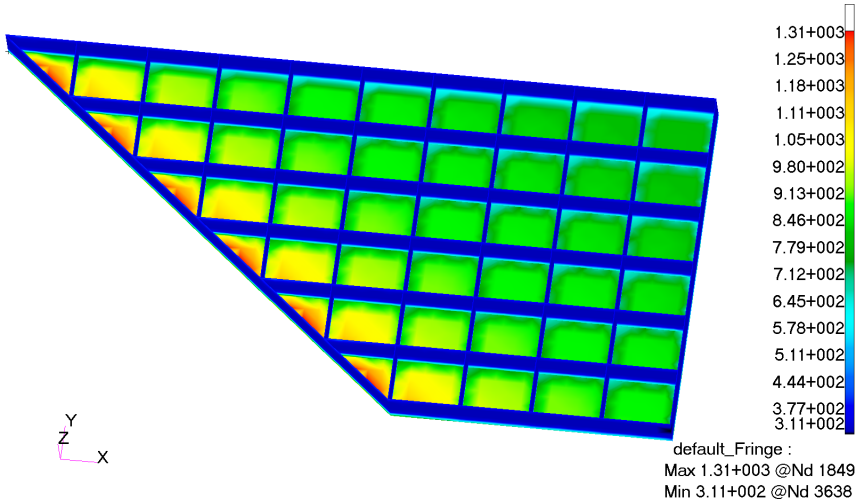

(a) Temperatures at 50 s.

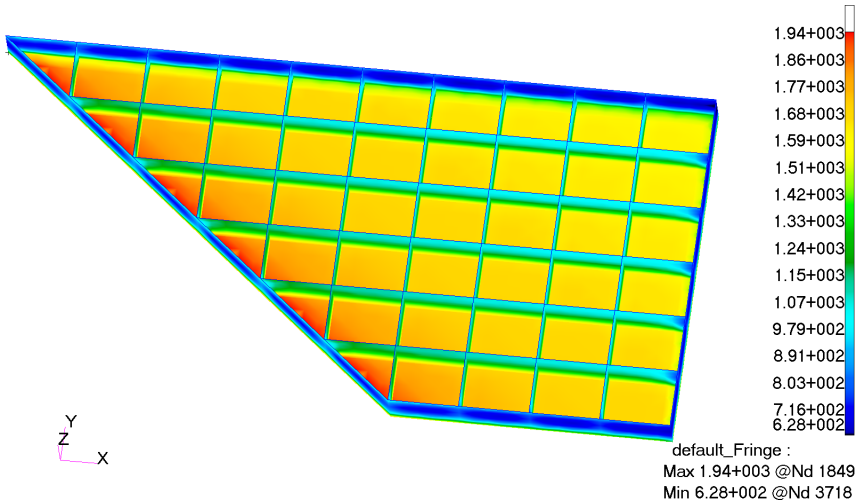

(b) Temperatures at 2,000 s.

Figure 7.7: Nodal Temperatures [K] from transient thermal finite element analysis at 50 seconds and 2,000 seconds.

of interest. As described previously, static structural solutions are performed at each time instant to obtain the structural response. For this work, the structural response to thermal loads is computed in intervals of 200 s. Note that refinement in the temporal resolution of the structural solution is addressed in subsequent chapters. The z-direction displacements for two selected nodes over time are given in Fig. 7.8. Figure 7.8(a) gives the displacements of node 1117 (located on the bottom surface at the leading edge of the root), and Fig. 7.8(b) gives the displacements of node 1167 (located on the bottom surface at the trailing edge of the root). Examining these results, it is observed that the z-direction displacements at both locations increase from 0 – 200 s, after which point they begin to decrease asymptotically. This behavior is a result of the thermal gradient between the bottom and top surfaces of the structure. Initially, the bottom surface heats up faster than the top surface and therefore expands more. As the bottom surface begins to approach thermal equalibrium, the temperature difference between the bottom and top surfaces decreases. This results in the decrease in displacement that is shown to occur beginning at 200 s into the transient.

In order to illustrate the spatial variation of the structural displacements, the deformed configuration of the structure is generated at three different time instants. The deformed configuration is shown with contours of z-direction displacements at 200 s, 400 s, and 2,000 s in Fig. 7.9 with the top surface hidden for visualization purposes. The results in Fig. 7.9 illustrate the effect of the control surface angle of attack in that the bottom surface expands more than the top surface, resulting in a concave-up curvature of the structure. Furthermore, comparing Figs. 7.9(a), 7.9(b), and 7.9(c), we can see that the maximum z displacement decreases from 200 s – 2,000 s. This is again a result of the fact that the bottom surface approaches thermal equilibrium faster than the top surface as described above. Once the bottom surface reaches thermal equilibrium, the temperature difference between the bottom and top surfaces begins to decrease, thus leading to a decrease in maximum structural displacements. These results confirm the time-domain displacement histories shown in Fig. 7.8.

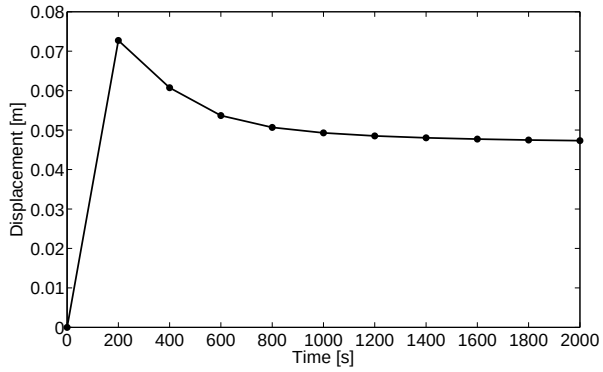

(a) Node 1117 (bottom surface, leading edge, root).

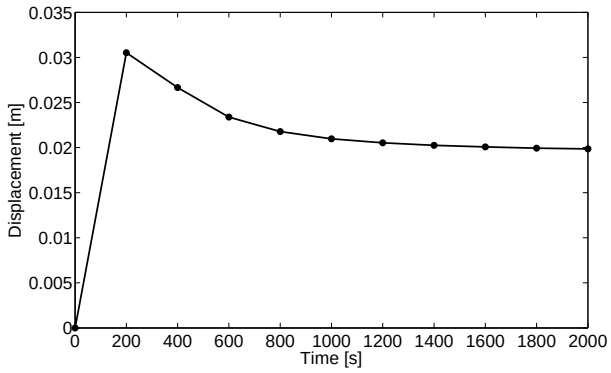

(b) Node 1167 (bottom surface, trailing edge, root).

Figure 7.8: z-direction nodal displacements vs. time for two selected nodes.

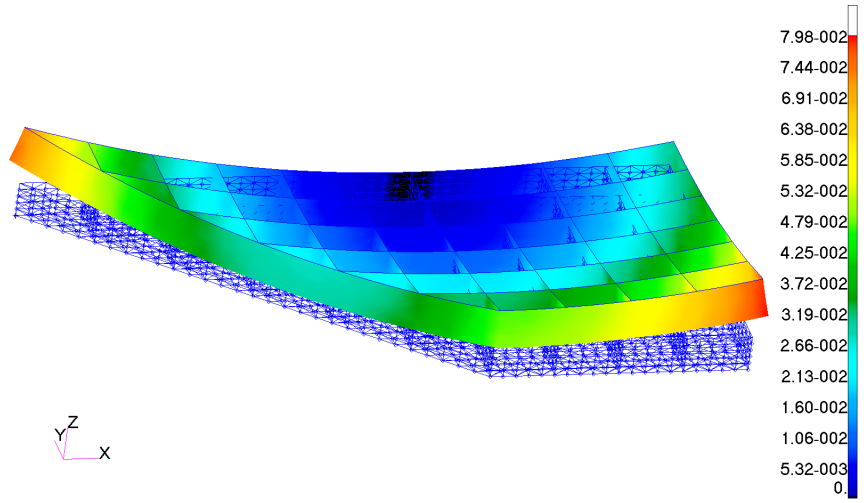

(a) Displacements at 200 s.

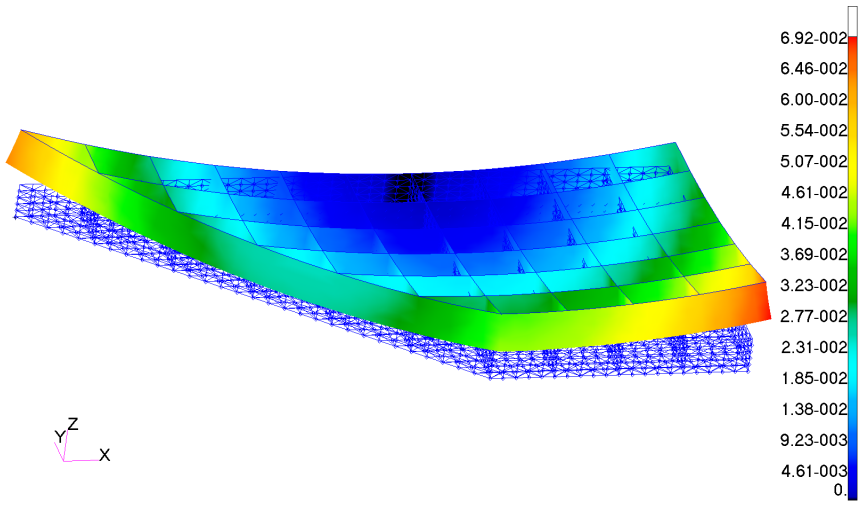

(b) Displacements at 400 s.

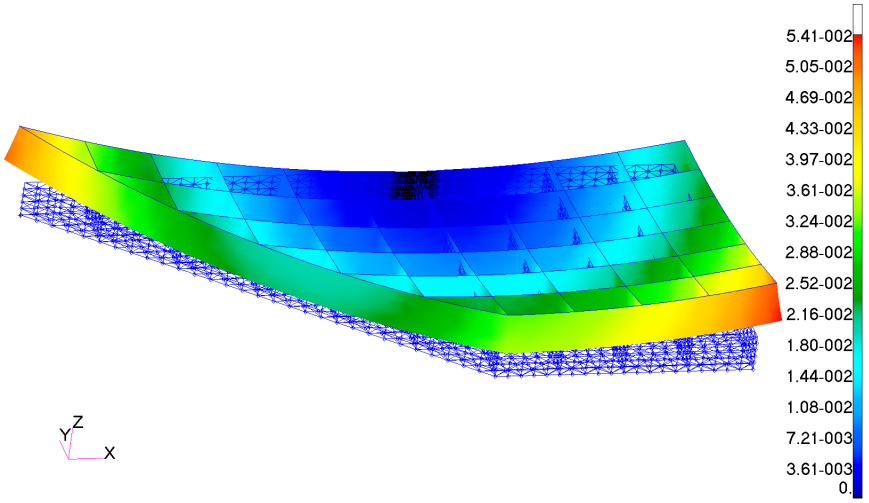

(c) Displacements at 2,000 s.

Figure 7.9: Structural displacements [m] in z direction at 200, 400, and 2,000 seconds.

With the nodal displacements known at the time instants of interest, the deformed configuration is generated at these time instants. Based on the deformed configuration, the quasi-steady oblique shock/Prandtl-Meyer expansion aerodynamic formulation described previously is used to compute the flow properties over the outer surfaces of the structure at each time instant. Plots of the aerodynamic pressures at node 1117 (bottom surface, leading edge, root) and node 1167 (bottom surface, trailing edge, root) over time are given in Fig. 7.10(a) and Fig. 7.10(b), respectively. Note that these plots include only the normal pressure components obtained from the oblique shock/Prandtl-Meyer expansion fan relations and do not include the shear stress contribution. Examining Fig. 7.10(a), we see an increase in pressure between 0 and 200 s. Because node 1117 is located on the bottom surface of the structure, as the bottom surface heats up and the structure deforms concave up, the flow turning angle at the leading edge on the bottom surface becomes larger, resulting in a higher pressure. Beyond 200 s, the structure begins to relax and the pressure asymptotically decreases. The converse situation occurs for node 1167. As this node is located at the trailing edge as opposed to the leading edge, when the structure deforms concave up, there exists an expansion of the flow over the bottom surface. Therefore, the pressure at this location is lowest at 200 s because this is the time instant at which the structures obtains its maximum curvatuve. Beyond 200 s, the pressure then begins to increase asymptotically as the temperature distribution evolves and the curvature decreases.

To provide understanding of the spatial distribution of the normal aerodynamic pressures, they are plotted over the top and bottom surfaces at 200 s as shown in Fig. 7.11. Figure 7.11(a) shows the spatial distribution of the pressures over the bottom surface while Fig. 7.11(b) shows the spatial distribution of the pressures over the top surface. As in Fig. 7.10, Figs. 7.11(a) and 7.11(b) show only the normal pressure components and do not include the shear stress contribution due to skin friction. The effect of angle of attack is seen as the pressures are higher in general on the bottom surface than on the top, thus generating lift. However, we see that the effect of the deformation results in the pressure

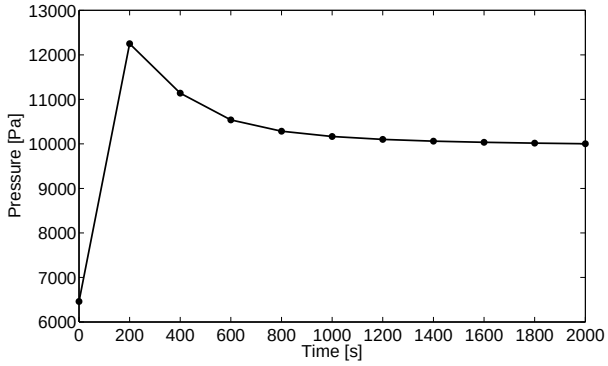

(a) Node 1117 (bottom surface, leading edge, root).

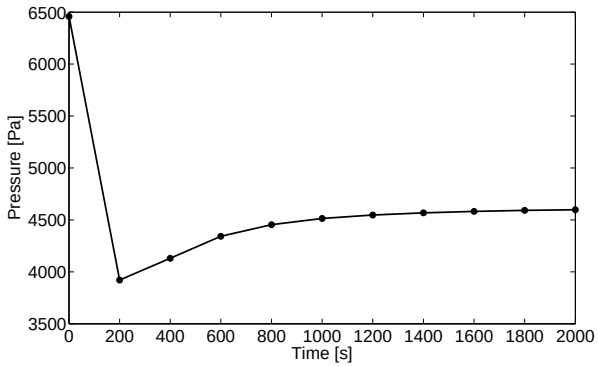

(b) Node 1167 (bottom surface, trailing edge, root).

Figure 7.10: Local normal pressure values vs. time for two selected nodes.

decreasing along the chord on the bottom surface and increasing along the chord on the top surface. This effect is due to the fact that the curvature causes expansion of the flow over the bottom surface and compression of the flow over the top surface due to the curvature induced by thermal loads. The extent to which the flow is expanded or compressed is a result of the deformation level of the structure resulting from the thermal loads.

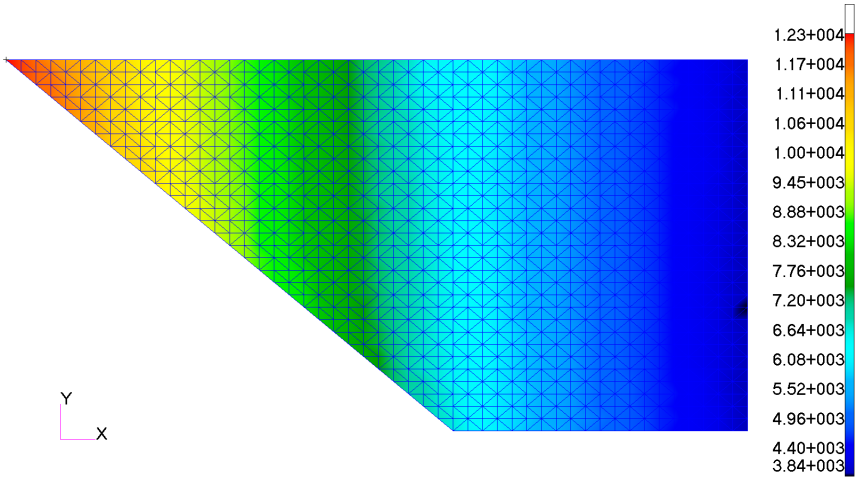

(a) Bottom surface pressures.

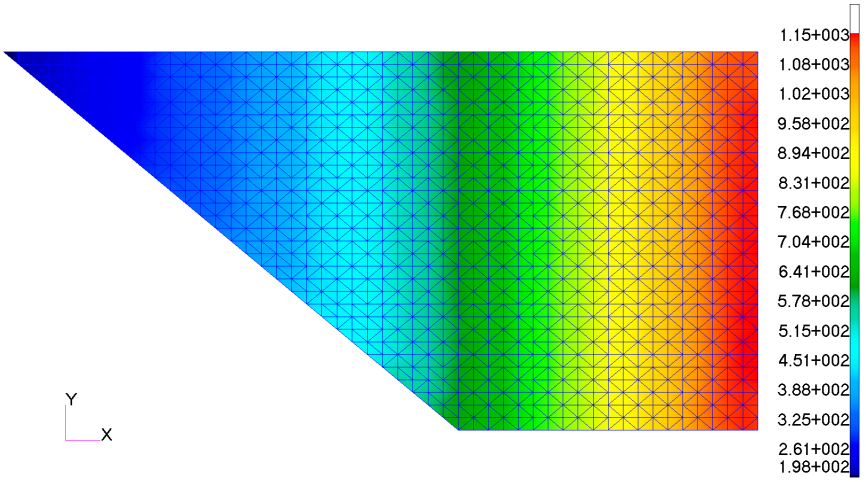

(b) Top surface pressures.

Figure 7.11: Normal component of aerodynamic pressures [Pa] over top and bottom surfaces of structure at 200 s.

In a manner similar to that of Fig. 7.11, the spatial distribution of the shear stress over the outer surfaces is shown in Fig. 7.12 for the time instant at 200 s. Specifically, Fig. 7.12(a) shows the shear stress over the bottom surface at 200 s and Fig. 7.12(b) shows

the shear stress over the top surface at 200s. As shown in Eq. (A.49), the skin friction coefficient is inversely proportional to the Reynolds number. Therefore, in an undeformed case, the shear stress will be highest at the leading edge and decrease along the chord toward the trailing edge. However, the results shown in Fig. 7.12 are generated over the deformed structural configuration at 200 s. The effect of spatial variation in flow properties on the shear stress can thus be seen. Examining Fig. 7.12(b), it can be observed that the effect of Reynolds number on the shear stress is counteracted by the compression of the flow over the top surface due to its curvature. Therefore, the shear stress increases slightly beginning at the zero-slope location for each span-wise station of the control surface. Note that for the results shown in Fig. 7.12, the wall temperatures are assumed to be at a uniform value of 311 K which was the wall temperature value used in the aerodynamic heating calculation. This assumption is addressed in subsequent results.

As this study is aimed at providing insight into the impact of aerothermoelastic effects on HSV dynamics and control, it thus remains to quantify the effect of the deformations on the aerodynamic forces generated by the control surface for this case. To this end, the aerodynamic pressures are integrated at 200 s intervals to calculate the control surface lift and drag forces from 0 – 2,000 s. In order to integrate the pressures, the pressures over each finite element at the top and bottom surfaces of the structures are determined by averaging the corresponding nodal pressures and assuming the pressure to be uniform over the element. This averaging process is performed for both the normal pressures as well as the shear stress. Once the element-uniform normal pressures and shear stresses are computed, they are multiplied by the corresponding element area for each finite element at the outer surface of the structure to give the values of the elemental forces. Normal and tangent vectors to the deformed configuration are then calculated for each element. The forces due to normal pressures are then taken to act in the direction opposite of the local outward normal direction to the deformed configuration for each element. The forces due to shear stress are taken to act in the direction of the local tangent to the deformed

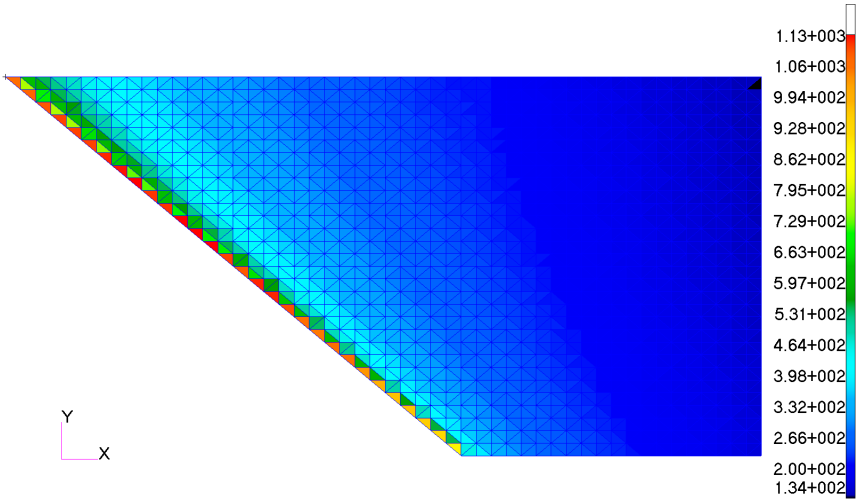

(a) Bottom surface shear stress.

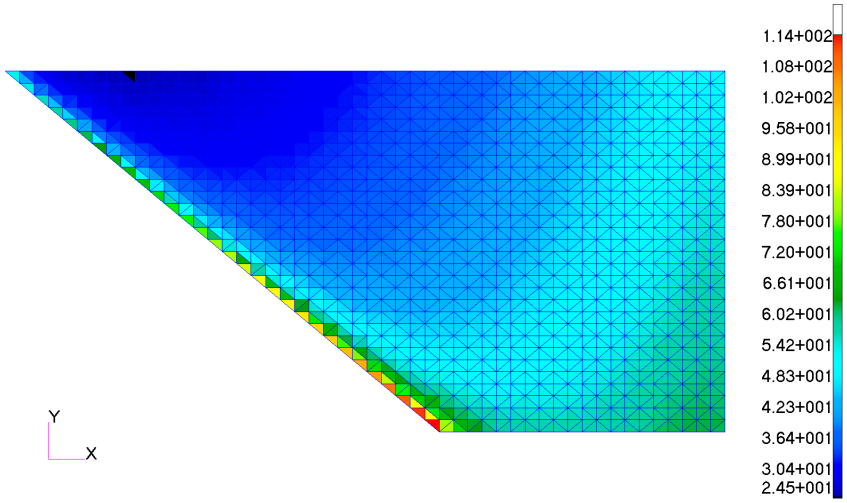

(b) Top surface shear stress.

Figure 7.12: Shear stress [Pa] over top and bottom surfaces of structure at 200 s.

configuration for each element. These local normal and tangential force components are then resolved into the freestream direction to compute their contribution to the overall drag, and into the direction normal to the freestream to compute their contribution to the overall lift. Finally, each element contribution is summed to give the total lift and drag forces generated by the control surface.

The contributions of normal pressures and shear stresses to the aerodynamic forces are first examined independently prior to presenting the total lift and drag force results. The contributions due to normal aerodynamic pressures are examined first. Results are plotted in Figs. 7.13 and 7.14, which show the contributions of normal aerodynamic pressures to the total lift and drag forces, respectively. As shown in Fig. 7.13, the lift force decreases up to approximately 400 s, then increases asymptotically to a new value which is lower than the lift generated by the undeformed control surface. Conversely, the drag force increases between 0 – 200 s and then begins asymptotically decreasing to a new value which is higher than the drag generated by the undeformed control surface. The initial decrease in lift and initial increase in drag are a result of the structure undergoing displacements due to thermal loads as the bottom surface of the structure heats up faster than the top. As the structure begins to relax, the lift and drag values begin to converge to the new values. Note that the change in forces is a result of two effects. The first effect is the change in magnitude of the pressure values as the structure deforms. The second effect is a result of the change in orientation of the local surface normals as the structure deforms.

Plots of the contributions of shear stress to the total lift and drag forces are given in Figs. 7.15 and 7.16, respectively. For the contribution of the shear stress to the total lift force, it can be observed that this quantity is always a negative value. This is due to the fact that the shear stress acts in the direction of the local tangent to the control surface at every point. Due to the leading-edge-up angle of attack, this results in shear stresses that act in a direction that is opposite of the positive lift direction. However, note that the contribution of shear stresses to the total lift force is small relative to that of the normal aerodynamic

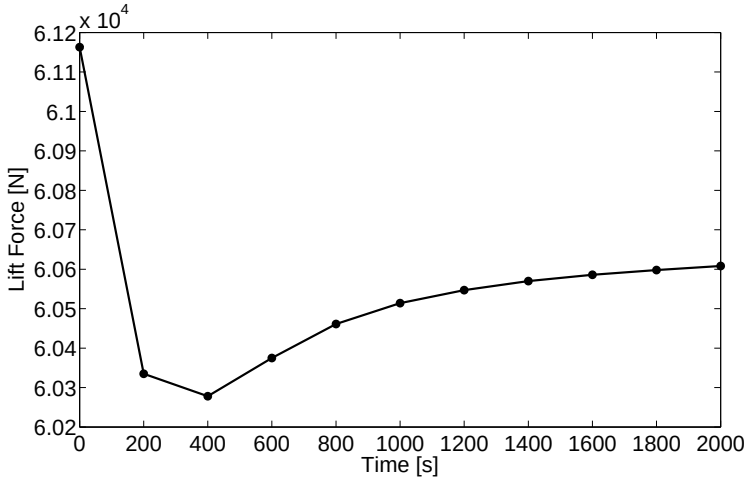

Figure 7.13: Lift force vs. time due to normal aerodynamic pressure.

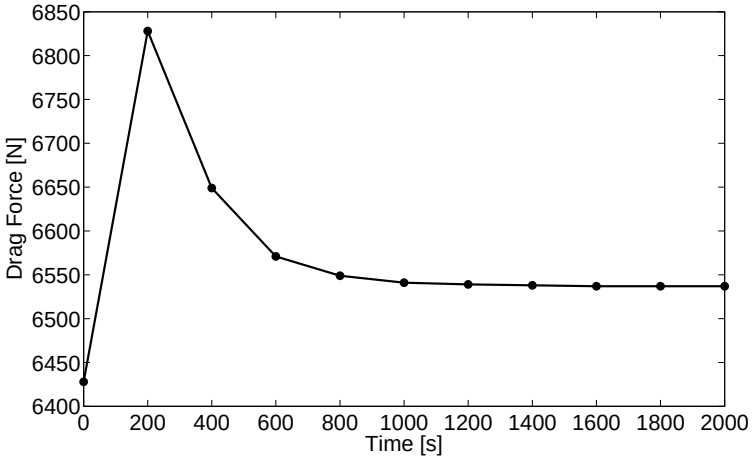

Figure 7.14: Drag force vs. due to normal aerodynamic pressure.

pressures. Examining Fig. 7.16, it can be observed that the contribution of shear stresses to total drag is more pronounced than its contribution to total lift. However, the drag force due to shear stress is approximately half of that due to normal aerodynamic pressures. As mentioned previously, note that the contributions of shear stress to total lift and drag shown in Figs. 7.15 and 7.16 assume a constant wall temperature of 311 K. This assumption is addressed in subsequent discussion.

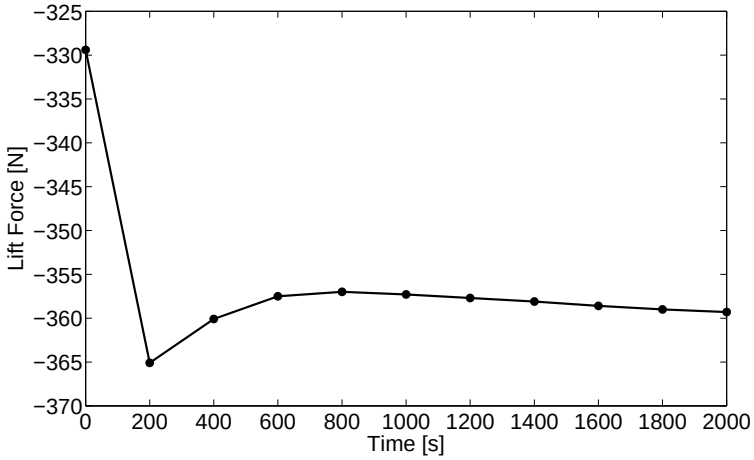

Figure 7.15: Lift force vs. time due to shear stress assuming a constant wall temperature.

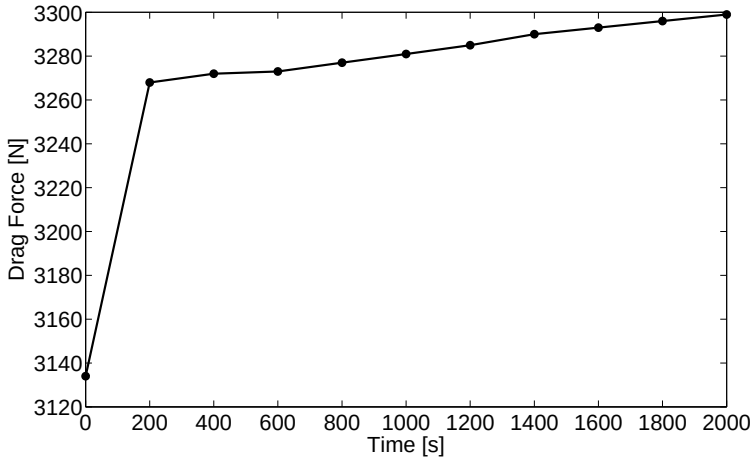

Figure 7.16: Drag force vs. time due to shear stress assuming a constant wall temperature.

Figure 7.17 shows a plot of the total lift force over time for the Mach 8 cruise trajectory including both shear stress and normal pressure contributions. We see the effect

of the changing temperature gradient in the transient lift behavior. As the bottom surface approaches thermal equilibrium and the structure approaches its maximum displacement, the lift curve decreases to a minimum value. After the bottom surface reaches equilibrium and the temperature difference between the top and bottom surfaces begins to decrease, the amount of curvature in the structure begins to decrease. This results in smaller flow turning angles, which leads to less expansion over the bottom surface and less compression over the top surface. Thus, the lift begins to increase from this point to the end of the time period considered. A similar, but opposite trend occurs for the drag behavior as shown in Fig. 7.18. The maximum relative change in lift is found to be 1.5%, while that for drag was found to be 5.6%, with respect to the initial values. Comparing Fig. 7.13 to Fig. 7.17, it can be observed that total lift force and the lift force due to normal aerodynamic pressures follow the same trend and are close in magnitude. This provides evidence that the total lift force is dominated by the normal pressure component. Comparing Fig. 7.14 to Fig. 7.18, it can be observed that the total drag force and the drag force due to normal aerodynamic pressures follow the same trend. However, comparison of the magnitudes of the drag forces between the two plots shows that impact of normal aerodynamic pressures on total drag force is not as pronounced as it is for total lift force.

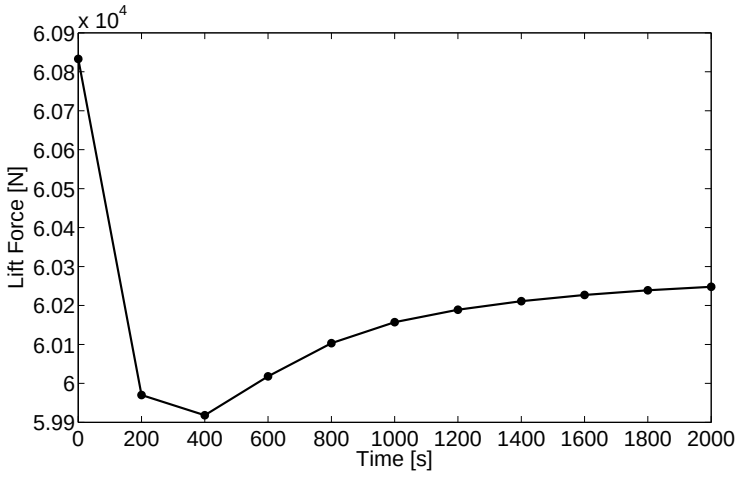

Figure 7.17: Total lift force vs. time assuming a constant wall temperature.

As was discussed with regard to Figs. 7.15 and 7.16, the shear stress computations in

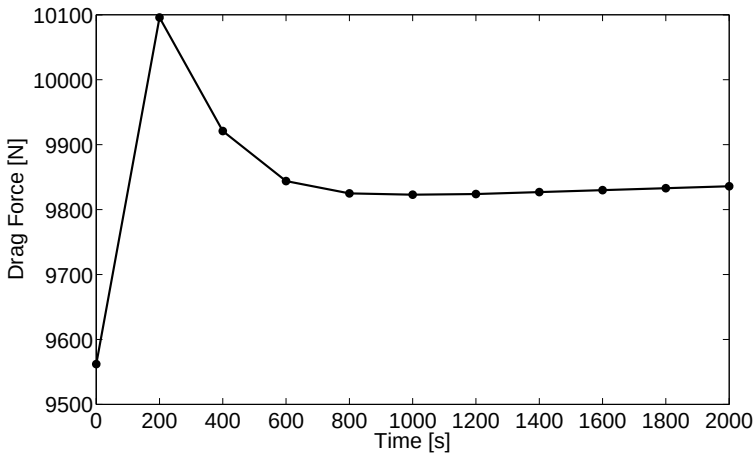

Figure 7.18: Total drag force vs. time assuming a constant wall temperature.

those figures assumed a time-independent wall temperature of 311 K. However, as shown in Eq. (A.42) of Appendix A, the Eckert reference temperature is a function of the wall temperature. This dependence on wall temperature ultimately impacts the reference viscosity and reference density of the flow used in the skin friction calculation. To assess the impact of transient wall temperature on the control surface lift and drag, these forces are again computed, except this time updating the wall temperature at each time instant based on the results of the transient thermal simulation. Note that the contributions of normal aerodynamic pressures to total lift and drag are not affected by the wall temperature update. The lift and drag forces due to shear stress are shown in Figs. 7.19 and 7.20, respectively, including the update of the wall temperature. Comparing Fig. 7.19 to Fig. 7.15, it can be observed that the increase in wall temperature results in the contribution of shear stress to total lift force becoming less negative as compared with the case of a time-independent wall temperature. Comparing Fig. 7.20 to Fig. 7.16, updating of the wall temperature is found to result in a decrease in skin friction drag as compared with the case in which the wall temperature is held constant over time. Specifically, the assumption of a time-independent wall temperature is found to result in up to a 46% error in skin friction drag prediction.

The total lift and drag forces are recomputed using the results from Figs. 7.19 and 7.20 in order to incorporate the effect of a time-varying wall temperature. Plots of the result-

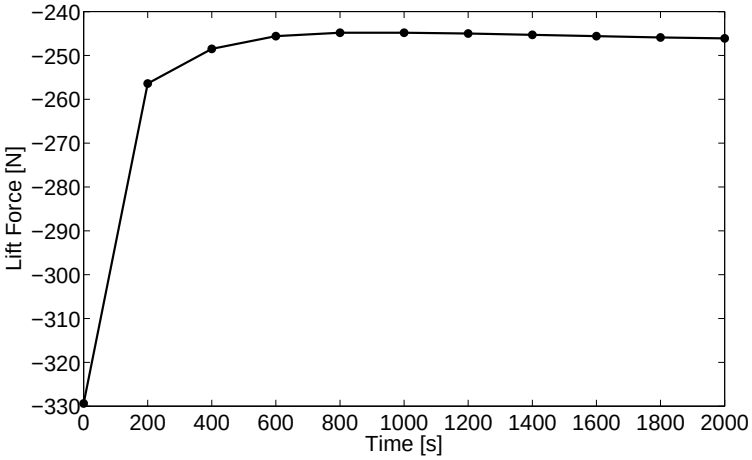

Figure 7.19: Lift force vs. time due to shear stress including wall temperature update.

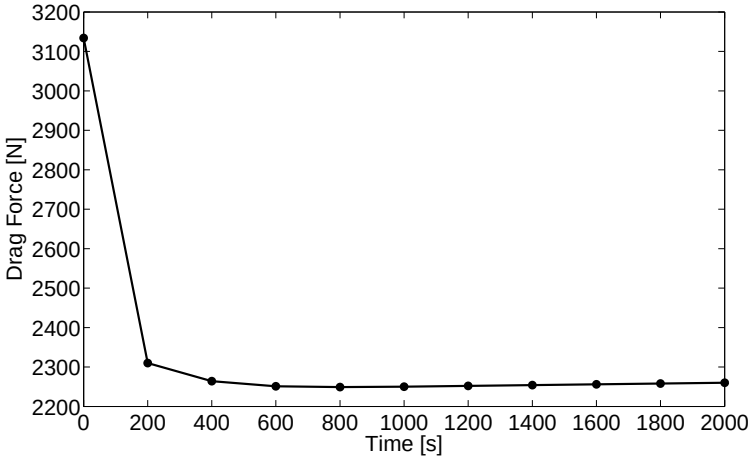

Figure 7.20: Drag force vs. time due to shear stress including wall temperature update.

ing total lift and drag forces are given in Fig. 7.21 and Fig. 7.22, respectively. Comparing Fig. 7.21 to Fig. 7.17, the trend of the total lift force curve is not found to change significantly as a result of updating the wall temperature at every time instant. However, comparing Fig. 7.22 to Fig. 7.18, a significant change in the trend of the total drag force curve is found when including the time-dependence of the wall temperature. The effect of heating of the structure is found to result in a decrease in total drag with respect to the initial value as shown in Fig. 7.22. As shown in Fig. 7.18, assumption of a constant wall temperature in the shear stress calculation would result in the prediction of an increase in total drag with respect to the initial value. Therefore, the effect of wall temperature on shear stress is important to consider in the modeling of hypersonic vehicle structures. For the results shown in Fig. 7.21 the maximum change in lift relative to the initial value is found to be a 1.3% decrease. Similarly, based on the results shown in Fig. 7.22, the maximum change in drag with respect to the initial value is found to be an 8.1% decrease.

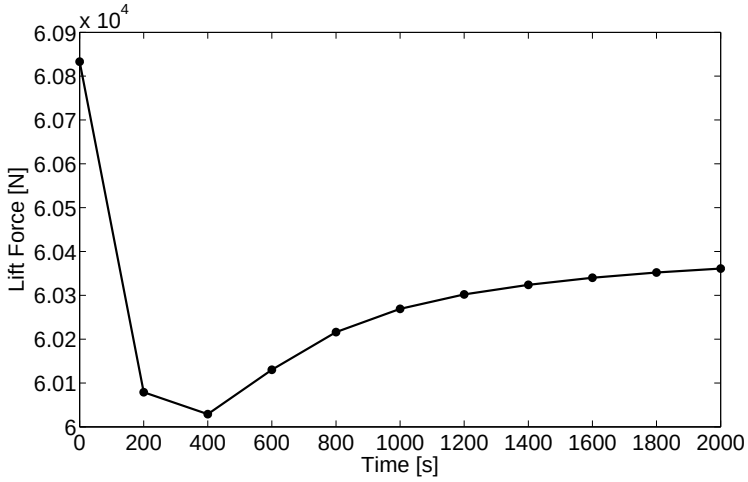

Figure 7.21: Total lift force vs. time including wall temperature update.

7.4 Concluding Remarks

An integrated aerothermoelastic modeling framework has been employed for assessment of the impact of quasi-static structural deformation due to thermal loads on aerody-

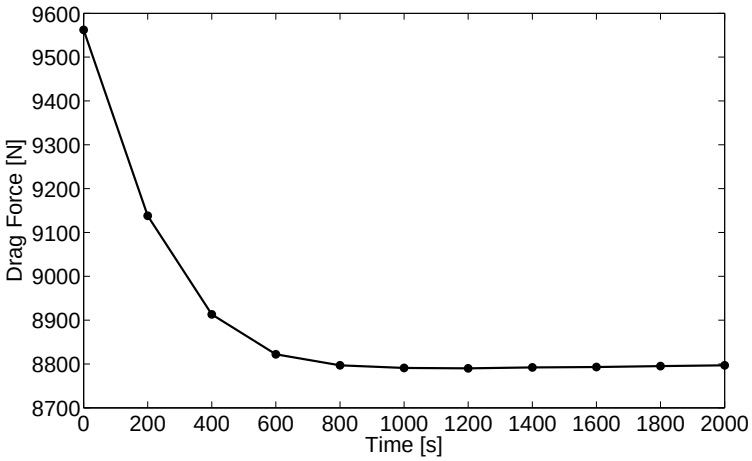

Figure 7.22: Total drag force vs. time including wall temperature update.

namic forces as they affect vehicle controllability. The framework represents a step toward assessing the impact transient aerothermoelastic effects HSV response. As the control surfaces are expected to account for a significant portion of the aerodynamic lift, drag, and moments acting on the vehicle, this study utilized a representative control surface structure to exemplify the methodology. The thermal model consists of a finite element formulation with heat flux and radiation boundary conditions at the outer surfaces. The nodal values of the heat flux boundary condition were calculated using Eckert's reference temperature method with flow properties evaluated over the undeformed configuration. Transient thermal finite element analysis was carried out to generate the nodal temperatures at the time instants of interest.

The temperature distributions were then used at the selected time instants to generate thermal loads on the structure and linear static structural finite element analysis was performed to calculate nodal displacements. With the nodal displacements known, the deformed configuration was generated for the purposes of aerodynamic analysis. The oblique shock and Prandtl-Meyer expansion fan relations were used to calculate the quasi-steady aerodynamic flow parameters over the deformed control surface. Note that this study employed these relations in a local sense and used relative flow turning angles between nodes

to capture the spatial variation in flow properties resulting from deformation. Integration of the calculated pressures over the top and bottom surfaces yielded the total aerodynamic lift and drag forces acting on the control surface.

The aerothermoelastic solution process was carried out at selected time instants to investigate how the lift and drag change over time for a constant-Mach, constant-altitude cruise trajectory. Due to the 6° angle of attack, the temperature on the bottom surface was found to be greater than that on the top surface. Transient thermal results showed that the temperature at the leading edge of the root on the bottom surface exceeds 1,400 K, while the temperature at the leading edge of the root on the top surface only reaches 923 K. This temperature difference between the bottom and top surfaces of the structure leads to a concave up curvature resulting from differential thermal expansion. As a result of this curvatuve, the flow is compressed along the chordwise direction over the top surface and is expanded along the chordwise direction over the bottom surface. Deformation due to thermal loads therefore leads to a spatial variation in the aerodynamic pressures. These pressures were integrated over the outer surfaces of the structure at selected time instants to assess the effect of deformation on overall control surface lift and drag forces. The maximum relative change in lift was found to be 1.3% and the maximum relative change in drag was 8.1% as compared with the undeformed case.

Chapter VIII

Unsteady Reduced-Order Aerothermoelastic Modeling

This chapter addresses the use of the unsteady, reduced-order aerothermoelastic framework described in Chapter VI. The unsteady framework employed here uses reduced-order models for the thermal and structural dynamics solutions as opposed to full-order finite element models. Additionally, this chapter also employs a reduced-order model for the aerodynamic heating solution as opposed to using the Eckert reference temperature formulation. Because ROMs are used in the unsteady framework, one component of this chapter involves addressing the error incurred via the use of reduced-order representations. In order to assess the error of each ROM, representative simulations are conducted and the output of the ROM is compared with the output of the corresponding full-order solution. For the transient thermal and structural dynamic components, the full-order solution is taken to be the high-fidelity finite element solution. For the aerodynamic heating component, the full-order solution is taken to be that obtained from a high-fidelity CFD model. Once the error is characterized for each ROM, the ROMs are integrated into the unified aerothermoelastic simulation environment. Representative simulations are then conducted using this framework in order to assess the impact of aerothermoelastic effects on overall HSV dynamics and controllability.

8.1 Overview of Formulation

Recall that Chapter VII discussed the use of a quasi-steady framework in order to assess the impact of deformation due to thermal loads on control surface lift and drag. While the thermal loads are slowly changing and result in a structural response that is close to quasi-static, an unsteady framework is required to capture structural response to the complete combined loading environment experienced by HSV structures. In addition to thermal loads, an HSV structure will experience loads due to aerodynamic pressures, vehicle rigid body motion, actuator inputs, and acoustic pressure. These additional loads are expected to be capable of producing a dynamic structural response, and thus an unsteady framework is required. Thus, this chapter investigates the impact of aerothermoelastic effects using models that capture transient phenomena.

The quasi-steady framework of Chapter VII made use of full-order models for the structural and thermal solutions (based on finite element representations) and a fundamental model for the aerodynamic heating solution (based on the Eckert reference temperature method). Due to the large numbers of states involved in the thermal and structural representations of the HSV structures of interest in this dissertation, use of full-order thermal and structural models within a fully unsteady aerothermoelastic simulation framework is not desirable. In order to reduce the number of states in the transient thermal model, this chapter employs a reduced-order thermal based on POD as described in Chapter II. Similarly, the Ritz-based modal solution methodology described in Chapter IV is employed for the structural dynamic solution.

In addition to the thermal and structural ROMs, the aerothermoelastic framework employed in this chapter also makes use of a CFD-based aerothermal ROM for the aerodynamic heating computation as opposed to Eckert reference temperature formulation employed in Chapter VII. As described in Section A.2.2 of Appendix A, the reduced-order aerothermal model (ROAM) is based on a parameterization of the variables that govern the aerodynamic heating process. While the ROAM is not the work of the author of this dis-

sertation, a brief overview of its implementation is presented here to highlight the manner in which it interfaces with the other components of the reduced-order aerothermoelastic solution process. The parameters that comprise the ROAM consist of the flight condition parameters Mach number (M_∞), angle of attack (α), and altitude (h). Additionally, the heat flux is a function of the structural deformation and the wall temperatures, T_w. As described in Appendix A, the ROAM takes advantage of the fact that the structural and thermal ROMs use reduced-basis representations of the response. Thus, the wall temperature is parameterized in terms of the thermal POD modal coordinates, $c_i(t)$, and the structural deformation is parameterized in terms of the structural modal coordinates, $d_i(t)$. Note that the maximum number of parameters used in the aerothermal ROM is limited. Thus, subsets of the total number of thermal POD modal coordinates and structural modal coordinates are used in the ROAM in order to reduce the number of parameters involved in the kriging process. For the current study, the number of thermal POD modal coordinate parameters used in the ROAM, n_t, is chosen to be five. Similarly, the number of structural modal coordinate parameters employed in the ROAM, n_s, is also chosen to be five.

One main goal of this chapter is to demonstrate the coupling of multiple, dissimilar ROMs within an unsteady aerothermoelastic framework and to assess the accuracy of each ROM under fully coupled conditions. While ROM error assessments were conducted in previous chapters for the various ROMs in isolation, this chapter focuses on the resulting ROM error when fully coupled effects are considered in the validation cases. Once the accuracy of each ROM is characterized, the framework is used to quantify the impact of aerothermoelastic effects on the net aerodynamic forces generated by a representative HSV control surface. Furthermore, studies are conducted to assess the necessary robustness of the HSV control system required to account for changing aerodynamic forces under aerothermoelastic effects.

8.2 Control Surface Model

The control surface model used in the current chapter is based on the same geometry that was shown in Fig. 3.2 and Fig. 3.3 in Chapter III. These figures giving the planform and cross-sectional geometry are shown again in Fig. 8.1 and Fig. 8.2, respectively, for reference.

The finite element representation used for the full-order thermal and structural modeling aspects of the current study was given in Fig. 4.15 of Chapter IV and is shown again in Fig. 8.3 with the top surface removed for visualization purposes. As in Chapter IV, the model consists of an outer heat shield layer, a middle insulation layer, and an inner skin layer along with chordwise and spanwise stiffeners. This material stacking scheme is depicted in Fig. 3.4 of Chapter III. The materials for the heat shield, insulation, and skin layers are René 41, Min-K, and TIMETAL 834, respectively. The heat shield layer and insulation layer are each 3.8 mm thick, and the skin layer is 6.35 mm thick. The material used for the stiffeners is TIMETAL 834 and the thickness of all stiffeners is 25.4 mm (1 in). The structural and thermal material properties used in the model are given in Table 3.1 and Table 3.2 of Chapter III. The model contains 2,812 thermal degrees of freedom and 8,074 structural degrees of freedom.

The heat shield and insulation are each modeled using one layer of 6-node solid wedge elements, resulting in two elements in the thickness direction of the TPS. Recent work [162] suggests that refinement of the mesh in the thickness direction of the TPS may improve the thermal solution, however this is not explored in the current work. The top and bottom skins and stiffeners are modeled using 3-node, 2-dimensional triangular elements. Of the 6,886 elements in the model, 3,456 are solid elements and 3,430 are triangular elements. The control surface is taken to be all-moveable about a hinge line located at the mid-chord [60] and will thus be connected to the vehicle main body through a torque tube. This attachment is modeled by constraining the region indicated by the gray circle in Fig. 8.3 in all degrees of freedom. In addition, the nodes at the root are constrained against translation in the y

direction. Because the stiffness of the insulation layer is neglected, rigid (RBE2) elements are used between each skin node and the corresponding node at the outer surface of the insulation layer to prevent singularities in the solution.

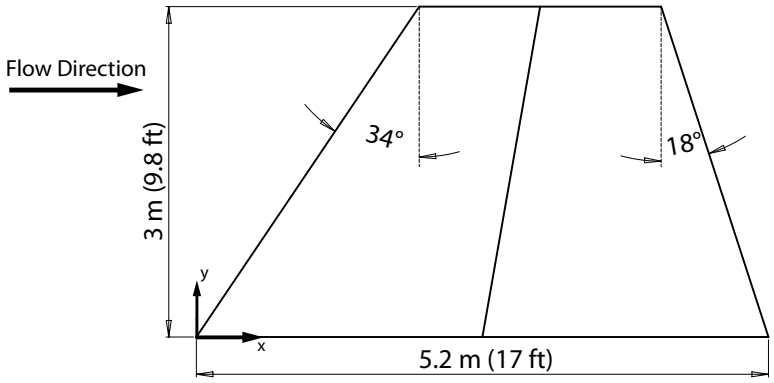

Figure 8.1: Planform geometry of control surface model.

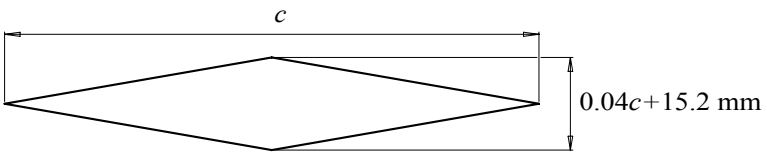

Figure 8.2: Cross-sectional geometry of control surface model.

8.3 Results and Discussion

8.3.1 Selection of Thermal and Structural Modes

In order to use the various ROMs in the aerothermoelastic solution, thermal and structural mode shapes must first be selected. The thermal POD modes are extracted from temperature snapshots which are representative of the expected dynamics in order for the basis to most closely span the space of the transient thermal solution throughout the simulation. The temperature snapshots are taken by sampling the transient temperature distribution every second from 0 - 5,000 s for the case of $\alpha = 6°$, Mach 8, at an altitude of 26 km (85,000

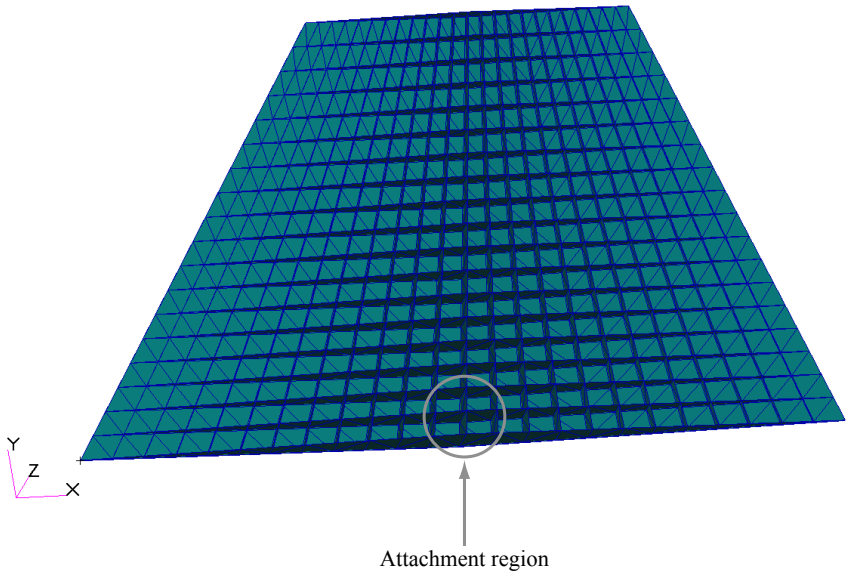

Figure 8.3: Finite element model of control surface used in study.

ft). For this simulation, Δt_{AE} and Δt_{HT} are each 1 s and Δt_{AT} is 4 s. To calculate the aerodynamic heating in this simulation, the Eckert reference temperature method is used. The details of the implementation of the Eckert reference temperature formulation are given in Appendix A. Using the 5,001 snapshots, the thermal snapshot matrix is assembled, its SVD is taken, and the POD modes are extracted. The first 24 eigenvalues of the correlation matrix are given in the semi-log plot shown in Fig. 8.4. Based on the magnitudes of the eigenvalues, the first 12 POD modes are used in the reduced-order thermal solution.

The strategy for selecting the structural reference modes is to solve the free vibration problem at a reference thermal state that approximates the average temperature distribution (and thus, average stiffness distribution) over the length of a mission. These modes contain both the effect of material degradation with temperature as well as geometric stiffness effects due to thermal stresses. The thermal state at which to evaluate the structural reference modes is calculated by averaging the temperatures for each node of the model over the 5,001 thermal snapshots used to generate the thermal modes. Contour plots showing the temperature distribution of the reference thermal state are given in Fig. 8.5. Although the maximum temperature on the bottom surface of the structure for the reference thermal state

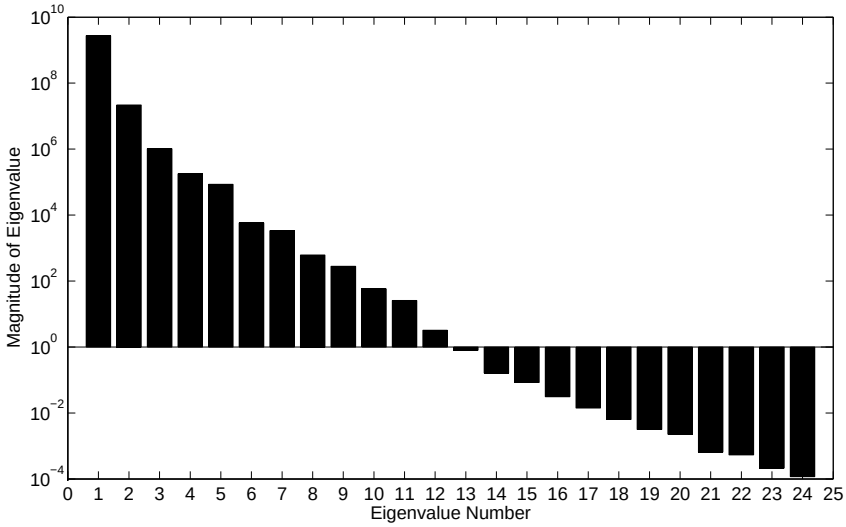

Figure 8.4: First 24 eigenvalues of correlation matrix.

exceeds the maximum application temperature of the heat shield, temperature-dependent material property data has been extrapolated beyond this point and subsequent simulations will bound the flight parameters to ensure that the maximum temperature stays within feasible range.

The structural ROM utilizes the first six structural dynamic reference modes at the reference thermal state which are given in Fig. 8.6. The structural displacements are expected to be dominated by thermal loads early in the transient as the structure approaches thermal equilibrium and the bottom surfaces heats faster than the top surface for positive angles of attack. The thermal loads change on a slow time scale, and it is expected that the structural response to the thermal loads can be approximated in a quasi-static manner. Therefore, accuracy of the structural ROM is expected to increase by augmenting the original six-mode basis with a seventh mode that is computed based on the static deformed configuration due to the applied thermal loads in the reference thermal state. The inclusion of this mode is likely to capture the quasi-static response due to slowly changing thermal loads which would otherwise not be captured with the original six structural dynamic eigenmodes. This additional seventh mode is shown in Fig. 8.6(g). To assess the effect of including this mode, structural ROM validation cases are run with both the six-mode and seven-mode bases.

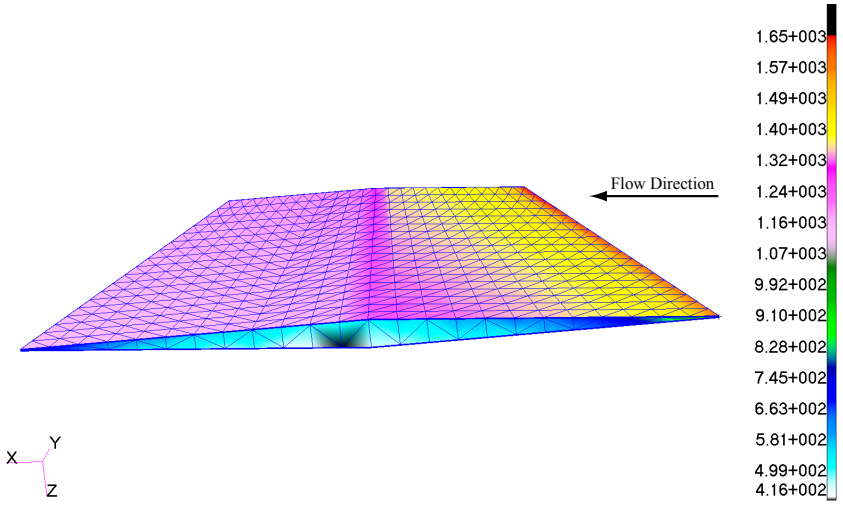

(a) Bottom surface temperatures.

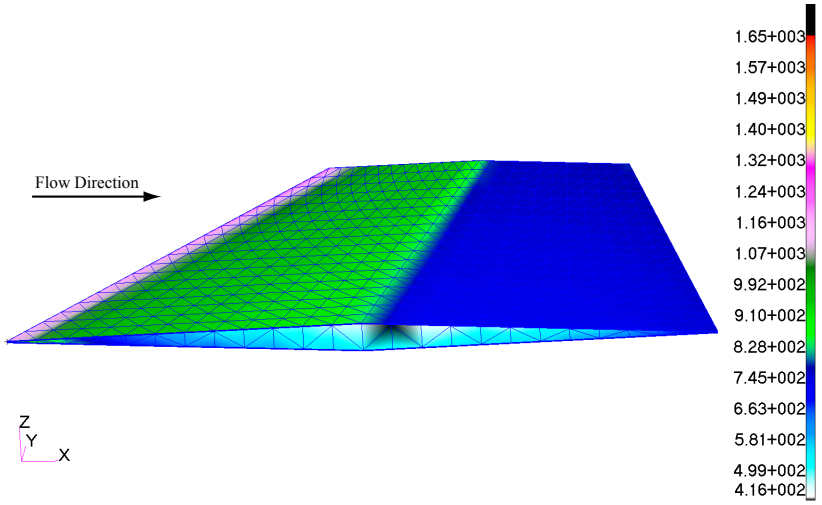

(b) Top surface temperatures.

Figure 8.5: Temperature distribution [K] at reference thermal state over outer surfaces of structure.

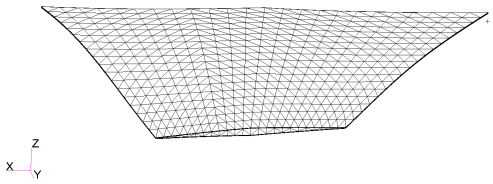

(a) Mode 1: 25 Hz.

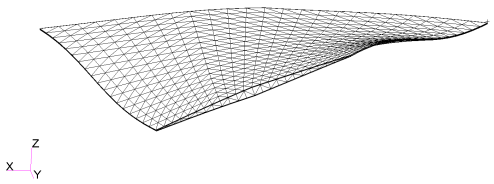

(b) Mode 2: 35 Hz.

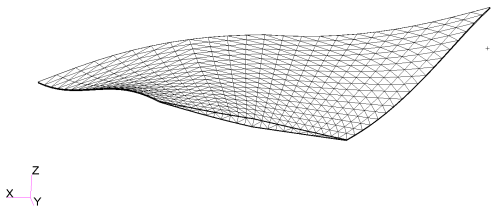

(c) Mode 3: 52 Hz.

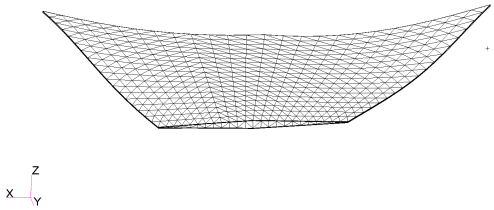

(d) Mode 4: 54 Hz.

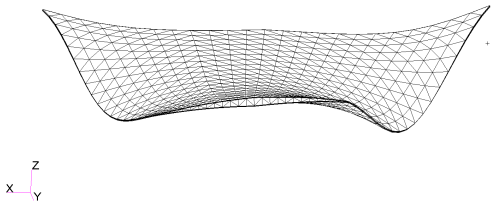

(e) Mode 5: 83 Hz.

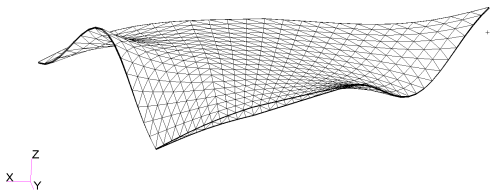

(f) Mode 6: 93 Hz.

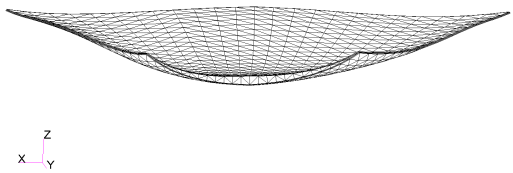

(g) Mode 7: Based on static deflection due to thermal loads in reference thermal state.

Figure 8.6: Structural mode shapes based on reference thermal state.

8.3.2 Summary of ROM Error Characterization

To validate the various ROMs, sample aerothermoelastic cases are run to compare each ROM against the corresponding high-fidelity solution. The error incurred due to model reduction is quantified using two different error metrics. The first is the normalized root mean squared error (NRMSE). Expressed as a percentage, the NRMSE is given by

$$\text{NRMSE } [\%] = \frac{\sqrt{\frac{1}{s}\sum_{i=1}^{s}\left(\text{ROM}_i - \text{Full}_i\right)^2}}{\text{Max(Full)} - \text{Min(Full)}} \times 100, \tag{8.1}$$

where i is the i-th nodal value of interest, "ROM" represents a solution vector of the reduced-order model, "Full" represents a solution vector of the full-order model, and s is the total number of data points in the solution vector. The second error metric to be used in validation of the reduced-order models is the L_∞ error. Expressed as a percentage, the L_∞ error is given by

$$L_\infty \ [\%] = \frac{\text{Max}\left(|\text{ROM} - \text{Full}|\right)}{\text{Max(Full)} - \text{Min(Full)}} \times 100. \tag{8.2}$$

A summary of the average NRMSE and L_∞ for each ROM is given in Table 8.1. Note that the average error is calculated differently for the thermal and structural ROMs than for the aerothermal ROM due to differences in the way the validation of each are carried out. For validation of the thermal and structural ROMs, aerothermoelastic simulations are run and the error of the ROM with respect to the corresponding full-order model is computed over the duration of the simulation as a function of time. Thus, the average errors for the thermal and structural ROMs given in Table 8.1 are calculated by averaging the corresponding error metric over the duration of the simulation. The case IDs over which the simulation errors are time-averaged are given in the table. The flight conditions corresponding to each case ID are detailed in the next section. Validation of the aerothermal ROM is carried out by generating 500 evaluation cases with the parameters for each point chosen based on

Latin Hypercube parameter space sampling. The average error of the aerothermal ROM is calculated by averaging each error metric over the 500 evaluation cases. The use of the 500 evaluation cases from Latin Hypercube Sampling is denoted in table as: "From LHS". As this study represents the first attempt to integrate transient thermal, structural dynamic, and aerothermal ROMs into a unified aerothermoelastic framework, specific areas for ROM improvement have been brought to light by this study. However, the primary focus of this chapter is to implement the ROM framework and use it to assess the effect of aerothermoelasticity on HSV performance. Detailed analysis of the trade-off between number of aerothermoelastic states and ROM accuracy as well as development of techniques for improving the error of the ROMs is not within the scope of the current chapter.

Table 8.1: Summary of average error of the various ROMs for selected cases.

ROM	Case	Average NRMSE [%]	Average L_∞ [%]
Thermal	1RF	2.19	16.4
	2RF	4.52	28.8
Structural	4FR (7 Mode)	8.52	28.7
Aerothermal	From LHS	1.46	7.74

8.3.2.1 Validation of Reduced-Order Thermal and Structural Models

Two different sets of flight conditions are used for validation of the thermal and structural ROMs. The altitude, Mach number, angle of attack, time step sizes, and initial temperatures for each case are summarized in Table 8.2. The first letter in the case ID specifies the thermal model used and the second letter specifies the structural model used, where "R" denotes the ROM and "F" denotes the full-order model. The second column in the table indicates whether the ROM or full-order model is used for the thermal solution, and the third column indicates whether the ROM or full-order model is used for the structural solution. Note that the full-order structural model is used in the thermal ROM validation cases (cases 1RF and 2RF), and the full-order thermal model is used in the structural ROM

validation cases (cases 1FR and 2FR). The Eckert reference temperature method is used to calculate aerodynamic heat flux for all thermal and structural ROM validation cases. The initial conditions for the thermal problem are a uniform temperature distribution of 293 K for all cases. Larger time steps are taken for the thermal ROM validation cases as the time scale of the heat transfer process is slower than that of the structural dynamics, and resolution of high-frequency structural dynamic oscillations is not of interest in the thermal ROM validation cases.

Table 8.2: Parameters for aerothermoelastic simulations used to validate thermal and structural ROMs.

Case	Thermal	Structural	h	M_∞	α	Δt_{AE}	Δt_{HT}	Δt_{AT}	T_0
1RF	ROM	Full-Order	26 km	8	3°	1 s	1 s	4 s	293 K
2RF	ROM	Full-Order	36 km	6	1.5°	1 s	1 s	4 s	293 K
1FR	Full-Order	ROM	26 km	8	3°	1 ms	1 ms	10 ms	293 K
2FR	Full-Order	ROM	36 km	6	1.5°	1 ms	1 ms	10 ms	293 K

Validation of the thermal ROM is performed by running aerothermoelastic simulations on the control surface using the Eckert reference temperature formulation for the thermal boundary conditions with both the full-order and reduced-order thermal models. Plots of the time-history of the POD error for cases 1RF and 2RF are given in Figs. 8.7 and 8.8, respectively. The NRMSE percentage error shows good agreement with the full-order model in both cases. Based on the time-history of the L_∞ error, it is evident that the thermal ROM has some difficulty capturing the steep temperature gradients within the initial portion of the transient. However, as the structure approaches thermal steady state and the temperature gradients and loads decrease, the accuracy of the thermal ROM improves.

The structural ROM is compared against the high-fidelity structural model using the same flight conditions as used in the thermal ROM validation cases. For the structural ROM validation cases, 1FR and 2FR, the aeroelastic time step size, Δt_{AE}, is chosen based on the desire to resolve the structural reference modes with a minimum of 10 temporal sampling points for the highest frequency mode. The highest frequency of the chosen

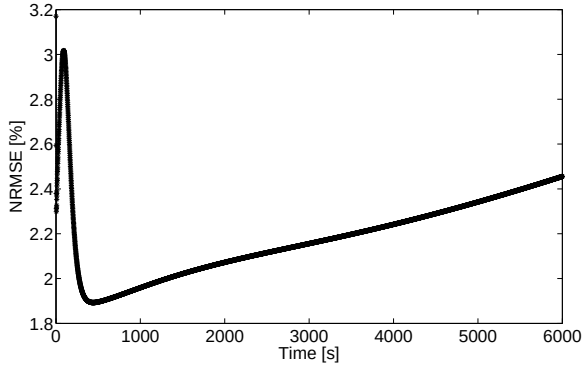

(a) NRMSE vs. time.

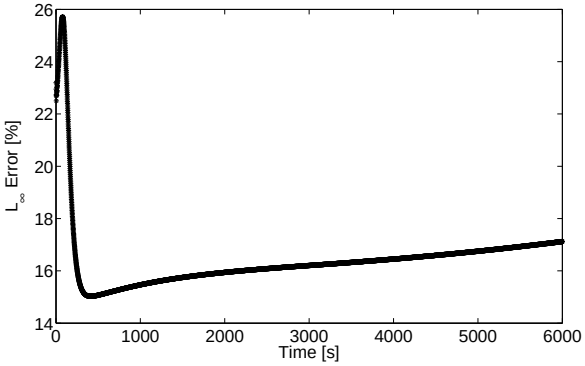

(b) L_∞ error vs. time.

Figure 8.7: Error of POD thermal model for case 1RF based on nodal temperatures.

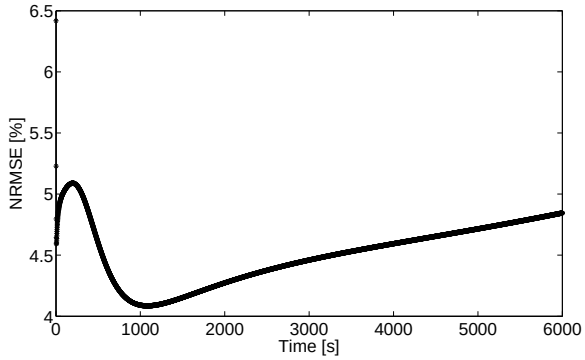

(a) NRMSE vs. time.

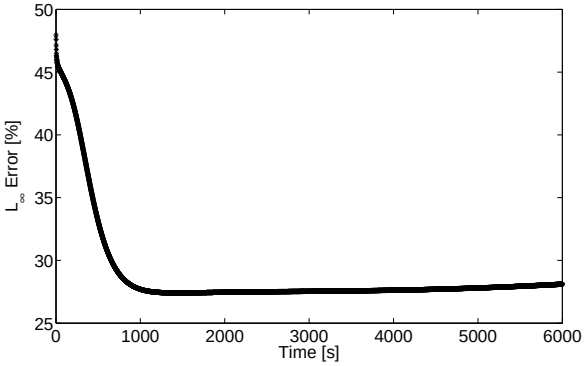

(b) L_∞ error vs. time.

Figure 8.8: Error of POD thermal model for case 2RF based on nodal temperatures.

reference modes is 93 Hz, however, recall that this mode was calculated at the reference thermal state with elevated temperatures. Thus, to account for the fact that the frequency of this mode may be slightly higher when the structure is at lower temperatures, Δt_{AE} is chosen to be 1 ms based on a maximum frequency of 100 Hz with 10 temporal sampling points within one cycle. The heat transfer time step is chosen to be of the same size as the aeroelastic time step ($\Delta t_{HT} = \Delta t_{AE}$) and the time between updates of the thermal boundary conditions, Δt_{AT}, is chosen to be 10 ms. The solution vectors used to compute the difference between the high-fidelity and ROM structural solutions are vectors of the displacement in the z direction for the nodes at the outer surface of the finite element model at each time instant. Due to the small size of the time step and relatively long run times, the error is computed for the time range 0 – 6 s. Plots of the time-history of the errors for case 1FR using both the six-mode and seven-mode bases are given in Fig 8.9. The error for case 2FR is shown in Fig. 8.10. Both error metrics for both cases show an oscillating error in the initial part of the transient. This is due to initial high-frequency structural oscillations which are not captured by the structural ROM. As these oscillations are damped out, a decrease in the error of the structural ROM is observed. Note that these cases do not show a large difference in accuracy between the six-mode solution and seven-mode solution. This is likely due to the fact that the temperatures do not get high enough in the time range considered for the thermal loads to make a significant enough impact on the response. The structural dynamic response for longer time histories is studied next and will allow for further assessment of the difference between the six-mode and seven-mode structural ROMs over longer simulation times.

While a small aeroelastic time step size allows for the resolution of structural dynamic oscillations, in situations in which the thermal loads are dominant over the aerodynamic loads, it may be possible to capture the structural response with a larger aeroelastic time step because the thermal loads change on a much slower time scale than the aerodynamic loads. The largest heat flux in the above validation cases is most likely to occur in the ini-

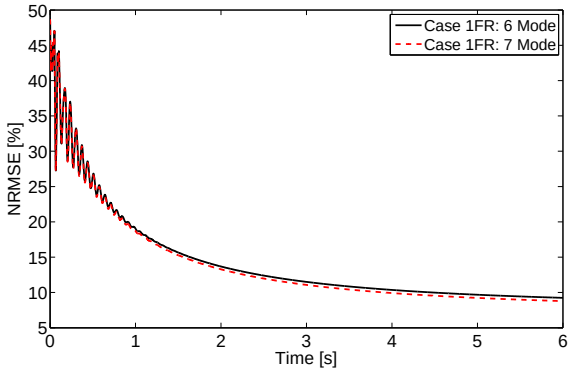

(a) NRMSE vs. time.

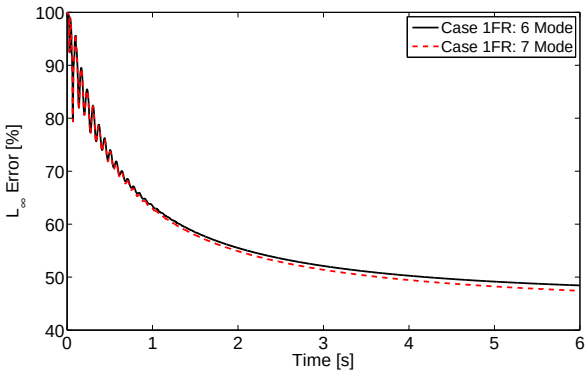

(b) L_∞ error vs. time.

Figure 8.9: Error of structural ROM for case 1FR based on z displacements of surface nodes.

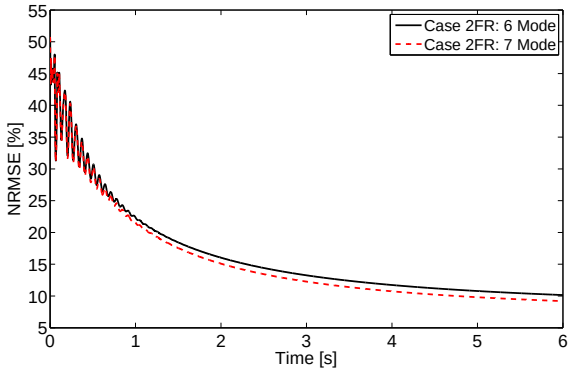

(a) NRMSE vs. time.

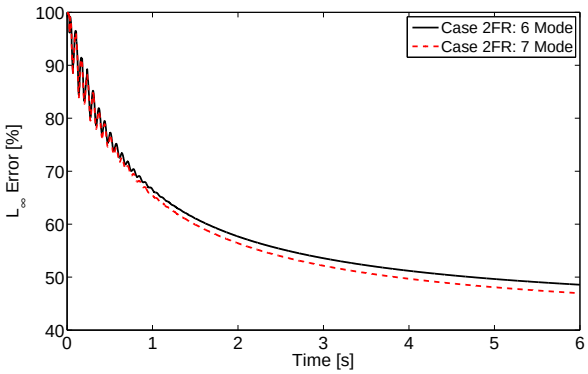

(b) L_∞ error vs. time.

Figure 8.10: Error of structural ROM for case 2FR based on z displacements of surface nodes.

tial transient of the simulation. This is due to the fact that the difference between the initial wall temperature of the structure and the initial recovery temperature is large, which leads to high aerodynamic heating. Furthermore, the difference between the initial wall temperature and the environment temperature is small which means that the heat flux radiated from the structure to the environment is small. Therefore, one might expect the highest thermal loads to occur in the initial part of the transient in cases where the structure has a low initial temperature. To assess the effect larger time step sizes on the accuracy of the structural response, simulations are run with the full-order thermal and structural models using different time step sizes. These cases are denoted 3FF and 4FF and are summarized in Table 8.3. Note that the time step sizes for case 4FF are each 100 times larger than those for case 3FF. Additionally, the difference in structural response between the full-order structural model and structural ROM for equal-sized large size time steps is assessed using case 4FR. This case is also summarized in Table 8.3.

Table 8.3: Parameters for aerothermoelastic simulations used to assess effect of time step size on structural response.

Case	Thermal	Structural	h	M_∞	α	Δt_{AE}	Δt_{HT}	Δt_{AT}	T_0
3FF	Full-Order	Full-Order	26 km	8	3°	1 ms	1 ms	10 ms	293 K
4FF	Full-Order	Full-Order	26 km	8	3°	0.1 s	0.1 s	1 s	293 K
4FR	Full-Order	ROM	26 km	8	3°	0.1 s	0.1 s	1 s	293 K

A comparison of the z displacement of node 247 which is located at the midchord of the tip on the bottom surface is given for both cases in Fig. 8.11. Though case 4FF fails to capture the high-frequency oscillations due to the initial excitation because of its larger time steps, these oscillations are subsequently damped out and the nodal responses show good agreement following the initial oscillations. To assess the difference in z displacements between cases 3FF and 4FF for all nodes at the surface, the NRMSE and L_∞ error are calculated for the time range 0.1 - 6 s in intervals of 0.1 s. Case 3FF as treated as the reference and the errors are calculated based on the difference in the solution vectors from cases 3FF and 4FF at each time instant. The plots of the error given in Fig. 8.12 show good

agreement between the two solutions beyond approximately 1 s. The error of the structural

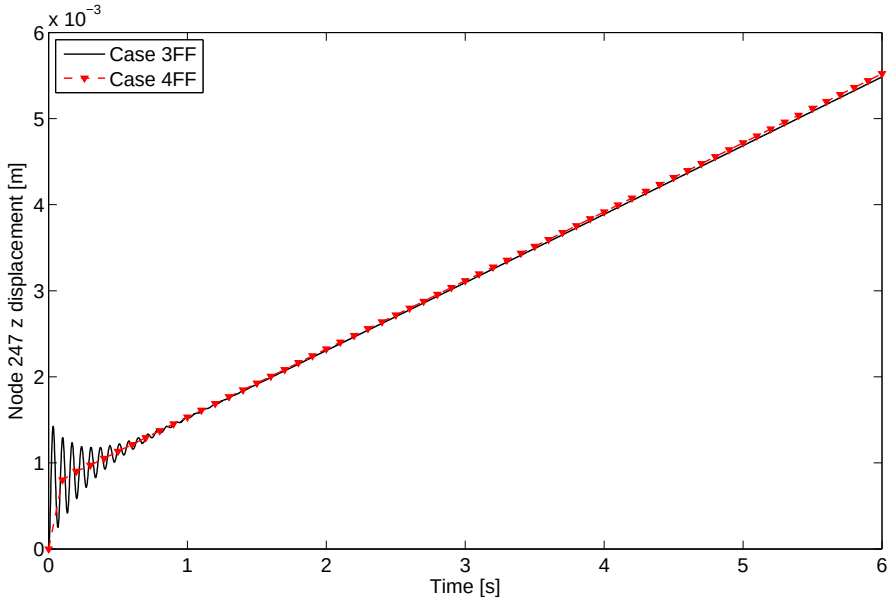

Figure 8.11: Node 247 z displacements: case 3FF vs. case 4FF

ROM for larger time steps is assessed by computing the NRMSE and L_∞ error between cases 4FF and 4FR. The use of larger time steps allows for error quantification over a longer time record for the same amount of computational time. Plots of the error as a function of time are given in Fig. 8.13. Improvement of the structural ROM by addition of the seventh mode is observed in Fig. 8.13 after approximately 50 s. This is likely due to the fact that by this time the temperatures have increased to the point where the thermal loads have a significant impact on the structural response. Though the initial NRMSE of case 4FR is approximately 39%, it improves to below 10% within 5 s. The displacement histories of node 247 for cases 4FF and 4FR with both the six-mode and seven-mode models are given in Fig. 8.14 to illustrate the level of structural displacements for these flight conditions.

8.3.2.2 Validation of Reduced-Order Aerothermal Model

As the ROAM is not the work of the author of this dissertation, detailed discussion of the error associated with this component is omitted from the discussion. However, a summary

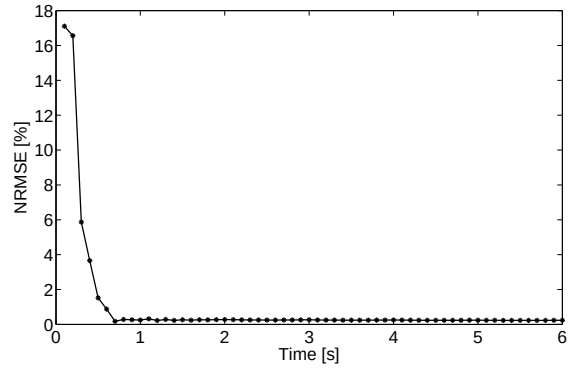

(a) NRMSE vs. time.

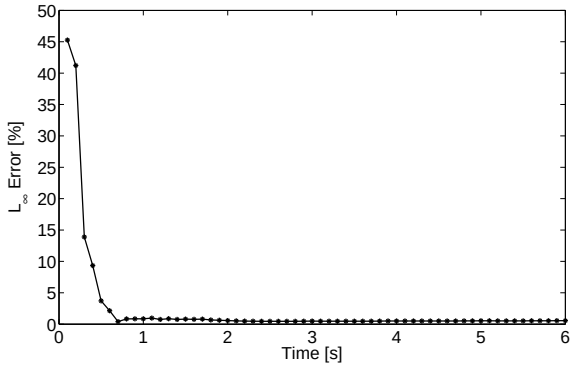

(b) L_∞ error vs. time.

Figure 8.12: Error of case 3FF with respect to case 4FF based on z displacements of surface nodes.

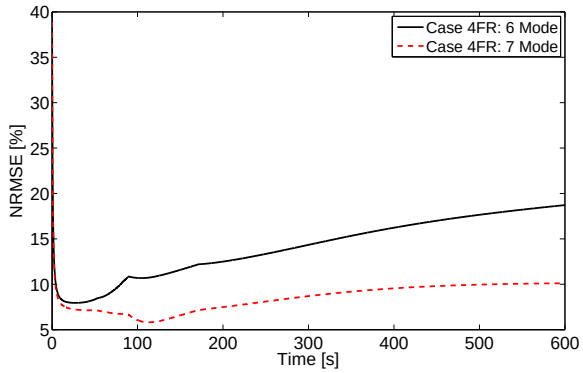

(a) NRMSE vs. time.

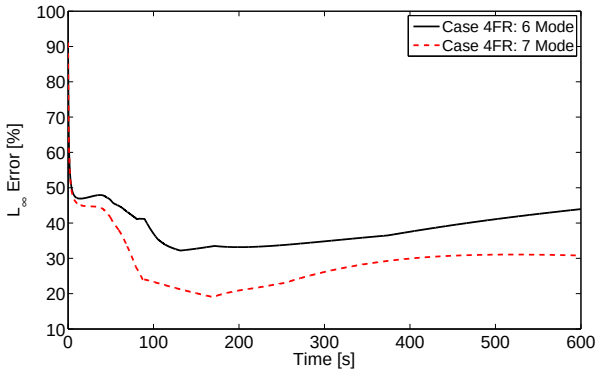

(b) L_∞ error vs. time.

Figure 8.13: Error of case 4FR with respect to case 4FF based on z displacements of surface nodes.

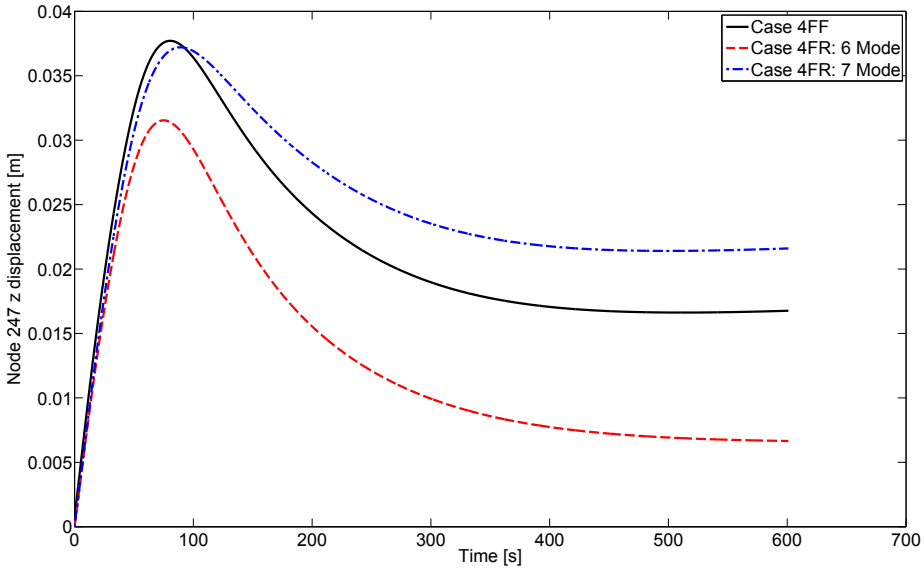

Figure 8.14: Node 247 z displacements: case 4FF vs. case 4FR.

of the ROAM errors is presented to provide context of the accuracy of this component of the solution. Before selecting the sample points to be used in generating the ROAM, bounds must first be established on each of the parameters involved. A summary of the bounds chosen for the parameters in the ROAM is given in Table 8.4. In the table, w represents the nodal deflections of the structure in the z direction, L is the distance from the attachment point (located at the root mid-chord) to the node of interest, and T_∞ is the freestream temperature. The bounds on the flight condition parameters M_∞, α, and h are established based on the operation range of interest for the study. The bounds on w/L are established based on assumed linearity of the structural response. Finally, the bounds on T_w are chosen based on the operating conditions as well as the maximum application temperature of the materials that compose the structure. For this study, the ROAM is generated based on 2,000 sample points optimized to maximize the minimum distance between the points over 500 iterations.

Table 8.4: Bounds of parameters used to construct the aerodynamic heating ROAM.

5.0	$\leq M_\infty \leq$	10.0
-5.0°	$\leq \alpha \leq$	5.0°
25.0 km	$\leq h \leq$	45.0 km
-10%	$\leq w/L \leq$	10%
T_∞	$\leq T_w \leq$	1500 K

Since this work represents an initial step in coupling aerodynamic heating, heat transfer, and structural dynamic reduced-order models, the number of modes required from the heat transfer and structural reduced-order models in order to accurately model the aerodynamic heating is uncertain. Thus, as a first step in accessing the aerothermoelastic response of the control surface, the first five thermal POD modes (n_t = 5) and the first five free vibration structural modes (n_s = 5) are included in the ROAM. The ROAM is generated based on 2,000 sample points and is evaluated based on 500 sample points. Both sets of sample points are created using LHS. The NRMSE and L_∞ error metrics are used to quantify the accuracy of the ROAM. These error metrics are computed for each evaluation case,

resulting in a vector of 500 NRMSE and L_∞ values for the ROAM. In order to provide scalar metrics of the model quality, the average NRMSE and average L_∞ over the 500 evaluation cases are computed, and the overall maximum L_∞ error over all 500 evaluation points is identified. The average NRMSE is 1.46%, the average L_∞ error is 7.74%, and the overall maximum L_∞ at any point on the control surface over all 500 evaluation points is 27.54%. It is important to note that a concern for this approach in high Mach number flows is accurate shock-capturing [163]. However, the average NRMSE and average L_∞ demonstrate that this does not significantly degrade the model.

8.3.3 Influence of Aerothermoelastic Effects on Aerodynamic Forces

The ROM error analysis presented above has revealed that enrichment of the basis representations for the transient thermal and structural dynamic ROMs may improve the level of errors in the ROMs, particularly early in the transient when the dynamics are changing on a relatively fast time scale. As improvement of ROM accuracy is not within the scope of the current chapter, it is not discussed further in the current study. The ROMs are now used within the aerothermoelastic framework to assess the effect of aerothermoelasticity on the total lift and drag forces acting on the control surface. All simulations from this point forward use the corresponding ROM for the aeroheating, heat transfer, and structural dynamic response components of the aerothermoelastic solution. For these simulations, aeroelastic iterations are first carried out to bring the structure to aeroelastic equilibrium prior to beginning the aerothermoelastic simulation. To find the total aerodynamic forces, the pressures are integrated over the outer surfaces of the structure. The pressures consist of a component in the direction of the local normal to the deformed configuration due to aerodynamic pressures and a component in the direction of the local tangent to the deformed configuration due to viscous stress. The viscous stress is computed using local skin friction coefficients for each finite element using an Eckert reference temperature formulation. Note that local normal and tangent vectors for each finite element are updated at each aeroelastic time step

based on the deformed configuration at the end of the time step.

The time-marching aerothermoelastic cases used for this part of the study are summarized in Table 8.5, where "LD" denotes that these cases are used for lift and drag assessment. Cases 1LD and 2LD represent constant-Mach, constant-α cruise at an initial uniform stress-free temperature of 293 K. These cases are run for longer time-histories (0 - 1,200 s) to allow the temperature distribution to more fully evolve and to assess the response over a wide range of thermal conditions. Cases 3LD and 4LD are based on the ascent phase of a proposed trajectory for a single-stage-to-orbit mission of a blended wing body configuration typical of a transatmospheric hypersonic vehicle [144]. Curve fits to the data points given in Ref. 144 are used to obtain the time-dependence of the altitude and Mach number and two different angles of attack are selected. The time-dependence of the altitude, $h_a(t)$, for the ascent cases 3LD and 4LD is given by

$$h_a(t) = -7 \times 10^{-5} t^2 + 0.06t + 25, \tag{8.3}$$

and the time-dependence of the Mach number, $M_{\infty,a}$, for cases 3LD and 4LD is given by

$$M_{\infty,a}(t) = 0.03t + 5. \tag{8.4}$$

As the ROMs in this work are valid for a specific range of flight parameters, only the Mach 5 – 10 portion of the ascent trajectory is considered. Difficulty arises in determining the initial temperatures for the Mach 5 – 10 ascent because the ROMs do not permit simulation from take-off to Mach 5. Thus to obtain the initial temperatures, a cruise condition at the initial altitude (25 km) and initial Mach number (Mach 5) is simulated for 163 s which is the amount of time the vehicle takes to reach Mach 5 for the given trajectory. This initial temperature distribution is denoted as "163 s cruise" in the table. After the initial cruise segment, the temperature distribution is stored for use as the initial temperature distribution for the ascent segment, time is reset to zero, and the ascent trajectory is commenced. As

the simulation time for these cases is shorter (0 - 172 s), the corresponding time step sizes for these cases are chosen to be smaller.

Table 8.5: Cases for assessment of transient lift and drag.

Case	h [km]	M_∞	α	Δt_{AE} [s]	Δt_{HT} [s]	Δt_{AT} [s]	T_0
1LD	26	8	3°	0.1	0.1	1	293 K unif.
2LD	36	6	1.5°	0.1	0.1	1	293 K unif.
3LD	$h_a(t)$	$M_{\infty,a}(t)$	3°	0.01	0.01	0.1	163 s cruise
4LD	$h_a(t)$	$M_{\infty,a}(t)$	1.5°	0.01	0.01	0.1	163 s cruise

First, the total lift force, L, and drag force, D, are calculated over the undeformed (rigid) control surface at initial flight conditions for each case. Aerothermoelastic simulation for the elastic control surface is then carried out for each case and the total lift and drag are calculated at each aeroelastic time step. Plots of the transient lift force for the two cruise trajectories are given in Fig. 8.15, and plots of the transient lift force for the two ascent trajectories are given in Fig. 8.16. Similarly, plots of the transient drag force for the cruise trajectories and ascent trajectories are shown in Fig. 8.17 and Fig. 8.18, respectively. These figures show results for both the rigid and elastic control surfaces. Note that the rigid case contains no aerothermoelastic effects and the skin friction is computed at initial flight conditions at a uniform temperature of 293 K.

To assess the relative impact of flexibility on the total forces, the percentage differences between the lift and drag of the elastic structure are calculated with respect to the lift and drag produced by the rigid structure. Results for the relative change in lift for the cruise trajectories and ascent trajectories are given in Fig. 8.19 and Fig. 8.20, respectively. Similarly, plots of the relative change in drag force for the cruise trajectories and ascent trajectories are given in Fig. 8.21 and Fig. 8.22, respectively. For cases 1LD and 2LD, there is an initial abrupt change in the lift and drag forces due to the high temperature gradients as the structure begins to heat from room temperature and approach equilibrium temperature. At the end of the time-history shown for these cases, the total lift and drag begin to level off as the temperature gradients in the structure decrease. For ascent trajectory represented

by cases 3LD and 4LD, both the lift and drag are monotonically decreasing for the complete duration of the simulation. The initial abrupt change in the aerodynamic forces that was seen in the cruise trajectory cases is not present in the ascent trajectory cases because the initial temperature distribution is much higher than that used for cases 1LD and 2LD. Though the trend of the elastic and rigid control surfaces is similar for both lift and drag in cases 3LD and 4LD, the percentage difference between rigid and elastic drag is more pronounced than that for the lift. Note that the initial percentage change in lift and drag for cases 3LD and 4LD is nonzero due to the fact that the aerothermoelastic solution is time-marched at a cruise condition prior to beginning the simulation such that the structure is in a thermoelastically deformed state at initial time (see Fig. 8.20 and Fig. 8.22).

To assess the level of heating for each of the cases, the maximum nodal temperature is plotted as a function of time for each of the cases. Maximum temperatures for the cruise and ascent trajectories are given in Fig. 8.23 and Fig. 8.24, respectively. For cases 1LD and 2LD, there is a steep increase in the maximum temperature in the initial portion of the transient as the structure heats up from room temperature. As the structure approaches equilibrium temperature, the gradient in the maximum temperature begins to decrease. For the ascent trajectory cases 3LD and 4LD, we see a monotonic increase in maximum temperature for the time range considered. For all cases, the maximum temperature remains below 1,500 K over the complete duration of the simulations.

To determine the effect of aerothermoelasticity on aerodynamic performance and necessary control input, the iterative routine described in Section 6.5 of Chapter VI is utilized. Cases 1LD and 2LD are used as example cases and α_{min} is updated and stored every time the thermal boundary conditions are updated. Thus, α_{min} is updated every 10 aeroelastic iterations (once per second) based on the relative time step sizes used for these cases. Recall that the initial (baseline) angle of attack is 3° for case 1LD and 1.5° for case 2LD. Plots of the time-history of α_{min} for the two cases are given in Fig. 8.25. Note that the maximum residue, $\mathcal{R}$, is 0.3 N for case 1LD and 0.05 N for case 2LD. As seen in the figures,

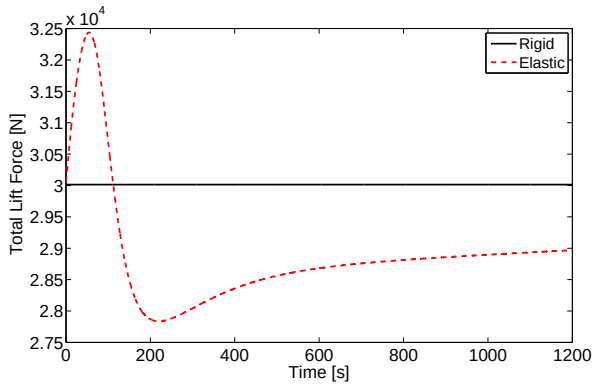

(a) Case 1LD.

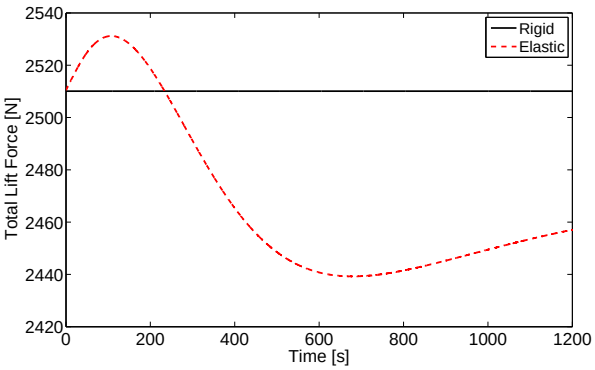

(b) Case 2LD.

Figure 8.15: Time-history of total lift force for cruise trajectories.

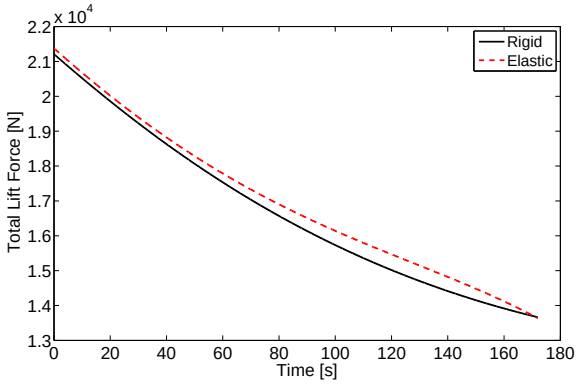

(a) Case 3LD.

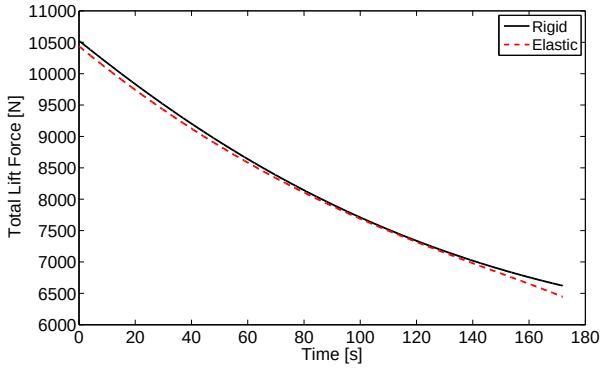

(b) Case 4LD.

Figure 8.16: Time-history of total lift force for ascent trajectories.

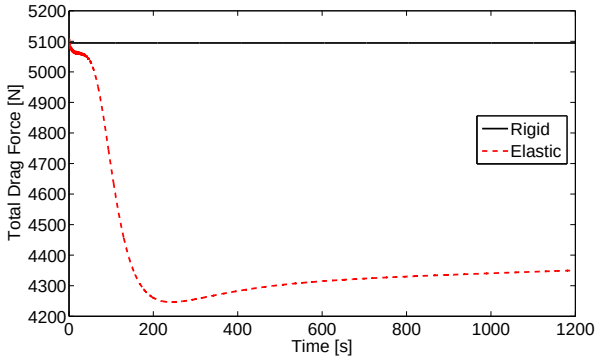

(a) Case 1LD.

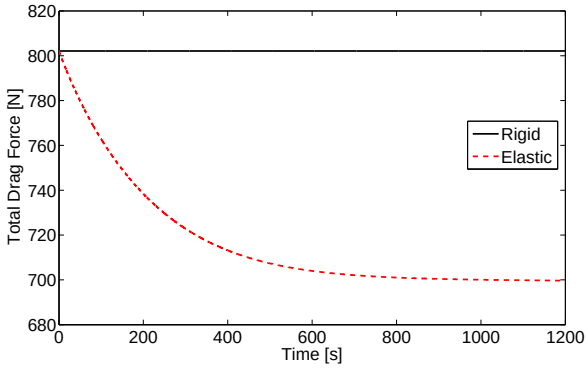

(b) Case 2LD.

Figure 8.17: Time-history of total drag force for cruise trajectories.

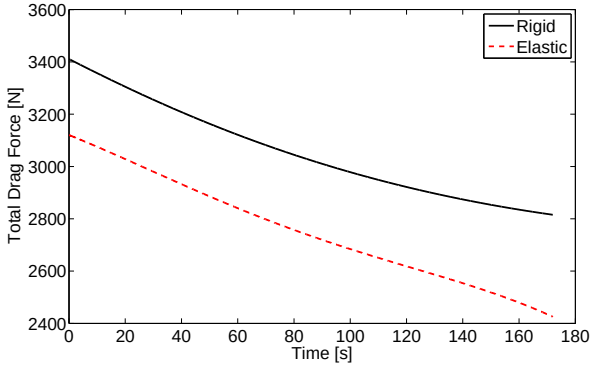

(a) Case 3LD.

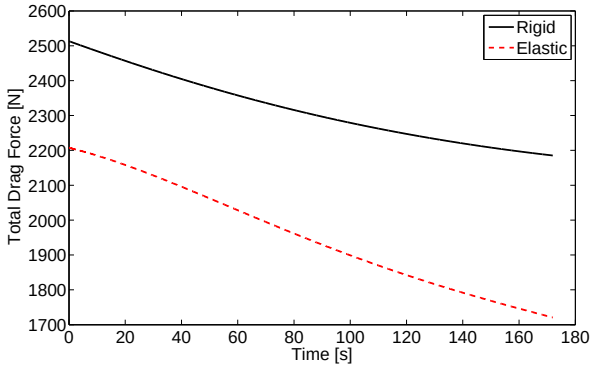

(b) Case 4LD.

Figure 8.18: Time-history of total drag force for ascent trajectories.

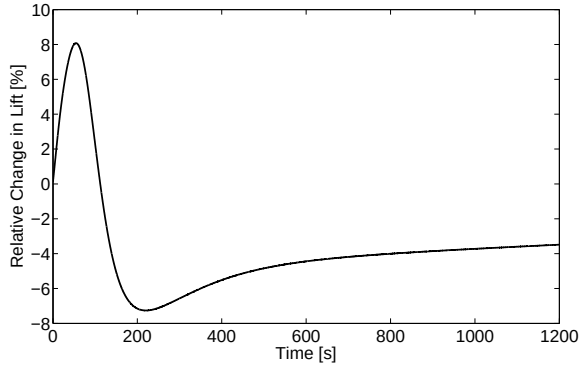

(a) Case 1LD.

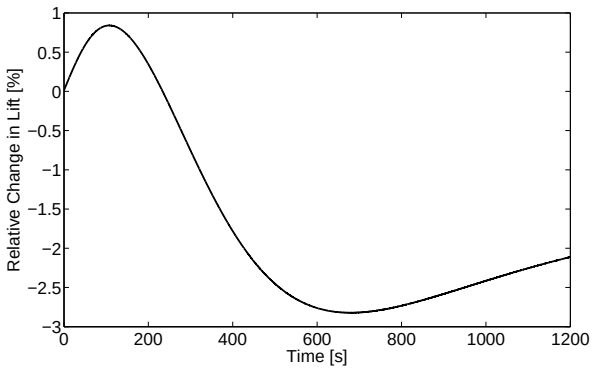

(b) Case 2LD.

Figure 8.19: Time-history of percentage change in lift force for cruise trajectories.

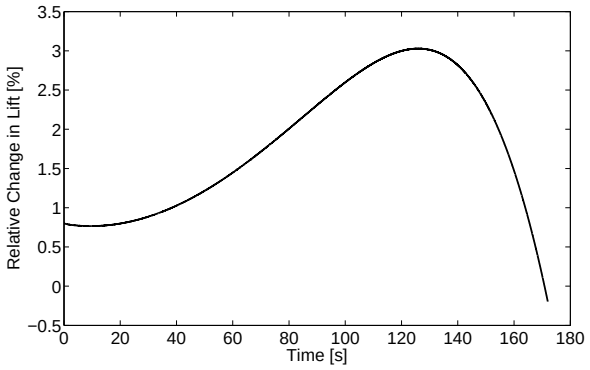

(a) Case 3LD.

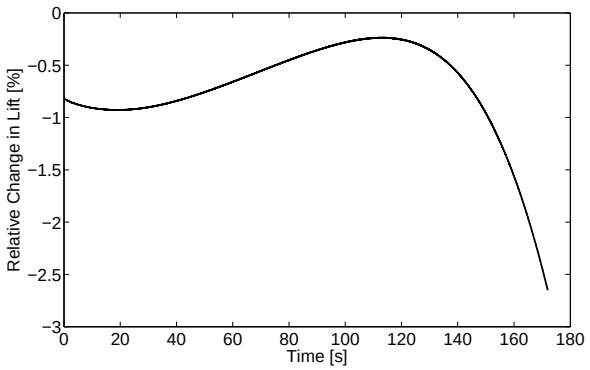

(b) Case 4LD.

Figure 8.20: Time-history of percentage change in lift force for cruise trajectories.

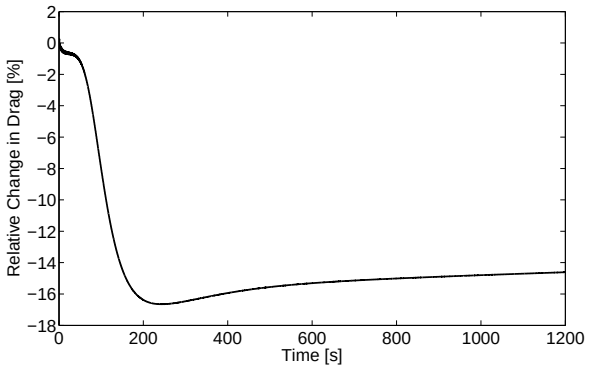

(a) Case 1LD.

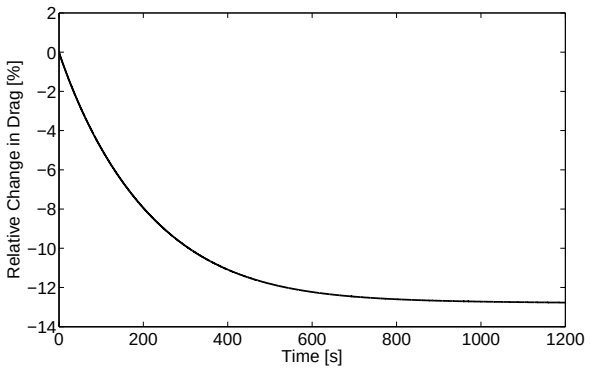

(b) Case 2LD.

Figure 8.21: Time-history of percentage change in drag force for cruise trajectories.

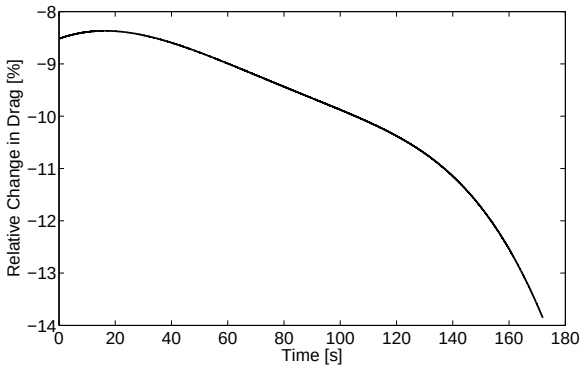

(a) Case 3LD.

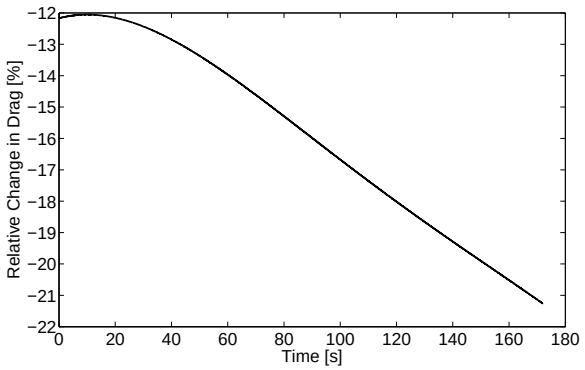

(b) Case 4LD.

Figure 8.22: Time-history of percentage change in drag force for ascent trajectories.

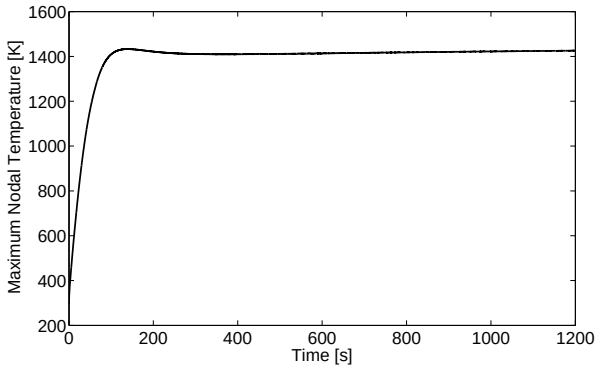

(a) Case 1LD.

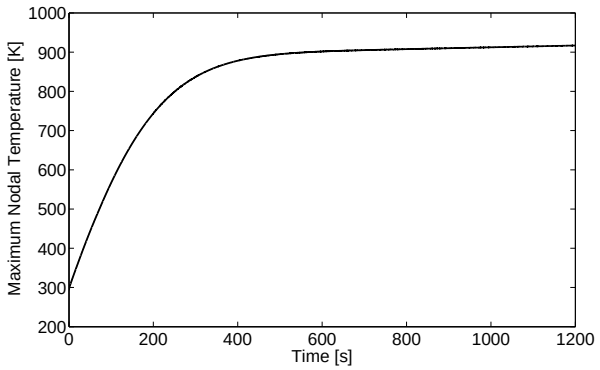

(b) Case 2LD.

Figure 8.23: Time-history of maximum nodal temperature for cruise trajectories.

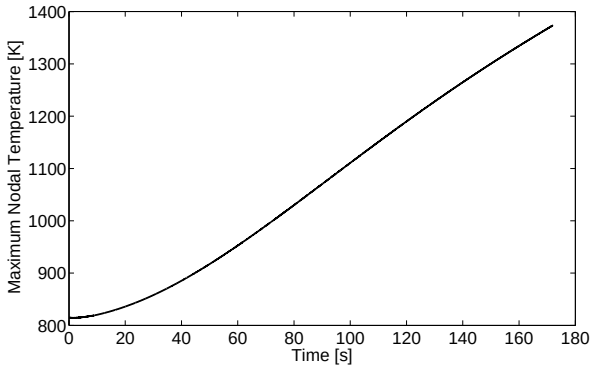

(a) Case 3LD.

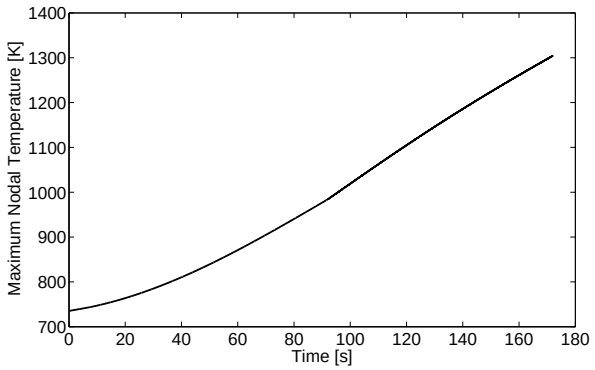

(b) Case 4LD.

Figure 8.24: Time-history of maximum nodal temperature for ascent trajectories.

the maximum absolute departure of α_{min} from the initial angle of attack is 7.6% for case 1LD and 2.8% for case 2LD. However, note that the largest departures from initial angle of attack occur early in the transient which is likely an effect of the low initial temperature and resultant large temperature gradients. For cases in which the initial temperature of the structure is higher, the deformation due to thermal loads will be lower and the impact on overall lift and drag will be less.

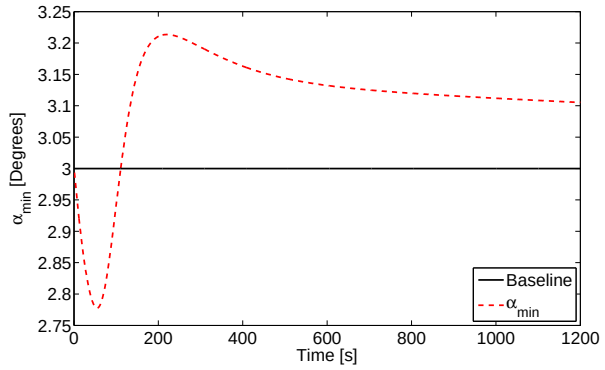

(a) Case 1LD.

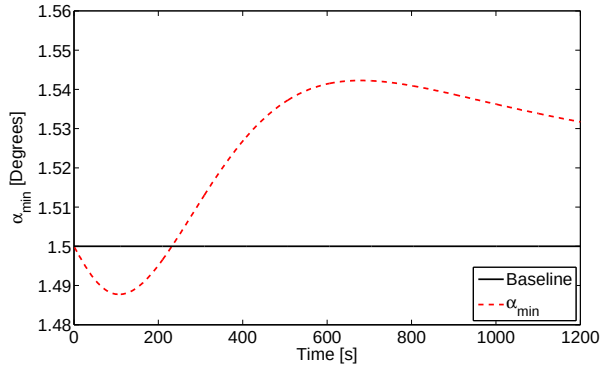

(b) Case 2LD.

Figure 8.25: Time history of α_{min} for cases 1LD and 2LD.

8.3.4 Assessment of Computational Cost

As this research is aimed at making aerothermoelastic analysis of HSVs feasible in a control evaluation and simulation setting, one important metric is the computational cost associated with the reduced-order framework. While reducing the number of aerother-

moelastic states for the purpose of control studies is the prime motivation for this work, simulation time is a practical consideration that must be taken into account. The average computational time for execution of each of the various components of the solution is given in Table 8.6 for both the full-order and reduced-order models. Note that the heat flux iteration using the reduced-order model also consists of calculation of the local skin friction coefficients for each element at the outer surface using the Eckert reference temperature method. The data assumes that the size of the aeroelastic time step is equal to the size of the heat transfer time step, and that one complete aerothermoelastic iteration contains ten aeroelastic subiterations ($\Delta t_{AE} = \Delta t_{HT}$, $\Delta t_{AT} = 10\Delta t_{AE}$). Therefore, one heat transfer iteration contains ten time steps of the thermal solution. The computational times for the unsteady aerodynamic iteration and aerodynamic force calculation are the same in both cases because the same model is used in both the full-order and reduced-order solutions. Table 8.6 also gives the average computational time to complete one full aerothermoelastic iteration for both the full-order and reduced-order models. Based on the relative time step sizes assumed, one aerothermoelastic iteration includes one heat flux and heat transfer iteration and ten structural iterations, unsteady aerodynamic iterations, and aerodynamic force calculations. The last column in Table 8.6 gives the ratio of the computational time for the full-order solution to that for the reduced-order solution. Recall that a summary of the average errors associated with each of the ROMs is given in Table 8.1.

The component of the reduced-order aerothermoelastic solution with the greatest computational cost is the structural iteration. Though a fixed basis is used for the structural dynamic response, the current framework still requires that finite element solver be called at every structural iteration to update the $8,074 \times 8,074$ physical stiffness matrix and pre- and post-multiply by the structural reference modes to obtain the generalized stiffness matrix. Recall that the physical stiffness update consists of updating the conventional stiffness matrix based on the temperature-dependence of material properties as well as solving a linear static problem to generate the geometric stiffness matrix. There exists potential for signif-

icant improvement in overall computational cost by utilizing reduced-order techniques to update the generalized stiffness matrix directly based on the temperature distribution. A kriging-based methodology for accomplishing this was discussed in Section 5.1.

Table 8.6: Comparison of computational cost between full-order and reduced-order models.

	CPU Time / Iteration [s]		
Iteration Type	Full-Order	Reduced-Order	Ratio
Heat Flux Iteration	375[a]	0.0924[b]	4,058
Heat Transfer Iteration (10 time steps)	0.215[b]	0.00246[b]	87.4
Structural Iteration (1 time step)	6.23[b]	4.78[b]	1.30
Unsteady Aerodynamic Iteration	0.162[b]		N/A
Aerodynamic Force Calculation	0.392[b]		N/A
Aerothermoelastic Iteration	443[c]	53.4[b]	8.30

[a] 17 2.60-GHz Opteron processors, 2.0 GB RAM.
[b] 1 2.53-GHz Intel Xeon E5540 processor, 3.0 GB RAM.
[c] Predicted time.

8.4 Concluding Remarks

This chapter presented a time-marching aerothermoelastic framework which makes use of reduced-order aerothermal, heat transfer, and structural dynamic models for computationally efficient simulation of hypersonic vehicles. The various components of the framework were fully coupled to capture the interactions among the various disciplines in a dynamic sense. The major components of the framework used for the various disciplines consist of:

- Aerothermal: CFD-based kriging surrogate with Latin Hypercube Sampling to calculate the aerodynamic heat flux at the outer surface
- Heat Transfer: Reduced-order POD modal formulation to obtain the transient temperature distribution

- Structural Dynamics: Ritz-based modal formulation to calculate the transient structural dynamic response

- Unsteady Aerodynamics: Piston theory unsteady flow solver with shock-expansion analysis to obtain steady flow conditions by turning flow through angle of attack

The time-step scheduling of the aerothermal, heat transfer, and structural dynamics solutions are intentionally partitioned to allow for different size time steps so that the different time scales governing the various processes can be resolved efficiently. The aerothermoelastic framework was applied to a representative HSV control surface as such a component is expected to have a strong impact on the overall vehicle flight dynamics.

Assessment of the transient lift and drag for four different sets of flight conditions provided insight into the impact of aerothermoelastic effects on the total aerodynamic forces. Of the two cruise trajectories considered, the maximum absolute relative changes in total lift and drag were 8% and 15%, respectively. Of the two ascent trajectories, the maximum absolute relative changes in total lift and drag were 3% and 21%, respectively. In general it appears that aerothermoelasticity has a larger effect on total drag than total lift. An iterative routine based on the angle of attack necessary to match the lift of the elastic control surface to that of the rigid control surface for the two cruise trajectories was utilized to assess HSV controllability under fully coupled aerothermoelastic effects. Of the two cruise trajectories considered here, the maximum deperature from the initial angle of attack was found to be 7.6%. However, this value is dependent on flight conditions and further study can provide insight into necessary variation in angle of attack for various maneuevers and trajectories. Furthermore, the degree to which aerothermoelasticity affects the forces generated by the control surfaces can be influenced by configuration parameters such as TPS thickness, skin thickness, overall size, etc. Use of the reduced-order framework presented in this chapter provides insight into the impact of aerothermoelasticity on hypersonic vehicles in a computationally efficient manner.

Chapter IX

Partitioned Vehicle Framework and Impact of Lifting Surface Inertia on Vehicle Response

This chapter describes a partitioned, time-marching formulation in which the individual substructures of the vehicle are modeled separately and forces and motion at the interface are exchanged between the two systems within each aeroelastic time step. The methodology is applied to a representative configuration consisting of an all-moveable hypersonic vehicle lifting surface model containing aerothermoelastic effects attached to a single degree of freedom oscillator representing the fuselage. Results are presented which demonstrate the agreement between the response obtained from the partitioned solution and that from a monolithic solution. The partitioned solution methodology is then used to investigate the impact of lifting surface-fuselage inertial coupling on overall vehicle dynamics. To further investigate elevator-to-pitch rate dynamics and lifting surface-fuselage inertial coupling, a control input corresponding to a change in lifting surface deflection angle is incorporated into the framework. Use of this input allows for assessment of the effect of lifting surface inertia as it impacts the relationship between elevator deflection angle and vehicle pitching moment.

9.1 Introduction

Chapter VIII discussed the use of an unsteady, reduced-order aerothermoelastic framework for HSV structures. That framework was used in Chapter VIII to assess the impact of control surface aerothermoelastic effects on the overall HSV dynamics and controllability. While the framework was successfully utilized to quantify the impact of aerothermoelastic effects on control surface transient lift and drag behavior, the control surface was considered in isolation with respect to the rest of the vehicle. As such, the structure was constrained by imposing a fixed condition at the attachment point using zero enforced displacements in that region. Thus, the mutual coupling and interdependence between the control surface and the rest of the vehicle was not addressed in Chapter VIII.

Hypersonic vehicles consist of multiple substructures, each containing different dominant physics. Aerodynamic heating is expected to have a strong impact on the response of the control surfaces of the vehicle, but its effect on the fuselage will likely not be as pronounced. The scramjet propulsion system consists of an inlet, isolator, combustor, and nozzle, resulting in a completely different set of physics than those associated with the fuselage and lifting surface structures. Therefore, direct or monolithic coupling of the vehicle substructures in the time-domain simulation is not straightforward. This chapter investigates the use of a partitioned, time-marching formulation which allows for coupling of vehicle substructures through the exchange of interface information. This approach is advantageous in that it does not require direct coupling of the substructures, therefore allowing for the models be of dissimilar form. To exemplify the methodology, the case of coupling an HSV lifting surface with a fuselage is considered, where the fuselage is represented by a single degree of freedom mass-spring system. This configuration allows for a simplified formulation that can be used to demonstrate and validate the partitioned approach while retaining enough of the essential physics to investigate inertial coupling effects between the lifting surface and fuselage. Once the partitioned solution approach is validated, it is used to study the impact of lifting surface inertia on the overall system dynamics. This inertial

coupling is an important phenomenon to investigate due to the fact that it may result in a complex-conjugate pair of zero in the elevator-to-pitch rate transfer function, thus altering the speed of response of the vehicle [109].

9.2 Simulation Framework

The simulation framework of the current work is based on a partitioned approach in which the equations of motion for each substructure are integrated separately and information is exchanged between them at pre-determined time intervals. In this work, the methodology is focused on the coupling between a hypersonic vehicle lifting surface and fuselage, although it is intentionlly general such that it can be employed for each of the various substructures of the vehicle. The advantage of using separate models for the fuselage and lifting surfaces is that each model can be tailored specific to the physics of interest for that component. In the current full-vehicle simulation framework, the equations of motion for the fuselage are derived in analytical form by approximating it as a 1D beam, while those for the lifting surfaces are based on a built-up finite element discretization. The effect of aerodynamic heating on the lifting surfaces is expected to be strong in comparison with its effect on the fuselage. As such, aerodynamic heating is only included in the lifting surfaces model. Therefore, the fuselage model will be dissimilar in form with respect to the lifting surface model, and a straighforward monolithic coupling is not easily facilitated. The use of independent models for the fuselage and lifting surface with information being exchanged between the two at the interface is advantageous in that it does not require a direct coupling between the two components. Additionally, the use of separate models for the fuselage and lifting surfaces allows for different time-integration schemes and time steps to be employed for each based on the expected time scales of the system dynamics. To couple the structures, interface information must be exchanged between the fuselage and lifting surfaces at specified intervals. Information is passed to the lifting surface equations of motion in the form of fuselage accelerations and displacements for the degrees of

freedom at the interface. Information is passed back to the fuselage equations of motion in the form of forces exerted by the lifting surface on the fuselage at the interface.

The aeroelastic framework for the flexible fuselage response has been developed by Frendreis and Cesnik [115]. A flowchart of this framework is given in Fig. 9.1. The structural model of the fuselage consists of a structural representation and appropriate boundary conditions. The structural representation is taken to be an analytical model based on an Euler-Bernoulli beam. The boundary conditions are chosen to reflect a structure in free flight, such as free-free boundary conditions for a beam. The unsteady aerodynamic model is comprised of a steady shock-expansion component with a piston theory correction to account for unsteady effects. In addition to aerodynamic loads, the fuselage also experiences propulsive loads, which are determined with a scramjet model. Since the lifting surfaces are not directly included in the fuselage aeroelastic analysis, their contribution is expressed as a set of resultant forces and moments applied at their attachment points. These loads are determined within the lifting surface aerothermoelastic framework, which is described subsequently. The coupled rigid body/structural equations of motion under loading from unsteady aerodynamics, propulsion, and the lifting surfaces provide the rigid body and structural responses of the fuselage. These are then used to determine the prescribed root motion of the lifting surface, which is passed to the lifting surface aerothermoelastic model.

In order to accurately capture the contributions of the lifting surfaces to the overall vehicle dynamics, aerothermoelastic effects on the lifting surfaces must be included. The aerothermoelastic model of the lifting surface used in the current chapter is based on the unsteady reduced-order modeling framework described in Chapter VI and shown in Fig. 6.2. For reference, this framework is shown again in Fig. 9.2. As the process was described in Chapter VI, the description is not repeated in the current chapter. However, the important point to emphasize here, as shown in Fig. 9.2, is that the interface motion determined from the fuselage equations of motion (EOMs) is passed to the lifting surface, and the interface

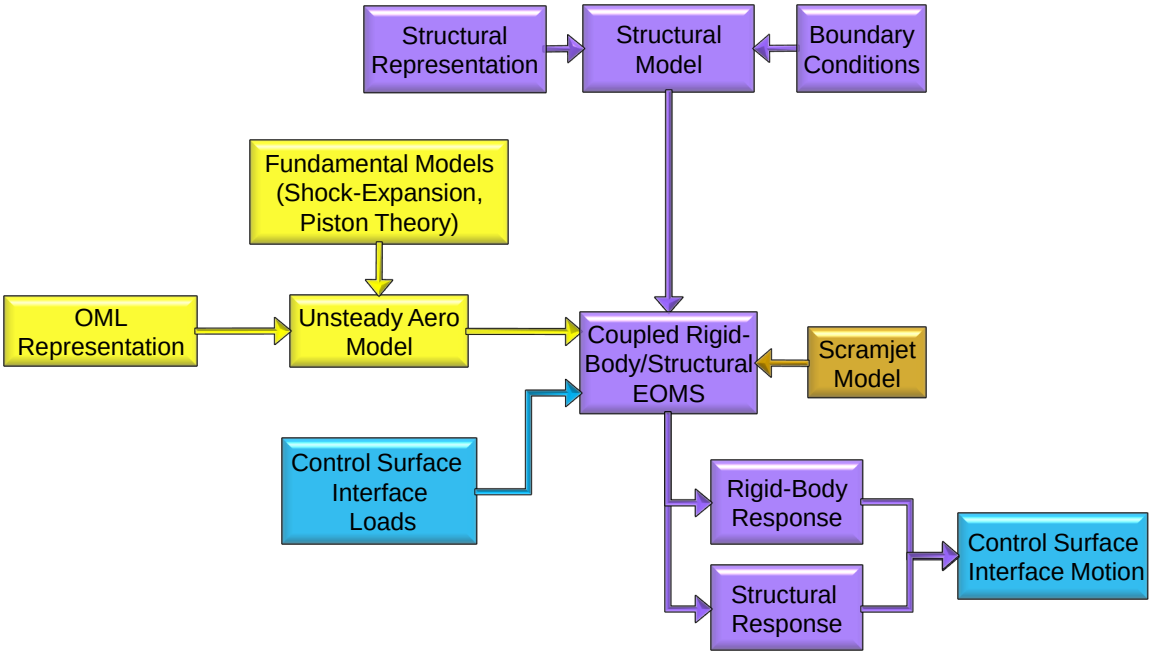

Figure 9.1: Fuselage aeroelastic simulation framework.

loads due to the lifting surface response are passed back to the fuselage EOMs.

A time-marching procedure with updates to the thermal and structural boundary conditions at specified intervals is utilized for computing the aerothermoelastic response of the lifting surfaces. Again, the time-marching procedure was outlined in Chapter VI and depicted in Fig. 6.4. For the partitioned solution, a modified form of that time-stepping schedule is employed, as shown in Fig. 9.3. The modification is due to the fact that iterations between the fuselage and lifting surface must be carried out within each aeroelastic time step due to interdependence of the two systems. In order to march the lifting surface structural dynamic solution forward in time, the enforced displacements and accelerations at the interface due to fuselage motion must be specified. However, the fuselage motion in turn depends on the loads that the lifting surface exerts on the fuselage at the interface. Therefore, within each aeroelastic time step, iterations are performed between the lifting surface and fuselage in which the lifting surface model passes interface loads to the fuselage, and the fuselage passes back interface motion. This iteration process is illustrated in Fig. 9.3 The mathematical details of how the iterations are performed are described in a

subsequent section.

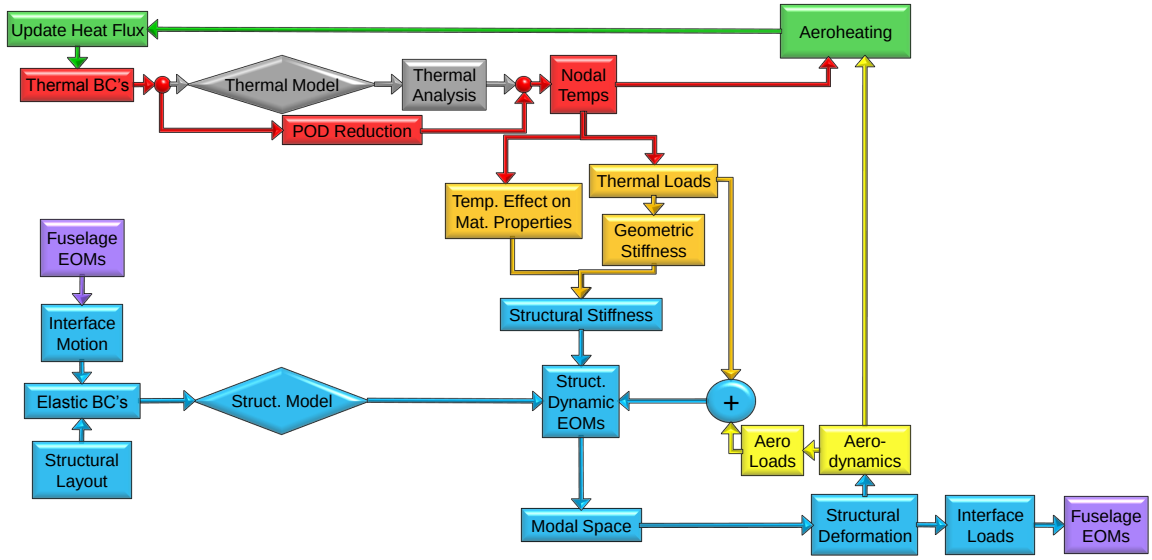

Figure 9.2: Reduced-order aerothermoelastic modeling framework for lifting surface model.

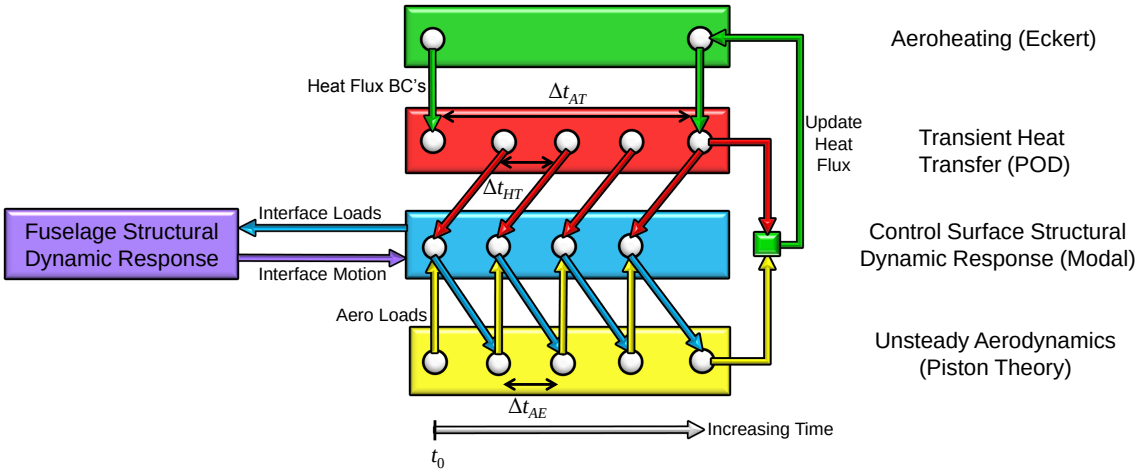

Figure 9.3: Overview of aerothermoelastic time-marching schedule for lifting surface model.

9.3 Formulation of Equations of Motion

9.3.1 Fuselage Equations of Motion

The equations of motion for the flexible hypersonic vehicle fuselage in 3D flight are derived using a Lagrangian approach. This approach is chosen instead of a Newtonian approach because it avoids the need to calculate internal forces within the structure. First, there are two frames of reference that must be introduced: an inertial Earth-fixed reference frame (E frame) and a moving, body-fixed reference frame (B frame). Next, the flight variables must be defined. The rigid body translational velocity of the vehicle (i.e., the velocity of the B frame origin with respect to the E frame origin) is represented by β, and the rigid body rotational velocity is represented by ζ. The structural deformations are expressed in terms of the structural modal coordinates, η. When the equations of motion are derived, it is assumed that the structural mode shapes are computed *a priori*. To derive the equations of motion using Lagrange's approach, the total kinetic and potential energies (T and V, respectively) are expressed in terms of the generalized coordinates and velocities, η, β, and ζ, as well as their time derivatives. Then, defining the Lagrangian as $\mathcal{L} \equiv T - V$, the equation of motion governing coordinate q_i is given by

$$\frac{d}{dt}\left(\frac{\partial \mathcal{L}}{\partial \dot{q}_i}\right) - \frac{\partial \mathcal{L}}{\partial q_i} = Q_i, \tag{9.1}$$

where Q_i is the generalized force corresponding to q_i. The equations of motion can then be assembled into a matrix equation of the form

$$\begin{bmatrix} & m_f & \end{bmatrix} \begin{Bmatrix} \dot{\beta} \\ \dot{\zeta} \\ \ddot{\eta} \end{Bmatrix} + \begin{bmatrix} & c_f & \end{bmatrix} \begin{Bmatrix} \beta \\ \zeta \\ \dot{\eta} \end{Bmatrix} + \begin{Bmatrix} 0 \\ 0 \\ k_f \eta \end{Bmatrix} = \begin{Bmatrix} Q_\beta \\ Q_\zeta \\ Q_\eta \end{Bmatrix}, \tag{9.2}$$

where m_f is the generalized mass matrix, c_f is the generalized damping matrix, and k_f is the generalized stiffness matrix. The mass and damping are not constant; e.g., the mass matrix will change throughout flight as fuel is burned. The damping matrix, which contains the gyroscopic acceleration terms, is dependent on the rigid body rotational velocity, ζ, and will also vary as the vehicle inertia changes. The details of this derivation of the equations of motion as applied to the free-free beam structure are available in Ref. 115.

Once the equations of motion are assembled, the next task is to determine the generalized forces, Q_β, Q_ζ, and Q_η. For the hypersonic vehicle fuselage, there are four sources of external loading: aerodynamics, propulsion, gravity, and resultant forces from the lifting surfaces that include the lifting surfaces in this particular partition. Since the vehicle is undergoing unsteady rigid body motion, as well as structural deflections, an unsteady aerodynamic model is required. The aerodynamic model used for the fuselage is based on a steady shock-expansion analysis with an unsteady correction computed using piston theory. These models are applied in a local inclination scheme at each panel of the OML, where the aerodynamic load on each panel is a function of its total velocity and orientation only.

The effect of the lifting surfaces on the fuselage dynamics is expressed as a set of resultant forces and moments at the lifting surface attachment points. The resultant forces and moments are determined by passing the fuselage motion at the lifting surface attachment point to the lifting surface equations of motion. Using this specified root motion, the resultant forces and moments are calculated by the lifting surface aerothermoelastic model. These resultant forces include contributions from both the aerodynamic loading and the unsteady structural response of the lifting surfaces. As described in section 9.4.2, the lifting surfaces are treated as all-moveable surfaces about a hinge line located at the mid-chord. Deflection of the lifting surfaces by the control system is therefore represented as enforced rotation about this line.

9.3.2 Lifting Surface Equations of Motion

The usage of the Eckert reference temperature formulation for calculating the aerodynamic heating over the lifting surface, the POD formulation for obtaining the transient temperature distribution of the lifting surface, and the third-order piston theory formulation for the lifting surface aerodynamic flow calculation are presented in previous chapters and are thus omitted here for brevity. Therefore, the emphasis of the current section is on the solution for the structural dynamic response of the lifting surface subjected to thermal and unsteady aerodynamic loads as well as enforced displacements and accelerations due to fuselage motion.

For a lifting surface with prescribed accelerations and displacements at degrees-of-freedom (DOFs) r, the equations of motion can be partitioned as

$$\begin{bmatrix} M_{rr} & M_{ru} \\ M_{ur} & M_{uu} \end{bmatrix} \begin{Bmatrix} \ddot{x}_r \\ \ddot{x}_u \end{Bmatrix} + \begin{bmatrix} K^*_{rr}(T) & K^*_{ru}(T) \\ K^*_{ur}(T) & K^*_{uu}(T) \end{bmatrix} \begin{Bmatrix} x_r \\ x_u \end{Bmatrix} = \begin{Bmatrix} F_r \\ F^H_u + F^A_u \end{Bmatrix}, \tag{9.3}$$

where M is the physical mass matrix, $x(t)$ are the physical degrees of freedom, $F^H(T)$ is the load vector due to heating, $F^A(t)$ is the load vector due to aerodynamic pressure, the subscript r corresponds to the restrained DOFs (those with prescribed accelerations and displacements), and the subscript u corresponds to the unrestrained DOFs (those without prescribed accelerations and displacements). The modified stiffness matrix, $K^*(T)$, is given by

$$K^*(T) \equiv K(T) + K_G(T), \tag{9.4}$$

where $K(T)$ is the conventional stiffness matrix that varies due to the temperature-dependence of the material properties and $K_G(T)$ is the geometric stiffness matrix resulting from thermal stresses. In this formulation, the equations of motion for the unrestrained lifting surface DOFs are cast in terms of the elastic displacements relative to the constraint motion caused by the enforced displacements at the restrained DOFs. The term "constraint motion" refers

to the displacements that the structure would undergo if the prescribed motion was applied statically and inertial effects were not present. Note that the term "constraint motion" is specifically used instead of "rigid body motion" because the number of DOFs with prescribed motion is greater than that required to constrain rigid body motion in this case. Such a formulation is advantageous because the constraint motion is accounted for separately and the equations of motion are associated only with the elastic response, thus the structural modal matrix does not need to be modified to include constraint modes. Therefore, the lifting surface structural modal matrix is composed only of elastic modes in this formulation. The first step is to calculate the constraint motion due to enforced motion at the unrestrained DOFs, denoted by x_u^C. This quantity is obtained by neglecting inertial loads and external loads in the second row of Eq. (9.3) and solving for x_u, i.e.,

$$x_u^C = -(K_{uu}^*)^{-1} K_{ur}^* x_r. \tag{9.5}$$

Note that a transformation, U, can be defined in Eq. (9.5) between x_u^C and x_r such that

$$x_u^C = U x_r \text{ , where } U = -(K_{uu}^*)^{-1} K_{ur}^*. \tag{9.6}$$

If the number of DOFs with prescribed motion were exactly equal to the minimum number of DOFs required to constrain rigid body motion, the columns of U would represent rigid body modes. Because in this case the number of DOFs with prescribed motion is greater than that required to constrain rigid body motion, the columns of U represent constraint modes.

The next step is to derive the equations governing the elastic deformation of the unrestrained DOFs, x_u^E, relative to the constraint motion. Expanding Eq. (9.3), one obtains

$$M_{rr}\ddot{x}_r + M_{ru}\ddot{x}_u + K^*_{rr}x_r + K^*_{ru}x_u = F_r \tag{9.7a}$$

$$M_{ur}\ddot{x}_r + M_{uu}\ddot{x}_u + K^*_{ur}x_r + K^*_{uu}x_u = F^H_u + F^A_u. \tag{9.7b}$$

Recall that the total motion of the unrestrained DOFs is the sum of the constraint motion plus the elastic motion, i.e.,

$$x_u = x^C_u + x^E_u. \tag{9.8}$$

Substituting Eq. (9.8) into Eq. (9.7b), one obtains

$$M_{ur}\ddot{x}_r + M_{uu}\left(\ddot{x}^C_u + \ddot{x}^E_u\right) + K^*_{ur}x_r + K^*_{uu}\left(x^C_u + x^E_u\right) = F^H_u + F^A_u, \tag{9.9}$$

and using Eq. (9.5) in Eq. (9.9), the system becomes

$$M_{ur}\ddot{x}_r + M_{uu}\left[-(K^*_{uu})^{-1}K^*_{ur}\ddot{x}_r + \ddot{x}^E_u\right] + K^*_{ur}x_r + K^*_{uu}\left[-(K^*_{uu})^{-1}K^*_{ur}x_r + x^E_u\right] = F^H_u + F^A_u. \tag{9.10}$$

Bringing all terms associated with the restrained DOFs to the right-hand side of Eq. (9.10), the equation becomes

$$\begin{aligned} M_{uu}\ddot{x}^E_u + K^*_{uu}x^E_u = &- M_{ur}\ddot{x}_r + M_{uu}(K^*_{uu})^{-1}K^*_{ur}\ddot{x}_r - K^*_{ur}x_r + \\ &K^*_{uu}(K^*_{uu})^{-1}K^*_{ur}x_r + F^H_u + F^A_u, \end{aligned} \tag{9.11}$$

and simplifying the right-hand side of Eq. (9.11) results in

$$M_{uu}\ddot{x}^E_u + K^*_{uu}x^E_u = \left[M_{uu}(K^*_{uu})^{-1}K^*_{ur} - M_{ur}\right]\ddot{x}_r + F^H_u + F^A_u. \tag{9.12}$$

The relation given by Eq. (9.12) is the system to be solved for the elastic motion of

the unrestrained DOFs, x_u^E, relative to the constraint motion, x_u^C. Note that the solution to Eq. (9.12) requires only the accelerations of the restrained DOFs, $\ddot{x}_r$, and not the displacements. However, x_r is required to compute the constraint motion, x_u^C. As discussed in Chapter IV, due to the large number of degrees of freedom, direct solution of Eq. (9.12) within the aerothermoelastic lifting surface framework is not desirable. Thus, again the approach taken in this work is to first perform an off-line calculation and select a reduced number of Ritz modes based on free vibration modes and load-dependent Ritz vectors [85] evaluated at a reference thermal state. These Ritz modes are then used as the modal basis for solution of the structural response throughout the simulation. The modal matrix containing the structural reference modes, Φ_s, will not be updated throughout the simulation, thus preventing the need to solve an eigenvalue problem of the full system during the course of the simulation. Though the reference modes will not be updated throughout the simulation, the stiffness matrix will be updated each time the structural dynamic response is calculated to account for temperature-dependent material properties and geometric stiffening. As discussed previously, an important result of solving only for the elastic response in Eq. (9.12) is that the structural basis must only contain elastic modes. Because the remainder of the motion is accounted for in Eq. (9.8), the structural modal matrix need not contain constraint modes.

The reduced-order system is obtained by first representing the elastic motion, $x_u^E(t)$, as a linear combination of the Ritz modes such that

$$x_u^E(t) = \Phi_s d(t), \tag{9.13}$$

where d represents the modal coordinates of the Ritz modes which are stored as columns of the modal matrix, Φ_s. Note that since the number of Ritz modes used in the modal expansion is much less than the number of physical degrees of freedom in the model, the computational cost of the solution is reduced. Once the modified stiffness matrix is known

at the current time instant, the system is reduced by substituting Eq. (9.13) into Eq. (9.12) and pre-multiplying the system by Φ_s^T to project the system onto the basis, i.e.,

$$\begin{aligned}\Phi_s^T M_{uu}\Phi_s\ddot{d}(t) + \Phi_s^T K_{uu}^*(T)\Phi_s d(t) = \\ \Phi_s^T\Big(\left[M_{uu}(K_{uu}^*(T))^{-1}K_{ur}^*(T) - M_{ur}\right]\ddot{x}_r(t) + F_u(t,T)\Big),\end{aligned} \tag{9.14}$$

where the net force, $F_u(t,T)$, is defined as

$$F_u(t,T) \equiv F_u^H(T) + F_u^A(t). \tag{9.15}$$

The generalized mass matrix, m_{uu}, generalized stiffness matrix, k_{uu}^*, and generalized net force vector, f_u, are then identified from Eq. (9.14) as

$$m_{uu} = \Phi_s^T M_{uu}\Phi_s \tag{9.16a}$$

$$k_{uu}^*(T) = \Phi_s^T K_{uu}^*(T)\Phi_s \tag{9.16b}$$

$$f_u(t,T) = \Phi_s^T F_u(t,T), \tag{9.16c}$$

and the reduced system in modal form is given as

$$m_{uu}\ddot{d}(t) + k_{uu}^*(T)d(t) = f_u(t,T) + \Phi_s^T\Big(\left[M_{uu}(K_{uu}^*(T))^{-1}K_{ur}^*(T) - M_{ur}\right]\ddot{x}_r(t)\Big). \tag{9.17}$$

As the mass of the structure is taken to be constant in this work, the reference modes are orthogonal with respect to the mass matrix and the generalized mass matrix, m_{uu}, reduces to the identity matrix. Since the modified stiffness matrix is continuously changing due to transient heating, we have no guarantee of orthogonality of the reference modes with respect to stiffness, and the equations are coupled. As such, the reduced-order system of equations in modal space is integrated numerically to calculate $d(t)$ at each aeroelastic time step. The numerical integration method employed here is that described in Section 4.2 of Chapter IV. As described previously, the scheme uses a central finite difference

representation for the velocity and acceleration at discrete times, given by [154]

$$\dot{d}^{(n)} = \frac{d^{(n+1)} - d^{(n-1)}}{2\Delta t_{AE}} \tag{9.18a}$$

$$\ddot{d}^{(n)} = \frac{d^{(n+1)} - 2d^{(n)} + d^{(n-1)}}{\Delta t_{AE}^2}, \tag{9.18b}$$

where the superscript (n) refers to the time level. The initial conditions, $d^{(0)}$ and $\dot{d}^{(0)}$, are used to generate the vectors $d^{(n-1)}$, $f_u^{(n-1)}$, and $f_u^{(n)}$ for the initial time step, $n = 0$, using

$$d^{(-1)} = d^{(0)} - \dot{d}^{(0)}\Delta t_{AE} \tag{9.19a}$$

$$f_u^{(-1)} = k_{uu}^* d^{(-1)} \tag{9.19b}$$

$$f_u^{(0)} = k_{uu}^* d^{(0)}. \tag{9.19c}$$

Note that this formulation assumes that the initial acceleration for all points is zero (initial velocity is constant). In order to maintain consistency with the central difference approximation for the modal accelerations, the enforced acceleration in Eq. (9.17), $\ddot{x}_r(t)$, is approximated at time level (n) using a central difference formula, i.e.,

$$\ddot{x}_r(t) = \frac{x_r^{(n+1)} - 2x_r^{(n)} + x_r^{(n-1)}}{\Delta t_{AE}^2}. \tag{9.20}$$

Substituting the finite difference approximations of the velocities and accelerations, Eqs. (9.18) and (9.20), into the equations of motion, Eq. (9.17), and averaging the applied loads over three adjacent time instants, the equations of motion are re-written as

$$H_1 d^{(n+1)} = H_2 + H_3 d^{(n)} + H_4 d^{(n-1)}, \tag{9.21}$$

where,

$$H_1 = \frac{1}{\Delta t_{AE}^2} m_{uu} + \frac{1}{3} k_{uu}^* \tag{9.22}$$

$$H_2 = \frac{1}{3}\left(f_u^{(n+1)} + f_u^{(n)} + f_u^{(n-1)}\right) + \Phi_s^T \left[M_{uu}(K_{uu}^*(T))^{-1}K_{ur}^*(T) - M_{ur}\right] \frac{x_r^{(n+1)} - 2x_r^{(n)} + x_r^{(n-1)}}{\Delta t_{AE}^2} \tag{9.23}$$

$$H_3 = \frac{2}{\Delta t_{AE}^2} m_{uu} - \frac{1}{3}k_{uu}^* \tag{9.24}$$

$$H_4 = \frac{-1}{\Delta t_{AE}^2} m_{uu} - \frac{1}{3}k_{uu}^*. \tag{9.25}$$

Note that Eq. (9.23) differs from the equation for H_2 in Chapter IV in that Eq. (9.23) includes loads due to accelerations at the interface in addition to aerodynamic and thermal loads. The vector of structural modal coordinates at the end of the time step, $d^{(n+1)}$, is obtained by decomposing H_1 and applying it to the right-hand side of Eq. (9.21). Once $d^{(n+1)}$ is obtained, the total motion of the unconstrained degrees of freedom in physical space is computed via Eqs. (9.5), (9.8), and (9.13) using

$$x_u^{(n+1)} = -(K_{uu}^*)^{-1}K_{ur}^* x_r^{(n+1)} + \Phi_s d^{(n+1)}. \tag{9.26}$$

Once the displacements of the unrestrained DOFs are known at a given time t, the force contribution due to lifting surface (wing) motion, F_r^W, can be calculated at time t by computing the quantity $M_{ru}\ddot{x}_u + K_{ru}^* x_u$ from the first row of Eq. (9.3) and moving it to the right-hand side to treat as a forcing function acting on the fuselage at the interface. This force contribution is computed using,

$$F_r^W(t,T) = -M_{ru}\frac{x_u^{(n+1)} - 2x_u^{(n)} + x_u^{(n-1)}}{\Delta t_{AE}^2} - K_{ru}^*\frac{x_u^{(n+1)} + x_u^{(n)} + x_u^{(n-1)}}{3}, \tag{9.27}$$

where the accelerations of the unrestrained DOFs, $\ddot{x}_u$, are calculated using a central difference and the displacements are averaged over three adjacent time levels in order to maintain

consistency with the numerical integration scheme. Once $F_r^W(t,T)$ is known, it can then be passed to the fuselage equations of motion in order to update the loads. In order to compute the net external force that the lifting surface (wing) exerts relative to the fuselage (body), $F_r^{W/B}$, the elastic motion of the unrestrained lifting surface DOFs relative to the interface DOFs is utilized. Therefore, $F_r^{W/B}$ is given by

$$F_r^{W/B} = -K_{ru}^* \left(x_u^E - x_{u,T}^E \right), \tag{9.28}$$

where $x_{u,T}^E$ is the elastic deformation caused by thermal loads. Note that $x_{u,T}^E$ must be substracted from x_u^E because thermal loads are internal to the system and do not result in external forces being exerted on the fuselage.

9.3.3 Methodology for Fuselage-Lifting Surface Coupling

As described previously, the flight dynamics simulation framework for the HSV is based on a partitioned approach in which the vehicle substructures are modeled independently and interface information is exchanged between substructures within each time step. The example case considered here focuses on the coupling of a hypersonic vehicle all-moveable lifting surface and fuselage. The equations of motion for the fuselage and the lifting surface are presented above, and thus the final step of the formulation is to couple the two systems. Referring to Eq. (9.3), the fuselage motion at the lifting surface-fuselage interface is given by

$$M_{rr}\ddot{x}_r(t) + K_{rr}x_r(t) = F_r + F_r^W(t,T), \tag{9.29}$$

where M_{rr} and K_{rr} are the mass and stiffness associated with the interface DOFs, $x_r(t)$ are the degrees of freedom corresponding to the fuselage displacement, and $F_r^W(t,T)$ is the force exerted by the lifting surface on the fuselage given in Eq. (9.27). The force component

F_r represents the force due to the weight of the fuselage and is given by,

$$F_r = M_f g, \tag{9.30}$$

where g is the gravitational acceleration. For uniformity, the same numerical integration scheme used for the lifting surface is also used for the fuselage, such that the fuselage displacement at the end of each aeroelastic time step, $(n+1)$, can be found from

$$I_1 x_r^{(n+1)} = I_2 + I_3 x_r^{(n)} + I_4 x_r^{(n-1)}, \tag{9.31}$$

where,

$$I_1 = \frac{1}{\Delta t_{AE}^2} M_{rr} + \frac{1}{3} K_{rr} \tag{9.32a}$$

$$I_2 = \frac{1}{3}\left(F_r^{(n+1)} + F_r^{(n)} + F_r^{(n-1)}\right) + F_r^W \tag{9.32b}$$

$$I_3 = \frac{2}{\Delta t_{AE}^2} M_{rr} - \frac{1}{3} K_{rr} \tag{9.32c}$$

$$I_4 = \frac{-1}{\Delta t_{AE}^2} M_{rr} - \frac{1}{3} K_{rr}. \tag{9.32d}$$

Note that F_r^W is already averaged over three adjacent time steps in Eq. (9.27), and therefore only F_r must be averaged in Eq. (9.32b).

The effect of the lifting surface response on the fuselage response can be seen by inspecting Eq. (9.31). Specifically, note that I_2 is a function of F_r^W, and F_r^W depends on $x_u^{(n+1)}$. Also, recall that $x_u^{(n+1)}$ is expressed in terms of the lifting surface modal coordinates, $d^{(n+1)}$. As shown in Eq. (9.23), $d^{(n+1)}$ in turn depends on $x_r^{(n+1)}$. We can therefore state that $d^{(n+1)}$ is a function of $x_r^{(n+1)}$. To highlight these dependencies, we rewrite Eq. (9.31) as

$$I_1 x_r^{(n+1)} = I_2\left(d^{(n+1)}\left(x_r^{(n+1)}\right)\right) + I_3 x_r^{(n)} + I_4 x_r^{(n-1)}. \tag{9.33}$$

Solution of Eq. (9.33) is complicated due to the fact that $d^{(n+1)}$ is unknown, and depends

on the solution to the fuselage response. In a manner analogous to Eq. (9.33), Eq. (9.21) for the lifting surface can be rewritten as

$$H_1 d^{(n+1)} = H_2\left(x_r^{(n+1)}\left(d^{(n+1)}\right)\right) + H_3 d^{(n)} + H_4 d^{(n-1)}, \tag{9.34}$$

where the dependence of H_2 on both the lifting surface and fuselage states at time $(n+1)$ is explicitly shown.

While both the fuselage and lifting surface systems could be combined into one (as shown in Eq. (9.3)) and solved monolithically, the goal of this work is to develop a methodology for time-marching multiple coupled systems of differential equations by treating each independently and exchanging interface information in a mathematically robust manner. The motivation for such an approach is due to the fact that the HSV will consist of multiple components, each of which will have its own model. As the models are likely to be of dissimilar form, direct monolithic coupling of the models is not easily facilitated. The philosophy of this work is therefore to treat each model as a black-box with respect to the other. Mathematically, this means that $I_2\left(d^{(n+1)}\left(x_r^{(n+1)}\right)\right)$ in Eq. (9.33) and $H_2\left(x_r^{(n+1)}\left(d^{(n+1)}\right)\right)$ in Eq. (9.34) are treated as unknown functions of $x_r^{(n+1)}$ and $d^{(n+1)}$, where information about these functions can only be obtained by evaluating them at specific input values.

Due to the unknown nature of H_2 and I_2, Eqs. (9.33) and (9.34) are each treated as if they are nonlinear in the other system's states (i.e., the fuselage system is treated as if it is nonlinear in the lifting surface states, and the lifting surface system is treated as if it is nonlinear in the fuselage states). Such an assumption preserves the generality of the methodology such that it is applicable to any two systems of differential equations that are nonlinearly coupled. Furthermore, the methodology is formulated such that if the two systems are only linearly coupled, the linear solution is recovered in only one iteration. Due to the assumption of nonlinear coupling, the equations are solved using an iterative

approach to bring the two systems to equilibrium at the end of each time step. As opposed to a pseudo-time-marching strategy in which the two components are successively marched in pseudo-time until the equilibrium state is reached, this work formulates the algorithm as a solution to a nonlinear root-finding problem and uses derivative information of the nonlinear function in order to converge to the equilibrium state more efficiently. A secant method is used in this work to increment the state at each iteration due to its property of being superlinearly locally convergent [131].

Before implementing the methodology, it must be decided which system will be the driving system and which system will be the driven system. The driving system is the one in which the secant method is used to compute the increment to the state at each iteration until convergence is achieved. The state vector for the driven system at time $(n+1)$ is merely updated by marching forward one step based on the state vector from the driving system at time $(n+1)$ for each iteration. Assuming that the driving system is chosen to be the fuselage system, we begin by moving all terms in Eq. (9.33) to the left-hand side and equating it to the residual at iteration k, $R\left(d_k^{(n+1)}\left(x_{r,k}^{(n+1)}\right)\right)$, i.e.,

$$I_1 x_{r,k}^{(n+1)} - I_2\left(d_k^{(n+1)}\left(x_{r,k}^{(n+1)}\right)\right) - I_3 x_r^{(n)} - I_4 x_r^{(n-1)} = R\left(d_k^{(n+1)}\left(x_{r,k}^{(n+1)}\right)\right). \quad (9.35)$$

Note that according to Eq. (9.33), the right-hand side of Eq. (9.35) should be equal to zero. However, this condition is only achieved when the lifting surface and fuselage are brought into equilibrium at the end of the time step, $(n+1)$. At intermediate iterations prior to reaching the equilibrium state, the left-hand side of Eq. (9.35) will be equal to a nonzero residual that is a function of the fuselage and lifting surface states. The process of bringing the lifting surface and fuselage to equilibrium is mathematically equivalent to driving the residual to zero in Eq. (9.35) by iterating on the fuselage state vector, $x_r^{(n+1)}$.

A summary of the algorithm used to bring the fuselage and lifting surface systems to equilibrium within each time step is given in Algorithm 9.3.1. The iteration procedure

begins with two initial guesses to the fuselage state at the end of the time step, $x_{r,0}^{(n+1)}$ and $x_{r,1}^{(n+1)}$, where the subscripts 0 and 1 refer to the iteration number. For each initial guess, H_2 is computed at step 3 using Eq. (9.23), and Eq. (9.21) is solved for the lifting surface state vector, $d_k^{(n+1)}$, at step 4. The total lifting surface displacements in physical space, $x_u^{(n+1)}$, are then computed using Eq. (9.26) in step 5. Once the motion of the lifting surface at time level $(n+1)$ is known, the loads imparted on the fuselage by the lifting surface at time level $(n+1)$ are calculated using Eq. (9.27) to give $F_r^W(t,T)$ in step 6. With these loads known, I_2 is computed from Eq. (9.32b). Using I_2, the left-hand side of Eq. (9.35) is evaluated giving the residual at step 8. At this point, if the residual is above the specified tolerance, an iteration loop begins in which the fuselage state is incremented using the fuselage states and residual values at the two previous iterations via the secant method. Iterations are carried out repeating steps 3 – 8 as described above, until the residual drops below the specified tolerance. At that point, the fuselage and lifting surface have been brought into equilibrium at the end of the current time step. The states for each component are then stored, the simulation marches to the next time step, and the iteration process is again carried out until equilibrium is achieved at the next time step. This process continues until the simulation is complete.

A schematic of the information flow for the iteration scheme is given in Fig. 9.4. The process begins with the fuselage state at time $(n+1)$ for the current iteration. Using the previous fuselage states and residual values, the fuselage state at the next iteration is computed using the secant method. Based on the new fuselage at time $(n+1)$, the fuselage interface accelerations are computed using a finite difference scheme. These accelerations are then passed to lifting surface equations of motion at time (n). Using these boundary conditions, the lifting surface are integrated forward in time to obtain the control surface state at time $(n+1)$ at the next ieration. Once the solution of the lifting surface equations of motion is known, the loads exerted by the lifting surface on the fuselage are computed, again using a finite difference scheme. These loads are then passed back to the fuselage

Algorithm 9.3.1 Iteration scheme used for bringing lifting surface and fuselage into equilibrium at each time step.

$x_{r,0}^{(n+1)}, x_{r,1}^{(n+1)} =$ Initial guesses
for $k = 0, 1$ **do**
  $H_2 = \frac{1}{3}\left(f_u^{(n+1)} + f_u^{(n)} + f_u^{(n-1)}\right) + \Phi_s^T \left[M_{uu}(K_{uu}^*(T))^{-1} K_{ur}^*(T) - M_{ur}\right] \frac{x_{r,k}^{(n+1)} - 2x_r^{(n)} + x_r^{(n-1)}}{\Delta t_{AE}^2}$
  $d_k^{(n+1)} = H_1^{-1}\left(H_2 + H_3 d^{(n)} + H_4 d^{(n-1)}\right)$
  $x_u^{(n+1)} = -(K_{uu}^*)^{-1} K_{ur}^* x_r^{(n+1)} + \Phi_s d_k^{(n+1)}$
  $F_r^W(t,T) = -M_{ru}\frac{x_u^{(n+1)} - 2x_u^{(n)} + x_u^{(n-1)}}{\Delta t_{AE}^2} - K_{ru}^* \frac{x_u^{(n+1)} + x_u^{(n)} + x_u^{(n-1)}}{3}$
  $I_2 = \frac{1}{3}\left(F_r^{(n+1)} + F_r^{(n)} + F_r^{(n-1)}\right) + F_r^W$
  $R_k = I_1 x_{r,k}^{(n+1)} - I_2\left(d_k^{(n+1)}\left(x_{r,k}^{(n+1)}\right)\right) - I_3 x_r^{(n)} - I_4 x_r^{(n-1)}$
end for
while $|R_1| > tol$ **do**
  $x_{r,2}^{(n+1)} = x_{r,1}^{(n+1)} - \frac{R_1\left(x_{r,1}^{(n+1)} - x_{r,0}^{(n+1)}\right)}{R_1 - R_0}$
  $H_2 = \frac{1}{3}\left(f_u^{(n+1)} + f_u^{(n)} + f_u^{(n-1)}\right) + \Phi_s^T \left[M_{uu}(K_{uu}^*(T))^{-1} K_{ur}^*(T) - M_{ur}\right] \frac{x_{r,2}^{(n+1)} - 2x_r^{(n)} + x_r^{(n-1)}}{\Delta t_{AE}^2}$
  $d_2^{(n+1)} = H_1^{-1}\left(H_2 + H_3 d^{(n)} + H_4 d^{(n-1)}\right)$
  $x_u^{(n+1)} = -(K_{uu}^*)^{-1} K_{ur}^* x_r^{(n+1)} + \Phi_s d_2^{(n+1)}$
  $F_r^W(t,T) = -M_{ru}\frac{x_u^{(n+1)} - 2x_u^{(n)} + x_u^{(n-1)}}{\Delta t_{AE}^2} - K_{ru}^* \frac{x_u^{(n+1)} + x_u^{(n)} + x_u^{(n-1)}}{3}$
  $I_2 = \frac{1}{3}\left(F_r^{(n+1)} + F_r^{(n)} + F_r^{(n-1)}\right) + F_r^W$
  $R_2 = I_1 x_{r,2}^{(n+1)} - I_2\left(d_2^{(n+1)}\left(x_{r,2}^{(n+1)}\right)\right) - I_3 x_r^{(n)} - I_4 x_r^{(n-1)}$
  $x_{r,0} = x_{r,1}$
  $x_{r,1} = x_{r,2}$
  $R_0 = R_1$
  $R_1 = R_2$
end while

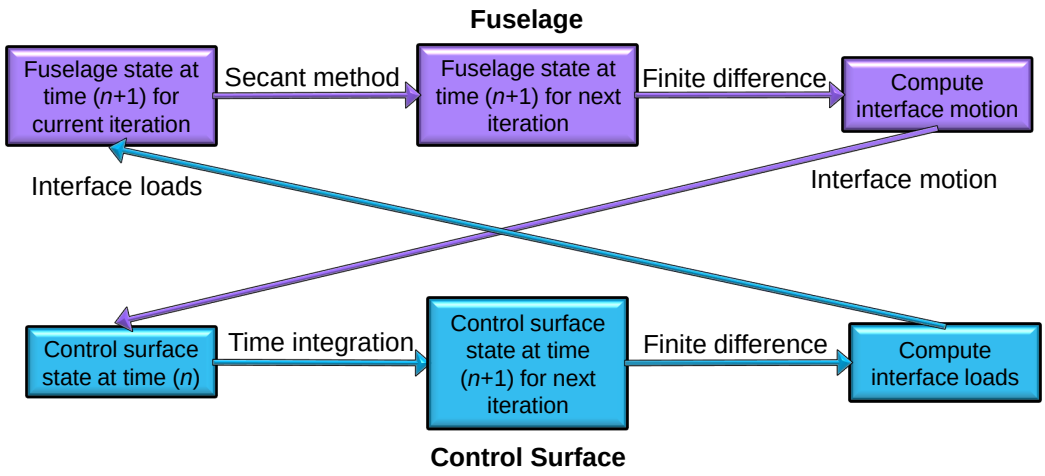

Figure 9.4: Schematic of fuselage-lifting surface coupling scheme.

system. The fuselage state is again incremented, except this time using the new loads from the lifting surface. At this point the process repeats and iterations are carried out until the forces exerted by the lifting surface on the fuselage are brought into equilibrium with the accelerations of the fuselage at the interface location.

9.4 Hypersonic Vehicle Representation

With the equations of motion for the HSV fuselage and lifting surface presented and the partitioned solution scheme outlined, the current section describes a representative HSV configuration to which the methodology is applied. The overall HSV geometry of interest for the current is first described. A representative HSV fuselage is outlined which contains separate structural and aerodynamic representations. The position of the lifting surfaces with respect to the fuselage geometry is also indicated. Next, the geometry of the all-moveable lifting surface to be connected to the HSV fuselage is outlined. While the fuselage and lifting surface geometry discussed collectively represent the overall HSV geometry of interest, this work is specifically interested in demonstrating the partitioned solution methodology used to couple these two structures. As such, a simplified configuration to be used in this work to exemplify the methodology is highlighted. The simplified

configuration consists of the all-moveable lifting surface attached to a single degree of freedom oscillator which replaces the fuselage. The use of this configuration will allow for a focus on the partitioned solution methodology and the effects of fuselage-lifting surface inertial coupling while still retaining the essential physics of the problem.

9.4.1 Fuselage Model

There are two components to the representation of the flexible hypersonic vehicle fuselage: the internal structural representation and the exterior OML. The internal structural representation models the elasticity of the aircraft and is used in determining the governing equations of motion for the vehicle. The OML models the vehicle exterior and is used in the unsteady aerodynamic and propulsive analyses. The structural representation for the vehicle can come in a variety of forms (e.g., analytical beam, 3D finite element model, etc.). An analytical beam representation has been implemented [115] to model the bending and torsion of the hypersonic vehicle fuselage.

The OML is a representation of the exterior of the vehicle that is used in determining the aerodynamic loads. Since the internal structure is able to deform, the OML must be able to deform as well; therefore, an OML consisting of a series of panels, as shown in Fig. 9.5, is chosen. Each panel in the model is triangular, so that it will remain planar under arbitrary deformations. This specific OML geometry was provided by VSI[1] and is described in Ref. 164. The OML includes both the fuselage as well as the scramjet cowl. The recessed region on the top of the fuselage is where a spacecraft would be mounted when the hypersonic vehicle is being used for launch purposes. The lifting surfaces at the aft section of the vehicle are all-moveable lifting surfaces that rotate about a hinge line located at their mid-chord. These surfaces are not considered part of the fuselage structure and are included in Fig. 9.5 only to illustrate their locations with respect to the fuselage.

[1] Vibroacoustics Solutions, Inc. 2214 229th Place Ames, Iowa 50014

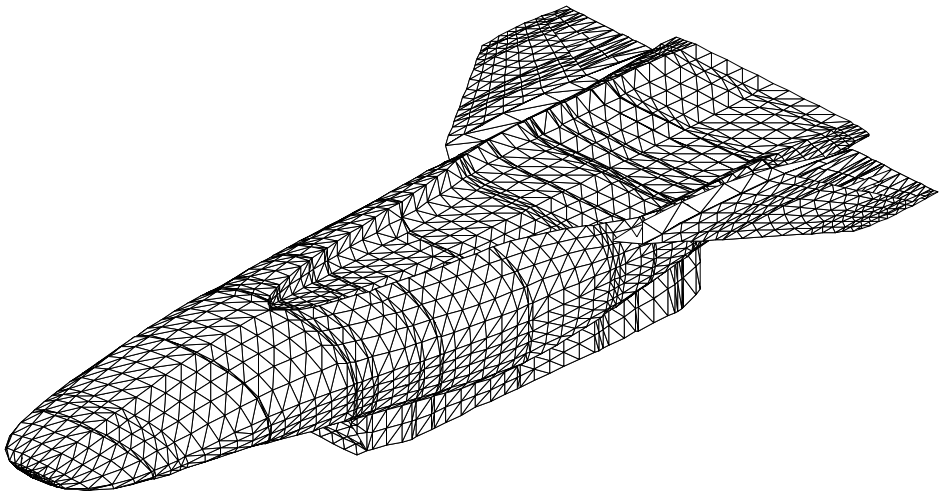

Figure 9.5: Isometric view showing fuselage outer mold line geometry and location of lifting surfaces.

9.4.2 Lifting Surface Model

The finite element model representing the all-moveable lifting surfaces depicted in Fig. 9.5 is employed in this study. The lifting surface geometry used in the current study is the same is that employed in Chapter VIII. As described in Chapter VIII, the planform and cross-sectional geometry are given in Fig. 3.2 and Fig. 3.3 of Chapter III, respectively. The finite element representation used for the full-order thermal and structural modeling aspects of the current study was given in Fig. 4.15 of Chapter IV and is shown again in Fig. 9.6 with the top surface removed for visualization purposes. As in Chapter IV, the model consists of an outer heat shield layer, a middle insulation layer, and an inner skin layer along with chordwise and spanwise stiffeners. This material stacking scheme is depicted in Fig. 3.4 of Chapter III. The materials for the heat shield, insulation, and skin layers are René 41, Min-K, and TIMETAL 834, respectively. The heat shield layer and insulation layer are each 3.8 mm thick, and the skin layer is 6.35 mm thick. The material used for the stiffeners is TIMETAL 834 and the thickness of all stiffeners is 25.4 mm (1 in). The model contains 2,812 thermal degrees of freedom and 8,074 structural degrees of freedom. The structural and thermal material properties used in the model are given in Table 3.1 and Table 3.2 of

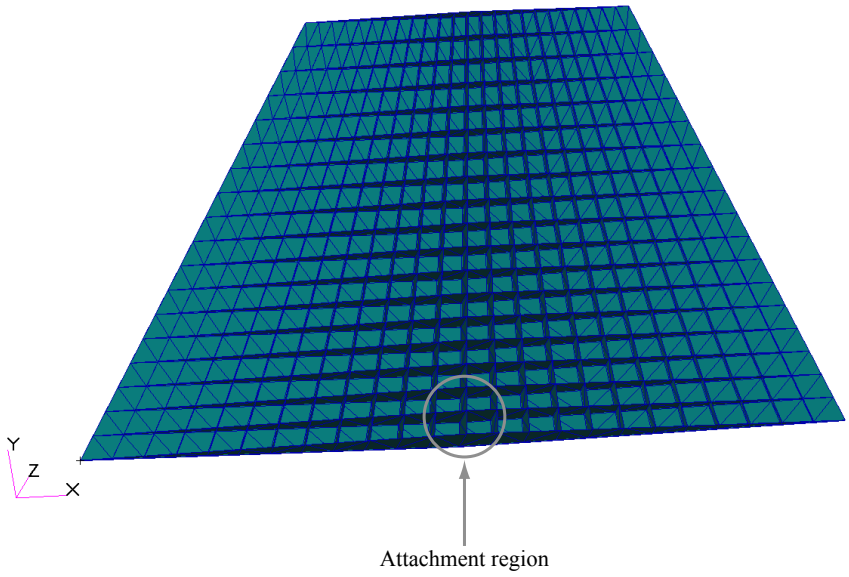

Figure 9.6: Finite element model of control surface used in study.

Chapter III. As stated previously, the lifting surface is taken to be all-moveable about a hinge line located at the mid-chord [60] and will thus be connected to the vehicle main body through a torque tube. This attachment is modeled by imposing the condition that lifting surface translates and rotates with the fuselage at the attachment region indicated by the gray circle in Fig. 9.6. Furthermore, for the cases in the chapter that involve a change in the control surface deflection angle, rotation about the hinge line is modeled by imposing enforced displacements at the interface DOFs that correspond to this rotation. In addition, the nodes at the root are constrained against translation in the y direction.

9.4.3 Simplified Fuselage-Lifting Surface Configuration

This chapter is motivated by two main objectives. The first is to develop and validate a partitioned solution methodology for coupling the various substructures of the HSV for time-domain flight dynamic simulation. The second is to use the partitioned solution methodology to assess the impact of lifting surface inertial effects on overall vehicle response. In order to focus specifically on these objectives, the fuselage representation described in Section 9.4.1 is replaced by a simplified representation for the purposes of this

study. This representation consists of a point mass attached to a spring which is then connected to the lifting surface. The lifting surface and single degree of freedom oscillator configuration is depicted in Fig. 9.7. Note that the motion of the fuselage mass is constrained such that it it is only permitted to translate in the z direction. Therefore, the enforced motion at the lifting surface attachment location only contains a z translational component. The attachment between the fuselage mass and the lifting surface in the full-order, monolithic representation is modeled by a rigid element (Nastran RBE2) that transfers the fuselage motion to the lifting surface DOFs located approximately within the attachment region shown in Fig. 9.6. Physically, the spring stiffness, K_f, represents the bending stiffness of the fuselage as well as the associated aerodynamic stiffness. The goal is to march the complete system in time by modeling the lifting surface and fuselage (point mass) independently and exchanging information between the two within each time step. While the partitioned solution methodology is applied to the configuration of Fig. 9.7 in this chapter, it is important to note that the approach is general in nature such that it can be applied to any configuration of interest, including the HSV representation shown in Fig. 9.5.

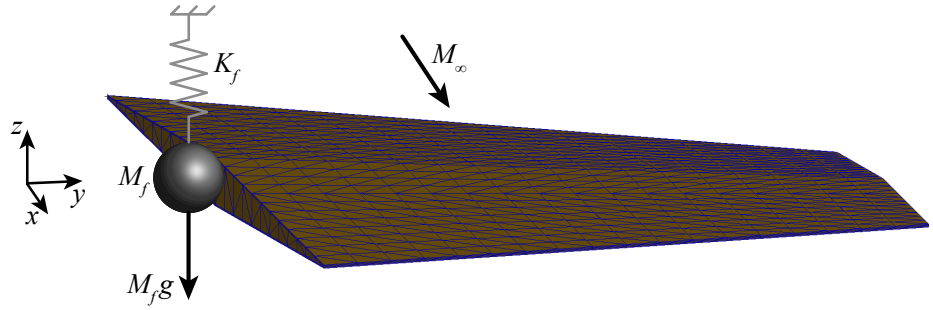

Figure 9.7: Representation of lifting surface and fuselage system.

9.5 Aerothermoelastic Lifting Surface ROM Generation

Prior to carrying out simulations, the thermal and structural dynamic ROMs to be used in the lifting surface framework must be created. The process for generating these ROMs is given in Fig. 6.3 and described in Chapter VI. Note that kriging ROMs are again utilized

to directly update $k^*_{uu}(T) = \Phi_S^T K^*_{uu}(T)\Phi_S$ and $F^H_u(T)$ shown in Eqs. (9.14) and (9.15), respectively. However, due to the large number of DOFs in the structural model, $K^*_{uu}(T)$ and $K^*_{ur}(T)$ on the right-hand sides of Eqs. (9.5) and (9.14) are approximated by evaluating them at the reference thermal state and holding them constant throughout the simulation.

The aerothermoelastic lifting surface ROM used in the current chapter is based on that created in Chapter VIII. The ranges in flight conditions used in ROM generation for that chapter are given in Table 9.1, where M_∞ is the freestream Mach number, α_{net} is the net lifting surface angle of attack, h is the altitude, and $\mathcal{T}^{(0)}$ is the uniform initial temperature condition. The thermal snapshots were based on 10 parallel aerothermoelastic simulations, resulting in a total of 49,510 thermal snapshots. Based on the POD eigenvalues, 32 POD modes were retained for the thermal ROM. Comparison of the thermal ROM to the full-order thermal model for one representative simulation showed that the L_∞ error remained below 3% throughout the complete time range considered.

Table 9.1: Bounds on flight conditions for aerothermoelastic lifting surface ROM.

5.0	$\leq M_\infty \leq$	8.0
0.0°	$\leq \alpha_{\text{net}} \leq$	4.0°
25.0 km	$\leq h \leq$	45.0 km
293 K	$\leq \mathcal{T}^{(0)} \leq$	1500 K

The current chapter makes use of the thermal ROM that was generated in Chapter VIII. However, additional studies are conducted in this chapter to identify a robust structural basis under thermal, aerodynamic, and base excitation loads. For the purpose of ROM assessment, the time-dependence of the enforced displacements in the z direction at the lifting surface attachment point, $w_a(t)$, is prescribed as

$$w_a(t) = \sum_{i=1}^{3} \mu_i \sin(\omega_i t), \tag{9.36}$$

where μ_i are real scalar coefficients and ω_i are circular frequencies representing the first three fuselage bending natural frequencies. These frequencies are computed based on ve-

hicle properties given in a previous work [115]. Table 9.2 gives the circular natural frequencies along with the corresponding values of the ordinary natural frequencies, f_i, in Hz as well as the scalar coefficients.

Table 9.2: Parameters used in time-dependence of enforced motion at lifting surface attachment point.

i	ω_i [rad/sec] / f_i [Hz]	μ_i
1	6.9 / 1.1	0.015
2	43.2 / 6.9	0.015
3	121.1 / 19.3	0.015

In order to determine to appropriate number of free vibration modes and load-dependent Ritz vectors to include in the structural basis, full-order and reduced-order simulations are performed under combined base excitation loads, thermal loads, and unsteady aerodynamic loads at the following flight conditions: M_∞ = 6.5, $\alpha_{\text{net}} = 2^\circ$, h = 35 km. The thermal load vector used in the simulations is held constant over time and is obtained based on the temperatures at the end of a 400 s aerothermal simulation beginning from room temperature at these flight conditions. By including both base excitation loads and thermal loads in the simulations, the ability of the basis to capture both highly unsteady response due to base motion as well as static response due to thermal deformation can be examined. Based on simulation results, the structural basis is chosen to consist of ten free vibration modes evaluated at the reference thermal state and five additional load-dependent Ritz vectors. The reference thermal state is obtained by averaging the 49,510 thermal snapshots taken in Chapter VIII. Of the ten free vibration modes employed in the basis, the natural frequency of the lowest frequency mode is 25 Hz, while that of the highest frequency mode is 186 Hz. Each of the five load-dependent Ritz vectors correspond to a static solution under a representative applied load. The applied load for each Ritz vector is chosen based on a POD analysis of the structural load vector which was carried out in Chapter VIII in order to identify the dominant spatial components of the structural loads.

Recall that two additional approximations are made in the structural dynamic ROM

besides the use of the modal subset. One involves the kriging approximations used to directly update the generalized stiffness matrix, $k^*_{uu}(T)$, and physical thermal load vector, $F^H_u(T)$, in Eqs. (9.14) and (9.15) as a function of temperature. The other involves the fact that $K^*_{uu}(T)$ and $K^*_{ur}(T)$ on the right-hand sides of Eqs. (9.5) and (9.14) are evaluated at the reference thermal state and held constant throughout the simulation. In order to distinguish the errors due to these approximations from the errors due to modal truncation, three different cases are simulated. Table 9.3 gives the structural model, either the full-order model or 15-mode ROM, that is used for each case. Table 9.4 gives a summary of the approximations that are made for each case.

Table 9.3: Structural model used in each of the three cases used in the structural dynamic ROM evaluation.

Case	Structural Model
E1	Full-order
E2	15-mode ROM
E3	15-mode ROM

Table 9.4: Summary of approximations made in each of the three cases used in the structural dynamic ROM evaluation.

Case	$k^*_{uu}(T)$	$F^H_u(T)$	$K^*_{uu}(T)$	$K^*_{ur}(T)$
E1	N/A	Actual T/Exact	Actual T/Exact	Actual T/Exact
E2	Actual T/Exact	Actual T/Exact	Actual T/Exact	Actual T/Exact
E3	Actual T/Kriging	Actual T/Kriging	Ref. T/Exact	Ref. T/Exact

In Table 9.4, the term "Actual T" indicates that a quantity is evaluated at the actual thermal state of the structure, while "Ref. T" indicates that the quantity is evaluated at the reference thermal state obtained by averaging the thermal snapshots. The term "Exact" in the table refers to the fact that no approximation is made when assembling the matrix or vector, while "Kriging" indicates that the corresponding kriging approximation is used. For case E1, the full-order structural model is used and all quantities are evaluated exactly at the actual thermal state. The full-order model does not require the generalized stiffness matrix as indicated by "N/A" in the third column for case E1. For this case, the physical

stiffness matrix, K^*_{uu}, on the left-hand side of Eq. (9.12) is evaluated exactly at the actual thermal state. Case E2 uses the 15-mode structural ROM with all quantities evaluated exactly at the actual thermal state. The 15-mode structural ROM is also used for case E3 and $k^*_{uu}(T)$ and $F^H_u(T)$ are again evaluated at the actual thermal state. However, for this case, these quantities are computed using the corresponding kriging approximations which provide improved computatinal efficiency. Additionally for case E3, $K^*_{uu}(T)$ and $K^*_{ur}(T)$ on the right-hand sides of Eqs. (9.5) and (9.14) are evaluated at the reference thermal state and held constant throughout the simulation. Therefore, the difference between cases E1 and E2 will demonstrate the error incurred solely due to the use of the modal subset in the structural ROM. The difference between cases E2 and E3 will illustrate the error incurred solely due to the kriging approximations of the generalized stiffness and physical thermal loads in addition to that due to evaluating $K^*_{uu}(T)$ and $K^*_{ur}(T)$ on the right-hand sides of Eqs. (9.5) and (9.14) at the reference thermal state instead of the actual thermal state. Note that case E1 represents the high-fidelity case used for comparison and case E3 represents the structural dynamic model that will be used in the remainder in the chapter.

Plots of the z-direction displacements from cases E1 – E3 for a duration of 1 s are given for two nodes located at the leading edge in Fig. 9.8. Similarly, plots of the z-direction displacements from cases E1 – E3 for two nodes located at the trailing are given in Fig. 9.9. Though there exist minor discrepancies at certain peaks, the results given in Fig. 9.8 and Fig. 9.9 provide evidence that the structural dynamic lifting surface ROM represented by case E3 is capable of capturing the full-order response represented by case E1 with reasonable accuracy. Therefore, the 15-mode structural dynamic ROM of the lifting surface represented by case E3 and as described above is used in the remainder of this study.

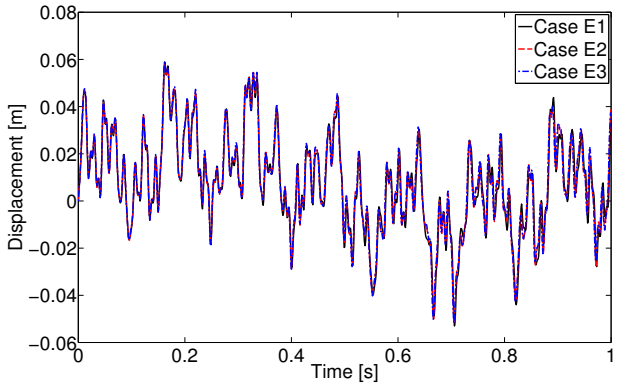

(a) Node 2 (bottom surface, root leading edge).

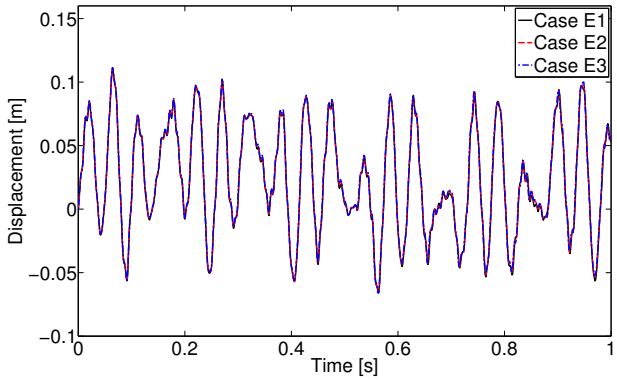

(b) Node 37 (bottom surface, tip leading edge).

Figure 9.8: Time-history of z displacements for two selected nodes at the leading edge for cases E1 – E3.

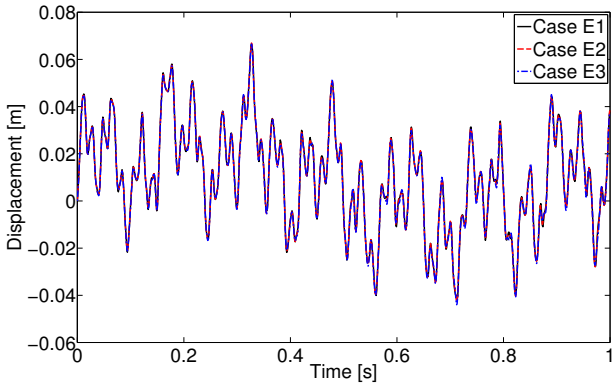

(a) Node 458 (bottom surface, root trailing edge).

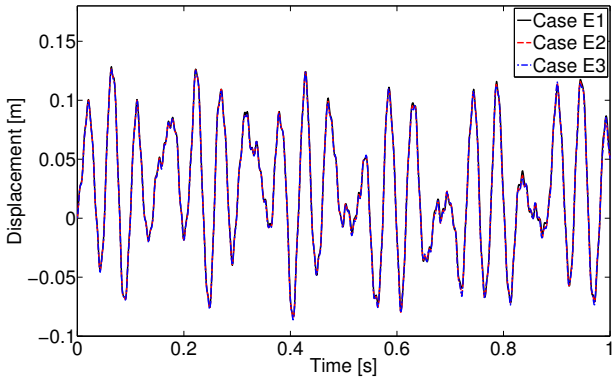

(b) Node 475 (bottom surface, tip trailing edge).

Figure 9.9: Time-history of z displacements for two selected nodes at the trailing edge for cases E1 – E3.

9.6 Lifting Surface-Fuselage Coupling: Results

9.6.1 Validation of Partitioned Solution Methodology

The fuselage-lifting surface configuration depicted in Fig. 9.7 is now used to illustrate the methodology. Before utilizing the partitioned fuselage and lifting surface models, the partitioned solution methodology is validated against a full-order monolithic solution performed within Nastran. For the validation, the fuselage mass is taken to be 222,222 kg based on vehicle properties given in a previous work [115]. The stiffness of the spring associated with the fuselage is chosen such that the natural frequency of the fuselage system is 10 Hz, and thus the spring stiffness is 8.77×10^8 N/m. Three validation cases, denoted P1, P2, and P3, are set up to validate the approach, where "P" denotes that these cases are used to validate the partitioned solution methodology. A summary of these cases is given in Table 9.5. Case P1 uses the monolithic system with the full-order structural model of the lifting surface and represents the reference case. Case P2 uses the partitioned approach with the full-order structural model of the lifting surface, while case P3 uses the partitioned approach with the previously described 15-mode structural ROM of the lifting surface. The difference between cases P1 and P2 illustrates the error due to use of the partitioned approach, while the difference between cases P2 and P3 illustrates the error due to the use of the lifting surface structural ROM. Note that for all three cases, the aerodynamic loads are omitted from the analysis, and the thermal loads are held constant based on those obtained after heating the structure for 400 s from room temperature. The aeroelastic time step sizes for both the fuselage and the lifting surface are chosen to be 0.001 s. The simulation is started by releasing the mass representing the fuselage from its equilibrium position at initial time. As the fuselage mass begins to oscillate, it in turn excites the lifting surface and induces structural dynamic oscillations.

A plot of the z-direction displacements from cases P1 – P3 for the fuselage node is given in Fig. 9.10. Similarly, plots of the z-direction displacements from cases P1 – P3 for

Table 9.5: Summary of three cases used to validate partitioned solution methodology.

Case	Fuselage-Lifting Surface Coupling	Lifting Surface Structural Model
P1	Monolithic	Full-order
P2	Partitioned	Full-order
P3	Partitioned	15-mode ROM

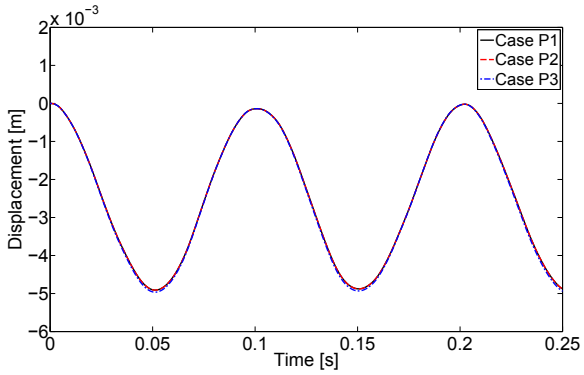

Figure 9.10: Time-history of z displacements at fuselage node for cases P1 – P3.

three selected nodes located on the lifting surface are given in Fig. 9.11. Examining the results, the first observation to be made is that, as expected, case P1 matches case P2 nearly exactly indicating that the partitioned approach is mathematically equivalent to the monolithic system approach. Comparing case P3 to case P2, it can be seen that the lifting surface structural ROM shows only minor discrepancies with respect to the full-order model, and thus the accuracy of this ROM is sufficient for the purposes of this study. As shown in Fig. 9.10, the fuselage node oscillates at approximately 10 Hz which was the targeted frequency for the uncoupled single DOF spring/mass system. For the properties chosen for this case, the loads imparted by the lifting surface on the fuselage do not cause the fuselage to deviate significantly from a single DOF oscillation response. Subsequent studies will further explore the extent to which the lifting surface motion impacts the fuselage response under different types of excitations. Finally, it should be noted that only one iteration was required for convergence at all time steps for cases P2 and P3. This is due to the fact that the R is a linear function of $x_r^{(n+1)}$ for the configuration under investigation. Thus, once R is evaluated at the two initial guesses generated in step 1 of Algorithm 9.3.1, the slope of

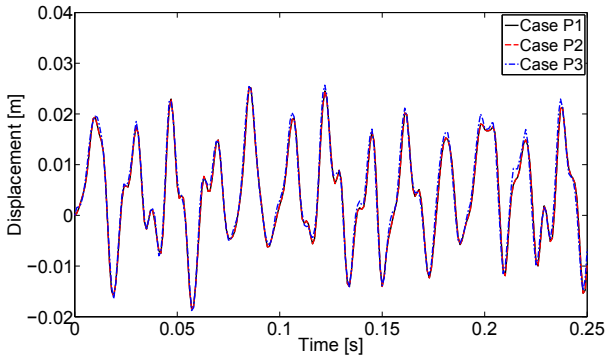

(a) Node 2 (bottom surface, root leading edge).

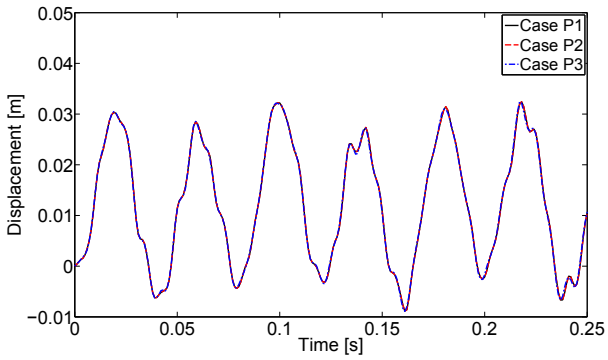

(b) Node 247 (bottom surface, tip mid-chord).

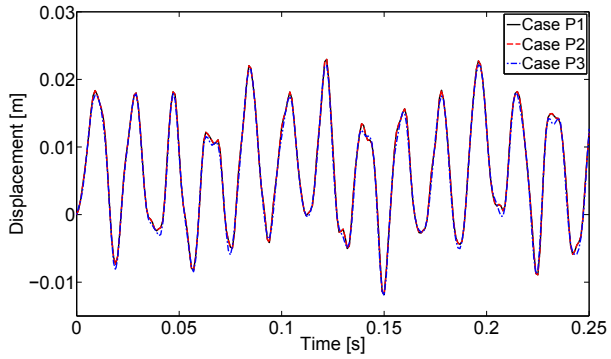

(c) Node 458 (bottom surface, root trailing edge).

Figure 9.11: Time-history of z displacements at three selected nodes located in lifting surface for cases P1 – P3.

R is known and the converged value of $x_r^{(n+1)}$ can be obtained in the first iteration of the secant method. However, the methodology is intentionally formulated to be general such that the problem need not be linear. If the problem is in fact linear, then the linear solution is recovered in the minimum number of iterations.

9.6.2 Impact of Lifting Surface Inertia on Fuselage z Direction Response

With the lifting surface ROM and partitioned solution methodology validated, the framework is now used to assess the impact of lifting surface inertial loads. In order to assess these effects, the coupled fuselage-lifting surface formulation described previously is used to perform simulations of the system depicted in Fig. 9.7 in which lifting surface inertial effects are both present and absent. For the case in which lifting surface inertial effects are present, the coupled formulation described previously, which includes lifting surface structural dynamics, is employed. For the case in which lifting surface inertial effects are absent, the coupled formulation is modified such that the solution for the lifting surface deformation is reduced to the solution of a static problem subjected to thermal and aerodynamic loads with the constraint motion imposed instantaneously. Elimination of lifting surface inertial effects is achieved by modifying Eq. (9.7b) to include only static terms such that it becomes

$$K_{ur}^{*} x_r + K_{uu}^{*} x_u = F_u^H + F_u^A. \tag{9.37}$$

In order to maintain consistency with the dynamic lifting surface solution, Eq. (9.37) is solved in a manner analogous to that derived in Eqs. (9.8) – (9.17). Therefore, for the static lifting surface case, the equations governing the lifting surface modal coordinates are reduced to

$$k_{uu}^{*}(T) d(t) = f_u(t, T). \tag{9.38}$$

The net external force exerted by the lifting surface relative to the fuselage, $F_r^{W/B}$, is again calculated using Eq. (9.28) for the static lifting surface case. However, for the static lifting

surface case, x_u^E will not include elastic deformation due to lifting surface inertia, and will thus allow for assessing the impact of lifting surface inertia on the loads that the lifting surface exerts on the fuselage.

Before performing simulations, M_f is adjusted such that the fuselage weight is exactly balanced by the z-direction force produced by the lifting surface at $M_\infty = 6.5$, $\alpha_{\text{net}} = 2°$, $h = 35$ km. To calculate this force, the lifting surface is first heated for 400 s at these flight conditions in order to obtain a representative temperature distribution. It is then fixed at its attachment point and brought to elastic equilibrium under thermal loads and aerodynamic loads. Once elastic steady state is obtained, $F_r^{W/B}$ is calculated in order to obtain the z force that is generated by the lifting surface and transferred the fuselage. Additionally, the spring stiffness associated with the fuselage is set such that the fuselage natural frequency is 10 Hz in the absence of lifting surface inertia.

All simulations in this section begin by heating the lifting surface for 400 s at $M_\infty = 6.5$, $\alpha_{\text{net}} = 2°$, $h = 35$ km and bringing it to elastic equilibrium under thermal and aerodynamic loads. As the weight of the fuselage is equal to the z force produced by the lifting surface under these conditions, the fuselage will be at its equilibrium position at the beginning of the simulation. The simulation is then started at these flight conditions by time-marching the partitioned lifting surface-fuselage formulation forward in the manner described previously. For the results presented, the time step sizes are chosen as follows: $\Delta t_{AE} = \Delta t_{HT} = 0.001$ s and $\Delta t_{AT} = 0.1$ s. Though the thermal and aerodynamic loads will change over time as the simulation progresses, the impact of these loads on the response of the system is minimal as they change on a slow time scale. Thus, it is necessary to perturb the equilibrium conditions such that structural dynamic oscillations are induced into the system so that the impact of lifting surface inertial effects can be examined. The method used here to perturb the equilibrium is to apply a change in flow direction for a short period of time, which corresponds to a change in lifting surface net angle of attack, α_{net}. The flow direction is instantaneously incremented at time t_i by an amount $\Delta\alpha_{\text{net}}$, held

it at this value for a time duration of Δt_α, and then decremented back to the original value of α_{net} at time $t_d = t_i + \Delta t_\alpha$. The results presented in this study use $\Delta\alpha_{\text{net}} = 8^\circ$ which corresponds to increasing α_{net} from 2° to 10° at t_i, holding at 10° for a time duration of Δt_α, and then decrementing back to 2° at t_d. The values of Δt_α that are used in the simulations are 0.03 s and 0.1 s. Note that for the results presented, $\Delta\alpha_{\text{net}}$ is applied at 0.01 s into the transient ($t_i = 0.01$ s).

The displacements of the mass representing the fuselage are shown in Fig. 9.12 for a one second time-history where "CS Dynamic" refers to the case which utilizes the structural dynamic solution to obtain the lifting surface response at each aeroelastic time step, while "CS Static" refers to the case which utilizes the static solution to obtain the lifting surface response at each aeroelastic time step. Figure 9.12(a) shows results for the case of $\Delta t_\alpha = 0.03$ s, while Fig. 9.12(b) shows results for the case of $\Delta t_\alpha = 0.1$ s. For $\Delta t_\alpha = 0.03$ s, α_{net} is decremented back from 10° to 2° just before the fuselage reaches the peak of its response. However, for $\Delta t_\alpha = 0.1$ s, α_{net} is not decremented back from 10° to 2° until the fuselage has approximately returned its equilibrium position. Therefore, comparing Fig. 9.12(a) to Fig. 9.12(b), it can be seen that the fuselage undergoes significantly higher amplitude oscillations for the case of $\Delta t_\alpha = 0.03$ s than for the case of $\Delta t_\alpha = 0.1$ s.

Comparing the "CS Dynamic" and "CS Static" cases in Fig. 9.12(a), one can observe a difference in frequency of oscillation resulting from the inclusion of lifting surface inertia. Recall that the mass and stiffness properties associated with the fuselage were set such that its natural frequency would be 10 Hz in the absence of lifting surface inertia. Examining the "CS Static" case in Fig. 9.12(a), this 10 Hz natural frequency is observed. However, by including lifting surface inertia, the frequency of fuselage oscillation is reduced as shown by the "CS Dynamic" case in Fig. 9.12(a). Note that for the case of $\Delta t_\alpha = 0.03$ s, lifting surface inertia has only a minor effect on the amplitude of fuselage oscillation for the "CS Dynamic" case. Examining Fig. 9.12(b) it can be seen that when Δt_α is increased to 0.1 s, lifting surface inertia has a more prominent effect on the amplitude of the fuselage response.

This is due to the fact that α_{net} is decremented back to 2° approximately at the same time that the fuselage reaches its equilibrium position. Thus in the "CS Static" case for $\Delta t_\alpha = 0.1$ s, the amplitude of fuselage oscillation is reduced significantly. The result is that the forces acting on the fuselage due to its own inertia and stiffness are smaller compared to the lifting surface inertial loads beyond t_d for $\Delta t_\alpha = 0.1$ s. Therefore, lifting surface inertia has a more prominent effect on fuselage amplitude of oscillation beyond t_d for this case.

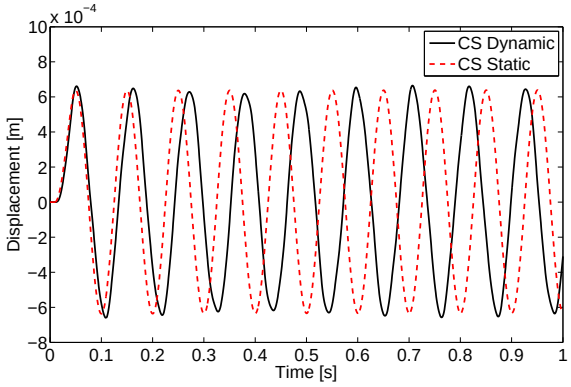

(a) Δt_α = 0.03 s.

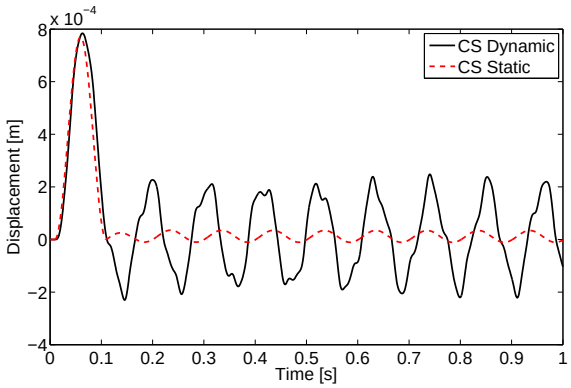

(b) Δt_α = 0.1 s.

Figure 9.12: Fuselage displacements for two values of Δt_α with and without lifting surface inertial effects.

In order to examine the frequency content of the fuselage response, the fast Fourier transform (FFT) is performed on the fuselage response for the time-history beginning at t_d. Because the FFT assumes that the input sequence is a power of two in length [131], the FFT is performed on a signal in the time range $0.041 \text{ s} \leq t \leq 1.064$ s for $\Delta t_\alpha = 0.03$ s

and in the range $0.111 \text{ s} \leq t \leq 1.134 \text{ s}$ for $\Delta t_\alpha = 0.1$ s. Therefore, the output signal is of length 1,024 for both values of Δt_α. The single-sided amplitude spectrums of the fuselage displacements are given in Fig. 9.13(a) and Fig. 9.13(b) for the cases of $\Delta t_\alpha = 0.03$ s and $\Delta t_\alpha = 0.1$ s, respectively. For both values of Δt_α, the first peak at nonzero frequency occurs at approximately 8.79 Hz for the "CS Dynamic" case and at approximately 9.77 Hz for the "CS Static" case, indicating that exclusion of lifting surface inertia results in an 11% overprediction in the lowest-frequency fuselage oscillation component. Based on the frequency of oscillation, it can be concluded that this mode is associated with the single DOF mass-spring fuselage system.

In addition to this fuselage mode, results from the "CS Dynamic" case show higher frequency oscillation components associated with lifting surface modes. For both values of Δt_α, the second and third major peaks occur at approximately 26.4 Hz and 54.7 Hz, respectively. In order to determine which lifting surface modes these frequencies correspond to, the first ten lifting surface natural frequencies are computed at the actual thermal state of the structure which is obtained by heating the lifting surface for 400 s at the previously described flight conditions. These first ten natural frequencies are given in Table 9.6. Based on the frequencies shown in the table, it can be concluded that the second major peaks for the "CS Dynamic" cases in both Figs. 9.13(a) and 9.13(b) correspond to the first lifting surface mode, while the third major peaks correspond to either the third or fourth lifting surface mode. It should be noted that Chapter IV described a mode switching phenomenon that was found to occur between lifting surface modes three and four as the structure is heated. This phenomenon is likely due to the fact that these modes are close in frequency. Though there are three noticeable peaks present in the FFT results of the fuselage displacements, the lowest frequency mode clearly contributes most significantly to the response for both values of Δt_α.

Plots of the lifting surface z displacements at node 247 (located on the bottom surface at the mid-chord of the tip) are shown in Figs. 9.14(a) and 9.14(b) for $\Delta t_\alpha = 0.03$ s and

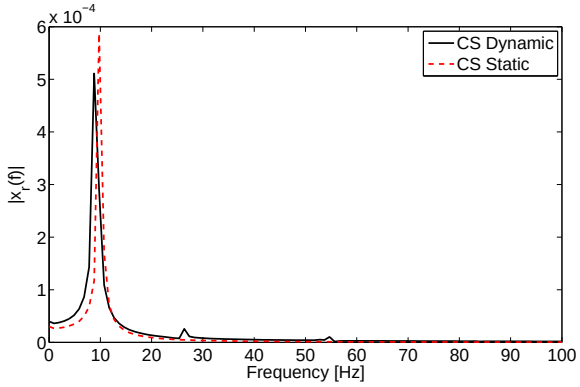

(a) $\Delta t_\alpha = 0.03$ s.

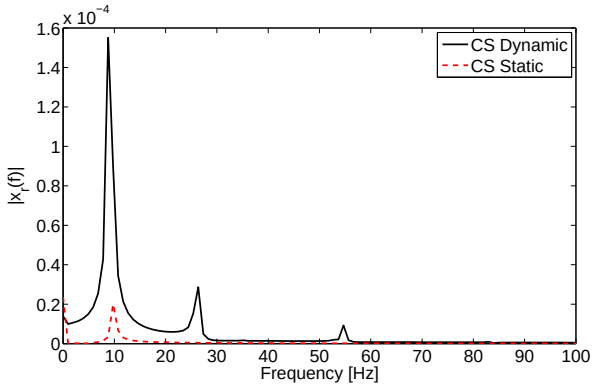

(b) $\Delta t_\alpha = 0.1$ s.

Figure 9.13: FFT of fuselage response for two values of Δt_α with and without lifting surface inertial effects.

Table 9.6: First ten lifting surface natural frequencies evaluated thermal state obtained by heating structure for 400 s at $M_\infty = 6.5$, $\alpha_{\text{net}} = 2°$, and $h = 35$ km.

Mode Number	Natural Frequency [Hz]
1	25.1
2	35.6
3	53.2
4	54.3
5	86.1
6	98.1
7	130
8	144
9	163
10	183

$\Delta t_\alpha = 0.1$ s, respectively. For the "CS Static" case in both figures, there is an instantaneous jump in displacement at $t_i = 0.01$ s. This is due to the increase in aerodynamic pressure loads on the structure induced by the increased angle of attack. Because the lifting surface response is calculated using a static solution for the "CS Static" cases, the increase in displacement is instantaneous for these cases. Between t_i and t_d for the static cases, the lifting surface motion approximately follows the constraint motion imposed by the fuselage. At t_d when α_{net} is decremented back to 2°, the static lifting surface displacement instantaneously drops due to the decrease in aerodynamic loads. Beyond t_d, the lifting surface motion in the "CS Static" case is approximately the same as the fuselage motion with an offset due to static deformation under thermal and aerodynamic loads. Note that while the thermal and aerodynamic loads do change over time in the static case, their effect on lifting surface deformation is essentially a static effect as these loads change on a slow time scale. Comparing the "CS Dynamic" cases to the "CS Static" cases, it can be observed that sustained structural dynamic oscillations are induced in the lifting surface which lead to higher displacement levels than would be predicted if only a static lifting surface solution was used.

The FFT's of the lifting surface response at node 247 are taken for the same time periods as used in generating Figs. 9.13(a) and 9.13(b). The single-sided amplitude spectrums for the two values of Δt_α are given in Figs. 9.15(a) and 9.15(b). For both values of Δt_α, the first major peak at nonzero frequency occurs at approximately 8.79 Hz in the "CS Dynamic" case and at approximately 9.77 Hz in the "CS Static" case. For the "CS Dynamic" case, the second major peak occurs at approximately 26.4 Hz for both values of Δt_α. The frequencies of the first two lifting surface peaks are the same as those for the first two fuselage peaks. While these first two peaks contribute most significantly to the lifting surface response for the "CS Dynamic" case, there exist three additional smaller peaks for both values of Δt_α which occur at approximately 35.2 Hz, 54.7 Hz, and 83.0 Hz. Referring to Table 9.6, these three peaks correspond roughly with lifting surface modes two, three/four,

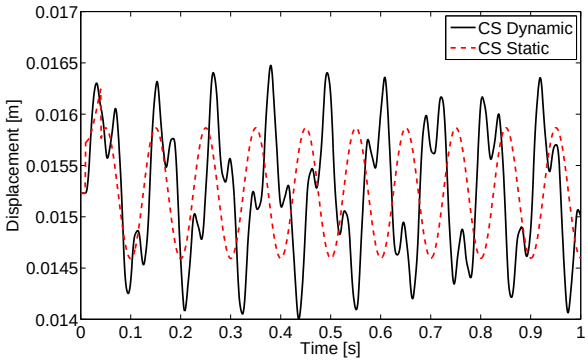

(a) $\Delta t_\alpha = 0.03$ s.

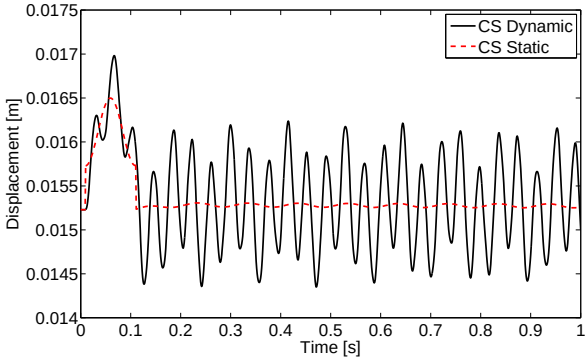

(b) $\Delta t_\alpha = 0.1$ s.

Figure 9.14: Lifting surface z displacements at node 247 (bottom surface, tip, mid-chord) for two values of Δt_α with and without lifting surface inertial effects.

and five, respectively. Comparing the lifting surface FFT results with those of the fuselage, it can be seen that while lifting surface modes 1 – 5 are all excited at least to a small extent in the lifting surface response, only lifting surface modes one and three/four appear to have an effect on the fuselage response. However, as was the case for the fuselage, the two lowest frequency modes contribute most significantly to the lifting surface response.

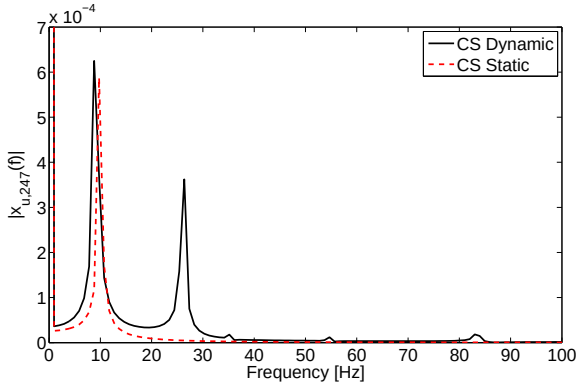

(a) $\Delta t_\alpha = 0.03$ s.

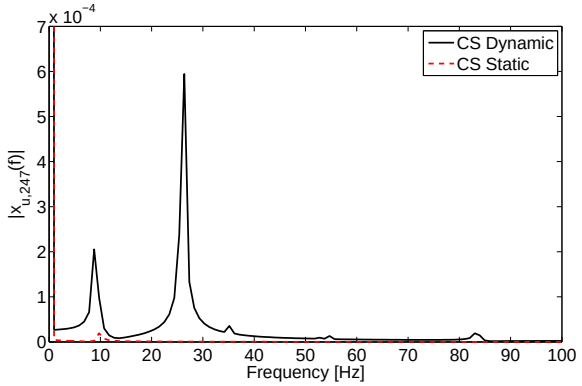

(b) $\Delta t_\alpha = 0.1$ s.

Figure 9.15: FFT of lifting surface response at node 247 (bottom surface, tip, mid-chord) for two values of Δt_α with and without lifting surface inertial effects.

The loads exerted by the lifting surface on the fuselage, $F_r^{W/B}$, are shown in Fig. 9.16 for the two values of Δt_α. As expected, in the "CS Static" cases, $F_r^{W/B}$ is approximately constant with an instantaneous increase at t_i and instantaneous decrease at t_d due to the change in α_{net}. Examining the "CS Dynamic" results, $F_r^{W/B}$ is shown to oscillate approximately about the static value due to the lifting surface inertial effects. As shown by the

fuselage displacements in Fig. 9.12, the extent to which the fuselage responds to these high-frequency oscillations in $F_r^{W/B}$ depends upon the inertia and stiffness of the fuselage itself. Based on the results presented for this time history, the maximum absolute ratio of $F_r^{W/B}$ for the dynamic case to that for the static case is seven for $\Delta t_\alpha = 0.03$ s and eight for $\Delta t_\alpha = 0.1$ s. These results indicate that lifting surface inertia can have a noticeable effect on fuselage loads. However, the extent to which lifting surface inertial loads impact the fuselage response is dependent on the fuselage inertia as well as the frequency content of the lifting surface inertia loads.

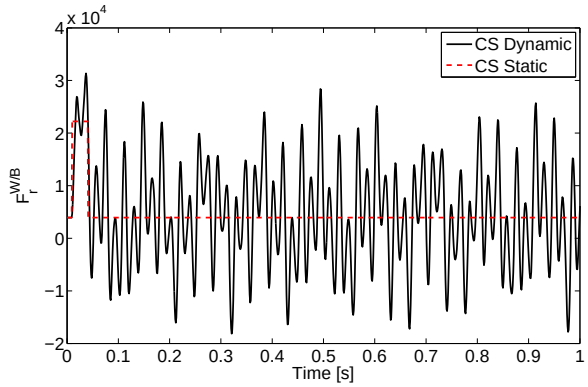

(a) Δt_α = 0.03 s.

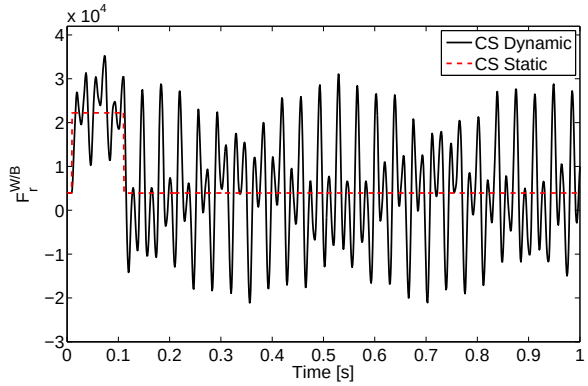

(b) Δt_α = 0.1 s.

Figure 9.16: $F_r^{W/B}$ for two values of Δt_α with and without lifting surface inertial effects.

Plots of the FFT of the $F_r^{W/B}$ time-history for the two values of Δt_α are given in Figs. 9.17(a) and 9.17(b). In both plots, noticeable peaks occur for the "CS Dynamic" case at approximately 8.79 Hz, 26.4 Hz, 52.7 Hz, 54.7 Hz, 84.0 Hz, 121 Hz, 132 Hz, 146

Hz, and 160 Hz. While the modes at these frequencies each contribute to $F_r^{W/B}$ at least to a small extent, the modes corresponding to the first four of these frequencies contribute most significantly. Referring to Table 9.6, these four frequencies roughly correspond to fuselage mode 1, lifting surface mode 1, lifting surface mode 3, and lifting surface mode 4. The most dominant contribution to $F_r^{W/B}$ comes from the 54.7 Hz mode for both values of Δt_α. However, it is interesting to note that the 54.7 Hz mode is not the most dominant mode in either the fuselage response or lifting surface response.

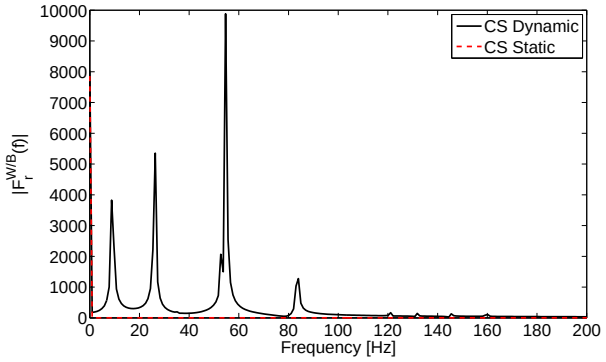

(a) $\Delta t_\alpha = 0.03$ s.

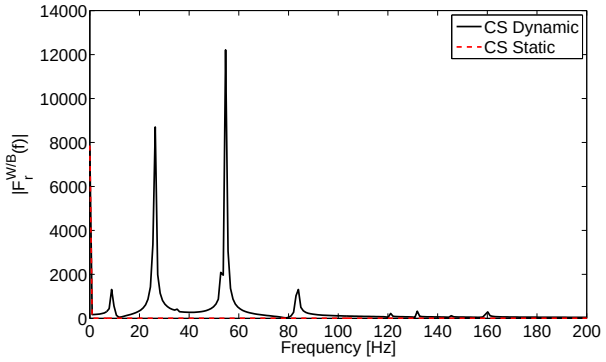

(b) $\Delta t_\alpha = 0.1$ s.

Figure 9.17: FFT of $F_r^{W/B}$ response for two values of Δt_α with and without lifting surface inertial effects.

9.6.3 Impact of Lifting Surface Inertia Under Commanded Change in Deflection Angle

The next aspect of this study involves investigation of the impact of lifting surface inertial loads under a commanded change in lifting surface deflection angle imposed via the control system. The importance of understanding such lifting surface-fuselage inertial coupling has been discussed in a recent paper [109] which referred to this coupling as the "tail-wags-dog" effect. The discussion in Ref. 109 highlights the fact that this effect typically results in a complex-conjugate pair of zeros in the elevator-to-pitch rate transfer function and can affect the speed of response of the system.

As a step toward assessing the extent to which the overall vehicle pitch response is affected by lifting surface inertia under commanded changes in deflection angle, a control input corresponding to lifting surface deflection angle is incorporated into the aerothermoelastic ROM framework. Note that all simulations conducted in this section do not include the fuselage mass depicted in Fig. 9.7, and consist of enforced lifting surface motion due to rotation about the hinge line. In order to capture the relationship between the input command from the controller and the resulting output rotation applied to the lifting surface, actuator dynamics are incorporated into the lifting surface model. The equation relating the input command, δ_{cmd}, to the output lifting surface deflection angle, δ, is given by [165]

$$\ddot{\delta} = -2\zeta_\delta \omega_\delta \dot{\delta} - \omega_\delta^2 \delta + \omega_\delta \delta_{\text{cmd}}, \tag{9.39}$$

where $\zeta_\delta = 1$ and $\omega_\delta = 20$. Note that in reality, δ_{cmd} would come from the control system. However, a control system is not present in the current framework, and thus δ_{cmd} is a prescribed function that is determined *a priori* in this chapter. A schematic illustrating the geometry associated with the lifting surface deflection angle is given in Fig. 9.18, where x_B and z_B represent the body-fixed axis system. As shown in Fig. 9.18, δ is taken to be positive leading edge up. Figure 9.18 is intended solely to give the geometry associated

with the problem and does not correspond to a specific vehicle configuration as this study considers rotation rotation of a lifting surface about its in hinge in isolation. Note that the net lifting surface angle of attack, α_{net}, is given by

$$\alpha_{\text{net}} = \alpha + \delta, \tag{9.40}$$

where α is the vehicle angle of attack.

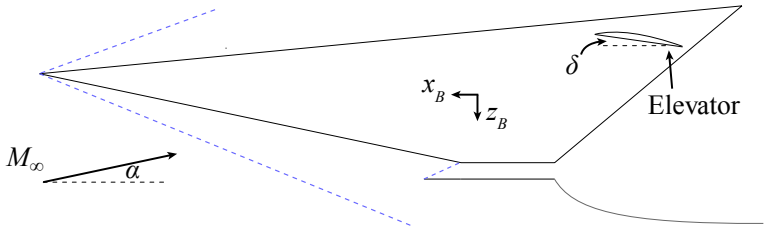

Figure 9.18: Schematic illustrating geometry associated with lifting surface deflection angle and vehicle angle of attack.

9.6.3.1 Commanded Step Increase in Lifting Surface Deflection Angle

For the first example case of a change in lifting surface deflection angle, the input command is taken to be a step change in deflection angle that is applied at 0.01 s into the simulation. The input step command corresponds to an instantenous increase in the desired value of δ from 0° to 3.9°. Because the simulations are carried out for $\alpha = 0.1^\circ$, the final value of δ is chosen to be 3.9° such that the total flow angle with respect to the lifting surface remains within the bounds on α_{net} given in Table 9.1. The functional form of the the input command is given by

$$\delta_{\text{cmd}}(t) = 20H(t-\tau)\left[3.9^\circ \frac{\pi}{180^\circ}\right], \tag{9.41}$$

where $H(t-\tau)$ is the Heaviside step function and τ is the time delay which is taken to be 0.01 s in this case. A plot showing $\delta(t)$ based on the input command of Eq. (9.41) is given

in Fig. 9.19, where δ has been converted from radians to degrees for visualization purposes.

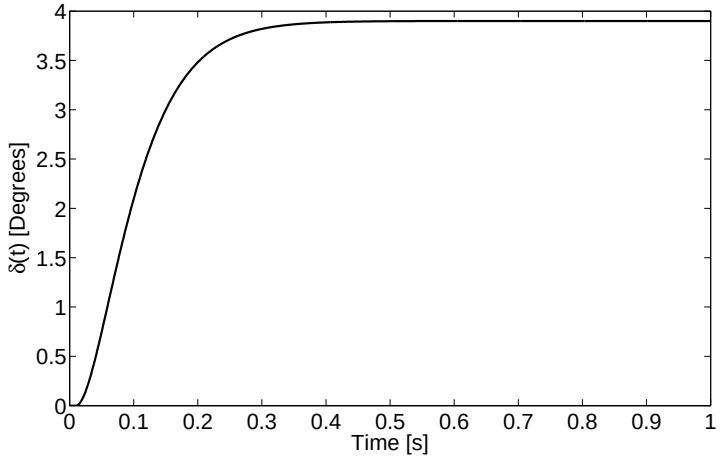

Figure 9.19: Time-history of applied lifting surface deflection angle, $\delta(t)$.

Simulations are carried out using the input command described above at $M_\infty = 6.5$ and $h = 35$ km. The time step sizes are chosen as follows: $\Delta t_{AE} = \Delta t_{HT} = 0.001$ s and $\Delta t_{AT} = 0.1$ s. As was done in the previous section, the lifting surface is first heated for 400 s at this Mach number and altitude at $\alpha = 0.1^\circ$ and $\delta = 0^\circ$. Using the temperature distribution obtained at the end of the 400 s period, the lifting surface is brought to aerothermoelastic equilibrium, and the simulation is then started from initial time. The vehicle angle of attack, α, is held at 0.1° throughout the simulation, and δ is given by the time-history shown in Fig. 9.19. The entries of x_u corresponding to the z displacements of node 37 (located at the bottom surface, tip, leading edge) and node 475 (located on the bottom surface, trailing edge) are plotted as a function of time in Fig. 9.20. Note that x_u includes both the constraint motion due to the change in lifting surface deflection angle, x_u^C, as well as the elastic motion relative to the constraint motion, x_u^E, as given in Eq. (9.8). As in the previous section, the "CS Dynamic" case includes lifting surface structural dynamics, while the "CS Static" case uses only a static solution to obtain the lifting surface response at each time step. Comparing the two cases for the time range $0.5 \text{ s} \leq t \leq 2.0$

s, it is found that exclusion of lifting surface inertia results in a maximum absolute percent error of 5.6% for the node 37 z displacements and 2.3% for the node 475 z displacements.

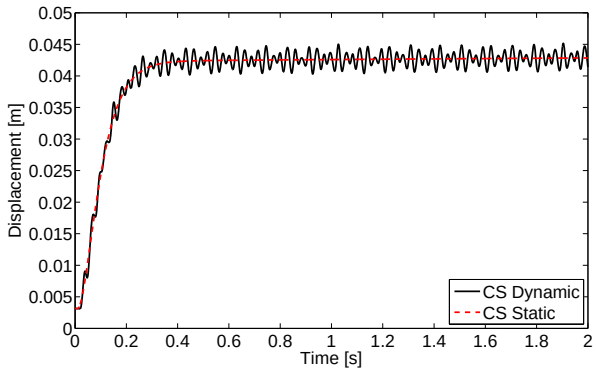

(a) Node 37 (bottom surface, tip, leading edge).

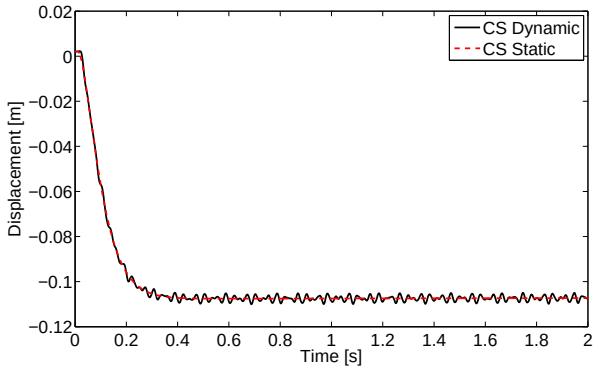

(b) Node 475 (bottom surface, tip, trailing edge).

Figure 9.20: Lifting surface total displacements, x_u, in z direction under commanded change in deflection angle with and without lifting surface inertial effects for two selected nodes.

In order to remove the effect of the constraint displacements due to the lifting surface deflection angle, the elastic displacements relative to the constraint motion, x_u^E, are also analyzed. The entries of x_u^E corresponding to the z displacements of nodes 37 and 475 are plotted in Fig. 9.21. By isolating the elastic component of the displacements, the effect of lifting surface inertia on its response can be seen more clearly. For the "CS Static" case, there is a small monotonic increase in elastic displacements over time due to increased steady aerodynamic loads and thermal loads as δ is increased. Examining the "CS Dynamic" results, it is observed that the change in lifting surface deflection angle induces

noticeable structural dynamic oscillations about the statically deformed state. Comparing the "CS Dynamic" case with the "CS Static" case for the time range 0.5 s $\leq t \leq$ 2.0 s, inclusion of lifting surface inertia results in elastic displacements of up to 1.7 times and 1.9 times the corresponding static displacements for node 37 and 475, respectively. The maximum absolute elastic displacements in the "CS Dynamic" case for the complete time histories shown in Figs. 9.21(b) and 9.21(a) are 0.0062 m (0.24 in) for node 37, and 0.0053 m (0.21 in) for node 475.

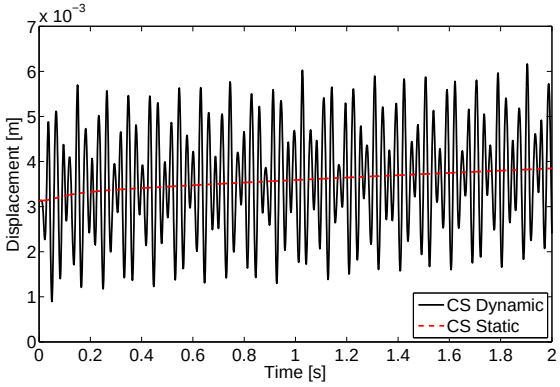

(a) Node 37 (bottom surface, tip, leading edge).

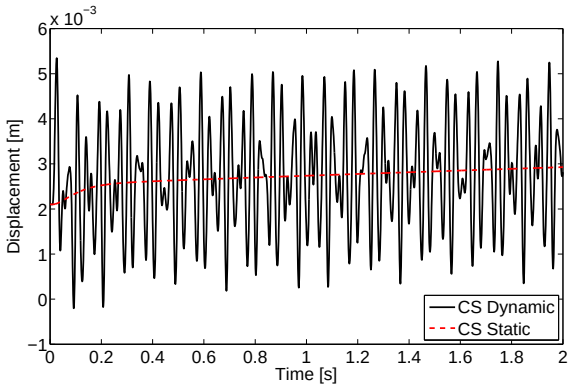

(b) Node 475 (bottom surface, tip, trailing edge).

Figure 9.21: Lifting surface elastic displacements, x_u^E, in z direction under commanded change in deflection angle with and without lifting surface inertial effects.

While examination of the displacement time-histories of the lifting surface provides insight into the response of the system, one of the main goals of this study is to assess the impact of lifting surface inertia on the overall dynamics of the HSV. As discussed at

the beginning of the current section, an important result of lifting surface-fuselage inertial coupling is that the response of the vehicle pitch rate to changes in elevator deflection angle can be adversely affected. As a step toward quantifying such effects, the pitching moments exerted by the lifting surface about the fuselage at the attachment point, $M_y^{W/B}$, are examined for this case. The time-histories of $M_y^{W/B}$ for the static and dynamic lifting surface cases are given in Fig. 9.22(a) and Fig. 9.22(b), respectively. Note that a positive value of $M_y^{W/B}$ corresponds to a nose-up pitching moment due to the orientation of the lifting surface coordinate system. For the static lifting surface case, as δ approaches the commanded value of the deflection angle, $M_y^{W/B}$ asymptotically approaches a higher value. However, for the dynamic lifting surface case, the increase in $M_y^{W/B}$ over time is essentially indiscernible due to oscillations resulting from lifting surface inertia. For the time range 0.5 s $\leq t \leq$ 2.0 s, the maximum absolute ratio of $M_y^{W/B}$ from the dynamic lifting surface case to that from the static lifting surface case is 127, indicating that lifting surface inertia can significantly impact the pitching moment from the lifting surface under commanded changes in lifting surface deflection angle. Therefore, exclusion of lifting surface inertia may result in errors in vehicle pitch response prediction.

For the static lifting surface case, $M_y^{W/B}$ initially drops when the commanded change in δ is first applied at 0.01 s. This is due to the velocity induced as the lifting surface begins to rotate about the hinge line. This velocity leads to unsteady aerodynamic pressure loads which counteract the positive moment caused by the steady pressure loads. Once δ reaches a certain deflection angle, the negative moment caused by the unsteady aerodynamic pressure loads is balanced out by the positive moment due to the steady pressure loads, and $M_y^{W/B}$ begins to increase. Additionally, small discontinuities in $M_y^{W/B}$ are observed for the static lifting surface case at 0.1 s, 0.2 s, and 0.3 s. These discontinuities are a result of the updating of the skin friction which occurs along with the updating of the thermal boundary conditions in intervals of 0.1 s. The increase in lifting surface deflection angle leads to increased dynamic pressure and thus elevated skin friction. Because the skin fric-

tion on the bottom surface is increased by a greater amount than that on the top surface due to the positive lifting surface angle of attack, there is an instantaneous decrease in $M_y^{W/B}$ each time the skin friction is updated up to approximately 0.3 s.

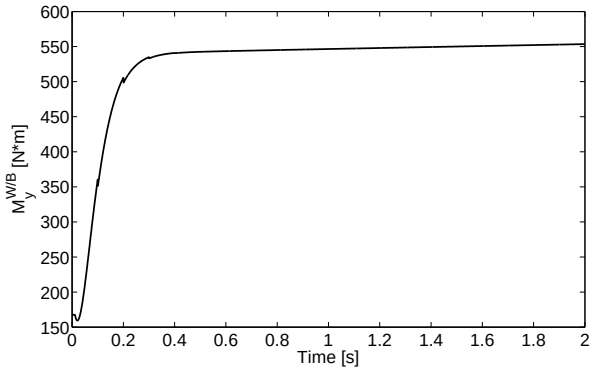

(a) Static lifting surface case.

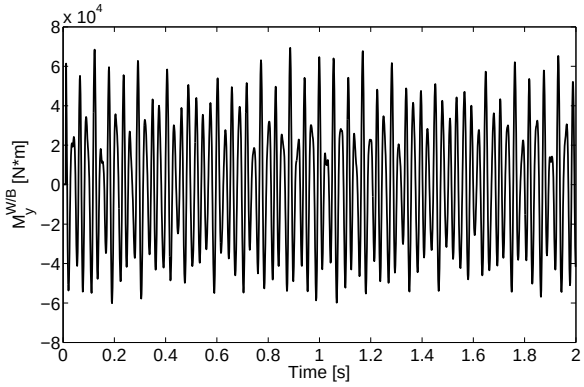

(b) Dynamic lifting surface case.

Figure 9.22: Time-domain response of $M_y^{W/B}$ for both static and dynamic lifting surface cases.

To assess the frequency content of the $M_y^{W/B}$ time-history, the FFT of the dynamic lifting surface case is taken for the time range 0.5 s $\leq t \leq$ 1.523 s. The resulting single-sided amplitude spectrum is given in Fig. 9.23. As shown in the figure, there exist three main lifting surface structural dynamic modes which contribute to the $M_y^{W/B}$ response. The frequencies of the first three peaks are approximately 25.4 Hz, 35.2 Hz, and 52.7 Hz. In order to identify which lifting surface modes correspond to these three peaks, the first four lifting surface free vibration mode shapes and frequencies are computed at the

corresponding thermal state. This thermal state is obtained by heating the structure for 400 s at the following flight conditions: $M_\infty = 6.5$, $\alpha = 0.1°$, $\delta = 0°$, and $h = 35$ km. The resulting mode shapes and their frequencies are given in Fig. 9.24. Based on the frequencies given in Fig. 9.24, the first, second, and third peaks in Fig. 9.23, roughly correspond with lifting surface mode one, mode two, and mode three or four, respectively. The dominant peak in Fig. 9.23 is the second peak, which corresponds roughly with lifting surface mode two. Examining the mode shape of lifting surface mode two, it is clear that this mode has a significant torsion component about the attachment location, and one would therefore expect that this mode would contribute most significantly to the $M_y^{W/B}$ dynamic response. Thus, if one were designing a control system aimed at stabilizing the HSV pitching moment, the second lifting surface mode would be the most critical mode to control.

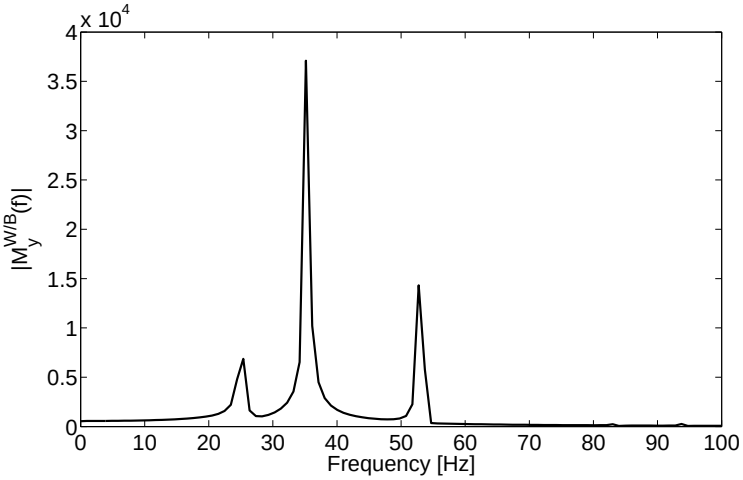

Figure 9.23: Frequency-domain response of $M_y^{W/B}$ for dynamic lifting surface case.

In addition to assessing overall vehicle response, another important consideration in the design and analysis of hypersonic vehicles is heating levels. While lifting surface inertial effects lead to oscillations in the forces and moments exerted by the lifting surface on the fuselage, such oscillations are not expected in the temperature-histories of the lifting surface due to the disparity between the aeroelastic and aerothermal time scales. Structural

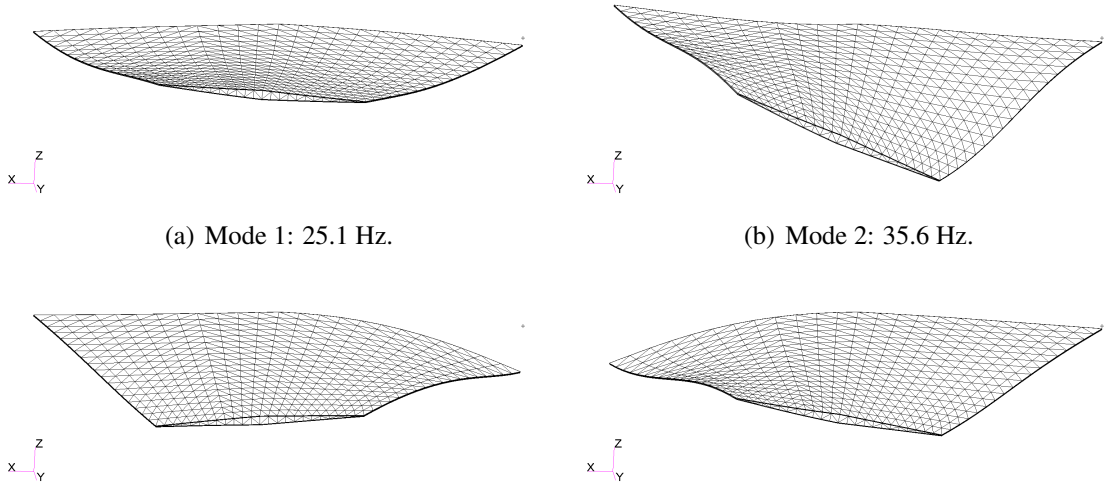

(a) Mode 1: 25.1 Hz.

(b) Mode 2: 35.6 Hz.

(c) Mode 3: 53.2 Hz.

(d) Mode 4: 54.3 Hz.

Figure 9.24: First four free vibration modes evaluated at thermal state obtained by heating structure for 400 s at $M_\infty = 6.5$, $\alpha = 0.1°$, $\delta = 0°$, and $h = 35$ km.

dynamic oscillations of the lifting surface lead to oscillations in the aeroheating boundary conditions at the outer surface. However, because the heat transfer process occurs on a slower time scale relative to the aeroelastic response, it is not expected that the time-histories of the nodal temperatures of the lifting surface will respond to such oscillations in the thermal boundary conditions. To verify these expectations, the minimum and maximum nodal temperatures over time are plotted in Fig. 9.25(a) and Fig. 9.25(b), respectively. Each figure gives the temperature time-history for both the dynamic and static lifting surface case in order to highlight the effect of lifting surface inertia on the temperature response. As expected, due to the disparate time scales of the aerothermal and aeroelastic processes, there exists no noticeable difference in the temperature response between the dynamic and static lifting surface cases for either the minimum and maximum temperatures. Thus, if one were solely interested in the evolution of temperature throughout the structure, these results indicate that a quasi-static solution would be sufficient to capture the thermal response. Note that the initial slope of Fig. 9.25(a) is positive, while that of Fig. 9.25(b) is close to zero. This indicates that the maximum nodal temperature has approximately reached its steady state value at the end of the initial 400 s heating process, while the minimum temperatures

are still increasing at this point. As expected, the increase in lifting surface deflection angle leads to an increase in dynamic pressure and therefore an increase in both the minimum and maximum nodal temperatures. However, the increase in temperature due to increased deflection angle is small for the short time-history given in Fig. 9.25(a) and Fig. 9.25(b).

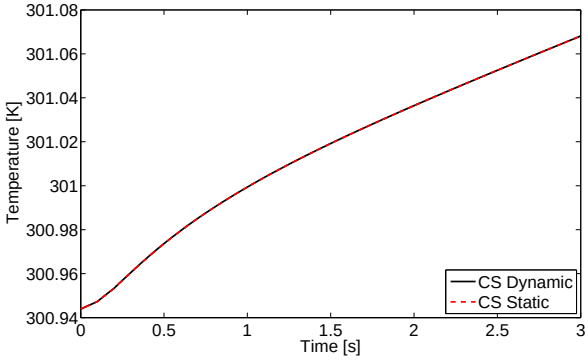

(a) Minimum nodal temperatures.

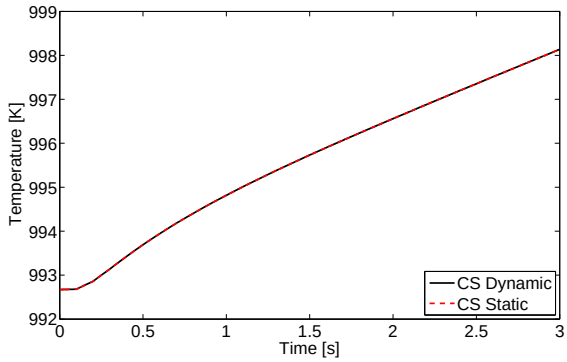

(b) Maximum nodal temperatures.

Figure 9.25: Minimum and maximum nodal temperatures over time for both static and dynamic lifting surface cases.

9.6.3.2 Commanded Step Increase and Decrease in Lifting Surface Deflection Angle

The next case analyzed consists of a commanded step increase in δ of 3.9° issued at 0.01 s into the transient and a subsequent command to return δ to 0° issued at 0.4 s into the transient. The input command, δ_{cmd}, for this case is given by

$$\delta_{\text{cmd}}(t) = 20H(t-0.01)\left[3.9^\circ \frac{\pi}{180^\circ}\right] + 20H(t-0.4)\left[-3.9^\circ \frac{\pi}{180^\circ}\right]. \tag{9.42}$$

A plot showing $\delta(t)$ based on the input command of Eq. (9.42) is given in Fig. 9.26, where δ has been converted from radians to degrees for visualization purposes. As in the previous case, the flight conditions for this case are $M_\infty = 6.5$, $h = 35$ km, and $\alpha = 0.1°$. The time step sizes are: $\Delta t_{AE} = \Delta t_{HT} = 0.001$ s and $\Delta t_{AT} = 0.1$ s. Again, the lifting surface is first heated at these flight conditions for 400 s at the initial lifting surface deflection angle, $\delta = 0°$. The lifting surface is then brought to aerothermoelastic equilibrium prior to beginning time-marching.

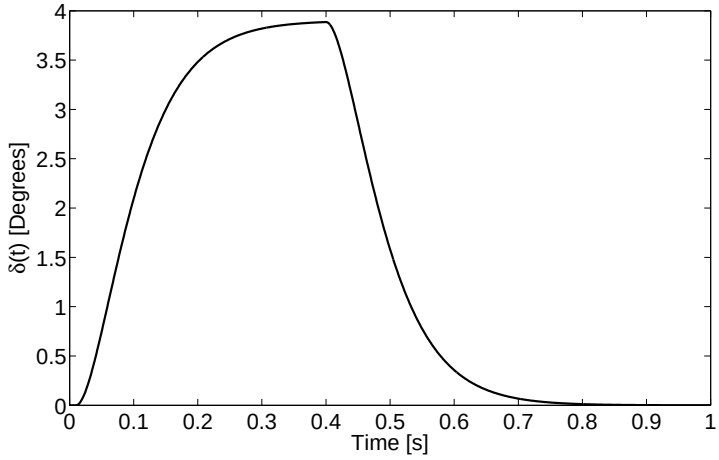

Figure 9.26: Time-history of applied lifting surface deflection angle, $\delta(t)$.

The entries of x_u corresponding to the z direction displacements of node 37 (located on the bottom surface, tip, leading edge) and node 475 (located on the bottom surface, tip, trailing edge) are given in Fig. 9.27(a) and Fig. 9.27(a), respectively, for both the dynamic and static lifting surface cases. Recall that x_u contains both the constraint motion due to enforced rotation of the lifting surface about the hinge line and well as elastic deformation relative to the constraint motion. To remove the displacement components due to constraint motion, the elastic displacements, x_u^E, of nodes 37 and 475 are plotted in Fig. 9.28(a) and Fig. 9.28(b), respectively, for both the dynamic and static lifting surface cases. For the "CS Static" case in both figures, a slight increase in elastic displacement up to 0.4 s is observed as δ is increased and the aerodynamic pressure and thermal loads increase. As δ begins to

return back to 0° starting at 0.4 s, the aerodynamic pressure loads decrease and the elastic displacements therefore decrease slightly beginning at 0.4 s. The "CS Dynamic" results in both figures illustrate the effect of lifting surface structural dynamics which result in significant oscillations in the elastic displacements about the static values. For the time range considered, inclusion of lifting surface inertia results in elastic displacements of up to 1.9 times and 2.5 times the corresponding static elastic displacements for node 37 and 475 respectively.

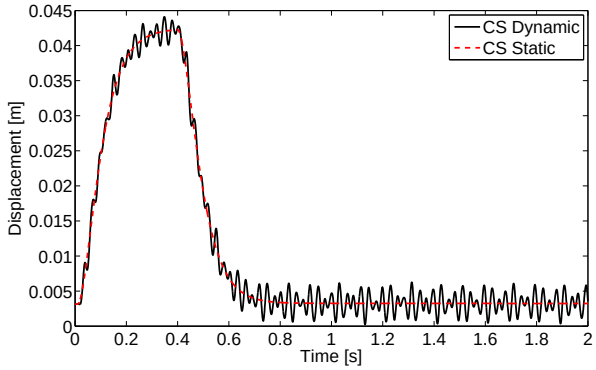

(a) Node 37 (bottom surface, tip, leading edge).

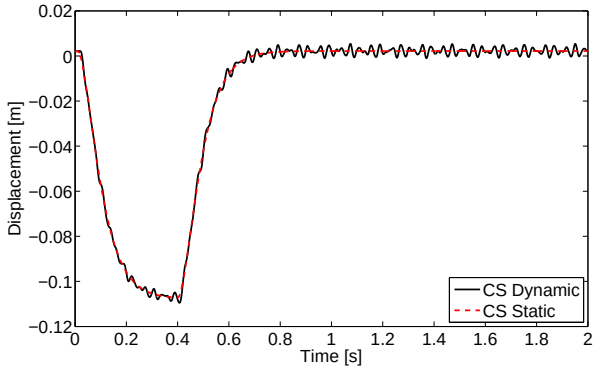

(b) Node 475 (bottom surface, tip, trailing edge).

Figure 9.27: Lifting surface total displacements, x_u, in z direction under commanded change in deflection angle with and without lifting surface inertial effects for two selected nodes.

Plots of the pitching moment exerted by the lifting surface on the fuselage, $M_y^{W/B}$, are given in Fig. 9.29(a) and Fig. 9.29(b) for the static and dynamic lifting surface case, respectively. Examining Fig. 9.29(a), the static pitching moments results follow approx-

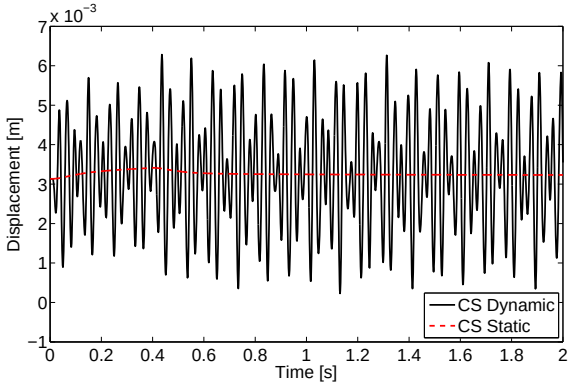

(a) Node 37 (bottom surface, tip, leading edge).

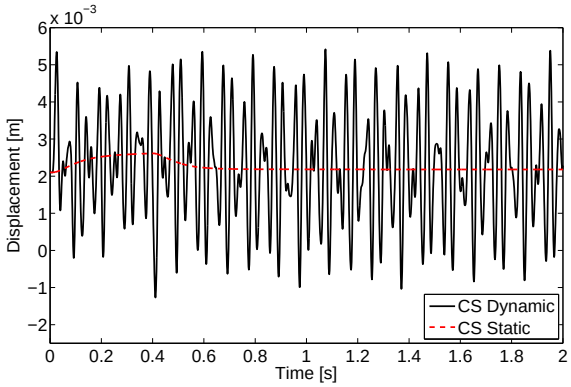

(b) Node 475 (bottom surface, tip, trailing edge).

Figure 9.28: lifting surface elastic displacements, x_u^E, in z direction under commanded change in deflection angle with and without lifting surface inertial effects.

imately the same trend as that of the time-history of δ given in Fig. 9.26. However, the static value of $M_y^{W/B}$ initially decreases when δ first begins to increase at initial time and initially increases when δ first begins to return back to 0° at 0.4 s. As discussed before, this effect is due to the unsteady aerodynamic loads induced by the instantaneous velocity of the lifting surface at these time instants. Additionally, slight discontinuities are observed in Fig. 9.29(a) in intervals of 0.1 s again due to the updating of the skin friction coefficients which is performed each time the thermal boundary conditions are updated. Examining Fig. 9.29(b), significant oscillations in $M_y^{W/B}$ are found to occur when lifting surface inertia is included. For the time range considered, the maximum absolute ratio of $M_y^{W/B}$ from the dynamic lifting surface case to that from the static lifting surface case is 528, again indicating the significant role of lifting surface inertia with regard to the pitching moment it generates on the fuselage.

The minimum and maximum temperatures over time for this case are given in Fig. 9.30(a) and Fig. 9.30(b), respectively, for both the dynamic and static lifting surface cases. As in the previous section, there is not a noticeable difference in the temperature response when comparing the "CS Dynamic" case with the "CS Static" case, indicating that inertial effects do not impact the thermal response. The minimum temperature is monotonically increasing throughout the complete time-history shown in the plot. However, the rate of increase in the minimum temperature is not uniform throughout the transient due to the effect of the change in δ. As δ begins to increase from 0° to 3.9°, the minimum temperature begins to increase at a faster rate. Because the thermal boundary conditions are updated in intervals of 0.1 s, though δ begins decreasing back to 0° at 0.4 s, the effect of the decreasing deflection angle on the minimum temperature is not observed until 0.5 s. Thus, at approximately 0.5 s, the minimum temperature begins increasing at a slower rate due to the decreased deflection angle. The maximum temperature remains nearly constant initially until the thermal boundary conditions are first updated at 0.1 s, at which point it begins to increase due to the increase in δ. At 0.5 s, the rate of increase in the maximum temperature drops due

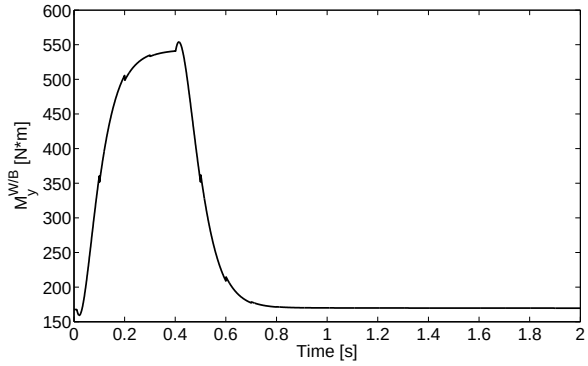

(a) Static lifting surface case.

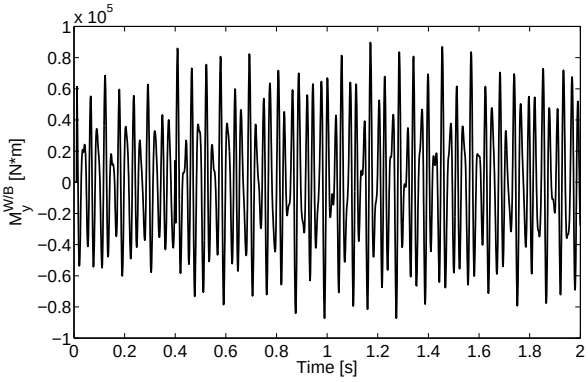

(b) Dynamic lifting surface case.

Figure 9.29: Time-domain response of $M_y^{W/B}$ for both static and dynamic lifting surface cases.

to the fact that δ is decreasing at this point. At 0.6 s, δ has nearly returned to 0° and the maximum temperature begins decreasing slightly at this instant. Beyond approximately 1.2 s, the maximum temperature begins increasing slightly likely due to the conduction of heat from lower temperature regions to higher temperature regions.

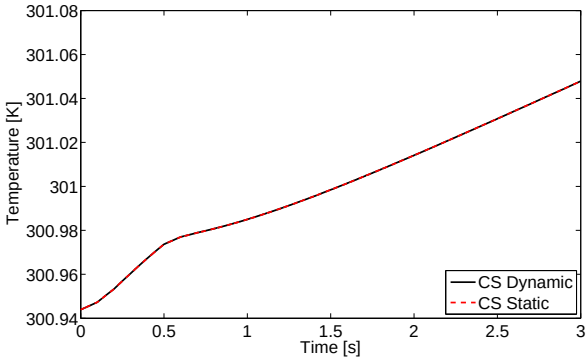

(a) Minimum nodal temperatures.

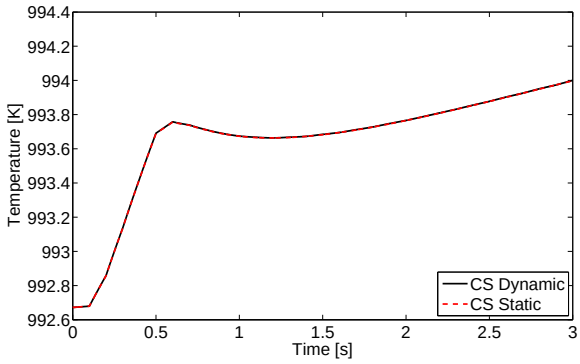

(b) Maximum nodal temperatures.

Figure 9.30: Minimum and maximum nodal temperatures over time for both static and dynamic lifting surface cases.

9.7 Concluding Remarks

This chapter investigates the impact of inertial loads due to lifting surface structural dynamics on overall vehicle response. Due to the dissimilar nature of the fuselage and lifting surface models used in the full-vehicle simulations, a direct monolithic coupling of these models is difficult. Thus, a partitioned solution methodology is introduced in

which the fuselage and lifting surface are each modeled independently and information is exchanged between the two within each aeroelastic time step to bring the systems into equilibrium. This approach is advantageous in that each component can be formulated independently with respect to the other, and thus coupling of the models is reduced to input/output exchanges of information. The partitioned solution approach described in this work makes use of an iterative routine based on the secant method is outlined for efficiently bringing the two systems to equilibrium within each aeroelastic time step. Comparison of the partitioned approach with a monolithic approach demonstrates that the partitioned approach is mathematically equivalent to the monolithic system.

Using the partitioned solution scheme, the effect of lifting surface inertial loads on overall vehicle response was examined for a configuration in which the fuselage was represented as a single-DOF oscillator having a translational displacement degree of freedom in the z direction. Comparison between a simulation which included lifting surface structural dynamics and a simulation which only used a static lifting surface solution showed that exclusion of lifting surface inertia results in an 11% overprediction in the frequency of the dominant fuselage oscillation component. It was also observed that the extent to which lifting surface inertia impacts the amplitude of fuselage oscillation is strongly dependent on the inertia of the fuselage itself. Examining the frequency content of the lifting surface response at one particular node, it was found that while lifting surface modes 1 – 5 were all excited at least to a small extent, the most dominant modes in the lifting surface response were the fuselage mode and the first lifting surface mode. Additionally, the loads exerted by the lifting surface on the fuselage at the attachment point were investigated. Based on the results presented, exclusion of lifting surface inertia was found to result in an error in attachment point loads by up to a factor of 8. However, the extent to which these attachment point loads impact fuselage response was found to be highly dependent on fuselage inertia. The frequency content of the attachment point loads showed that a 54.7 Hz mode had the greatest contribution to the loads. However, this mode did not significantly contribute

to the fuselage response, indicating that the impact of attachment point loads on fuselage response is also depend on their frequency content.

In order to assess the impact of lifting surface inertial effects resulting from lifting surface rotation, a control input corresponding to lifting surface deflection angle was incorporated into the framework. An actuator model was used to convert the commanded change in deflection angle to the deflection angle applied by the actuator. Simulations were carried out for two different time-histories of the commanded lifting surface deflection angle. The first case consisted of a commanded step increase in lifting surface deflection angle. The second case consisted of a commanded step increase followed by a subsequent step decrease in lifting surface deflection angle. Both the total and elastic lifting surface displacements were examined for the cases of a static lifting surface solution and a dynamic one. Lifting surface inertia was found to result in an increase in the elastic displacements at one particular location by a factor of 1.9 for the first case and a factor of 2.5 for the second case with respect to the corresponding static solution. The resulting pitching moments exerted by the lifting surface on the fuselage about the attachment point were also examined. Results indicated that inclusion of lifting surface inertia results in departure of the instantaneous pitching moment from the lifting surface by up to a factor of 130 for the first case and 530 for the second case when compared against the static lifting surface solution. Analysis of the frequency content of the moment results indicated that the second lifting surface mode contributes most significantly to the oscillations of the moment about the static value. Thus, this mode is the most critical mode to control with respect to HSV pitching moment stabilization. Finally, assessment of the minimum and maximum temperatures over time for both cases demonstrated that the thermal response of the lifting surface is insensitive to structural dynamic oscillations due to the disparity between the aeroelastic and aerothermal time scales.

Chapter X

Concluding Remarks

This chapter concludes the main body of the dissertation. It begins with a summary of the challenges associated with hypersonic flight as well as an outline of the material covered in the various chapters of the dissertation. A list of key novel contributions represented by this dissertation is then presented. Next, the principal conclusions obtained from the studies conducted are given. Finally, recommendations are outlined with regard to future research directions associated with the reduced-order aerothermoelastic modeling of hypersonic vehicle structures.

10.1 Summary

Complex coupling between multiple disciplines is exhibited in hypersonic vehicle flight. Boundary layer friction and stagnation effects lead to aerodynamic heating at the outer surface of the vehicle, resulting in heat being conducted through its internal structure. The spatial variation of temperatures leads to a change in the stiffness distribution of the structure which must be captured in order to accurately predict the vehicle dynamic response. In order to assess the impact of these effects on hypersonic vehicle flight dynamics and controllability, each of these disciplines and their coupling must be included in the analysis. However, inclusion of these effects in a full-order sense is infeasible due to the large number of states and long computational time associated with high-fidelity models. As such,

reduced-order representations of the essential physics are required.

The main goal of this dissertation is to develop an efficient methodology for incorporating fully coupled aerothermoelastic effects into full-vehicle 6-DOF HSV simulations. A schematic of the 6-DOF simulation framework, and was described in Chapter I, was shown in Fig. 1.4. The reduced-order modeling efforts of this dissertation focused primarily on the thermal and elastic components of the solution. In order to assemble a comprehensive aerothermoelastic framework, aerodynamic heating and unsteady aerodynamic effects were also included. The research into reduced-order aerothermoelastic modeling presented in this dissertation facilitates inclusion of such effects in HSV time-domain simulations.

This dissertation focused on the reduced-order aerothermoelastic modeling of hypersonic vehicle structures for the purposes of efficient control simulation and vehicle design. One major aspect of this research was associated with reduced-order modeling methodologies for obtaining low-order governing systems of equations given a high-fidelity reference model. As such, independent reduced-order modeling techniques were developed for the transient thermal and structural dynamic modeling aspects associated with hypersonic vehicle structures. Another major aspect of this research involved coupling the reduced-order models in a unified aerothermoelastic framework for use in assessing the impact of aerothermoelastic effects on hypersonic vehicle flight dynamics and controllability. The current chapter presents a summary of the main contributions of the research, the principal conclusions obtained, and recommendations for future research.

The dissertation began with a literature survey that outlined previous research in relevant areas. An overview of aerothermoelasticity was given in order to provide a context for the different disciplines addressed by this dissertation. Coupling mechanisms between the aerothermal, heat transfer, and structural dynamics components of the problem were summarized, and the strength of each of the various coupling mechanisms was discussed. A variety of research efforts were described which made approximations by neglecting certain couplings in order to improve the tractability of the problem. Following the survey of

aerothermoelasticity literature, a summary of research involving hypersonic aerodynamics and aerodynamic heating was provided. Though these components of the solution are not the primary focus of this dissertation, they must be included in the aerothermoelastic framework in order to model the full problem. As this work is motivated by the desire to improve the computational efficiency of aerothermoelastic simulation for the purposes of controllability analysis and vehicle design, the relevant literature associated with hypersonic vehicle flight dynamics was surveyed. This included a discussion of studies aimed at assessing the effect of hypersonic aerodynamics and aerodynamic heating on the flight dynamics. Finally, a review of reduced-order modeling research was presented in order to provide a context for the reduced-order model development presented in this dissertation.

Chapter II discussed the reduced-order modeling methodology employed for the transient thermal solution. The approach utilized in this dissertation is based on the proper orthogonal decomposition which provides an optimal modal representation of the response based on an *a priori* sampling of the full-order system. The description of the approach included both a derivation of the equations used to obtain the POD basis as well as the formulation used to solve for the time-dependent POD modal coordinates. Chapter III addressed the accuracy of the methodology under both time-independent and time-dependent thermal boundary conditions. As the goal of the POD approach is to treat the POD modes as Ritz vectors and keep the basis fixed throughout the simulation, the robustness of the basis to temporal variation in the boundary conditions must be addressed. Thus, the results presented in Chapter III were aimed at addressing the error associated with a fixed POD basis under time-varying heat flux boundary conditions.

In a manner similar to that of the transient thermal reduced-order modeling approach, the structural dynamic ROM formulation also utilizes a fixed-basis modal representation. An overview of the reduced-order structural dynamic modeling methodology was presented in Chapter IV. As in the case of the transient thermal ROM, the structural ROM expresses the response of the system as a linear combination of a set of basis vectors that are se-

lected *a priori*. However, POD is not used to obtain the basis vectors in the case of the structural dynamic ROM. Instead, the modal matrix is assembled using two different techniques. The first technique is described in Chapter IV and uses an eigenvalue solution at a reference thermal state in order to generate a subset of free vibration modes. One limitation of the vibration modes is that they do not adequately capture the quasi-static response of the structure due to thermal loads. Thus, the second technique, described in Chapter V involves the use of the load-dependent Ritz vector methodology to generate additional modes to be used in capturing the quasi-static response of the structure. The reference free vibration modes and load-dependent Ritz vectors are combined into a single modal matrix onto which the full-order equations of motion are projected in order to reduce the order of the system. Studies are presented in Chapter IV and Chapter V to assess the robustness of the basis under transient heating and to address the error incurred as a result of the various approximations that are made.

As discussed previously, while aerodynamics and aerodynamic heating are not the primary focus of this research, they are addressed in this dissertation as they are required in order to perform fully coupled aerothermoelastic simulations. The aerodynamic flow parameters are necessary to give the aerodynamic pressure loads over the structure, as well as to provide local flow conditions for the purposes of the aerodynamic heating computation. The aerodynamic heating component is necessary as it provides the heat flux boundary conditions (in combination with the thermal radiation) to be used in the transient thermal solution. As such, Appendix A discusses the aerodynamic and aerodynamic heating formulations employed in the aerothermoelastic framework of this dissertation. For the aerodynamics, both steady and unsteady formulations of the flow were examined. The steady formulation is based on the oblique shock and Prandtl-Meyer expansion fan relations which are used in combination with local flow turning angles over the deformed configuration. The unsteady aerodynamics are computed from a third-order piston theory representation based on nodal displacements and velocities of the structure. For the aerodynamic heating,

both a first-principles Eckert reference temperature formulation and a CFD-based reduced-order model were utilized in the aerothermoelastic framework. Note that the aerodynamic heating ROM was developed by Crowell and McNamara [52, 53, 26, 110, 51] and was incorporated into the aerothermoelastic framework of this dissertation in a joint effort [110].

With the individual components of the reduced-order aerothermoelastic framework addressed, Chapters VI – IX discussed the incorporation of these components into a unified framework. The unified framework was then used to perform studies to assess the impact of aerothermoelastic effects on HSV dynamics and controllability. Chapter VI provided an overview of the aerothermoelastic framework, a description of the ROM generation process, and a summary of the time-step scheduling for the various aspects of the solution. A quasi-steady version of the framework was employed in Chapter VII to assess the impact of control surface deformation under thermal loads on aerodynamic force generation. The fully unsteady aerothermoelastic framework was addressed in Chapter VIII and the error of each ROM was quantified in the context of full aerothermoelastic simulations. The framework was then used to assess the effect of aerothermoelasticity on control surface aerodynamics as well as necessary control input. Finally, Chapter IX discussed a partitioned solution framework for coupling the various substructures of the vehicle in order to perform full-vehicle, 6-DOF simulations. To illustrate the methodology, the coupling of the aerothermoelastic control surface ROM with a fuselage representation was taken as a case study. The partitioned solution framework was then used to assess the impact of control surface inertial effects on overall vehicle dynamics.

10.2 Key Novel Contributions

The developments presented in this dissertation represent novel contributions to the field in a variety of areas. A summary of those contributions is presented below:

1. An aerothermoelastic framework consisting of multiple, coupled, dissimilar reduced-

order models was created for hypersonic vehicle analysis and simulation.

2. A transient thermal reduced-order modeling methodology based on the proper orthogonal decomposition was developed for use within an aerothermoelastic framework under time-variation in boundary conditions and varying flight conditions.

3. A new parallelized procedure was developed for taking thermal snapshots in order to enrich the energy captured by the snapshots and to aid in thermal ROM robustness.

4. A fixed-basis Ritz vector methodology for reduced-order structural dynamic modeling under transient thermal effects was introduced and shown to accurately represent the structural dynamic response of hot structures.

5. A basis augmentation procedure was devised for capturing quasi-static structural response due to slowly changing thermal loads using a fixed structural basis within an aerothermoelastic framework.

6. A kriging-based technique was introduced for direct updating of the generalized stiffness matrix and physical thermal load vector as a function of the POD modal coordinates.

7. A novel approach was created for establishing *a priori* bounds on the POD modal coordinates for the purposes of kriging ROM generation.

8. A partitioned solution methodology was developed for coupling the various substructures of a hypersonic vehicle within a full-vehicle, 6-DOF simulation.

9. The partitioned solution enabled the quantitative assessment of the impact of:

   (a) fuselage-lifting surface inertial coupling on overall vehicle dynamics, and

   (b) control system commands on hinge forces and moments within a fully coupled aerothermoelastic environment.

10.3 Principal Conclusions

Using the capabilities described above, a number of fundamental conclusions have been derived from this research. A summary of those conclusions is presented below:

1. Assessment of the reduced-order transient thermal modeling methodology demonstrated its robustness for specific cases of prescribed time-varying thermal boundary conditions. Results from one case showed errors below 5% using only 5 POD modes. The thermal POD basis was also shown to be robust for the cases considered where the flight conditions used to generate the ROM were not the same as those in which the ROM is employed. One sample case showed that the error of a 6-mode POD thermal ROM remained below 15% when the POD modes were extracted from a case with time-independent boundary conditions and used for simulations of a case with time-dependent boundary conditions. Assessment of the error of the thermal ROM within two fully coupled aerothermoelastic simulations showed a time-averaged NRMSE of 2.2% and 4.5%, respectively, based on 12 POD basis vectors. Finally, comparison of the computational cost of the thermal ROM against that of the full-order thermal model showed that the ROM solution improved the computational cost by a factor of 86 – 372 and reduced the number of states by a factor of 469 while maintaining an average error of 8.2%. Thus, the thermal ROM was shown to provide an accurate representation of the full-order model while significantly reducing the computational cost and number of states for the cases considered. In order to further improve the accuracy of the thermal ROM, a framework was developed in which a sets of thermal snapshots were taken from a series of parallel aerothermoelastic simulations in order to further improve the robustness of the POD basis across a range of flight conditions. Assessment of the accuracy of a resulting 32-mode thermal ROM showed that the NRMSE and L_∞ error remained below 0.4% and 3%, respectively, over a 1,200 s time-history.

2. Quantification of the evolution of free vibration modes under transient heating using the modal assurance criterion (MAC) provided support for the use of a fixed basis structural ROM. The first six free vibration modes of a hypersonic vehicle control surface example case were tracked under transient heating based on an aerothermal solution at representative flight conditions. The modal assurance criterion was used to quantify the correspondence between the room temperature modes and the heated modes at each thermal time step. For modes one, two, five, and six, the minimum diagonal MAC value over the complete time-history was found to be 0.91, indicating that these modes do not deviate significantly from the corresponding unheated modes. A mode-switching phenomenon was found to occur between modes three and four. However, the space spanned by the heated modes at each time step was approximately the same as that of the unheated modes at each time step for this example case. This result therefore provided support for the use of a fixed-basis structural ROM. Investigation of the evolution of the first six natural frequencies for this case showed a maximum departure from the room temperature natural frequencies of 25% which occurred for mode 5.

3. The use of a fixed-basis structural ROM was found to provide relatively low error with regard to structural dynamic response for the cases simulated in this dissertation. Assessment of a structural ROM consisting of six free vibration modes and one static mode was shown to give a time-averaged NRMSE of 8.5% for one fully coupled aerothermoelastic case. Comparison of structural ROM results which only included free vibration modes against those which included an additional static mode provided evidence that basis augmentation could improve the structural dynamic ROM by better capturing quasi-static motion due to thermal loads. This realization led to the development of a load-dependent Ritz vector methodology for enriching the basis representation of the structural dynamics. Assessment of the methodology demonstrated that inclusion of load-dependent Ritz vectors led to an average improvement

in the L_∞ error of the structural dynamic ROM of 38% for one case with ten load-dependent Ritz vectors and six free vibration modes as compared with a case that only employed the six free vibration modes.

4. Development of a kriging-based methodology for directly updating the structural stiffness and thermal loads showed that the approach allowed for accurate generation of these quantities while reducing the computational cost of the structural ROM. The stiffness matrix was found to have a lower-order dependence on temperature than the thermal load vector for the specific model used. As a result, a second-order regression was used for the stiffness matrix ROM, while a third-order regression was required for the thermal load vector ROM. It was also found that greater accuracy can be obtained if kriging is used to generate the physical thermal load vector instead of the generalized thermal load vector. However, the kriging approach was applied to the generalized stiffness due to the large number of entries associated with the physical stiffness matrix. A kriging model of the generalized stiffness matrix using 20 design variables, 500 training points, and a second-order regression model was found to have an average NRMSE of 0.05% and a maximum L_∞ error of 1.3%. A kriging representation of the physical thermal load vector using 20 design variables, 5,000 training points, and a third-order regression model was found to have an average NRMSE of 0.1% and a maximum L_∞ error of 4.7%. The kriging model of the physical thermal load vector required 71 hours of computational time as compared with 0.05 hours in the case of the kriging ROM of the generalized stiffness matrix. However, note that because the physical thermal load vector ROM is not dependent on the structural modal matrix, it does not need to be recomputed if the structural modes are updated. Finally, the use of these kriging representations was shown to improve the computational cost of the structural dynamic ROM by a factor of five.

5. The methodology for obtaining bounds on the POD modal coordinate bounds was

shown to be robust with a minimum margin of safety of 11.2% on the upper bounds and 3.5% on the lower bounds. These measures of robustness were computed based on the bounds obtained from an independently generated set of ten additional aerothermoelastic simulations.

6. A full-order, quasi-steady framework was used to assess the impact of deformation due to thermal loads on the total aerodynamic forces generated by a hypersonic vehicle control surface. A positive control surface angle of attack led to higher heating levels on the bottom surface than on the top, resulting in a concave-up curvature of the structure. Transient thermal results showed that the temperature at the leading edge of the root on the bottom surface exceeded 1,400 K, while the temperature at the leading edge of the root on the top surface only reached 923 K. As a result of deformation due to thermal loads, the maximum relative change in lift was 1.3% and the maximum relative change in drag was 8.1% as compared with the case of an undeformed control surface.

7. A fully coupled aerothermoelastic framework was used to assess the difference between the total lift and drag produced by an elastic control surface under aerothermoelastic effects versus those forces produced by a rigid control surface. Results from two cruise trajectories showed maximum absolute relative changes in the total lift and drag for the elastic structure of 8% and 15%, respectively, compared with a rigid structure. For two ascent trajectories, results showed maximum absolute relative changes in total lift and drag of 3% and 21%, respectively. The iterative routine was used to assess the change in control surface angle of attack necessary to match the lift of the elastic control surface under aerothermoelastic effects to that of the rigid control surface. For the two cruise trajectories considered, the maximum deprature from the rigid angle of attack was found to be 7.6%. However, this value is likely to be highly dependent on flight conditions and initial thermal conditions.

8. A partitioned solution methodology for HSV substructure coupling was shown to capture the structural response results from a monolithic solution nearly identically, validating the mathematical formulation of the partitioned procedure. Examination of the fuselage response for this representative configuration showed that exclusion of lifting surface inertia results in an 11% overprediction in the lowest-frequency fuselage oscillation component. Assessment of the time-domain response of the fuselage showed that control surface inertia can significantly impact the amplitude of the fuselage motion. The frequency content of the lifting surface response for the cases examined showed that lifting surface modes 1 – 5 were all excited at least to a small extent. Analysis of the loads exerted by the lifting surface on the fuselage representation showed that lifting surface inertial effects result in amplification of the interface loads from the lifting surface by a factor of eight. However, it remains to be seen what effect the oscillations in interface loads will have on the overall vehicle flight dynamics in full-vehicle simulations.

9. Incorporation of a control input corresponding to a change in lifting surface deflection angle allowed for quantification of lifting surface inertial effects on vehicle moments. For the cases considered, lifting surface inertia was found to result in an amplification of elastic displacements by a factor of 2.5 at one particular location with respect to a quasi-static structural solution. The resulting pitching moments exerted by the lifting surface on the fuselage through the attachment point were also examined. For the two cases considered, lifting surface inertia was found to result in a variation of the hinge moment by up to a factor of 530 with respect to a quasi-static structural solution for the lifting surface. Therefore, lifting surface inertial effects are likely to have a significant impact on the vehicle pitch response and the dynamics of the structure must be included in the 6-DOF framework. Analysis of the frequency content of the moment results suggest that a 36 Hz lifting surface mode contributes most significantly to oscillations in the hinge moments. Examining

the corresponding mode shape, it is found to exhibit a noticeable torsion component about the attachment point, thus verifying that this mode is indeed critical with respect to pitching moment stabilization.

10.4 Recommendations for Future Research

While this dissertation represents significant advancements to the state of the art in the areas described in Section 10.2, there remains potential for further research in the area of aerothermoelastic modeling of hypersonic vehicle structures. A possible direction for future research of hypersonic vehicles involves multidisciplinary design optimization (MDO). While the aerothermoelastic ROM framework developed here was used to design the control surface structures employed in the studies, the design process used was largely based on trial and error. Thus, a systematic approach for designing and optimizing hypersonic vehicle structures is warranted. The aerothermoelastic ROM methodology developed in this dissertation would provide a basis for the analysis procedure. However, work must be done to pose the problem in an optimization-oriented sense. Specifically, design variables, constraints, and objectives must be identified which correspond to the essential physics of the problem. The problem of MDO of hypersonic vehicles is likely to be more complex than that of traditional lower-speed vehicles due to the number of disciplines and the level of coupling involved. For example, in addition to structural constraints such as stress allowables, thermal constraints must also be imposed so as to ensure that the temperatures of the vehicle due not exceed the material limits. Associated with the thermal constraints is the fact that control surface deflection angles must be bounded to ensure safe heating levels. Aeroelastic constraints are important to consider carefully as heating alters the stiffness of the vehicle, and can in itself induce an aeroelastic stability. Thermal buckling has also been found to be a significant consideration based on the work of this dissertation, and inclusion of this effect in an optimization framework is required. While the aerothermoelastic solution approach presented here is of a reduced-order form, additional

work may be required to identify areas for further reduction in computational cost for use in an optimization framework. For example, it was found in Chapter IX that the thermal solution is insensitive to structural dynamic oscillations. Therefore, if one were optimizing for thermal performance, a quasi-static structural solution would likely be sufficient for capturing the physics of interest.

The partitioned solution methodology developed in Chapter IX provided a straightforward formulation for coupling multiple vehicle substructures for the purposes of full-vehicle simulation. This methodology was exemplified via the case study of coupling a lifting surface and fuselage representation. However, further research is warranted in order to bring together an actual HSV fuselage, both control surfaces, and a scramjet propulsion system. The resulting framework would allow for use of the aerothermoelastic ROM of the control surface within a 6-DOF vehicle simulation framework. While previous efforts have addressed the flight dynamic stability of flexible hypersonic vehicles [115], they did not include the aerothermoelastic effects of the control surfaces. Therefore, extension of the framework of Ref. 115 to include the control surface aerothermoelastic ROM methodology of this dissertation would allow for the incorporation of important physics of the problem. In addition to vehicle stability analysis, development of a time-domain 6-DOF HSV flight dynamics framework is also recommended.

Another area for potential future research is associated with the inclusion of a vehicle control system. The research presented in this dissertation provided a step toward incorporation of control system effects into the aerothermoelastic framework by implementing a control input corresponding to control surface deflection angle. However, in this dissertation results were obtained by prescribing the time-history of the commanded control surface deflection angle. Thus potential for future work exists in terms of replacing the prescribed deflection angle command with an actual control law. Incorporation of a realistic control system would require formulation of the governing equations into a form that is amenable to control design. However, once a control system is developed, the framework is

in place to convert the deflection angle command into an enforced motion in the structural equations of motion. Addition of a control system to the pre-existing aerothermoelastic framework will allow for consideration of aerothermoservoelastic effects on the vehicle. Specifically, this would permit investigation into the interactions between the controller and control surface structural dynamics as well as the associated aeroelastic stability.

With regard to the overall aerothermoelastic framework, an important aspect that requires investigation is associated with adaptation in the various time steps sizes of the transient thermal, structural dynamic, and aerothermal solutions. Refinement of the time step sizes can significantly increase the computational cost of the aerothermoelastic solution. Therefore, research into adaptive time-step selection is critical in retaining sufficient accuracy while limiting computational expense. As the various physics of the problem each have different associated time scales, this factor must be taken into consideration when selecting time step sizes. Furthermore, due to the tightly coupled nature of the problem, another aspect that must be considered is the frequency at which information is exchanged between the various disciplines. This research has shown that when thermal gradients dominate the structural load vector, the structural response is close to quasi-static and larger time step sizes of the structural dynamic solution are permitted. However, certain loading conditions, such as a change in control surface deflection angle, can excite a more highly dynamic response which requires a smaller time step sizes. Thus, an adaptive time-stepping approach must consider the rate of change of the state vector of interest.

Additional areas for potential future research are associated with the transient thermal component of the solution. One specific area that warrants attention is nonlinear reduced-order transient thermal modeling. The configurations analyzed in this dissertation assumed that the material properties associated with the heat transfer process were temperature-independent. This assumption resulted in a linear system of transient thermal equations. However, thermal response predictions presented here demonstrate the temperatures can approach 1,500 K depending on the flight conditions of the vehicle. Thus, inclusion of

temperature-dependent material properties associated with the heat transfer process may be warranted.

If temperature-dependent material properties were to be included in the transient thermal model, the system would become nonlinear as the thermal capacitance and/or thermal conductivity matrix would become a function of the temperature. While there exist iterative techniques for solving nonlinear systems of ordinary differential equations in the full-order sense, such as the Newton-Raphson method, the impact of the nonlinearity on the reduced-order representation of the transient thermal system must be assessed. Specifically, the robustness of a fixed thermal POD basis under nonlinearities in addition to variation in flight conditions and thermal boundary conditions must be addressed. Furthermore, one advantage of using POD in the linear case is that the reduced-order system matrices can be obtained *a priori* and then used throughout the reduced-order simulation. However, in the nonlinear case, these matrices must be updated at each iteration in order to account for their dependence on temperature. Thus, in order to preserve the efficiency of the approach, computationally tractable methods for updating the generalized thermal capacitance and conductivity matrices as a function of temperature must be investigated. One potential means for achieving this might be based on the kriging methodology that was used in this dissertation to directly updated the generalized stiffness matrix and physical thermal load vector as a function of the thermal POD modal coordinates.

Also with regard to the thermal component of the framework, attention must be given to the modeling of the thermal internal radiation process. While the thermal model in this dissertation captured the effect of radiation to the environment at the outer surfaces of the structure, the effect of internal radiation was not considered. As the incorporation of internal radiation modeling into the thermal model would significantly increase its complexity, it is important to first assess whether or not this phenomenon impacts the physics of the problem significantly enough to warrant its inclusion in the framework. In order to account for the fraction of radiation coming from one surface that is incident on another, geometric

factors referred to as configuration factors, shape factors, or view factors must be computed [166]. Further complicating the radiation analysis is the fact that some materials have radiative properties that vary significantly with wavelength, surface temperature, and direction. Two recent works [162, 167] presented a thermal modeling formulation which included both external and internal radiation. In those works, both the conduction heat transfer and internal cavity radiation analysis were conducted via finite element meshes. While such an approach provides for an accurate representation of the internal radiation, it also increases the complexity of the thermal solution. Thus, if internal radiation effects are found to be important to include in the analysis, careful attention must be given to reducing the associated computational complexity and maintaining the reduced-order nature of the solution.

Appendix

Appendix A

Aerodynamics and Aerodynamic Heating

Chapters II through V describe the transient thermal and structural dynamic modeling formulations that are employed in this work. The remaining components of the HSV aerothermoelastic simulation framework involve the aerodynamic and aerodynamic heating aspects of the solution. An aerodynamic model is necessary to capture the aerodynamic pressure loads over the outer surfaces of the structure so that the aerodynamic load vector can be assembled. Additionally, the aerodynamic flow properties are needed to compute the aerodynamic heat flux over the outer surfaces of the structure. Relatively accurate solutions of hypersonic aerodynamics are available via full-order CFD solutions of the Navier-Stokes equations. However, the computational cost of performing such full-order CFD within an aerothermoelastic framework is prohibitive. Additionally, structural deformations results in unsteady aerodynamic effects which require deformation of the CFD mesh in order to adequately capture such effects. One approach that has been employed in the literature to make unsteady aerodynamic modeling computationally feasible involves the use of reduced-order models derived from the output of high-fidelity models. A variety of different strategies have been employed in the area of reduced-order unsteady aerodynamic modeling. Such strategies have included convolution and Volterra series [168, 169, 170, 171], POD [172], and Kriging [173, 174, 175, 176], among others.

While reduced-order modeling has been shown to effective in efficient modeling of unsteady aerodynamic flows, investigation of such an approach is beyond the scope of this work. Though the aerothermoelastic framework of this dissertation is intentionally formulated to be general enough to allow for the use of a reduced-order aerodynamic model, approximate or first-principles aerodynamic theories are used here. The advantage of such an approach is that the simplified and algebraic nature of the governing equations allows for a direct implementation of the methodology without the need to run high-fidelity simulations *a priori* in order to generate an aerodynamic ROM. This dissertation considers both quasi-steady and fully unsteady aerodynamic effects. For the quasi-steady aerodynamics, a localized oblique shock/Prandtl-Meyer expansion fan formulation is used to compute the steady flow properties over the statically deformed structural configuration at each time step. For the fully unsteady aerodynamics, a third-order piston theory formulation is employed to account for both the deformations and velocities of the structure resulting from solution of the structural dynamic equations of motion. While piston theory is an approximate unsteady aerodynamic theory, it has been investigated for use in hypersonic flow applications in a variety of studies [49, 30, 177, 178, 179, 180] and has been shown to provide sufficient accuracy as compared with Navier-Stokes CFD [4, 22].

As in the case of the aerodynamic model, an approximate or first-principles aerodynamic heating model is also employed in the aerothermoelastic framework of this dissertation for the purpose of computing the heat flux boundary conditions to use in the transient thermal solution. The specific technique employed in this work is the Eckert reference temperature method [181, 182, 183] which gives a simplified formula for the Stanton number associated with high speed flows by using ideas from incompressible flow theory and "correcting" for compressibility effects by evaluating thermodynamic and transport properties at a reference temperature [1, 184]. The Eckert reference temperature method has been employed widely for use in aerodynamic heating and skin friction predictions in high speed flows [185, 186, 63, 187, 188, 189]. In addition to the Eckert reference temperature

method, the use of a CFD-based reduced-order aerodynamic heating model developed by Crowell and McNamara [52,53,26,110,51] within the aerothermoelastic formulation is also investigated for the purposes of improving the accuracy and efficiency of the aeroheating calculation.

The current section begins by describing the quasi-steady aerodynamic formulation. Both the oblique shock and Prandtl-Meyer expansion fan relations that are included in the quasi-steady formulation are presented. A localized shock/expansion formulation for capturing the spatial variation in flow properties due to structural deformation is then described. The unsteady aerodynamic formulation based on third-order piston is also given. With regard to aerodynamic heating, the Eckert reference temperature method is discussed. Finally, a brief overview of the reduced-order aerodynamic heating model developed by Crowell and McNamara is presented in order to illustrate how it is incorporated into the reduced-order aerothermoelastic framework.

A.1 Aerodynamics

A.1.1 Quasi-Steady Aerodynamic Formulation

For situations in which the structural response changes a slow time scale, as is the case when slowly varying thermal loads are dominant, a quasi-steady aerodynamic formulation is expected to provide a reasonable approximation to the aerodynamic flow properties over the deformed structure. The quasi-steady aerodynamic formulation used here, based on oblique shock/Prandtl-Meyer expansion theory, is presented in the current section. Note that though the thermal and structural analyses in this work are based on models containing a nonzero airfoil thickness, the quasi-steady aerodynamic formulation treats the airfoil as if it were a zero-thickness plate and neglects leading edge, trailing edge, and thickness effects. Therefore, though the finite element mesh employed in the thermal and structural analyses is used aerodynamic flow calculations, the top and bottom surfaces of this model

are treated as if they compose the top and bottom surfaces of a plate with zero thickness for aerodynamics purposes. Inherent in this formulation is the assumption that the deformations of the top and bottom surfaces are approximately equal, and that the deformation of one surface with respect to the other (i.e., local change in airfoil thickness due to deformation) is negligible as compared with the overall gross deformation of the airfoil.

A.1.1.1 Oblique Shock Relations

When a supersonic or hypersonic flow is turned into itself, an oblique shock will be formed. Such a phenomenon is a result of strong disturbances which propagate by molecular collisions at the speed of sound [190] due to an imposed flow turning angle, θ. These disturbances coalesce into an oblique shock wave that makes an angle β with the freestream. Note that the physical mechanism that leads to an oblique shock is essentially the same as that which creates a Mach wave, and the Mach wave can be described as an infinitely weak oblique shock.

The geometry associated with an oblique shock caused by a wedge in supersonic flow is given in Fig. A.1, where V_1 and M_1 are the velocity and Mach number upstream of the shock, respectively. The wedge half-angle is θ and results in an oblique shock at an angle β with respect to the direction of V_1. The variables u_1 and w_1 correspond to the components of V_1 perpendicular and parallel to the shock, respectively. Similarly, the variables $M_{1,n}$ and $M_{1,t}$ correspond to the upstream values of the Mach number perpendicular (normal) and parallel (tangential) to the shock, respectively. Analogously, the variables with a subscript 2 represent the corresponding quantities downstream of the shock. Control volume analysis based on the integral form of the conservation equations leads to the result that the tangential component of the flow velocity is preserved across an oblique shock waves. Control volume analysis of the velocity component normal to the shock wave leads to the oblique shock relations. Therefore, the change in flow properties across an oblique shock wave are governed by the normal component of the freestream velocity.

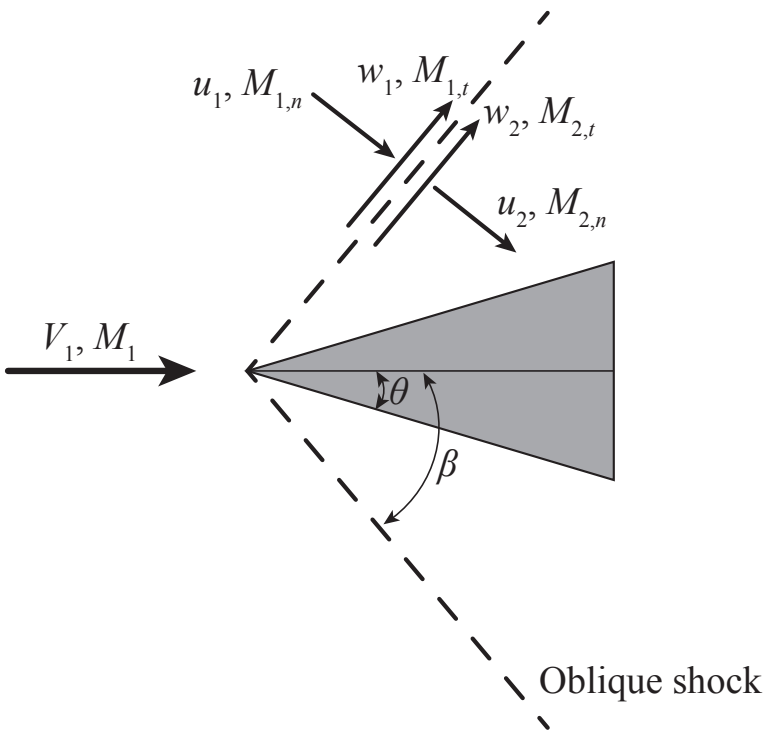

Figure A.1: Geometry associated with the oblique shock.

For the case of an oblique shock, the first step in the analysis is to compute the angle that the shock makes with the freestream, β, using [191]

$$\sin^6\beta + b\sin^4\beta + c\sin^2\beta + d = 0, \tag{A.1}$$

where the coefficients, b, c, and d, are given by

$$\begin{aligned} b &= \frac{-M_1^2+2}{M_1^2} - \gamma\sin^2\theta \\ c &= \frac{2M_1^2+1}{M_1^4} + \left[\frac{(\gamma+1)^2}{4} + \frac{\gamma-1}{M_1^2}\right]\sin^2\theta \\ d &= -\frac{\cos^2\theta}{M_1^4}, \end{aligned} \tag{A.2}$$

where γ is the ratio of specific heats. Alternatively, the relationship between the flow

turning angle, shock angle, and upstream Mach number can be expressed as [190]

$$\tan\theta = 2\cot\beta\left[\frac{M_1^2\sin^2\beta - 1}{M_1^2\left(\gamma + \cos 2\beta\right) + 2}\right], \tag{A.3}$$

which is commonly referred to as the θ-β-M relation. For a given value of M_1, there exists an upper bound on the flow deflection angle, θ_{max}. If the geometry of the problem is such that $\theta > \theta_{\text{max}}$, a solution for a straight oblique shock wave does not exist, and the shock will be curved and detached. If $\theta < \theta_{\text{max}}$, the θ-β-M relations predict two possible values of β for a given Mach number. The larger value of β corresponds to the strong shock solution, while the smaller value corresponds to the weak shock solution. The weak shock solution is favored in typical situations, and is thus selected in the formulation presented here.

With β known for the weak shock solution, the post-shock flow properties are computed using [190, 191]

$$\frac{\rho_2}{\rho_1} = \frac{(\gamma+1)M_1^2\sin^2\beta}{(\gamma-1)M_1^2\sin^2\beta + 2} \tag{A.4}$$

$$\frac{p_2}{p_1} = 1 + \frac{2\gamma}{\gamma+1}\left(M_1^2\sin^2\beta - 1\right) \tag{A.5}$$

$$M_2^2\sin^2(\beta-\theta) = \frac{M_1^2\sin^2\beta + \frac{2}{\gamma-1}}{\frac{2\gamma}{\gamma-1}M_1^2\sin^2\beta - 1} \tag{A.6}$$

$$\frac{T_2}{T_1} = \frac{\left[2\gamma M_1^2\sin^2\beta - (\gamma-1)\right]\left[(\gamma-1)M_1^2\sin^2\beta + 2\right]}{(\gamma+1)^2 M_1^2\sin^2\beta}, \tag{A.7}$$

where M_1, p_1, ρ_1, and T_1 are the Mach number, static pressure, static density, and static temperature upstream of the shock and M_2, p_2, ρ_2, and T_2 are the Mach number, static pressure, static density, and static temperature downstream of the shock. Taking $\gamma = 7/5$, the relations given in Eqs. (A.4) – (A.7) become

$$\frac{\rho_2}{\rho_1} = \frac{6M_1^2\sin^2\beta}{M_1^2\sin^2\theta + 5} \tag{A.8}$$

$$\frac{p_2}{p_1} = \frac{7M_1^2\sin^2\beta - 1}{6} \tag{A.9}$$

$$M_2^2 \sin^2(\beta - \theta) = \frac{M_1^2 \sin^2 \beta + 5}{7M_1^2 \sin^2 \beta - 1} \tag{A.10}$$

$$\frac{T_2}{T_1} = \frac{\left(7M_1^2 \sin^2 \beta - 1\right)\left(M_1^2 \sin^2 \beta + 5\right)}{36M_1^2}. \tag{A.11}$$

Note that the above relations apply to a completely perfect fluid (both thermally and calorically perfect), which implies [191]

$$p = \rho RT \tag{A.12}$$

$$\frac{dp}{p} - \frac{d\rho}{\rho} - \frac{dT}{T} = 0 \tag{A.13}$$

$$h = c_p T, \tag{A.14}$$

where R is the ideal gas constant, h is the enthalpy, and c_p is the specific heat at constant pressure. Examining the oblique shock relations, it can be observed that the post-shock flow properties are a function of both the upstream Mach number and the shock angle. This is in contrast with the normal shock relations in which the post-shock flow properties are a function of the upstream Mach number only.

A.1.1.2 Prandtl-Meyer Expansion Fan Relations

When a supersonic or hypersonic flow is turned away itself, a Prandtl-Meyer expansion fan occurs. The geometry associated with the expansion is given in Fig. A.2. Region 1 in the figure refers to the flow upstream of the expansion, while region 2 refers to the flow downstream of the expansion. The upstream bound is the forward Mach line which makes an angle μ_1 with the freestream, or upstream, flow direction, while the downstream bound is the rearward Mach line which makes an angle μ_2 with the downstream flow direction. Because the expansion occurs over a series of continuous Mach waves, and since the change in entroy, ds, is equal to zero for each Mach wave, the expansion process is isentropic. This is not true of an oblique shock wave which always experiences an increase in entropy.

The goal of the Prandtl-Meyer expansion formulation is to compute the properties of

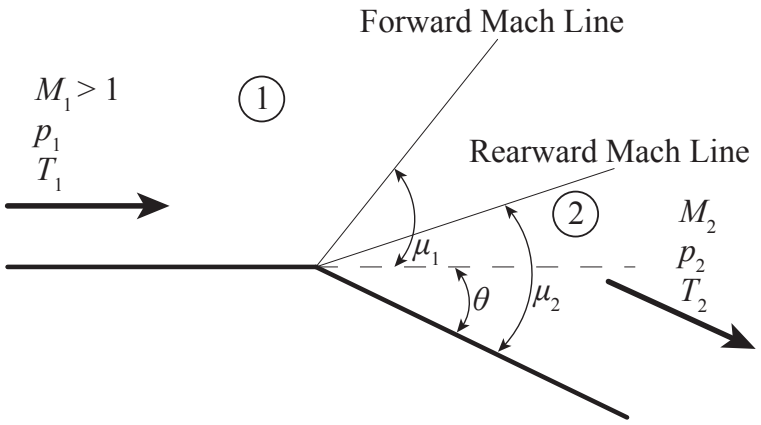

Figure A.2: Geometry associated with Prandtl-Meyer expansion wave [192].

the post-expansion flow (region 2) given the the freestream (region 1) flow properties and flow turning angle, θ. The calculation of flow properties behind an expansion begins by calculating the Prandtl-Meyer function, ν, based on the Mach number upstream of the expansion, M_1, using [192]

$$\nu(M_1) = \sqrt{\frac{\gamma+1}{\gamma-1}}\tan^{-1}\sqrt{\frac{\gamma-1}{\gamma+1}(M_1^2-1)} - \tan^{-1}\sqrt{M_1^2-1}. \tag{A.15}$$

Note that Eq. (A.15) assumes a calorically perfect gas. Using $\nu(M_1)$ and the flow turning angle, θ, the Prandtl-Meyer function based on downstream Mach number, M_2, is found using

$$\nu(M_2) = \nu(M_1) + \theta. \tag{A.16}$$

Once $\nu(M_2)$ is known, we can again use the expression for the Prandtl-Meyer function given in Eq. (A.15), except in this case we use M_2 instead of M_1:

$$\nu(M_2) = \sqrt{\frac{\gamma+1}{\gamma-1}}\tan^{-1}\sqrt{\frac{\gamma-1}{\gamma+1}(M_2^2-1)} - \tan^{-1}\sqrt{M_2^2-1}. \tag{A.17}$$

This equation is solved numerically for M_2 to give the Mach number downstream of the expansion. Because an expansion fan is isentropic, the total temperature, T_t, and total pressure, p_t, are constant across the expansion. We can therefore use the isentropic flow

relations to calculate the remaining flow properties based on M_1 and M_2 using [192]

$$\frac{T_2}{T_1} = \frac{T_2/T_{t,2}}{T_1/T_{t,1}} = \frac{1 + \frac{\gamma-1}{2}M_1^2}{1 + \frac{\gamma-1}{2}M_2^2} \tag{A.18}$$

$$\frac{p_2}{p_1} = \frac{p_2/p_{t,2}}{p_1/p_{t,1}} = \left[\frac{1 + \frac{\gamma-1}{2}M_1^2}{1 + \frac{\gamma-1}{2}M_2^2}\right]^{\frac{\gamma}{\gamma-1}}. \tag{A.19}$$

A.1.1.3 Localized Shock/Expansion Formulation

For the quasi-steady aerodynamic formulation, the oblique shock and Prandtl-Meyer relations described above are implemented. As the goal of the formulation is to capture the steady flow properties over an arbitrarily deformed structure at each time instant, the methodology is applied in a local sense to capture the effect of flow turning due to structural deformations. As opposed to performing computationally intensive CFD analysis at every time step, the use of such an analytical formulation for the aerodynamics model is consistent with the control-oriented and vehicle design modeling philosophy that the framework remain numerically tractable and efficient. Thus, such an approach captures the physics of the spatially varying aerodynamic flow parameters while remaining on a low enough order to be used in control system and vehicle design studies. As the methodology is applied to a control surface structure in this dissertation, the description of the formulation presented in the current section is focused the application of the methodology to such a structure.

As mentioned previously, the flow is assumed to be calorically perfect and a constant specific heat is used. Once the freestream flow parameters are initialized, the structural displacements at a given time are computed and the deformed configuration is generated. To find the aerodynamic flow properties over the deformed surface using the shock/expansion relations, a flow turning angle must be computed at various within the model. As the structure is discretized using a finite element representation, the same discretization is used in the aerodynamics solution. The local flow turning angle at each node is thus found by calculating the relative change in angle between the surface tangent at the current node and the

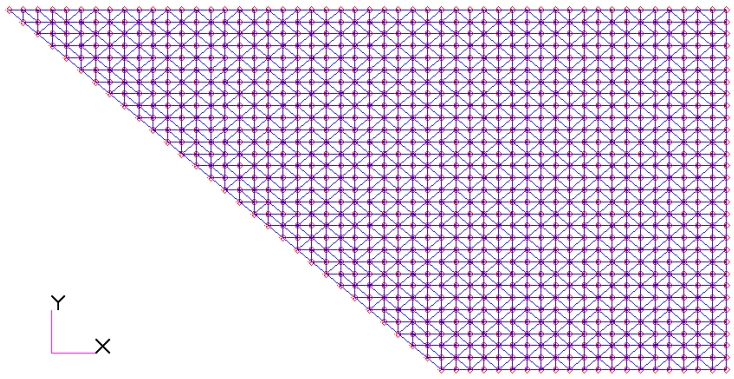

Figure A.3: Top surface of finite element model illustrating arrangement of nodes in chordwise strips.

surface tangent at the node directly upstream. To allow for such calculation of the turning angle, the flow is assumed to occur in chordwise strips along the surface and the nodes of the finite element model are arranged to lie in rows along the chordwise direction. An example mesh is shown in Fig. A.3, illustrating the chordwise mesh alignment.

The finite element mesh shown in Fig. A.3 allows for straightforward identification of the upstream node. The flow turning angle calculation is accomplished by identifying the node at the same station in the y direction which is the closest node directly upstream of the node of interest. Based on the deformed configuration, the unit vector normal to the deformed surface is found at each node. The surface normal vector for the i-th node is denoted $\hat{n}_i$. Note that because a particular node may be connected to multiple elements each having a different normal direction, a standard averaging scheme is employed to best represent the direction of the normal to the surface at that point. As the flow is taken to occur purely in the chordwise direction and no cross-flow is assumed, the normal is then projected onto a plane parallel to the x-z plane. Based on the plane defined by the surface normal, a unit vector tangent to the deformed surface at each node is then found. The surface tangent at node i is denoted as $\hat{s}_i$. Again, due to the chordwise flow assumption, we take the tangent that lies in a plane parallel to the x-z plane defined in Fig. A.3.

Once all of the nodal normal and tangent vectors are known, the Mach number, pres-

sure, and temperature can be found at each node. The aerodynamic solution process begins by calculating the flow parameters at the leading edge node at the root of the structure. The flow turning angle is calculated as the angle that the freestream flow vector makes with the surface tangent at this node. Once the flow turning angle is known, the appropriate oblique shock or expansion fan relation is used along with the freestream flow properties to calculate the resulting Mach number, pressure, and temperature at that node. The process is successively repeated for each node along the chord in the current chordwise strip. Once the trailing edge node is reached, the solution moves along the span toward the tip to the next row of nodes until the node at the trailing edge of the tip is reached.

It is important to bear in mind that flow parameter calculations for nodes at the leading edge differ from those for nodes in the interior and trailing edge. This is because the interior and trailing edge nodes use the Mach number, pressure, and temperature at the upstream node for the upstream conditions. The leading edge nodes, however, use the freestream properties as the upstream conditions for the flow. Additionally, for nodes not at the leading edge, the flow turning angle is the difference between the angle that the surface tangent at the current node makes with the freestream direction and the angle that surface tangent at the upstream node makes with the freestream direction. The angle that the local tangent at node i makes with the freestream direction is denoted as Θ_i. A schematic summarizing the calculation of the local flow turning angles is shown in Fig. A.4. The figure shows a representative deformed configuration composed of three nodes. At each node, a local normal, $\hat{n}$, and local tangent, $\hat{s}$, are shown along with the freestream direction, V_∞. Additionally, the angle between the local tangent and freestream directions, Θ_i, is depicted for each of the three nodes. Based on the description of the methodology above, the flow turning angle experienced in moving from node 1 to node 2 in the figure is given by $\Theta_2 - \Theta_1$ and the turning angle for node 3 is given by $\Theta_3 - \Theta_2$.

With the nodal pressures known at the top and bottom surfaces of the structure, the value of the element-uniform pressure is found by averaging the values at the corresponding

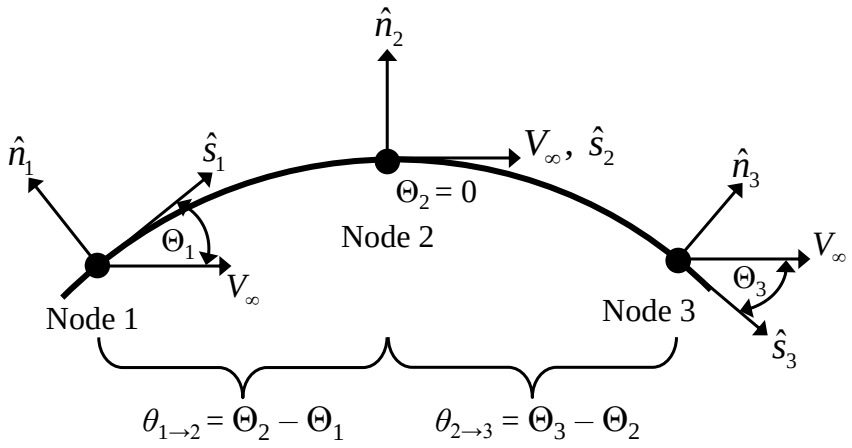

Figure A.4: Illustration of calculation of local flow turning angle for use in shock/expansion relations.

nodes for each element. To find the resulting force acting normal to the surface of the element, the elemental normal pressure value is multiplied by the area of the element and projected in the direction of the element normal. The component of the force contributing to drag is found by projecting the resulting force vector in the direction of the freestream flow. Similarly, the component of the force contributing to lift is found by projecting the force vector in the direction perpendicular to the freestream flow. In addition to normal pressure forces, the resultant force and moment calculations also include the effect of wall shear stress due skin friction. The skin friction forces act tangent to the deformed configuration and are computed based on the local skin friction coefficients obtained from the Eckert reference temperature formulation described in a subsequent section.

As with the normal pressure force, the element-uniform wall shear stress is multiplied by the element area to calculate the force acting on element. Because the force due to shear will not necessarily be acting in the direction of the freestream, this force is also resolved into lift and drag components. Once the values contributing to lift and drag from both normal pressure and wall shear stress contributions are found, they are summed to give the overall lift and drag forces on the control surface.

A.1.2 Unsteady Aerodynamic Formulation

While a quasi-steady aerodynamic formulation is useful in situations in which the structural response is close to quasi-static, a fully unsteady aerodynamic formulation is required to capture structural dynamic motion. The unsteady aerodynamic modeling in this dissertation is accomplished via the use of piston theory. Piston theory provides a closed-form expression which relates the local pressure resulting from a body's motion to the normal component of the fluid velocity at the location of interest. Early development of piston theory was performed by Lighthill [193] who discussed its application to oscillating airfoils. Ashley and Zartarian [194] further discussed the theory and applied it to a variety of aeroelastic problems.

In high Mach number flows over an airfoil, shock waves and expansion fans form at small angles to the undisturbed flow [193]. This realization results in two main conclusions:

1. Gradients in the freestream direction are small compared with gradients perpendicular to the freestream.

2. Because the velocity components parallel to shock waves and expansion fans remain unchanged, velocity components perpendicular to the flow are large compared with the disturbances to components parallel to the flow.

These facts contribute to the formulation of Hayes' hypersonic equivalence principle [195, 1, 196], which states that "*the steady hypersonic flow over a slender body is equivalent to an unsteady flow in one less space dimension*". The combination of these results lead to the conclusion that in a two-dimensional inviscid flow, a plane slab of fluid that is initially perpendicular to the freestream remains approximately so as it swept downstream [193]. Goldsworthy [197] showed that relative error of this realization of the flow is of the order $1/M^2$. This relative error assumes that the product $M\delta$ is bounded, where δ is the maximum inclination (radians) of the airfoil surface to the freestream.

In the piston theory formulation, the unsteady pressure is calculated at a specific location as if it were the face of a piston moving into a one-dimensional channel. The boundary of the fluid slab corresponding to the airfoil surface moves normal to the flow with velocity V_n and can be expressed in terms in terms of the freestream velocity, V_∞, the position of the outer surface of the structure, $Z\left(x,y,t\right)$, and the angle of attack, α by

$$V_n = \frac{\partial Z(x,y,t)}{\partial t} + V_\infty \left[\frac{\partial Z(x,y,t)}{\partial x} + \alpha\right], \tag{A.20}$$

where x is the freestream direction. Note that $Z(x,y,t)$ is a function of the elastic deformation of the structure and the geometry of the outer mold line and is given by

$$Z(x,y,t) = w_d(x,y,z,t) + Z_{str}(x,y), \tag{A.21}$$

where w_d is the displacement in the z direction normal to the flow direction and $Z_{str}(x,y)$ is a function describing the geometry of the outer mold line of the structure. For the implementation in this dissertation, the calculations of the spatial and temporal partial derivatives in Eq. (A.20) are performed using finite difference approximations at the nodal locations of the finite element grid and are again evaluated in chordwise strips.

Before proceeding further with the derivation, it must be stated a limiting condition on piston theory is that the magnitude of the normal piston velocity, V_n, must not exceed the speed of sound in the undisturbed fluid [193]. This condition can be written

$$w_{d,max}\omega + V_\infty \delta < a_\infty, \tag{A.22}$$

where $w_{d,max}$ is the maximum displacement, ω is the frequency of oscillation, and a_∞ is the freestream speed of sound. This relation can be rewritten as

$$M_\infty \left[\delta + \frac{w_{d,max}}{c}\frac{\omega c}{V_\infty}\right] < 1, \tag{A.23}$$

where c is the chord length so that $\omega c/V_\infty$ is the frequency parameter. Note that reasonable accuracy may still be obtained for compression of up to 3.5 times and expansion of down to 0.2 times the freestream pressure [193]. Additionally, the formulation assumes that the Mach number is sufficiently large, i.e.

$$M_\infty^2 >> 1, \tag{A.24}$$

where a sufficiently large Mach number can be considered to be approximately $M \geq 4$ [193].

The pressure on the face of a piston moving in a channel of perfect gas with velocity V_n, assuming only simple waves are generated and entropy remains unchanged, is given by [194]

$$\frac{p}{p_\infty} = \left(1 + \frac{\gamma - 1}{2}\frac{V_n}{a_\infty}\right)^{\frac{2\gamma}{\gamma-1}}, \tag{A.25}$$

where p is the surface pressure, p_∞ is the freestream pressure, and γ is the ratio of specific heats. Depending on the magnitude of V_n/a_∞, Eq. (A.25) may be approximated by the linear relation,

$$p - p_\infty = \rho_\infty a_\infty V_n, \tag{A.26}$$

by the second-order binomial expansion

$$p - p_\infty = \rho_\infty a_\infty^2 \left[\left(\frac{V_n}{a_\infty}\right) + \frac{\gamma+1}{4}\left(\frac{V_n}{a_\infty}\right)^2\right], \tag{A.27}$$

or by the third-order expansion

$$p - p_\infty = \rho_\infty a_\infty^2 \left[\left(\frac{V_n}{a_\infty}\right) + \frac{\gamma+1}{4}\left(\frac{V_n}{a_\infty}\right)^2 + \frac{\gamma+1}{12}\left(\frac{V_n}{a_\infty}\right)^3\right]. \tag{A.28}$$

Note that Eqs. (A.26) – (A.28) make use of the istentropic flow relation for the speed of

sound in an ideal gas,

$$a_\infty^2 = \frac{\gamma p_\infty}{\rho_\infty}. \tag{A.29}$$

Due to the hypersonic flow regime considered in this work, the third-order piston theory relation given by Eq. (A.28) is utilized here. The pressure coefficient, C_p, based on third order expansion of Eq. (A.25) is given by [22]

$$C_p = \frac{2}{M_\infty^2}\left[\frac{V_n}{a_\infty} + \frac{(\gamma+1)}{4}\left(\frac{V_n}{a_\infty}\right)^2 + \frac{(\gamma+1)}{12}\left(\frac{V_n}{a_\infty}\right)^3\right], \tag{A.30}$$

where pressure coefficient for compressible flow is given by [190]

$$C_p = \frac{2}{\gamma M_\infty^2}\left(\frac{p}{p_\infty} - 1\right). \tag{A.31}$$

Note that for a given value of V_n/a_∞, the pressure value may vary continuously between the extremes of a simple wave and a shock/expansion. Thus, any approximate pressure prediction that lies reasonably close to both is acceptable. Lighthill [193] found that the third-order piston theory approximation produces pressures that lie within 6% of the simple wave and shock-expansion predictions, thus providing support for the use of third-order piston theory.

One restriction on the use of piston theory in this work is that the magnitude of the piston velocity, V_n, must never exceed the speed of sound in the undisturbed fluid, as given by Eq. (A.23). As the control surface is likely to undergo relatively large changes in angle of attack, it is expected that this assumption would be violated if piston theory was used in isolation. To reduce V_n and decrease the likelihood that this assumption is violated, the flow is turned through the rigid angle of attack at the leading edge using the oblique shock and Prandtl-Meyer expansion theory relations described in the previous section. Use of these relations allows for α to be removed from the expression for the normal velocity given in Eq. (A.20), and therefore reduces the slope used in the calculation of the piston

velocity. Thus, the freestream velocity, V_∞, in Eq. (A.20) then becomes the post-shock or post-expansion velocity corresponding to the flow over the top or bottom surface as calculated using the shock/expansion relations.

A.2 Aerodynamic Heating

A.2.1 Eckert Reference Temperature Method

In order to compute the aerodynamic heat flux due to boundary layer flow, the Eckert reference temperature method [181, 182, 183] is employed. As described in the introduction to this chapter, this semi-empirical approach uses boundary layer relations from incompressible flow theory and "corrects" for compressibility by evaluating the thermodynamic and transport properties at a reference temperature. The aerodynamic heating solution is associated with the aerodynamic solution due to the fact that boundary layer edge properties of the flow are required for the aeroheating computation. As in the case of the aerodynamics, the aerodynamic heating formulation is applied here in a local sense to capture the spatial variation in the thermal boundary conditions. This variation is a result of structural deformation which alters the flow properties, as well as spatial variation in the wall temperature at the outer surface of the structure.

In order to calculate the spatially varying heat flux resulting from aerodynamic heating, the local freestream pressure, temperature, and Mach number at the edge of the boundary layer must first be found. For the quasi-steady aerodynamic formulation, the equations governing each of these parameters are given in Section A.1.1. For the unsteady aerodynamic formulation, the piston theory equations governing the local pressure are given in Section A.1.2. Thus, for the third-order piston theory representation, it remains to compute the local temperature and Mach number at the edge of the boundary layer. To find these properties, isentropic flow is assumed between the leading edge and the location of interest on the surface of the structure. For an isentropic process, the total pressure and total

temperature remain constant and one can write

$$p_t = p_\infty \left(1 + \frac{\gamma - 1}{2} M_\infty^2\right)^{\frac{\gamma}{\gamma - 1}} = p_e \left(1 + \frac{\gamma - 1}{2} M_e^2\right)^{\frac{\gamma}{\gamma - 1}} \tag{A.32}$$

$$T_t = T_\infty \left(1 + \frac{\gamma - 1}{2} M_\infty^2\right) = T_e \left(1 + \frac{\gamma - 1}{2} M_e^2\right), \tag{A.33}$$

where p_e, T_e, and M_e are the local flow properties at the edge of the boundary layer. Using these relations, we can then express ratios between the freestream pressure and temperature and the local pressure and temperature as

$$\frac{p_e}{p_\infty} = \left(\frac{1 + \frac{\gamma-1}{2} M_\infty^2}{1 + \frac{\gamma-1}{2} M_e^2}\right)^{\frac{\gamma}{\gamma-1}} \tag{A.34}$$

$$\frac{T_e}{T_\infty} = \frac{1 + \frac{\gamma-1}{2} M_\infty^2}{1 + \frac{\gamma-1}{2} M_e^2}. \tag{A.35}$$

Note that the local pressure from piston theory is used in Eq. (A.34) to compute M_e. With M_e known, it is then used in Eq. (A.35) to compute T_e. Once the values of the local aerodynamic parameters are known over the outer surface of the model, the aerodynamic heating computation can be carried out.

From Holman [127], the convective heat flux at the surface of a structure is given by

$$\dot{q}_{aero} = h(T_w - T_r), \tag{A.36}$$

where h is the heat transfer coefficient, T_w is the wall temperature, and T_r is the recovery temperature or adiabatic wall temperature. Because the process that brings the fluid to rest in the boundary layer is irreversible, and because not all of the free-stream kinetic energy is converted to thermal energy in this process [127], a recovery factor is introduced, which is given by

$$r_f = \frac{T_r - T_e}{T_t - T_e}. \tag{A.37}$$

Using Eq.(A.33), the total temperature is found from

$$T_t = T_e \left[1 + (\gamma - 1)\frac{M_e^2}{2}\right], \tag{A.38}$$

where $\gamma = 1.4$ is used in this dissertation. The recovery factor is calculated based on the Prandtl number, Pr, and depends on whether the flow is laminar or turbulent. For laminar flow, r_f is given by

$$r_f = Pr^{1/2} \quad \text{(Laminar flow)}, \tag{A.39}$$

and for turbulent flow, r_f is given by

$$r_f = Pr^{1/3} \quad \text{(Turbulent flow)}. \tag{A.40}$$

This dissertation assumes turbulent flow throughout in order to provide a conservative estimate of heating levels. The Prandtl number is a dimensionaless quantity given by the relation

$$Pr = \frac{c_p \mu}{\kappa}, \tag{A.41}$$

where μ is the dynamic viscosity and κ is the thermal conductivity. However, Pr is approximated by assuming a constant value of 0.7 [127] in this dissertation. Due to the large property variations across the boundary layer in the hypersonic flow, the constant-property heat transfer relations are used with the properties evaluated at a reference temperature, T^*, as proposed by Eckert [183]. The reference temperature is given by

$$T^* = T_e + 0.50\,(T_w - T_e) + 0.22\,(T_r - T_e)\,. \tag{A.42}$$

Once the reference temperature is known, the reference density, ρ^*, and reference dynamic viscosity, μ^*, are calculated using the ideal gas law and Sutherland's law, respectively.

Sutherland's law gives the dynamic viscosity, μ, based on the temperature, T, using

$$\mu = \mu_{\text{Suth}} \left(\frac{T}{T_{\text{Suth}}} \right)^{3/2} \frac{T_{\text{Suth}} + S}{T + S}, \tag{A.43}$$

where T_{Suth} is a Sutherland reference temperature, μ_{Suth} is the known viscosity at T_{Suth}, and S is Sutherland's constant for the species of interest.

With the reference quantities known, the Reynolds number at the reference state is found using

$$Re_x^* = \frac{\rho^* V_e x_d}{\mu^*}, \tag{A.44}$$

where x_d is the distance from the leading edge and V_e is the velocity of the flow at the outer edge of the boundary layer. With the local Reynolds number known, the next step is to calculate the skin friction coefficient, c_f. The skin friction coefficient is used to determine the shear stress at the wall, τ_w, using

$$\tau_w = c_f \frac{\rho V_e^2}{2}. \tag{A.45}$$

Note that the wall shear stress can also be obtained from the relation

$$\tau_w = \mu \left[\frac{\partial U}{\partial z} \right]_w. \tag{A.46}$$

The relation used to obtain the skin friction coefficient depends on the flow regime. For incompressible flow laminar flow over a flat plate, the skin friction coefficient based on Re_x^* is given by [192]

$$c_f^* = \frac{0.664}{\sqrt{Re_x^*}} \quad \text{(Laminar flow)}. \tag{A.47}$$

Note that this is a classical result based on exact solution of the boundary layer equations. Schlichting [198] has surveyed experimental measurements of friction coefficients for turbulent flow on flat plates. Based on the results of that survey, the local skin friction coeffi-

cient for flow over a flat plate with Reynolds numbers in the range $5 \times 10^5 \leq Re_x^* \leq 10^7$ is given by

$$c_f^* = \frac{0.0592}{(Re_x^*)^{1/5}} \quad (\text{Turbulent flow},\ 5 \times 10^5 \leq Re_x^* \leq 10^7). \tag{A.48}$$

For turbulent flow over a flat plate with Reynolds numbers in the range $10^7 \leq Re_x^* \leq 10^9$, the local skin friction coefficient is obtained from the Schultz-Grunow relation [199] which is given by

$$c_f^* = \frac{0.370}{(\log_{10} Re_x^*)^{2.584}} \quad (\text{Turbulent flow},\ 10^7 \leq Re_x^* \leq 10^9). \tag{A.49}$$

Once the skin friction is known, the reference Stanton number, St^*, can be found using the Colburn-Reynolds analogy given by

$$St^* = \frac{c_f^*}{2} Pr^{-2/3}. \tag{A.50}$$

The Colburn-Reynolds analogy expresses the relation between fluid friction and heat transfer for laminar flow over a flat plate. Equation (A.50) can also be applied to turbulent flow over a flat plate [127], and is therefore used in this work. Finally, the heat transfer coefficient is found using the definition of Stanton number,

$$h = St^* c_p \rho^* V_e. \tag{A.51}$$

Note that the flow is assumed to be calorically perfect for the purposes of this study and thus a constant value of specific heat, c_p, is used. Using the aerodynamic heat flux given by Eq. (A.36) and radiation boundary conditions along with the initial temperatures, the temperature distribution can then be propagated forward in time using the transient thermal solution. Note that the heat flux is averaged over each element at the outer surface of the structure and is therefore assumed to be element-uniform. Finally, recall that the aerodynamic forces at the outer surface of the structure includie wall shear stress due to skin

friction. The local wall shear stresses, τ_w, over each finite element at the outer surface are calculated based on the local values of c_f^* obtained from Eq. (A.49) using

$$\tau_w = \frac{1}{2}\rho^* V_e^2 c_f^*. \tag{A.52}$$

A.2.2 Reduced-Order Aerodynamic Heating

In addition to the Eckert reference temperature method, this dissertation also explores the use of a CFD-based reduced-order aerothermal model (ROAM) developed by Crowell and McNamara [52, 53, 26, 110, 51]. While the development of the reduced-order aerodynamic heating methodology does not represent the work of the author of this dissertation, a brief summary of the approach is provided here in order to facilitate an understanding of how the reduced-order aerothermal model is coupled with the reduced-order transient thermal and structural dynamic models. The aerothermal ROM is based on a kriging representation that is derived from high-fidelity steady-state CFD solutions to the Navier-Stokes equations. Given a vector of input parameters, the kriging function provides a vector of heat flux information over the outer surface of the structure. The kriging function is generated by performing CFD solutions for various combinations of the input parameters, where the sample points are determined using Latin Hypercube Sampling.

As a result of aerothermoelastic coupling, the aerodynamic heat flux is dependent on the structural deformation as well as the wall temperature of the structure. Thus, parameters representing these two effects must be included in the aerothermal ROM. One approach to parameterizing the structural deformation and wall temperature would be to treat each structural and thermal degree of freedom in the finite element model as a parameter in the problem. However, for realistic structures, the number of degrees of freedom in the structural and thermal finite element models would result in a paramters space that would be too large to realistically sample. Therefore, alternative approaches for parameterizing the structural deformation and wall temperature must be considered. Recall that the reduced-

order transient thermal and structural dynamic models use a reduced-basis representation. Thus, the transient thermal response is written as a linear combination of a relatively small number POD modes, i.e.

$$T(t) = c_1(t) \begin{Bmatrix} \varphi_1^{(1)} \\ \vdots \\ \varphi_s^{(1)} \end{Bmatrix} + c_2(t) \begin{Bmatrix} \varphi_1^{(2)} \\ \vdots \\ \varphi_s^{(2)} \end{Bmatrix} + \cdots + c_r(t) \begin{Bmatrix} \varphi_1^{(r)} \\ \vdots \\ \varphi_s^{(r)} \end{Bmatrix}, \tag{A.53}$$

and the structural dynamic response is written as a linear combination of a relatively small number of Ritz modes, i.e.

$$x(t) = d_1(t) \begin{Bmatrix} \phi_1^{(1)} \\ \vdots \\ \phi_s^{(1)} \end{Bmatrix} + d_2(t) \begin{Bmatrix} \phi_1^{(2)} \\ \vdots \\ \phi_s^{(2)} \end{Bmatrix} + \cdots + d_r(t) \begin{Bmatrix} \phi_1^{(r)} \\ \vdots \\ \phi_s^{(r)} \end{Bmatrix}. \tag{A.54}$$

The form of the models represented by Eqs. (A.53) and (A.54) naturally leads to the use of the modal coordinates of the POD modes, $c_i(t)$, to represent the wall temperature in the aerothermal ROM and the use of the modal coordinates of the Ritz modes, $d_i(t)$, to represent the structural deformation in the aerothermal ROM. Note that the advantage of using reduced-basis representations for the transient thermal and structural dynamic models now becomes twofold – not only are the sizes of the governing equations reduced, but feasible parameterizations of the wall temperatures and deformation are now provided for efficiently capturing the effects of these two components of the aerothermoelastic solution.

Bibliography

[1] Anderson, J. D., *Hypersonic and High Temperature Gas Dynamics*, McGraw-Hill, 1989.

[2] Ouzts, P. J., "The Joint Technology Office on Hypersonics," *Proceedings of the 15th AIAA International Space Planes and Hypersonic Systems and Technologies Conference, Dayton, Ohio*, AIAA 2008-2576.

[3] Heppenheimer, T. A., "Facing the Heat Barrier: A History of Hypersonics," Tech. Rep. NASA SP-2007-4232, National Aeronautics and Space Administration, Washington, DC, 2007.

[4] McNamara, J. J. and Friedmann, P. P., "Aeroelastic and Aerothermoelastic Analysis in Hypersonic Flow: Past, Present, and Future," *AIAA Journal*, Vol. 49, No. 6, June 2011, pp. 1089–1122.

[5] Livne, E. and Weisshaar, T. A., "Aeroelasticity of Nonconventional Airplane Configurations – Past and Future," *Journal of Aircraft*, Vol. 40, No. 6, November–December 2003, pp. 1047–1065.

[6] Bertin, J. J. and Cummings, R. M., "Fifty Years of Hypersonics: Where We've Been and Where We're Going," *Progress in Aerospace Sciences*, Vol. 39, No. 6–7, April 2011, pp. 511–536.

[7] Houchin, II, R. F., *US Hypersonic Research and Development: The Rise and Fall of Dyna-Soar, 1944–1963*, Routledge, 2006.

[8] Houchin, II, R. F., "Hypersonic Technology and Aerospace and Doctrine," *Air Power History*, Vol. 46, No. 3, 1999, pp. 4–17.

[9] Chase, R. L. and Tang, M. H., "A History of the NASP Program from the Formation of the Joint Program Office to the Termination of the HySTP Scramjet Performance Demonstration Program," *Proceedings of the 15th AIAA International Space Planes and Hypersonic Systems and Technologies Conference, Dayton, Ohio*, AIAA 1995-6031.

[10] Sumrall, J., Lane, C., and Cusic, R., "VentureStar (TM)... Reaping the Benefits of the X-33 Program," *Acta Astronautica*, Vol. 44, No. 7–12, 1999, pp. 727–736.

[11] McClinton, C. R., Rausch, V. L., Sitz, J., and Reukauf, P., "Hyper-X Program Status," *Proceedings of the 39th AIAA Aerospace Sciences Meeting and Exhibit, Reno, Nevada*, AIAA 2001-0828.

[12] Neuenhahn, T., Olivier, H., and Paull, A., "Development of the HyShot Stability Demonstrator," *Proceedings of the 25th AIAA Aerodynamic Measurement Technology and Ground Testing Conference, San Francisco, California*, AIAA 2006-2960.

[13] Mansour, N. N., Pittman, J. L., and Olson, L. E., "Fundamental Aeronautics Hypersonics Project: Overview," *Proceedings of the 39th AIAA Thermophysics Conference, Miami, Florida*, AIAA 2007-4263.

[14] Walker, S. H. and Rodgers, F., "Falcon Hypersonic Technology Overview," *Proceedings of the 13th AIAA/CIRA International Space Planes and Hypersonics Systems and Technologies Conference, Capua, Italy*, AIAA 2005-3253.

[15] Hank, J. M., Murphy, J. S., and Mutzman, R. C., "The X-51A Scramjet Engine Flight Demonstration Program," *Proceedings of the 15th AIAA International Space Planes and Hypersonic Systems and Technologies Conference, Dayton, Ohio*, AIAA 2008-2540.

[16] Dolvin, D. J., "Hypersonic International Flight Research and Experimentation (HIFiRE) Fundamental Sciences and Technology Development Strategy," *Proceedings of the 15th AIAA International Space Planes and Hypersonic Systems and Technologies Conference, Dayton, Ohio*, AIAA 2008-2581.

[17] McClinton, C. R., "X-43–Scramjet Power Breaks the Hypersonic Barrier: Dryden Lectureship in Research for 2006," *Proceedings of the 44th AIAA Aerospace Sciences Meeting and Exhibit, Reno, Nevada*, AIAA 2006-1.

[18] Bolender, M. A. and Doman, D. B., "Nonlinear Longitudinal Dynamical Model of an Air-Breathing Hypersonic Vehicle," *Journal of Spacecraft and Rockets*, Vol. 44, No. 2, March–April 2007, pp. 374–387.

[19] Chavez, F. R. and Schmidt, D. K., "Analytical Aeropropulsive/Aeroelastic Hypersonic-Vehicle Model with Dynamic Analysis," *Journal of Guidance, Control, and Dynamics*, Vol. 17, No. 6, November–December 1994, pp. 1308–1319.

[20] Bertin, J. J., *Hypersonic Aerothermodynamics*, American Institute of Aeronautics and Astronautics, Reston, Virgina, 1994.

[21] Friedmann, P. P., "Renaissance of Aeroelasticity and Its Future," *Journal of Aircraft*, Vol. 36, No. 1, January–February 199, pp. 105–121.

[22] McNamara, J. J. and Friedmann, P. P., "Aeroelastic and Aerothermoelastic Analysis of Hypersonic Vehicles: Current Status and Future Trends," *Proceedings of the 48th AIAA/ASME/ASCE/AHS/ASC Structures, Structural Dynamics, and Materials Conference, Honolulu, Hawaii*, AIAA 2007-2013.

[23] Rogers, M., "Aerothermoelasticity," *Aerospace Engineering*, Vol. 17, No. 10, October 1958, pp. 34–43,64.

[24] Culler, A. J., *Coupled Fluid-Thermal-Structural Modeling and Analysis of Hypersonic Flight Vehicle Structures*, Ph.D. thesis, The Ohio State University, Columbus, Ohio, 2010.

[25] McNamara, J. J., *Aeroelastic and Aerothermoelastic Behavior of Two and Three Dimensional Lifting Surfaces in Hypersonic Flow*, Ph.D. thesis, University of Michigan, Ann Arbor, Michigan, 2005.

[26] Culler, A. J., Crowell, A. R., and McNamara, J. J., "Studies on Fluid-Structural Coupling for Aerothermoelasticity in Hypersonic Flow," *Proceedings of the 50th AIAA/ASME/ASCE/AHS/ASC Structures, Structural Dynamics, and Materials Conference, Palm Springs, California*, AIAA 2009-2364.

[27] Bisplinghoff, R. L., "Some Structural and Aeroelastic Consierations of of High-Speed Flight," *Journal of the Aeronautical Sciences*, Vol. 23, No. 4, April 1956, pp. 289–329,367.

[28] Bisplinghoff, R. L. and Dugundji, J., *Influence of Aerodynamic Heating on Aeroelastic Phenomena*, Pergamon Press, 1958.

[29] Garrick, I. E., "A Survey of Aerothermoelasticity," *Aerospace Engineering*, Vol. 22, No. 1, January 1963, pp. 140–147.

[30] Mei, C., Motagaly, K. A., and Chen, R., "Review of Nonlinear Panel Flutter at Supersonic and Hypersonic Speeds," *Applied Mechanics Review*, Vol. 52, No. 10, October 1999, pp. 321–332.

[31] Pourtakdoust, S. H. and Fazelzadeh, S. A., "Nonlinear Aerothermoelastic Behavior of Skin Panel with Wall Shear Stress Effect," *Journal of Thermal Stresses*, Vol. 28, No. 2, 2005, pp. 147–169.

[32] Gee, D. J. and Sipcic, S. R., "Coupled Thermal Model for Nonlinear Panel Flutter," *AIAA Journal*, Vol. 37, No. 5, May 1999, pp. 642–650.

[33] Dechaumphai, P., Thornton, E. A., and Wieting, A. R., "Flow-Thermal-Structural Study of Aerodynamically Heated Leading Edges," *Journal of Spacecraft and Rockets*, Vol. 26, No. 4, July–August 1989, pp. 201–209.

[34] Thornton, E. A. and Dechaumphai, P., "Coupled Flow, Thermal, and Structural Analysis of Aerodynamically Heated Panels," *Journal of Aircraft*, Vol. 25, No. 11, November 1988, pp. 1052–1059.

[35] Kontinos, D., "Coupled Thermal Analysis Method with Application to Metallic Thermal Protection Panels," *Journal of Thermophysics and Heat Transfer*, Vol. 11, No. 2, April–June 1997, pp. 173–181.

[36] Culler, A. J. and McNamara, J. J., "Studies on Fluid-Thermal-Structural Coupling for Aerothermoelasticity in Hypersonic Flow," *AIAA Journal*, Vol. 48, No. 8, August 2010, pp. 1721–1738.

[37] Culler, A. J. and McNamara, J. J., "Coupled Flow-Thermal-Structural Analysis for Response Prediction of Hypersonic Vehicle Skin Panels," *Proceedings of the 51st AIAA/ASME/ASCE/AHS/ASC Structures, Structural Dynamics, and Materials Conference, Orlando, Florida*, AIAA 2010-2965.

[38] Praveen, G. N. and Reddy, J. N., "Nonlinear Transient Thermoelastic Analysis of Functionally Graded Ceramic-Metal Plates," *Int. J. Solids Structures*, Vol. 35, No. 33, 1998, pp. 4457–4476.

[39] K. -J. Sohn and J. -H. Kim, "Structural Stability of Functionally Graded Panels Subjected to Aero-Thermal Loads," *Composite Structures*, Vol. 82, No. 3, 2008, pp. 317–325.

[40] Ibrahim, H. H., Tawfik, M., and Al-Ajmi, M., "Thermal Buckling and Nonlinear Flutter Behavior of Functionally Graded Material Panels," *Journal of Aircraft*, Vol. 44, No. 5, 2007, pp. 1610–1618.

[41] Navazi, H. M. and Haddadpour, H., "Aero-Thermoelastic Stability of Functionally Graded Plates," *Composite Structures*, Vol. 80, No. 4, 2007, pp. 580–587.

[42] Haddadpour, H., Navazi, H. M., and Shadmehri, F., "Nonlinear Oscillations of a Fluttering Functionally Graded Plate," *Composite Structures*, Vol. 79, No. 2, 2007, pp. 242–250.

[43] Prakash, T. and Ganapathi, M., "Supersonic Flutter Characteristics of Functionally Graded Flat Panels Including Thermal Effects," *Composite Structures*, Vol. 72, No. 1, 2006, pp. 10–18.

[44] Perez, R., Wang, X. Q., and Mignolet, M. P., "Nonlinear Reduced-Order Models for Thermoelastodynamic Response of Isotropic and Functionally Graded Panels," *AIAA Journal*, Vol. 49, No. 3, 2011, pp. 630–641.

[45] Matney, A., Perez, R., and Mignolet, M. P., "Nonlinear Unsteady Thermoelastodynamic Response of a Panel Subjected to an Oscillating Flux By Reduced Order Models," *Proceedings of the 52nd AIAA/ASME/ASCE/AHS/ASC Structures, Structural Dynamics, and Materials Conference, Denver, Colorado*, AIAA 2011-2016.

[46] Thuruthimattam, B. J., Friedmann, P. P., McNamara, J. J., and Powell, K. G., "Modeling Approaches to Hypersonic Aerothermoelasticity with Application to Reusable Launch Vehicles," *Proceedings of the 44th AIAA/ASME/ASCE/AHS/ASC Structures, Structural Dynamics, and Materials Conference, Norfolk, Virginia*, AIAA 2003-1967.

[47] McNamara, J. J., Thuruthimattam, B. J., Friedmann, P. P., and Powell, K. G., "Hypersonic Aerothermoelastic Studies for Reusable Launch Vehicles," *Proceedings of the 45th AIAA/ASME/ASCE/AHS/ASC Structures, Structural Dynamics, and Materials Conference, Palm Springs, California*, AIAA 2004-1590.

[48] McNamara, J. J., Friedmann, P. P., Powell, K. G., and Thuruthimattam, B. J., "Three-dimensional Aeroelastic and Aerothermoelastic Behavior in Hypersonic Flow," *Proceedings of the 46th AIAA/ASME/ASCE/AHS/ASC Structures, Structural Dynamics, and Materials Conference, Austin, Texas*, AIAA 2005-2175.

[49] McNamara, J. J., Friedmann, P. P., Powell, K. G., and Thuruthimattam, B. J., "Aeroelastic and Aerothermoelastic Behavior in Hypersonic Flow," *AIAA Journal*, Vol. 46, No. 10, October 2008, pp. 2591–2610.

[50] Crowell, A. R., Culler, A. J., and McNamara, J. J., "Two-Way Coupled Aerothermoelastic Modeling and Simulation of Hypersonic Vehicle Structures," *Proceedings of the International Forum on Aeroelasticity and Structural Dynamics*, Seattle, WA, June 2009, IFASD-2009-94.

[51] McNamara, J. J., Culler, A. J., and Crowell, A. R., "Aerothermoelastic Modeling Considerations for Hypersonic Vehicles," AIAA 2009-7397.

[52] Crowell, A. R., McNamara, J. J., Kecskemety, K. M., and Goerig, T. W., "A Reduced Order Aerothermodynamic Modeling Framework for Hypersonic Aerothermoelasticity," *Proceedings of the 51st AIAA/ASME/ASCE/AHS/ASC Structures, Structural Dynamics, and Materials Conference, Orlando, Florida*, AIAA 2010-2969.

[53] Crowell, A. R., McNamara, J. J., and Miller, B. A., "Surrogate Based Reduced-Order Aerothermodynamic Modeling for Structural Response Prediction at High Mach Numbers," *Proceedings of the 52nd AIAA/ASME/ASCE/AHS/ASC Structures, Structural Dynamics, and Materials Conference, Denver, Colorado*, AIAA 2011-2014.

[54] Schmidt, D. K., "Dynamics and Control of Hypersonic Aeropropulsive/Aeroelastic Vehicles," *Proceedings of the 1992 AIAA Guidance, Navigation, and Control Conference, Hilton Head, South Carolina*, AIAA 1992-4326.

[55] McRuer, D., "Design and Modeling Issues for Integrated Airframe/Propulsion Control of Hypersonic Flight Vehicles," *Proceedings of the 1991 American Control Conference, Boston, MA*, June 1991, pp. 729–734.

[56] Bilimoria, K. D. and Schmidt, D. K., "Integrated Development of the Equations of Motion for Elastic Hypersonic Vehicles," *Journal of Guidance, Control, and Dynamics*, Vol. 18, No. 1, January–February 1995, pp. 73–81.

[57] Parker, J. T., Serrani, A., Yurkovich, S., Bolender, M. A., and Doman, D. B., "Control-Oriented Modeling of an Air-Breathing Hypersonic Vehicle," *Journal of Guidance, Control, and Dynamics*, Vol. 30, No. 3, May–June 2007, pp. 856–869.

[58] Oppenheimer, M. W., Skujins, T., Doman, D. B., and Cesnik, C. E. S., "Canard-Elevon Interactions on a Hypersonic Vehicle," *Proceedings of the 2008 AIAA Atmospheric Flight Mechanics Conference, Honolulu, Hawaii*, AIAA 2008-6383.

[59] Skujins, T., Cesnik, C. E. S., Oppenheimer, M. W., and Doman, D. B., "Applicability of an Analytical Shock/Expansion Solution to the Elevon Control Effectiveness for a 2-D Hypersonic Vehicle Configuration," *Proceedings of the 2008 AIAA Atmospheric Flight Mechanics Conference, Honolulu, Hawaii*, AIAA 2008-6384.

[60] Oppenheimer, M. W. and Doman, D. B., "A Hypersonic Vehicle Model Developed with Piston Theory," *Proceedings of the 2006 AIAA Atmospheric Flight Mechanics Conference, Keystone, Colorado*, AIAA 2006-6637.

[61] Oppenheimer, M. W., Skujins, T., Bolender, M. A., and Doman, D. B., "A Flexible Hypersonic Vehicle Model Developed with Piston Theory," *Proceedings of the 2007 AIAA Atmospheric Flight Mechanics Conference, Hilton Head, South Carolina*, AIAA 2007-6396.

[62] Bolender, M. A., Oppenheimer, M. W., and Doman, D. B., "Effects of Unsteady and Viscous Aerodynamics on the Dynamics of a Flexible Air-Breathing Hypersonic Vehicle," *Proceedings of the 2007 AIAA Atmospheric Flight Mechanics Conference, Hilton Head, South Carolina*, AIAA 2007-6397.

[63] Culler, A. J., Williams, T., and Bolender, M. A., "Aerothermal Modeling and Dynamic Analysis of a Hypersonic Vehicle," *Proceedings of the 2007 AIAA Atmospheric Flight Mechanics Conference, Hilton Head, South Carolina*, AIAA 2007-6395.

[64] Guyan, R. J., "Reduction of Stiffness and Mass Matrices," *AIAA Journal*, Vol. 3, No. 2, 1965, pp. 380.

[65] Craig, Jr., R. R. and Bampton, M. C. C., "Coupling of Substructures for Dynamic Analysis," *AIAA Journal*, Vol. 6, No. 7, July 1968, pp. 1313–1319.

[66] Botto, D., Gola, S., Troncarelli, M. M., and Pasquero, G., "Component Modes Synthesis Applied to a Thermal Transient Analysis of a Turbine Disc," *Worldwide Aerospace Conference and Technology Showcase, Toulouse*, 2002.

[67] Botto, D., Zucca, S., Gola, M. M., and Salvano, S., "A Method for on Line Temperature Calculation of Aircraft Engine Turbine Discs," *ASME Turbo Expo, Amsterdam*, 2002.

[68] Botto, D., Zucca, S., and Gola, M. M., "A Methodology for On-Line Calculation of Temperature and Thermal Stress Under Non-Linear Boundary Conditions," *Int. J. Press. Vess. Pip.*, Vol. 80, No. 1, 2003, pp. 21–29.

[69] Botto, D., Zucca, S., and Gola, M. M., "Reduced-Order Models for the Calculation of Thermal Transients of Heat Conduction/Convection FE Models," *Journal of Thermal Stresses*, Vol. 30, No. 8, August 2007, pp. 819–839.

[70] Petit, D., Hachette, R., and Veyret, D., "A Modal Identification Method to Reduce a High-Order Model: Application to Heat Conduction Modelling," *International Journal of Modelling & Simulation*, Vol. 17, No. 3, 1997, pp. 242–250.

[71] Videcoq, E. and Petit, D., "Model Reduction for the Resolution of Multidimensional Inverse Heat Conduction Problems," *Int. J. Heat Mass Transfer*, Vol. 44, No. 10, 2001, pp. 1899–1911.

[72] Girault, M. and Petit, D., "Identification methods in nonlinear heat conduction. Part I: model reduction," *Int. Journal of Heat Mass Transfer*, Vol. 48, No. 1, 2005, pp. 105–118.

[73] Girault, M. and Petit, D., "Identification methods in nonlinear heat conduction. Part II: Inverse Problem Using a Reduced Model," *Int. Journal of Heat Mass Transfer*, Vol. 48, No. 1, 2005, pp. 119–133.

[74] Shore, C. P., "Reduction Method for Thermal Analysis of Complex Aerospace Structures," Technical Paper NASA-TP-2373, Langley Research Center, Jan. 1985.

[75] Balakrishnan, N. V., *Nonlinear Transient Thermal Analysis by the Force-Derivative Method*, Ph.D. thesis, Old Dominion University, Norfolk, Virginia, 1995.

[76] Camarda, C. J. and Haftka, R. T., "Development of Higher-Order Modal Methods for Transient Thermal and Structural Analysis," Tech. Rep. NASA TM-101548, NASA Langley Research Center, February 1989.

[77] Camarda, C. J., "Development of Advanced Modal Methods for Calculating Transient Thermal and Structural Response," Tech. Rep. NASA TM-104102, NASA Langley Research Center, December 1991.

[78] Coutinho, A. L. G. A., Landau, L., Wrobel, L. C., and Ebecken, N. F. F., "Modal Solution of Transient Heat Conduction Utilizing Lanczos Algorithm," *International Journal for Numerical Methods in Engineering*, Vol. 28, No. 1, 1989, pp. 13–25.

[79] Cardona, A. and Idelsohn, S., "Solution of Non-Linear Thermal Transient Problems by a Reduction Method," *International Journal for Numerical Methods in Engineering*, Vol. 23, No. 6, 1986, pp. 1023–1042.

[80] Nour-Omid, B., "Lanczos Method for Heat Conduction Analysis," *International Journal for Numerical Methods in Engineering*, Vol. 24, No. 1, 1987, pp. 251–262.

[81] Rose, T., "Using Residual Vectors in MSC/Nastran Dynamic Analysis to Improve Accuracy," *MSC World Users' Conference, Los Angeles, California*, March 1991.

[82] Qin, J. and Nguyen, D. T., "Structure/Load-Dependent Vectors for Linear Structural Dynamic Analysis," *Computers & Structures*, Vol. 50, No. 4, 1994, pp. 515–523.

[83] Rose, T. L., "Using Load-Based Ritz Vectors for Dynamic Analysis of Structures," *Proceedings of the 47th AIAA/ASME/ASCE/AHS/ASC Structures, Structural Dynamics, and Materials Conference, Newport, Rhode Island*, AIAA 2006-1929.

[84] Ricles, J. M. and Léger, P., "Use of Load-Dependent Vectors for Dynamic Analysis of Large Space Structures," *Commun. Numer. Methods Eng.*, Vol. 9, No. 11, 1993, pp. 897–908.

[85] Wilson, E. L., Yuan, M.-W., and Dickens, J. M., "Dynamic Analysis by Direct Superposition of Ritz Vectors," *Earthquake Engineering & Structural Dynamics*, Vol. 10, No. 6, Nov. – Dec. 1982, pp. 813–821.

[86] Idelsohn, S. R. and Cardona, A., "A Load-Dependent Basis for Reduced Nonlinear Structural Dynamics," *Computers & Structures*, Vol. 20, No. 1–3, 1985, pp. 203–210.

[87] Camarda, C. J., Haftka, R. T., and Riley, M. F., "An Evaluation of Higher-Order Modal Methods for Calculating Transient Structural Response," *Computers & Structures*, Vol. 27, No. 1, 1987, pp. 89–101.

[88] Leung, Y. T., "Fast Response Method for Undamped Structures," *Engineering Structures*, Vol. 5, No. 2, April 1983, pp. 141–149.

[89] Borino, G. and Muscolino, G., "Mode-Superposition Methods in Dynamic Analysis of Classically and Non-Classically Damped Linear Systems," *Earthquake Engineering & Structural Dynamics*, Vol. 14, No. 5, 1986, pp. 705–717.

[90] D'Aveni, A. and Muscolino, G., "Improved Dynamic Correction Method in Seismic Analysis of Both Classically and Non-Classically Damped Structures," *Earthquake Engineering & Structural Dynamics*, Vol. 30, No. 4, 2001, pp. 501–517.

[91] Benfratello, S. and Muscolino, G., "Mode-Superposition Correction Method for Deterministic and Stochastic Analysis of Structural Systems," *Computers & Structures*, Vol. 79, No. 26–28, 2001, pp. 2471–2480.

[92] Di Paola, M. and Failla, G., "A Correction Method for Dynamic Analysis of Linear Systems," *Computers & Structures*, Vol. 82, No. 15–16, 2004, pp. 1217–1226.

[93] Holmes, P., Lumley, J., and Berkooz, G., *Turbulence, Coherent Structures, Dynamical Systems and Symmetry*, Cambridge University Press, 1996.

[94] Liang, Y. C., Lee, H. P., Lim, S. P., Lin, W. Z., Lee, K. H., and Wu, C. G., "Proper Orthogonal Decomposition and its Applications–Part I: Theory," *Journal of Sound and Vibration*, Vol. 252, No. 3, 2002, pp. 527–544.

[95] Fic, A., Bialecki, R. A., and Kassab, A. J., "Solving Transient Nonlinear Heat Conduction Problems by Proper Orthogonal Decomposition and the Finite-Element Method," *Numerical Heat Transfer, Part B: Fundamentals*, Vol. 48, No. 2, Aug. 2005, pp. 103–124.

[96] Lumley, J. L., "The Structure of Inhomogeneous Turbulent Flows," *Atmospheric Turbulence and Radio Wave Propagation*, edited by A. Yaglon and V. Tatarsky, Nauka, Moscow, 1967, pp. 166–178.

[97] Krysl, P., Lall, S., and Marsden, J. E., "Dimensional Model Reduction in Non-Linear Finite Element Dynamics of Solids and Structures," *International Journal for Numerical Methods in Engineering*, Vol. 51, No. 4, 2001, pp. 479–504.

[98] Placzek, A., Tran, D., and Ohayon, R., "Hybrid proper orthogonal decomposition formulation for linear structural dynamics," *Journal of Sound and Vibration*, Vol. 318, No. 4-5, December 2008, pp. 943–964.

[99] Hall, K. C., Thomas, J. P., and Dowell, E. H., "Proper Orthogonal Decomposition Technique for Transonic Unsteady Aerodynamic Flows," *AIAA Journal*, Vol. 38, No. 10, October 2000, pp. 1853–1862.

[100] Atwell, J. A. and King, B. B., "Proper Orthogonal Decomposition for Reduced Basis Feedback Controllers for Parabolic Equations," *Mathematical and Computer Modelling*, Vol. 33, No. 1–3, 2001, pp. 1–19.

[101] Bialecki, R. A., Kassab, A. J., and Fic, A., "Proper Orthogonal Decomposition and Modal Analysis for Acceleration of Transient FEM Thermal Analysis," *International Journal for Numerical Methods in Engineering*, Vol. 62, No. 6, 14 Feb. 2005, pp. 774–797.

[102] Bialecki, R. A., Kassab, A. J., and Fic, A., "Reduction of the Dimensionality of Transient FEM Solutions Using Proper Orthogonal Decomposition," *Proceedings of the 36th AIAA Thermophysics Conference, Orlando, Florida*, AIAA 2003-4207.

[103] Önder Efe, M. and Özbay, H., "Proper Orthogonal Decomposition for Reduced Order Modeling: 2D Heat Flow," *Proceedings of the 2003 IEEE Conference on Control Applications, Istanbul, Turkey*, 2003.

[104] Park, H. M., Chung, O. Y., and Lee, J. H., "On the solution of inverse heat transfer problem using the Karhunen-Loève Galerkin Method," *Int. J. Heat Mass Transfer*, Vol. 42, No. 1, 1999, pp. 127–142.

[105] Park, H. M. and Jung, W. S., "The Karhunen-Loève Galerkin Method for the Inverse Natural Convection Problems," *Int. J. Heat Mass Transfer*, Vol. 44, No. 1, 2001, pp. 155–167.

[106] Ostrowski, Z., Bialecki, R. A., and Kassab, A. J., "Estimation of Constant Thermal Conductivity by Use of Proper Orthogonal Decomposition," *Computational Mechanics*, Vol. 37, No. 1, Dec. 2005, pp. 52–59.

[107] Tzong, G., Jacobs, R., and Liguore, S., "Air Vehicle Integration and Technology Research (AVIATR) Task Order 0015: Predictive Capability for Hypersonic Structural Response and Life Prediction: Phase 1-Identification of Knowledge Gaps, Volume 1–Nonproprietary Version," Tech. Rep. AFRL-RB-WP-TR-2010-3068, V1, Air Force Research Laboratory, Wright-Patterson Air Force Base, 2010.

[108] Zuchowski, B., "Air Vehicle Integration and Technology Research (AVIATR) Task Order 0015: Predictive Capability for Hypersonic Structural Response and Life Prediction: Phase 1-Identification of Knowledge Gaps, Volume 1–Nonproprietary Version," Tech. Rep. AFRL-RB-WP-TR-2010-3068, Air Force Research Laboratory, Wright-Patterson Air Force Base, 2010.

[109] Bolender, M. A., "An Overview on Dynamics and Controls Modelling of Hypersonic Vehicles," *Proceedings of the 2009 American Control Conference, St. Louis, MO*, June 2009, pp. 2507–2812.

[110] Falkiewicz, N. J., Cesnik, C. E. S., Crowell, A. R., and McNamara, J. J., "Reduced-Order Aerothermoelastic Framework for Hypersonic Vehicle Control Simulation," *AIAA Journal*, Vol. 49, No. 8, August 2011.

[111] Skujins, T. and Cesnik, C. E. S., "Reduced-Order Modeling of Hypersonic Vehicle Unsteady Aerodynamics," *Proceedings of the 2010 Atmospheric Flight Mechanics Conference, Toronto, Ontario, Canada*, AIAA 2010-8127.

[112] Skujins, T. and Cesnik, C. E. S., "Reduced-Order Modeling of Hypersonic Unsteady Aerodynamics Due to Multi-Modal Oscillations," *Proceedings of the 17th AIAA International Space Planes and Hypersonic Systems and Technologies Conference, San Francisco, California*, AIAA 2011-2341.

[113] Skujins, T. and Cesnik, C. E. S., "On the Applicability of an Unsteady Aerodynamic ROM to the Transonic Regime," *Proceedings of the 2011 Atmospheric Flight Mechanics Conference, Portland, Oregon*, AIAA 2011-6525.

[114] Frendreis, S. G. V., Skujins, T., and Cesnik, C. E. S., "Six-Degree-of-Freedom Simulation of Hypersonic Vehicles," *Proceedings of the 2009 AIAA Atmospheric Flight Mechanics Conference, Chicago, Illinois*, AIAA 2009-5601.

[115] Frendreis, S. G. V. and Cesnik, C. E. S., "3D Simulation of Flexible Hypersonic Vehicles," *Proceedings of the 2010 AIAA Atmospheric Flight Mechanics Conference, Toronto, Ontario, Canada*, AIAA 2010-8229.

[116] Torrez, S. M., Driscoll, J. F., Ihme, M., and Fotia, M. L., "Reduced-Order Modeling of Turbulent Reacing Flows with Application to Ramjets and Scramjets," *Journal of Propulsion and Power*, Vol. 27, No. 2, March–April 2011, pp. 371–382.

[117] Dalle, D. J., Fotia, M. L., and Driscoll, J. F., "Reduced-Order Modeling of Two-Dimensional Supersonic Flows with Applications to Scramjet Inlets," *Journal of Propulsion and Power*, Vol. 26, No. 3, May–June 2010, pp. 545–555.

[118] Torrez, S. M., Dalle, D. J., and Driscoll, J. F., "Multidisciplinary Optimization of the Fuel Consumption of a Dual Mode Scramjet-Ramjet," *Proceedings of the 47th AIAA/ASME/SAE/ASEE Joint Propulsion Conference & Exhibit, San Diego, California*, AIAA 2011-5757.

[119] Dalle, D. J., Torrez, S. M., and Driscoll, J. F., "Performance Analysis of Variable-Geometry Scramjet Inlets Using a Low-Order Model," *Proceedings of the Proceedings of the 47th AIAA/ASME/SAE/ASEE Joint Propulsion Conference & Exhibit, San Diego, California*, AIAA 2011-5756.

[120] Dalle, D. J., Torrez, S. M., and Driscoll, J. F., "Reduced-Order Modeling of Reacting Supersonic Flows in Scramjet Nozzles," *Proceedings of the 46th AIAA/ASME/SAE/ASEE Joint Propulsion Conference & Exhibit, Nashville, Tennessee*, AIAA 2010-6958.

[121] Torrez, S. M., Dalle, D. J., and Driscoll, J. F., "Dual Mode Scramjet Design to Achieve Improved Operational Stability," *Proceedings of the 46th AIAA/ASME/SAE/ASEE Joint Propulsion Conference & Exhibit, Nashville, Tennessee*, AIAA 2010-6957.

[122] Torrez, S. M., Driscoll, J. F., Dalle, D. J., and Micka, D. J., "Scramjet Engine Model MASIV: Role of Mixing, Chemistry, and Wave Interaction," *Proceedings of the 45th AIAA/ASME/SAE/ASEE Joint Propulsion Conference & Exhibit, Denver, Colorado*, AIAA 2009-4939.

[123] Huebner, K., Dewhirst, D., Smith, D., and Byrom, T., *The Finite Element Method for Engineers*, John Wiley & Sons, Inc., 4th ed., 2001.

[124] Chandrupatla, T. and Belegundu, A., *Introduction to Finite Elements in Engineering*, Prentice-Hall, Inc., 3rd ed., 2002.

[125] Dhondt, G. D. C., *The Finite Element Method for Three-Dimensional Thermomechanical Applications*, John Wiley & Sons, 2004.

[126] Çengel, Y. A. and Turner, R. H., *Fundamentals of Thermal-Fluid Sciences*, McGraw-Hill, Inc., 2001.

[127] Holman, J. P., *Heat Transfer*, McGraw-Hill, Inc., 8th ed., 1997.

[128] Sirovich, L., "Turbulence and the Dynamics of Coherent Structures, Part I: Coherent Structures," *Quarterly of Applied Mathematics*, Vol. XLV, No. 3, 1987, pp. 561–571.

[129] Gunzburger, M. and Peterson, J., "Reduced-Order Modeling of Complex Systems with Multiple System Parameters," *Large-Scale Scientific Computing, 5th International Conference, Sozopol, Bulgaria*, edited by I. Lirkov, S. Margenov, and J. Wasniewski, Vol. LNCS 3743, Springer Verlag, 2006, pp. 15–27.

[130] Trefethen, L. N. and Bau, III, D., *Numerical Linear Algebra*, Society for Industrial and Applied Mathematics, 1997.

[131] Heath, M. T., *Scientific Computing : An Introductory Survey*, McGraw-Hill, 2nd ed., 2002.

[132] Chatterjee, A., "An introduction to the proper orthogonal decomposition," *Current Science*, Vol. 78, No. 7, April 2000, pp. 808–817.

[133] Wood, W. L. and Lewis, R. W., "A Comparison of Time Marching Schemes for the Transient Heat Conduction Equation," *Int. J. Numer. Methods Eng.*, Vol. 9, No. 3, 1975, pp. 679–689.

[134] Hirsch, C., *Numerical Computation of Internal & External Flows*, Butterworth-Heinemann, 2nd ed., 2007.

[135] Hughes, T. J. R., "Unconditionally Stable Algorithms for Nonlinear Heat Conduction," *Computer Methods in Applied Mechanics and Engineering*, Vol. 10, 1977, pp. 135–139.

[136] Pendleton, E., Moster, G., and Farmer, M., "Transonic Aeroelastic Models of Hypersonic Highly Swept Lifting Surfaces: Design, Analyses, and Test," *Proceedings of the 35th AIAA/ASME/ASCE/AHS/ASC Structures, Structural Dynamics, and Materials Conference, Hilton Head, South Carolina*, AIAA 1994-1489-574.

[137] Pendleton, E., Moster, G., and Keller, D., "Transonic Aeroelastic Models of Highly Swept Hypersonic Lifting Surfaces," *Journal of Aircraft*, Vol. 32, No. 6, Nov. - Dec. 1995, pp. 1169–1176.

[138] Spain, C. V., Zeiler, T. A., Bullok, E. P., and Hodge, J. S., "A Flutter Investigation of All-Moveable NASP-Like Wings at Hypersonic Speeds," *Proceedings of the 34th AIAA/ASME/ASCE/AHS/ASC Structures, Structural Dynamics, and Materials Conference, La Jolla, California*, AIAA-93-1315.

[139] Shih, P., Prunty, J., and Mueller, R., "Thermostructural Concepts for Hypervelocity Vehicles," *Journal of Aircraft*, Vol. 28, No. 5, May 1991, pp. 337–345.

[140] Myers, D., Martin, C., and Blosser, M., "Parametric Weight Comparison of Advanced Metallic, Ceramic Tile, and Ceramic Blanket Thermal Protection Systems," Tech. Rep. NASA TM-210289, Langley Research Center, June 2000.

[141] Orton, G. and Scuderi, L., "A Hypersonic Cruiser Concept for the 21st Century," *Proceedings of the 1998 World Aviation Conference, Anaheim, California*, AIAA 1998-5525.

[142] Wieting, A., Dechaumphai, P., Bey, K., Thornton, E., and Morgan, K., "Application of Integrated Fluid-Thermal-Structural Analysis Methods," *Thin-Walled Structures*, Vol. 11, No. 1-2, 1991, pp. 1–23.

[143] Leatherwood, J., Clevenson, S., Powell, A., and Daniels, E., "Acoustic Testing of High-Temperature Panels," *Journal of Aircraft*, Vol. 29, No. 6, Nov. - Dec. 1992, pp. 1130–1136.

[144] Blevins, R., Bofilios, D., Holehouse, I., Hwa, V., Tratt, M., Laganelli, A., Pozefsky, P., and Pierucii, M., "Thermo-Vibro-Acoustic Loads and Fatigue of Hypersonic Flight Vehicle Structure," Tech. Rep. AFRL-RB-WP-TR-2009-3139, Air Force Research Laboratory, June 2009.

[145] Ellis, D., Pagel, L., and Schaeffer, D., "Design and Fabrication of a Radiative Actively Cooled Honeycomb Sandwich Structural Panel for a Hypersonic Aircraft," Tech. Rep. NASA-CR-2957, NASA, March 1978.

[146] Ko, W. and Fields, R., "Thermal Stress Analysis of Space Shuttle Orbiter Subjected to Reentry Aerodynamic Heating," Tech. Rep. NASA-TM-88286, NASA, Oct. 1987.

[147] Leyens, C. and Peters, M., *Titanium and Titanium Alloys*, Wiley-VHC, 2003.

[148] Department of Defense, *Military Handbook - MIL-HDBK-5H: Metallic Materials and Elements for Aerospace Vehicle Structures*, December 1998.

[149] Welsch, G., Boyer, R., and Collings, E. W., *Materials Properties Handbook: Titanium Alloys*, ASM International, 1994.

[150] Noor, A. K., editor, *Structures Technology: Historical Perspective and Evolution*, American Institute of Aeronautics and Astronautics, 1998.

[151] "Titanium IMI 834," `http://www.matweb.com/search/DataSheet.aspx?MatGUID=a74096c99aa6486382a9c9e1be0883c4&ckck=1`, Last Accessed 8/22/2011.

[152] Craig, R. R. and Kurdila, A. J., *Fundamentals of Structural Dynamics*, John Wiley & Sons, Inc., 2nd ed., 2006.

[153] Gould, P., *Introduction to Linear Elasticity*, Springer-Verlag, 2nd ed., 1994.

[154] MSC.Software Corporation, Santa Ana, CA, *MSC.Nastran Basic Dynamic Analysis User's Guide: Version 68*, 2004.

[155] Vosteen, L. F., "Effect of Temperature on Dynamic Modulus of Elasticity of Some Structural Alloys," Tech. Rep. NACA Technical Note 4348, Langley Aeronautical Laboratory, Langley Field, Virginia, August 1958.

[156] "Schwarzkopf Pansee PM 2000, Bar Grain Class 6 ODS Iron Alloy Bar," `http://www.matweb.com/search/DataSheet.aspx?MatGUID=3601ea51c9214945a63e9330afb457d3`, Last Accessed 8/20/2011.

[157] Allemang, R. J. and Brown, D. L., "A Correlation Coefficient for Modal Vector Analysis," *Proceedings of the International Modal Analysis Conference*, 1982, pp. 110–116.

[158] Sacks, J., Welch, W. J., Mitchell, T. J., and Wynn, H. P., "Design and Analysis of Computer Experiments," *Statistical Science*, Vol. 4, No. 4, 1989, pp. 409–435.

[159] Simpson, T. W., Mauery, T. M., Korte, J. J., and Mistree, F., "Kriging Models for Global Approximation in Simulation-Based Multidisciplinary Design Optimization," *AIAA Journal*, Vol. 39, No. 12, December 2001, pp. 2233–2241.

[160] Sasena, M. J., *Flexibility and Efficiency Enhancements for Constrained Global Design Optimization with Kriging Approximations*, Ph.D. thesis, University of Michigan, Ann Arbor, Michigan, 2002.

[161] "Titanium Ti-6Al-2Sn-4Zr-2Mo (Ti-6-2-4-2), Duplex Annealed," `http://www.matweb.com/search/DataSheet.aspx?matGUID=3a01802b122647028633c9fa10e6bae8`, Last Accessed 6/30/2009.

[162] Bhatia, M. and Livne, E., "Design-Oriented Thermostructural Analysis with External and Internal Radiation, Part 2: Transient Response," *AIAA Journal*, Vol. 47, No. 5, May 2009, pp. 1228–1240.

[163] Alonso, D., Vega, J. M., and Velazquez, A., "Reduced-Order Model for Viscous Aerodynamic Flow Past an Airfoil," *AIAA Journal*, Vol. 48, No. 9, September 2010, pp. 1946–1958.

[164] Vogel, J. M., Kelkar, A. G., Inger, G., Whitmer, C., Sidlinger, A., and Rodriguez, A., "Control-Relevant Modeling of Hypersonic Vehicles," *Proceedings of the 2009 American Control Conference, St. Louis, MO*, June 2009, pp. 2519–2524.

[165] Gibson, T. E., Crespo, L. G., and Annaswamy, A. M., "Adaptive Control of Hypersonic Vehicles in the Presence of Modeling Uncertainties," *Proceedings of the 2009 American Control Conference, St. Louis, MO*, June 2009, pp. 3178–3183.

[166] Siegel, R. and Howell, J., *Thermal Radiation Heat Transfer*, Taylor & Francis, 4th ed., 2002.

[167] Bhatia, M. and Livne, E., "Design-Oriented Thermostructural Analysis with External and Internal Radiation, Part 1: Steady State," *AIAA Journal*, Vol. 46, No. 3, March 2008, pp. 578–590.

[168] Silva, W. A., "Simultaneous Excitation of Multiple-Input/Multiple-Output CFD-Based Unsteady Aerodynamic Systems," *Journal of Aircraft*, Vol. 45, No. 4, July–August 2008, pp. 1267–1274.

[169] Silva, W. A., "Application of Nonlinear Systems Theory to Transonic Unsteady Aerodynamic Responses," *Journal of Aircraft*, Vol. 30, No. 5, September–October 1993, pp. 660–668.

[170] Raveh, D. E., Levy, Y., and Karpel, M., "Aircraft Aeroelastic Analysis and Design Using CFD-Based Unsteady Loads," *Proceedings of the 41st AIAA/ASME/ASCE/AHS/ASC Structures, Structural Dynamics, and Materials Conference and Exhibit, Atlanta, Georgia*, AIAA 2000-1325.

[171] Raveh, D. E., Levy, Y., and Karpel, M., "Efficient Aeroelastic Analysis Using Computational Unsteady Aerodynamics," *Journal of Aircraft*, Vol. 38, No. 3, May–June 2001, pp. 547–556.

[172] Lieu, T. and Farhat, C., "Adaptation of Aeroelastic Reduced-Order Models and Application to an F-16 Configuration," *AIAA Journal*, Vol. 45, No. 6, June 2007, pp. 1244–1257.

[173] Glaz, B., Liu, L., Friedmann, P. P., Bain, J., and Sankar, L. N., "A Surrogate Based Approach to Reduced-Order Dynamic Stall Modeling," *Proceedings of the 51st AIAA/ASME/ASCE/AHS/ASC Structures, Structural Dynamics, and Materials Conference, Orlando, Florida*, AIAA 2010-3042.

[174] Glaz, B., Liu, L., and Friedmann, P. P., "Reduced Order Nonlinear Unsteady Aerodynamic Modeling Using a Surrogate Based Approach," *Proceedings of the 2010 American Helicopter Society Aeromechanics Specialists Conference, San Francisco, CA*, January 2010.

[175] Glaz, B. and Friedmann, P. P., "Reduced-Order Nonlinear Unsteady Aerodynamic Modeling Using a Surrogate-Based Recurrence Framework," *AIAA Journal*, Vol. 48, No. 10, October 2010, pp. 2418–2429.

[176] Crowell, A. R., McNamara, J. J., and Miller, B. A., "Hypersonic Aerothermoelastic Response Prediction of Skin Panels Using Computational Fluid Dynamic Surrogates," *Journal of Aeroelasticity and Structural Dynamics*, Vol. 2, No. 2, June 2011, pp. 3–30.

[177] Gray, C. E., Mei, C., and Shore, C. P., "Finite Element Method for Large-Amplitude Two-Dimensional Panel Flutter at Hypersonic Speeds," *AIAA Journal*, Vol. 29, No. 2, 1991, pp. 290–298.

[178] Gray, C. E. and Mei, C., "Large-Amplitude Finite Element Flutter Analysis of Composite Panels in Hypersonic Flow," *AIAA Journal*, Vol. 31, No. 6, 1993, pp. 1099–1099.

[179] Bein, T., Friedmann, P., Zhong, X., and Nydick, I., "Hypersonic Flutter of a Curved Shallow Panel with Aerodynamic Heating," *Proceedings of the 34th AIAA/ASME/ASCE/AHS/ASC Structures, Structural Dynamics, and Materials Conference, La Jolla, California*, AIAA 1993-1318.

[180] Nydick, I., Friedmann, P. P., and Zhong, X., "Hypersonic Panel Flutter Studies on Curved Panels," *Proceedings of the 36th AIAA/ASME/ASCE/AHS/ASC Structures, Structural Dynamics, and Materials Conference, New Orleans, Louisiana*, AIAA 1995-1485.

[181] Eckert, E. R. G., "Engineering Relations for Heat Transfer and Friction in High-Velocity Laminar and Turbulent Boundary-Layer Flow Over Surfaces with Constant Pressure and Temperature," *Transactions of the American Society of Mechanical Engineers*, Vol. 78, No. 6, August 1956, pp. 1273–1283.

[182] Eckert, E. R. G., "Survey of Boundary Layer Heat Transfer at High Velocities and High Temperatures," Technical Report WADC Technical Report 59-624, Wright Air Development Center, April 1960.

[183] Eckert, E. R. G., "Survey on Heat Transfer at High Speeds," Technical Report ARL 189, Aeronautical Research Laboratory, University of Minnesota, Minneapolis, MN, December 1961.

[184] Thornton, E. A., *Thermal Structures for Aerospace Applications*, American Institute of Aeronautics and Astronautics, Inc, Reston, Virginia, 1996.

[185] Valdevit, L., Vermaak, N., Hsu, K., Zok, F. W., and Evans, A. G., "Design of Actively Cooled Panels for Scramjets," *Proceedings of the 14th AIAA/AHI Space Planes and Hypersonic Systems and Technologies Conference, Canberra, Australia*, AIAA 2006-8069.

[186] Mangin, B., Benay, R., Chanetz, B., and Chpoun, A., "Optimization of Viscous Waveriders Derived from Axisymmetric Power-Law Blunt Body Flows," *Journal of Spacecraft and Rockets*, Vol. 43, No. 5, September–October 2006, pp. 990–998.

[187] Simon, H. A., Liu, C. S., and Hartnett, J. P., "The Eckert Reference Formulation Applied to High-Speed Laminar Boundary Layers of Nitrogren and Carbon Dioxide," Technical Paper NASA-CR-420, National Aeronautics and Space Administration, April 1966.

[188] Bolender, M. A. and Doman, D. B., "Modeling Unsteady Heating Effects on the Structural Dynamics of a Hypersonic Vehicle," *Proceedings of the 2006 AIAA Atmospheric Flight Mechanics Conference and Exhibit, Keystone, Colorado*, AIAA 2006-6646.

[189] Rudd, L. and Pines, D., "Integrated Propulsion Effects on Dynamic Stability and Control of Hypersonic Waveriders," *Proceedings of the 36th AIAA/ASME/SAE/ASEE Joint Propulsion Conference and Exhibit, Huntsville, Alabama*, AIAA 2000-3826.

[190] Anderson, J. D., *Modern Compressible Flow: With Historical Perspective*, McGraw-Hill, Boston, 3rd ed., 2003.

[191] "Equations, Tables, and Charts for Compressible Flow," Tech. Rep. NACA-1135, National Advisory Committee for Aeronautics, Ames Aeronautical Laboratory, Moffett Field, CA, 1953.

[192] Anderson, J. D., *Fundamentals of Aerodynamics*, McGraw-Hill, Inc., 4th ed., 2007.

[193] Lighthill, M., "Oscillating Airfoils at High Mach Number," *Journal of the Aeronautical Sciences*, Vol. 20, No. 6, June 1953, pp. 402–406.

[194] Ashley, H. and Zartarian, G., "Piston Theory – A New Aerodynamic Tool for the Aeroelastician," *Journal of the Aeronautical Sciences*, Vol. 23, No. 12, 1956, pp. 1109–1118.

[195] Hayes, W. D., "On Hypersonic Similitude," *Quarterly of Applied Mathematics*, Vol. 5, No. 1, April 1947, pp. 105–106.

[196] Hayes, W. D. and Probstein, R. F., *Hypersonic Inviscid Flow*, Dover Publications, Inc, 2004.

[197] Goldsworthy, F. A., "Two-Dimensional Rotational Flow at High Mach Number Past Thin Aerofoils," *The Quarterly Journal of Mechanics & Applied Mathematics*, Vol. 5, No. 1, 1952, pp. 54–63.

[198] Schlichting, H., *Boundary Layer Theory*, McGraw-hill, New York, seventh ed., 1979.

[199] Schultz-Grunow, F., "Neues Widerstandsgesetz für glatte Platten," *Lüfifahrtforschüng*, Vol. 17, 1940, pp. 239.